Vol.2 ,No.1, October 2014

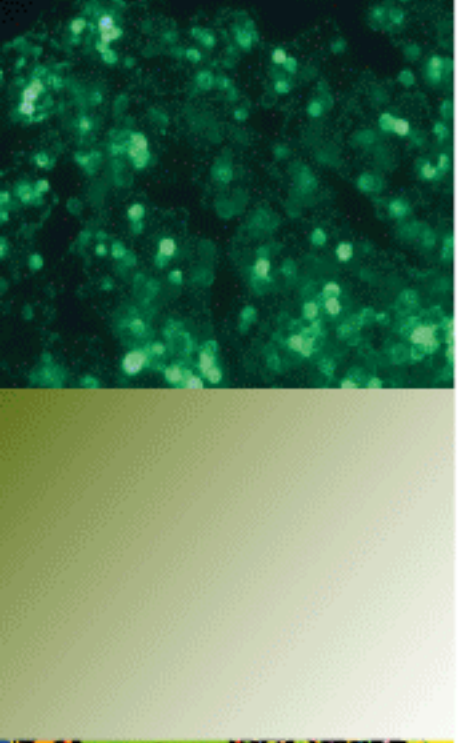

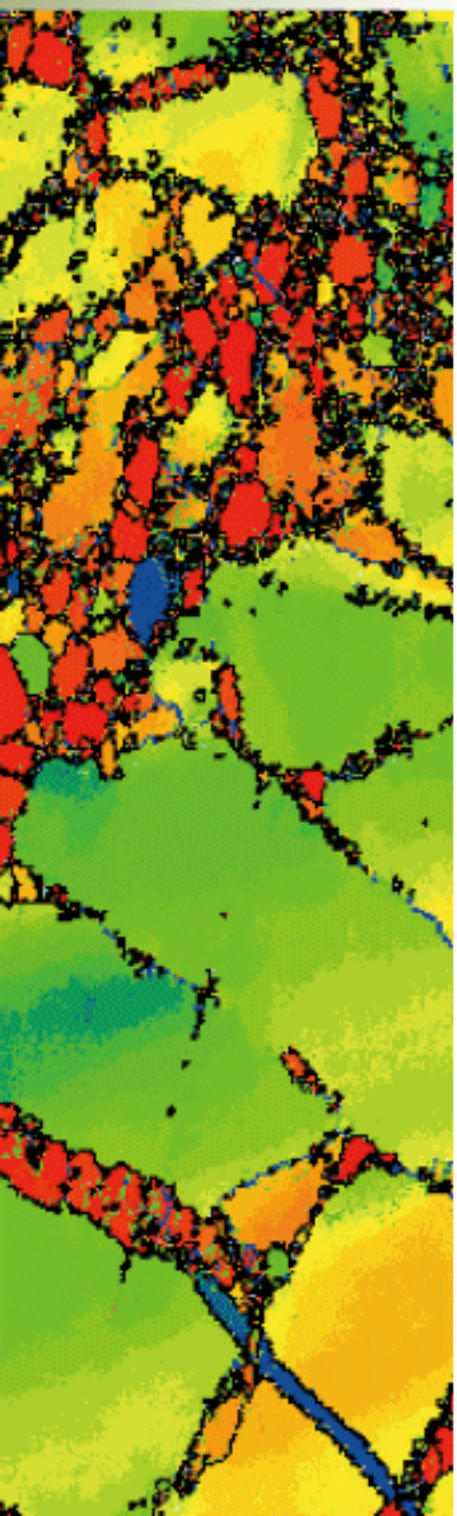

Transactions on GIGAKU

Special issue of
The 2nd International GIGAKU Conference in Nagaoka (IGCN), 2013

GIGAKU Press
Nagaoka University of Technology

Transactions on GIGAKU: Scope and Policy

Nagaoka University of Technology publishes an online, open access journal titled “Transactions on GIGAKU”, which is focused on the science and technology related to GIGAKU*. The mission of this journal is to spread out the concept of GIGAKU and the fruits of GIGAKU to the global world and to be a strong network for innovations in science and technology and for development of next generations of high-level human resources. This journal, therefore, covers research and education activities related to GIGAKU in broad areas.

* See ‘What is GIGAKU?’ below.

‘What is GIGAKU?’

GIGAKU is a term composed of two Japanese word-roots; GI and GAKU. The word GI〔技〕 literally stands for all kinds of arts and technology, and GAKU〔学〕stands for scientific disciplines in general when used as a suffix.

The term was originally coined to describe the fundamental philosophy of education and research of Nagaoka University of Technology (NUT) when it was established in 1976. Through this term the founders of NUT intended to express their recognition that all technical challenges in the real world require a scientific approach. And NUT has a relentlessly pursued GIGAKU since then.

Thirty-five years have passed and all surrounding conditions have changed dramatically during those years. We are witnessing rapidly globalizing economics and huge scale changes in demographic, industrial and employment structures. All those changes seem to necessitate the further evolution of GIGAKU. In response to this, NUT recently announced its new “Growth Plan” and a renewed definition of the term is given;

GIGAKU is a science of technologies, which gives us an angle to analyze and reinterpret diverse technical processes and objects and thus helps us to advance technologies forward. By employing a broad range of knowledge about science and engineering, management, safety, information technology and life sciences, GIGAKU provides us with workable solution and induces future innovations.

July 2012
Koichi Niihara, President of Nagaoka Univesrsity of Technology

Submission and Publishing

"Transactions on GIGAKU" publishes original papers focusing on education, science, and technology related to GIGAKU. Proposals for special issues aligned with conferences are strongly encouraged*, and guest editors are welcomed. Papers submitted are peer-reviewed before publication. Publication charge is free for all submitted papers.

* Please contact to Editor-in chief, itoy@mech.nagaokaut.ac.jp

Copyright

Contact

joho-kiban@jcom.nagaokaut.ac.jp

(Revised January 2014)

Editorial board of special issue of The 2nd International GIGAKU Conference in Nagaoka (IGCN),Vol2. of Transactions on GIGAKU

Transactions on GIGAKU

Volume 2, No. 1, October 2014

The 2nd International GIGAKU Conference in Nagaoka (IGCN)
(June 21-23, 2013, Nagaoka University of Technology, Nagaoka, Japan)

The IGCN is designed and organized to provide a cross-border, cross-sector, cross-disciplinary forum for those researchers, educators, and industrial leaders who are creating and practicing GIGAKU in various technology domains in various countries. Some papers presented in the IGCN are published in this first volume of Transactions on GIGAKU.

Table of contents

Nob. Harada, Weihua Jiang, Akira Tokuchi

16. Pages 02016/1-10

An Assessment of Radionuclide Transport in the Atmosphere -A Case Study of Hypothetical Reactor Accident in Ninh Thuan Province, Vietnam-

Ho Quoc Dung, Mikami Yoshiki

17. Pages 02017/1-6

Investigation of reaction selectivity for oxygen reduction in the presence of methanol at sputtered Co-C-N electrocatalyst

Sayoko Shironita, Yosuke Matsumoto, Minoru Umeda

Electronic Approach to Alloy Design

Masahiko Morinaga
Toyota Physical & Chemical Research Institute,
41-1 Nagakute, Aichi 480-1192, Japan
**E-mail: morinaga@toyotariken.jp*

Electronic approach to alloy design has recently made great progress. A unified approach based on the atomization energy concept is reviewed focusing mainly on the understanding of the chemical bond in hydrides without using the standard concept of covalent and ionic bonds. Namely, the atomization energies, ΔE_H for hydrogen atom and ΔE_M for metal atom in each hydride are evaluated by using the energy density analysis of the total energy, and then a ΔE_H vs. ΔE_M diagram is constructed. All the hydrides, including metal hydrides and complex hydrides can be located on this diagram, despite the significant differences in the nature of the chemical bond among them. Also, it is found in hydrocarbons, C_mH_n that the cohesive energy depends only on m and n. Furthermore, following this approach, the catalytic effect of metal oxides (e.g., Nb_2O_5) can be estimated quantitatively on the dehydrogenation reaction of MgH_2, expressed as, $MgH_2 \rightarrow Mg + H_2$. In addition, this approach is applied to a variety of transition metal-based compounds such as borides, carbides, nitrides, oxides and fluorides to make a new platform for the design of functional compounds.

1. Introduction

Nowadays, total energy calculation is so common in every field of materials science. However, as predicted by Wigner and Seitz [1], information of the chemical bond between atoms in solids is still limited along the total energy calculation alone. The Mulliken population analysis [2] is also widely used in the field of molecular orbital calculations, and the nature of the chemical bond between atoms is interpreted using the standard concept of covalent and ionic bonds. However, along this analysis it is still difficult to compare quantitatively the chemical bond strengths among a variety of materials, because both covalent and ionic interactions are operating in most materials. To solve this problem, the chemical bond should be estimated quantitatively in an energy scale.

Recently, Nakai has proposed a new analyzing method of the total energy called energy density analysis (EDA) [3]. In this method, the total energy of a system, computed by the Kohn-Sham-type density functional theory (DFT) [4], is partitioned into atomic energy densities, and the characteristics of the chemical bond are understood in terms of each atomic energy density instead of the total energy. Recently, we have applied this method to the analysis of the chemical bond between atoms in various hydrides and hydrocarbons for hydrogen storage [5,6] and also in oxides [7,8]. In this analysis, the atomization energy for each constituent atom is newly defined by subtracting the atomic energy density from the total energy of the isolated atom, and used for comparing quantitatively the nature of the chemical bond between atoms among a variety of materials in an energy scale. Such an atomization energy analysis is more quantitative than the analysis of covalent or ionic bonds in any materials. The usefulness of this approach is proved through the quantitative analysis of the catalytic effect of metal oxides on the dehydrogenation reaction of MgH_2 [9,10].

In this paper, this approach using atomization energy concept is reviewed in a consistent way.

2. Calculation Method

2.1 Geometry optimization and energy density analysis

The positions of hydrogen in the hydrides are sometimes difficult to be determined experimentally. So, the crystal structures of crystalline hydrides are optimized by the total energy minimization using a plane-wave pseudopotential method [11]. Also, the molecule structures of hydrocarbons are optimized using the AM1 method [12]. The electronic structures are obtained by the DFT calculation with the BLYP functional. For hydrides, the energy density analysis (EDA) is performed under the periodic boundary condition (PBC) by liking the original code for the EDA with Gaussian03. Similar calculations except for the PBC are also performed for hydrocarbons. It is confirmed from a series of calculations that the differences between calculated and experimental cohesive energies are less than 0.4 eV for binary hydrides and 0.2 eV for hydrocarbons [5].

2.2 Atomization energy

For binary hydrides, MH, the respective atomic energy densities of M and H are related closely to the nature of the chemical bond relevant to M and H atoms in MH [5]. When the energy of the isolated neutral atom, $E_{\mathrm{H}}^{\mathrm{atom}}$ (or $E_{\mathrm{M}}^{\mathrm{atom}}$) is taken as a reference, the atomization energy, ΔE_{H} (or ΔE_{M}) is defined as,

$$\Delta E_{\mathrm{H}} = E_{\mathrm{H}}^{\mathrm{atom}} - E_{\mathrm{H}}^{\mathrm{hydride}} \quad , \tag{1}$$

$$\Delta E_{\mathrm{M}} = E_{\mathrm{M}}^{\mathrm{atom}} - E_{\mathrm{M}}^{\mathrm{hydride}} \quad , \tag{2}$$

where $E_{\mathrm{M}}^{\mathrm{hydride}}$ and $E_{\mathrm{H}}^{\mathrm{hydride}}$ are the atomic energy densities for M and H in MH, respectively. In case of the ternary hydrides, (M1M2)H_n, ΔE_{M} is defined as $(\Delta E_{\mathrm{M1}} + \Delta E_{\mathrm{M2}})/n$, that is the average atomization energy of M1 and M2 to be counted per hydrogen atom. Even in the other type of ternary hydrides, ΔE_{M} is defined in a similar way.

The cohesive energy, E_{coh}, of the hydride per hydrogen atom is defined as,

$$E_{\mathrm{coh}} = \Delta E_{\mathrm{M}} + \Delta E_{\mathrm{H}} \quad . \tag{3}$$

Thus, ΔE_{M} and ΔE_{H} are the components of E_{coh}. The cohesive energy is the energy gained by arranging the atoms in a crystalline solid, as compared with the gas state. The atomization energy is a measure of the chemical bonding effect of the element on the stability of the hydride. By setting that $Y = \Delta E_{\mathrm{H}}$ and $X = \Delta E_{\mathrm{M}}$, we obtain a relation, $Y = -X + E_{\mathrm{coh}}$. So, E_{coh} is expressed as a point of intersection of this line and the *Y*-axis at *X* = 0.

For hydrocarbons expressed as a chemical formula, $\mathrm{C}_m\mathrm{H}_n$, ΔE_{H} and ΔE_{C} are defined as,

$$\Delta E_{\mathrm{H}} = E_{\mathrm{H}}^{\mathrm{atom}} - E_{\mathrm{H}}^{\mathrm{hydrocarbon}} \quad , \tag{4}$$

$$\Delta E_{\mathrm{C}} = (E_{\mathrm{C}}^{\mathrm{atom}} - E_{\mathrm{C}}^{\mathrm{hydrocarbon}}) \times (m/n) \quad . \tag{5}$$

Here, ΔE_{C} is the average atomization energy of carbon per hydrogen atom in $\mathrm{C}_m\mathrm{H}_n$ [5].

3. Atomization Energy Diagram for Hydrides and Hydrocarbons

A ΔE_{H} vs. ΔE_{M} diagram is hereafter called “atomization energy diagram”. The advantage of using the atomization energy is to know a role of each constituent element in the hydride formation that is never able to be obtained from the total energy calculation alone.

For a variety of crystalline hydrides, such as binary hydrides, perovskite-type hydrides, metal hydrides, complex hydrides, and hydrocarbons as well, an atomization energy diagram is constructed on an energy scale, as shown in Fig.1. It is stressed here that every hydride can be shown in one figure, although there are significant differences in the nature of the chemical bond among the hydrides and hydrocarbons. E_{coh}, given in Eq. 3 lies in the range of 3 – 9 eV. As a whole, this range

of E_{coh} is much smaller compared with the ranges of atomization energy, 0 eV $<\Delta E_H<$18 eV and –11 eV$<\Delta E_M<$5 eV. Thus, each atomic state is well controlled or balanced in the hydrides and –11 eV$<\Delta E_M<$5 eV. Thus, each atomic state is well controlled or balanced in the hydrides and hydrocarbons so as to make E_{coh} as large as possible. Among the hydrides, a binary hydride, AlH_3 (No.3), shows the smallest cohesive energy, 3.2 eV, so it releases hydrogen at a low temperature [13], but the re-hydrogenation reaction never occurs in the moderate condition because of its poor stability. This is also seen in a complex hydride, $Mg(AlH_4)_2$ (No.17), where both E_{coh} and ΔE_H values are small [14].

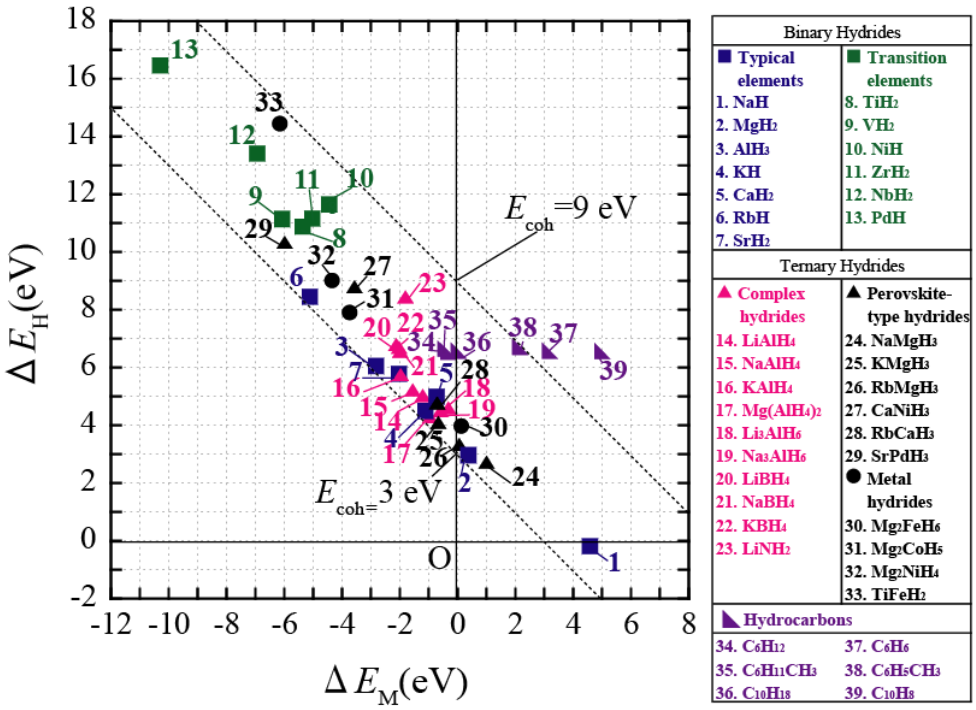

Fig. 1 Atomization energy diagram for hydrides and hydrocarbons.

It is evident from Fig.1 that hydrides of transition elements (e.g., NbH_2 (No.12)) have high ΔE_H values. The region of complex hydrides is overlapped with that of the hydrides of the more common elements on this diagram. Also, the locations of metal hydrides are distributed over the wide range of ΔE_H, and some of them are located near the region of complex hydrides. In fact, Mg_2NiH_4 (No.32), Mg_2CoH_5 (No.31) and Mg_2FeH_6 (No.30) are sometimes treated as complex hydrides instead of metal hydrides [15]. In Fig.1, Mg_2FeH_6 and Mg_2CoH_5 are located near the lower and upper region of complex hydrides, respectively. However, Mg_2NiH_4 is located in the region between the hydrides of transition elements and the complex hydrides, indicating the coexistence of the characteristics of both metal and complex hydrides in Mg_2NiH_4. Thus, the atomization energy diagram reflects important characteristics of the chemical bonds in hydrides.

For a variety of hydrocarbons, C_mH_n, including alkanes, cycloalkanes, alkenes, alkines and arenes, ΔE_H and ΔE_C are plotted against *m/n*, as shown in Fig.2. Here, ΔE_C is the atomization energy weighted by a factor, *m/n*, following Eq.5. ΔE_C is therefore the component of the cohesive energy partitioned into the carbon per hydrogen atom. As is evident from Fig.2, ΔE_C increases linearly with the *m/n* ratio. This indicates that the slope expressed as, $(E_C^{atom} - E_C^{hydrocarbon})$, is almost constant, regardless of the type of hydrocarbons. Also, ΔE_C is expressed approximately as,

$$\Delta E_C(\text{eV}) = 7.46 \times (m/n) - 4.46 \quad . \qquad (6)$$

On the other hand, ΔE_H is a constant, 6.76 eV, regardless of the type of hydrocarbons. So, the cohesive energy per hydrogen atom in hydrocarbons, E_{coh}, can be expressed as,

$$E_{coh}(\text{eV}) = 7.46 \times (m/n) + 2.30 \quad . \qquad (7)$$

This simple relationship is satisfied in all the hydrocarbons. Thus, by using the atomization energies, ΔE_C and ΔE_H, the nature of the chemical bonds in any hydrocarbons can be understood without using the usual concept of single or multiple C-C bonds.

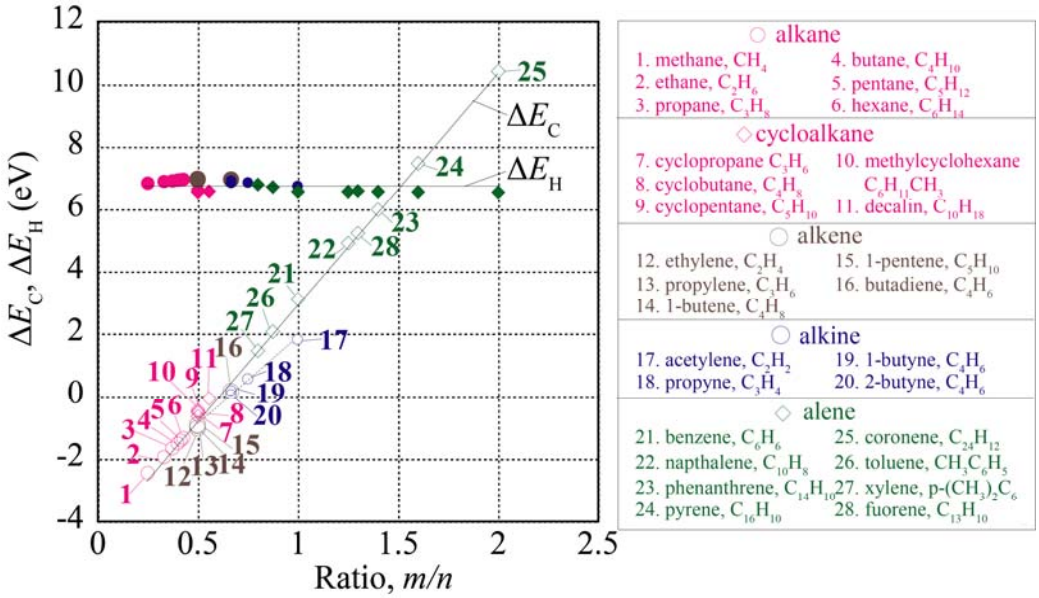

Fig. 2 Change in ΔE_C and ΔE_H with *m/n* in various hydrocarbons, C_mC_n.
ΔE_C and ΔE_H are expressed by solid and open symbols, respectively.

4. Application to Quantitative Evaluation of Catalytic Effect

The hydrogen desorption reaction of magnesium hydride (MgH_2), $MgH_2 \rightarrow Mg + H_2$, is accelerated by mixing some metal oxides (e.g., Nb_2O_5). To explain this catalytic activities of metal oxides, the atomization energy diagram, ΔE_M vs. ΔE_O, is calculated for binary metal oxides, M*x*O*y* [7], as shown in Fig.3. The contribution of each element in the oxide to the cohesive energy is understood from this figure. For example, the cohesive energy is nearly same between NbO_2 and Al_2O_3 (NbO_2: E_{coh} =10.1 eV, Al_2O_3: E_{coh} =10.7 eV). However, they are located in the very different positions in Fig.3. NbO_2 has a large ΔE_O value, but a very small ΔE_M value, indicating that the oxide ions in NbO_2 make a significant contribution to the cohesive energy. On the other hand, in case of Al_2O_3, the ΔE_O value is almost zero, but instead the ΔE_M value is very large. This indicates that the metal ions in Al_2O_3 contribute mainly to the cohesive energy. In this way, using the atomization energy diagram, the role of each constituent element in the stability of metal oxides can be understood in a straightforward manner.

The catalytic effect of metal oxides, M*x*O*y*, on the hydrogen desorption reaction has been measured experimentally with the MgH_2 specimens doped by 1mol% M*x*O*y* [16]. It is theoretically

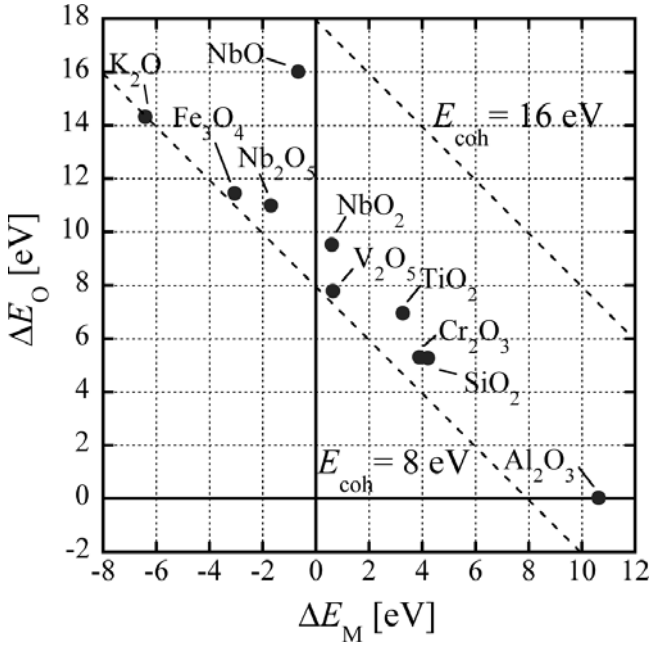

Fig.3 Atomization energy diagram for metal oxides.

estimated in a quantitative way using atomization energy concept [9]. As shown in Fig.4, the measured hydrogen desorption rate increases monotonously with increasing $y \times \Delta E_O$ values of metal oxides. This $y \times \Delta E_O$ value is the energy of oxide ions in one molecule unit of M*x*O*y*. The result shown in Fig.4 indicates clearly that the oxide ions in M*x*O*y* interact mainly with hydrogen atoms in MgH_2. In other words, the $y \times \Delta E_O$ value is a measure of the magnitude of the O-H interaction operating between M*x*O*y* and MgH_2, and hence it is indeed a good parameter to show the catalytic activities of metal oxides. The presence of the O-H interaction is confirmed experimentally through the observation of the O-H stretching mode in the FT-IR spectra during the dehydrogenation of the Nb_2O_5-catalyzed MgH_2 as shown in Fig.5 [10]. Namely, the spectrum is rather strong in (a) for H non-released specimen, but it becomes weak gradually from (b) for 2.3% H released specimen to (d) for all H released specimen with the progress of the dehydrogenation reaction in it.

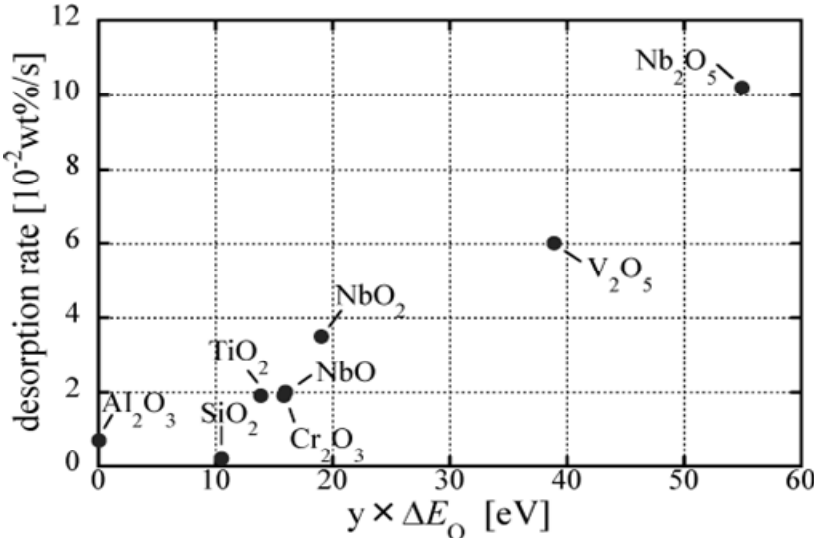

Fig.4 Correlation of $y \times \Delta E_O$ with the measured desorption rate of MgH_2 with 1 mol% M*x*O*y* oxide catalysts.

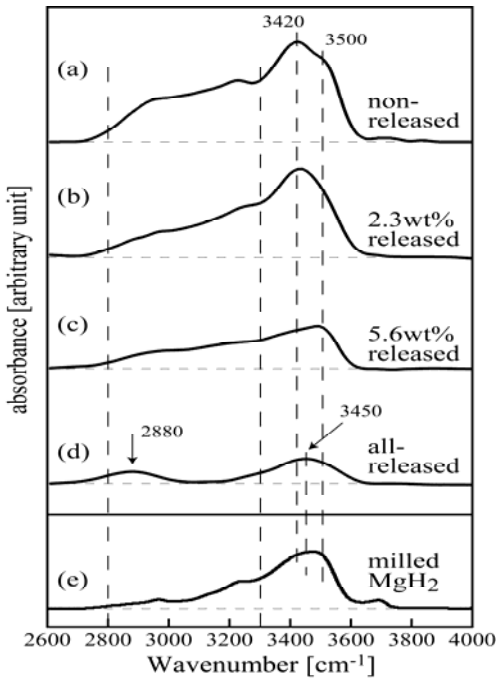

Fig.5 FT-IR spectra of MgH_2 with 1 mol% Nb_2O_5 in the region of 2600 to 4000 cm^{-1} where the O-H stretching mode works dominantly.

This approach is also found to be useful for the quantitative evaluation of the catalytic effect of metal chlorides (e.g., $TiCl_3$) on the decomposition reaction of $NaAlH_4$, expressed as, $NaAlH_4 \rightarrow 1/3Na_3AlH_6 + 2/3Al + H_2$ [17].

5. Atomization Energy Diagram for Transition Metal-based Compounds

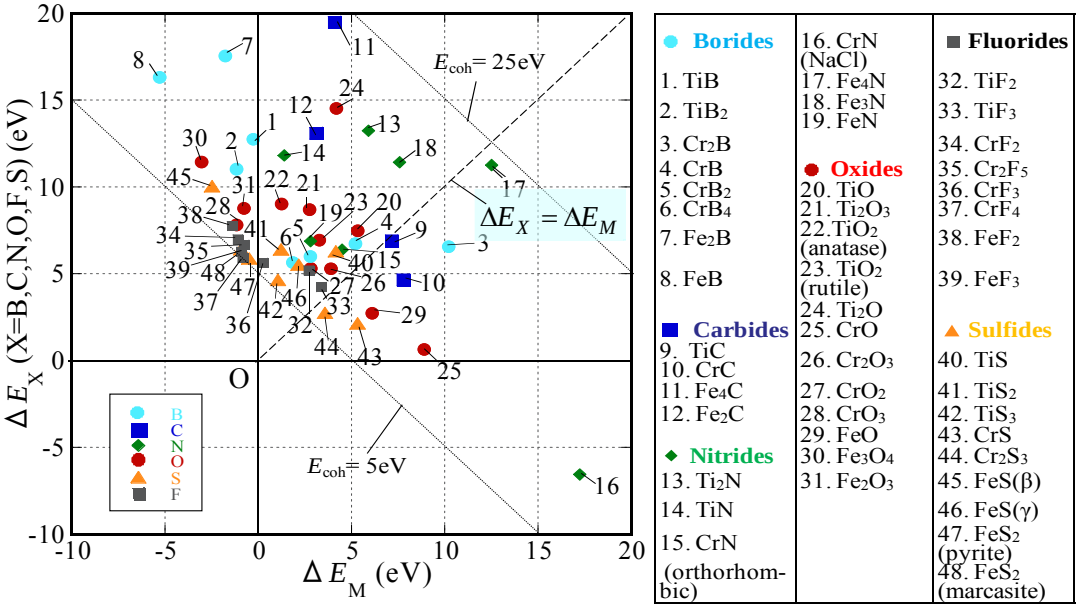

Fig.6 Atomization energy diagram for transition metal-based compounds.

The transition metal based-compounds such as borides, carbides, nitrides, oxides, fluorides and sulfides possess a variety of physical properties such as superconductivity (e.g.,$LaFeAsO_{1-x}F_x$), ferroelectricity (e.g.,$BaTiO_3$), ferromagnetism (e.g.,$Nd_2Fe_{14}B$) and proton conductivity (e.g., $SrTiO_3$). It is a real challenge to treat all these compounds by using the same calculation method of electronic structures, and to compare the characteristics of each compound in view of non-metal elements (e.g., B, C, N, O, F, S etc). The analysis of the atomization energy is suitable for this purpose, since any compounds are treatable in an energy scale even when the chemical bond characters are very different among the compounds. The atomization energy diagram is now being made for 3d transition metal-based compounds. A part of the results is shown in Fig.6 [18]. A final goal of this study is to develop a new method for the design of functional compounds, while keep standing on the common ground of non-metal elements rather than metal elements.

6. Conclusion

A unified approach based on the atomization energy concept is proposed for treating the chemical bond in hydrides and hydrocarbons. Also, this is found to be useful for the understanding of the bond character in the oxides and other compounds. It is concluded that this is a powerful electronic approach to design and develop new materials and to support the technical innovation for solving the energy and environmental issues in the 21st century.

Acknowledgments

The author would like to express sincere thanks to Prof. H. Yukawa, Prof. M. Yoshino of Nagoya University and Prof. H. Nakai of Waseda University for their collaboration on this study. This study was supported by a Grant-in-Aid for Scientific Research from the Ministry of Education, Culture, Sports, Science and Technology of Japan, and from the Japan Society for the Promotion of Science.

References

[1] E. P. Wigner and F. Seitz, Solid State Phys**. 1** (1955) 97.
[2] R. S. Mulliken, J. Chem. Phys. **23** (1955) 1833.
[3] H. Nakai, Chem. Phys. Lett., **363** (2002) 73.
[4] W. Kohn and L. J. Sham, Phys. Rev. **140** (1965) A1133.
[5] Y. Shinzato, H. Yukawa, M. Morinaga, T. Baba and H. Nakai, Acta Materialia, **55** (2007) 6673.
[6] Y. Shinzato, H. Yukawa, M. Morinaga, T. Baba and H. Nakai, Advances in Quantum Chemistry,**54** (2008) 145.
[7] Y. Shinzato, Y. Saito, M. Yoshino, H. Yukawa, M. Morinaga, T. Baba and H. Nakai, J. Phys .Chem. Solids, **72** (2011), 853.
[8] H. Hirate, H. Sawai, Y. Saito, H. Yukawa, M. Morinaga and H. Nakai, Journal of the American Ceramic Society, **93** (2010) 3449.
[9] H.Hirate, Y.Saito, I.Nakaya, H.Sawai, Y.Shinzato, H.Yukawa, M.Morinaga, T.Baba and H.Nakai, Int J Quant Chem., **109** (2009) 2793.
[10] H. Hirate, H. Sawai, H. Yukawa and M. Morinaga, Int J Quant Chem., **111** (2011) 2251.
[11] J.P. Perdew, K. Burke and Y. Wang, Phys. Rev. B, **54** (1996) 16533.
[12] M.J.S. Dewar and W. Thiei, J. Am. Chem. Soc. **99** (1977) 4899.
[13] J. Graetz, and J. J. Reilly, J. Alloys Compd., **424** (2006) 262.
[14] K. Komiya, N. Morisaku, Y. Shinzato, K. Ikeda, S. Orimo, Y. Ohki, K. Tasumi, H. Yukawa and M. Morinaga, J. Alloys Compd., **446** (2007) 237.
[15] K. Yvon, Chimia, **52** (1998) 613.
[16] G. Barkhordarian, T.Klassen and R.Bormann, J. Phys. Chem. B, **110** (2006) 11020.
[17] H. Hirate, Y. Saito, I. Nakaya, H. Sawai, H. Yukawa, M. Morinaga and H. Nakai, Int J Quant Chem., **111** (2011) 950.
[18] M.Morinaga, Y.Saito, K.Ito, H.Yukawa, M.Yoshino and H.Nakai, Bulletin of the Society for Discrete Variational Xα, **24** (2011) 85.

(Received: 26 June, 2013, Accepted: 17 October 2013)

Structural Analysis of TiO_2 Particles Synthesized from Ti-EDTA•NH_4 Complex

Keiji Komatsu[1*], Yasuhiro Hasebe[1], Tetsuo Sekiya[1], Atsushi Nakamura[1,2], Shigeo Ohshio[1], Hiroki Akasaka[1], Ikumi Toda[1], Hidetoshi Saitoh[1]

[1]Department of Materials Science and Technology, Nagaoka University of Technology,
[2]Chubu Chelest Co. Ltd., 3-3-3 Hinagahigashi, Yokkaichi, Mie 510-0886, Japan,
**E-mail: Keiji_Komatsu@mst.nagaokaut.ac.jp*

Porous TiO_2 particles with micro-scale particle size were synthesized from a Ti-ethylenediaminetetraacetic acid (EDTA)•NH_4 complex using a commercial flame spray apparatus. In addition, crystal structure, surface morphology, and organic constituents of the synthesized particles were investigated. A calibration curve method was used for quantitative analysis of the crystalline phases of the synthesized particles. The crystalline phase and the morphology of the particles varied after annealing in an electric furnace. Visual observation revealed that the porous TiO_2 particles were black in color and had a diameter of approximately 100 μm before annealing, and their color turned white after annealing. The weight ratio of the rutile phase of the particles increased from 61.9% to 84.3%, while that of the anatase phase decreased from 38.1% to 15.7% with increasing annealing temperature. Fourier transform infrared spectra confirmed that no organic constituent originating from the Ti-EDTA•NH_4 complex existed in the synthesized particles after annealing.

1. Introduction

Titanium oxide (TiO_2) has attracted significant research interests owing to its use in a wide range of applications, such as photocatalysts [1,2] and solar cells [3]. In addition , electric devices[4], medical and dental [5] applications for TiO_2 were reported. The synthesis of TiO_2 usually involves a liquid or gas phase, and the resulting TiO_2 can vary from being particle-like (micron- and nanosized) to film-like in morphology [6-8]. For example, highly oriented polycrystalline TiO_2 films have been fabricated by atmospheric chemical vapor deposition [9]. Characteristics of TiO_2, such as its electric properties, depend on its crystal structure and the method used to synthesize it.

The structural transition behavior of TiO_2 is important from the viewpoint of commercial applications. TiO_2 exists in three types of crystal phases: anatase, rutile, and brookite [10]. From a thermodynamic point of view, rutile is the stable phase, while anatase and brookite are metastable phases. Given the wide applicability of TiO_2, the structural behaviors of the anatase and rutile forms of TiO_2 have been investigated in great detail by adding other elements to these phases [11] and subjecting the mixture to tests involving annealing [12,13] and the application of pressure [14]. The results of these analyses have suggested that the structural behaviors of the different forms of TiO_2 depend on the synthesis method used.

Recently, a new synthesis technique based on metal-ethylenediaminetetraacetic acid (EDTA) complexes was developed for fabricating metal oxide films [15]. Y_2O_3 films were fabricated on a stainless steel (SUS) substrate using a Y-EDTA complex powder and a commercial flame sprayer. The metal-EDTA complexes generally decompose at 300–400°C in air, resulting in the formation of the metal oxide owing to oxidation. In another method, hollow metal oxide particles were fabricated from solutions of metal-EDTA complexes using a spray drying apparatus [16]. The thus-fabricated metal oxide particles are, owing to their suitable compositions, used for material design for phosphor synthesis [17,18]. A scanning electron microscope (SEM) image of the surface of the Y_2O_3 film fabricated from Y-EDTA complex powder is shown in Fig. 1. The Y_2O_3 particles of a flat morphology are seen in the image; these particles are indicated by the square labeled (a). The flat morphology was the result of the decomposition and oxidation of the Y-EDTA complex. In addition to the flat particles, spherical Y_2O_3 particles of diameters of 1–3 μm are also be observed; see the square labeled (b). These results suggest that it should be possible to fabricate dense, spherical TiO_2 particles on a large scale from Ti-based EDTA complexes

such as Ti-EDTA•NH_4.

In this study, we synthesized the TiO_2 particles from the Ti-EDTA•NH_4 complex using the flame spray apparatus. The structure of the TiO_2 particles after being subjected to annealing treatments was characterized; the characterization was described and discussed. Figure 2 shows a schematic of the reaction process that takes place when the metal-EDTA complex is introduced into a flame. First, the precursor melts and thermally decomposes, resulting in the production of the gaseous CO_2, H_2O, and NO_2 (Process 1 in Fig. 2). Metal ions, which are released from the chelating ligand, are then oxidized to metal oxide particles, which then undergo rapid cooling. These cooled particles then solidify rapidly (Process 2 in Fig. 2). The thus-synthesized TiO_2 particles were then annealed at 400–600°C in an electric furnace. The crystal structure, surface morphology, and the phase composition of the particles were then analyzed.

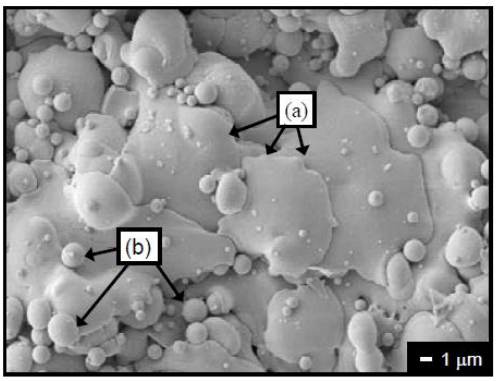

Fig. 1 SEM image of the surface of a Y_2O_3 film fabricated from a Y-EDTA complex. (a) Y_2O_3 particles with splatted morphologies (b) Y_2O_3 particles with spherical morphologies.

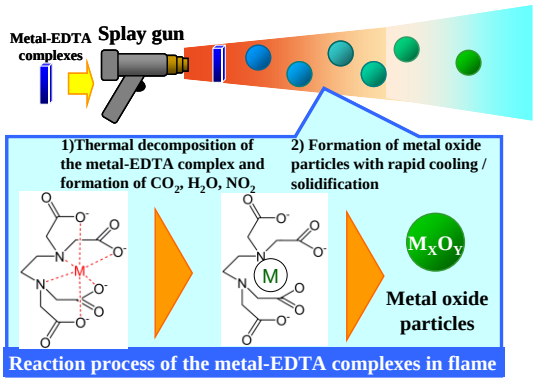

Fig. 2 Schematic of the reaction occurring when a metal-EDTA complex is introduced into a flame.

2. Experimental

First, the crystalline Ti-EDTA•NH_4 complex (Chubu Chelest Co., Ltd.), used as the precursor for the synthesis of the TiO_2 particles, was prepared. The prepared complex powder was then used to fabricate the particles. A schematic diagram and a photograph of the equipment used to prepare the TiO_2 particles are shown in Fig. 3. The conventional flame spray apparatus, consisting of a feed unit (5 MPE, Sulzer Metco) and a spray gun (6P-II, Sulzer Metco), was used to perform reactive spraying. This apparatus is generally used commercially for depositing metal films using an acetylene flame. The Ti-EDTA•NH_4 was then placed into the feed unit and transported by N_2 gas into the spray gun when the vibrator in the feed unit was turned on. A mixture of H_2 and O_2, with the gases flowing at the rates of 70 and 90 L/min, respectively, was used as the flame gas. When the Ti-EDTA powder was introduced into the flame, the EDTA decomposed thermally and the Ti present in the powder reacted with oxygen. The TiO_2 particles formed were then sprayed into a stainless container (Tokyo Screen Co., Ltd.) and collected. The spray nozzle was moved progressively in a longitudinal direction. The deposition duration was approximately 6 s in each area. Next, the obtained TiO_2 particles were annealed at 400–600°C for 1 h in an electric furnace.

The particle size distribution of raw Ti-EDTA powder was analyzed using a particle size analyzer (MT-3300, Nikkiso). The crystal structure of the synthesized TiO_2 particles was determined using an X-ray diffractometer (M03XHF22, MAC Science Co., Ltd.) employing Cu Kα radiation. The calibration curve method was applied for the quantitative determination of the phase composition of the particles. The calibration curve was prepared using commercial anatase TiO_2 powder (purity: ~99%, Sigma Aldrich). Commercial TiO_2 powder was annealed at 1000°C for 10 h in the muffle furnace. First, as-prepared TiO_2 powder was annealed to obtain the two types of TiO_2 phases, rutile and anatase. The annealed powders were then mixed with the commercial TiO_2 powder in the following percentages by weight: 0%, 20%, 40%, 60%, 80%, and 100%. The surface and cross-sectional morphologies of the TiO_2 particles were observed using field-emission scanning electron microscopy (FESEM) (JSM-6700F, JEOL Ltd.). The organic matter remaining in the films after the annealing process was investigated through

Fourier transform infrared (FTIR) spectroscopy (IMPACT-410, Nicolet) using the attenuated total reflection method.

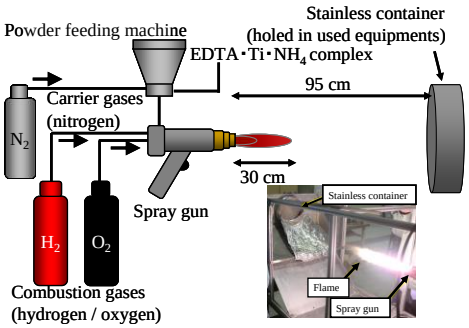

Fig. 3 Schematic diagram and photograph of the apparatus used to synthesize the TiO_2 particles.

3. Results and Discussion

Figure 4 shows an SEM image of the crystal particles of the Ti-EDTA•NH_4 complex. The particles of the complex were box-shaped and had a diameter of 50–200 μm. From the results of the measurement of the particle size distribution, the average diameter of the particles (median diameter D_{50}) was found to be 189.3 μm. The thermogravimetric (TG)-differential thermal analysis (DTA) profiles of the Ti-EDTA•NH_4 complex are shown in Fig. 5. Endothermic peaks can be seen at approximately 300°C; the maximum was noticed at approximately 470°C. These results suggest that the decomposition of the Ti-EDTA•NH_4 powder and the oxidation of Ti were both induced by the H_2-O_2 flame. The temperature of the H_2-O_2 flame was less than 1727°C(2000K).

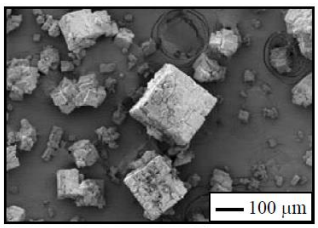

Fig. 4 SEM image of the crystals of the Ti-EDTA•NH_4 complex.

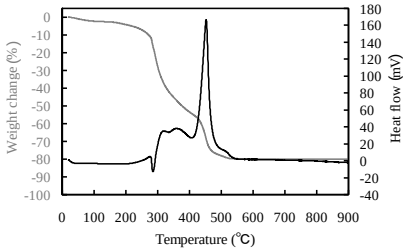

Fig. 5 TG-DTA profiles of the Ti-EDTA•NH_4 complex.

Photographs of the synthesized TiO_2 particles, before and after being annealed at 400–600°C in the muffle furnace, are shown in Fig. 6. Before being annealed, the color of the particles was black. As a result of the annealing treatment, the particles progressively turned white. As the annealing temperature was increased, the black particles first turned grayish black, then yellow, and then finally white. The initial black appearance is likely owing to the absence of oxygen and organic constituents (contained carbon atom species, such as the –COOH and -COO groups) in the as-fabricated particles. During the synthesis process, hydrogen gas, which was used as one of the combustion gases, acted as a reductant. We measured the weight of each sample before and after the annealing process to determine the reason for the absence of oxygen and organic constituents in the annealed particles. A decrease in weight of approximately 65% was confirmed. It is assumed that the organic constituents reacted with oxygen during the annealing treatments and were released from the particles in the form of CO_2.

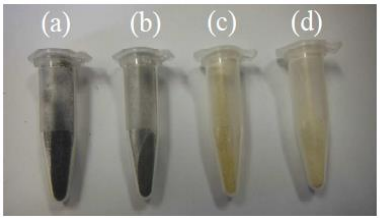

Fig. 6 A photograph of the particles synthesized from the Ti-EDTA•NH_4 complex (a) Before being annealed, (b) after annealing at 400°C, (c) after annealing at 500°C, and (d) after annealing at 600°C.

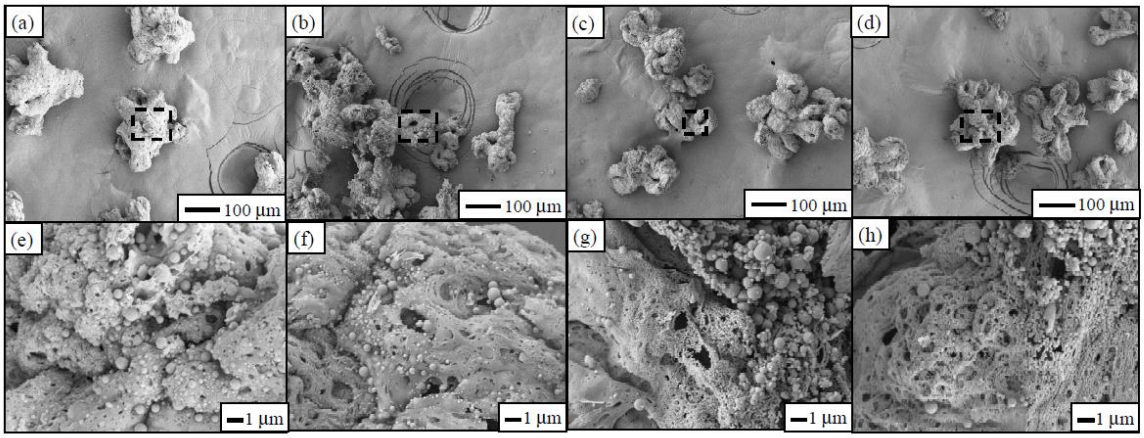

Fig. 7 SEM images of the particles synthesized from the Ti-EDTA•NH_4 complex. (a) Before being annealed (low magnification), (b) after annealing at 400°C for 1 h (low magnification), (c) after annealing at 500°C for 1 h (low magnification), (d) after annealing at 600°C for 1 h (low magnification), (e) before annealing (high magnification), (f) after annealing at 400°C for 1 h (high magnification), (g) after annealing at 500°C for 1 h (high magnification), and (h) after annealing at 600°C for 1 h (high magnification).

Figure 7 shows SEM images of the synthesized TiO_2 particles before and after being annealed at 400–600°C. It was confirmed that all the particles (i.e., both the unannealed and the particles annealed at different temperatures) were porous in structure (Figs. 7(a)-(d)). In addition, nonspherical, agglomerated secondary particles approximately 100 μm in diameter were observed. These secondary particles were composed of primary spherical particles that were 100 nm–1 μm in diameter (Figs. 7(e)-(h)). No facets of the crystalline planes were observed. These results indicated that the obtained particles were polycrystalline in nature.

Figure 8 shows the XRD profiles of the synthesized TiO_2 particles before and after annealing at 400–600°C. The profiles were matched with the International Centre for Diffraction Data (ICDD) database. All profiles contained diffraction peaks characteristic of anatase TiO_2 (ICDD Card No. 00-021-1272) and rutile TiO_2 (ICDD Card No. 00-021-1276). The peaks at 2θ = 27.4, 25.3, and 54.3° were assigned to the diffractions from the (110), (211), and (102) planes of anatase TiO_2 crystals, respectively. The peak at 2θ =36.0° was assigned to the diffraction from the (101) plane of rutile TiO_2 crystals. The other diffraction could be assigned to diffractions from anatase and rutile TiO_2 crystals. The intensities of the diffraction peaks changed with an increase in the annealing temperature, suggesting that the dominant crystalline phases of the particles changed with the annealing temperature. Hence, we performed a quantitative analysis of the obtained profiles to determine the weight ratios of the anatase and rutile phases in the synthesized particles. Table 1 shows the results of this quantitative analysis. The weight ratio of the rutile phase in the TiO_2 particles increased to 84.3% from 61.9%, while that of the anatase phase decreased to 15.7% from 38.1%. This suggests that metastable anatase TiO_2 transformed into stable rutile TiO_2.

Figure 9 shows the FTIR spectra of the synthesized TiO_2 particles before and after annealing at

400–600°C. A small absorption peak was observed in the FTIR spectrum of the unannealed particles; this indicates the existence of the carbon-hydrogen bonds (C–H (st.)) in the particles. Existence of the organic constituent decreased owing to annealing. Thus, it was concluded that TiO_2 particles were synthesized from a Ti-EDTA•NH_4 complex using the H_2-O_2 flame.

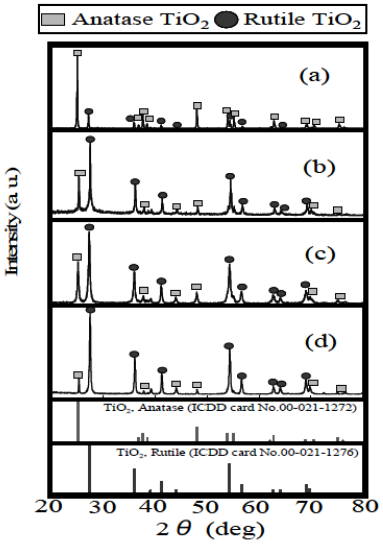

Fig. 8 XRD profiles of the synthesized metal oxide particles. (a) Before annealing, (b) after annealing at 400°C, (c) after annealing at 500°C, and (d) after annealing at 600°C.

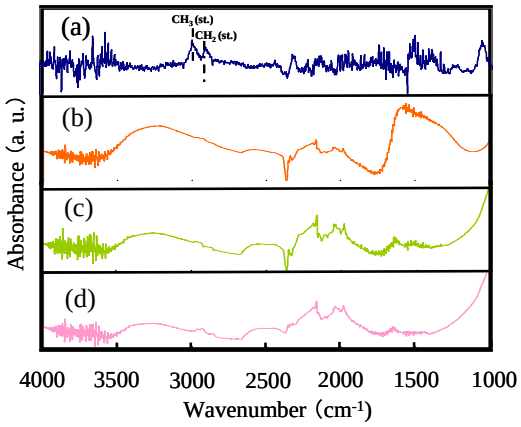

Fig. 9 FTIR spectra of the synthesized metal oxide particles. (a) Before annealing, (b) after annealing at 400°C, (c) after annealing at 500°C, and (d) after annealing at 600°C.

Table 1 Results of the quantitative analysis of the XRD profiles of the synthesized metal oxide particles.

	Weight ratio of each crystalline phase (%)	
Sample details	**Anatase**	**Rutile**
Before annealing	**38.1**	**61.9**
Annealed at 500℃ for 1 h	**36.7**	**63.3**
Annealed at 600℃ for 1 h	**15.7**	**84.3**

4. Conclusions

TiO_2 particles with diameters on the micrometer scale were synthesized from a Ti-EDTA•NH_4 complex with particles 50–200 μm in size by H_2–O_2 flame generated using the commercial flame spray apparatus. The synthesized TiO_2 particles were subjected to annealing treatments and their structure was elucidated. It was found that the particle characteristics of appearance, crystal structure, and organic constituent changed owing to the annealing treatment. The unannealed particles, which were black in color, progressively turned white after being annealed; however, their porosity remained unaffected. A quantitative analysis of the XRD profiles of the particles revealed that weight ratio of the rutile phase of the TiO_2 particles increased to 84.3% from 61.9, while the anatase phase content ratio decreased to 15.7% from 38.1%. Further, almost no organic components were present in the annealed TiO_2. Thus, anatase/rutile TiO_2 particles were successfully synthesized from the Ti-EDTA•NH_4 complex. The crystal structure of the synthesized particles changed after the annealing treatment.

References

[1] N. Rajalakshmi, N. Lakshmi, and K.S. Dhathathreyan, Inter. J. Hydrogen Energ., **33** (2008) 7521.

[2] U.I. Gaya and A. H. Abdullah, J. Photochem. Photobiolo. C: Photochem. Rev., **9** (2008) 1.

[3] J. Y. Kim, S. H. Kim, H.-H. Lee, K. Lee, W. Ma, X. Gong, and A. J. Heeger, Adv. Mater., **18** (2006) 572.

[4] M. D. Pickett, D. B. Strukov, J. L. Borghetti, J. J. Yang, G. S. Snider, D. R. Stewart, and R. S.Williams, J. Appl. Phys., **106** (2009) 074508.

[5] G. A. Crawford, N. Chawla, and J. E. Houston, J. Mech. Behav. Biomed. Mater., **2** (2009) 580.

[6] S. M. Gupta and M. Tripathi, Cent. Eur. J. Chem., **10** (2012) 279.

[7] H. B. Wu, H. H. Hng, and X. W. (David) Lou, Adv. Mater., **24** (2012) 2567.

[8] T. Nonoyama, T. Kinoshita, M. Higuchi, K. Nagata, M. Tanaka, K. Sato, and K. Kato, J. Am. Chem. Soc., **134** (2012) 8841.

[9] S. Tokita, N. Tanaka, S. Ohshio, and H. Saitoh, Jpn. J. Ceram. Soc., **111** (2003) 433.

[10] M. Landmann, E. Rauls, and W. G. Schmidt, J. Phys.: Condens. Matter., **24** (2012) 195503.

[11] L. Yue, W. H.-Qiang, and W. Z. -Biao, J. Env. Sci. **19** (2007) 1505.

[12] Y. Jian, P. Limei, X. Xiangxin,W. Mei, and Q. Tai, J. Rare Earths, **27** (2009) 2040.

[13] Y. Cui, J. Sun, Z. Hu, W. Yu, N. Xu, N. Xu, Z. Ying, and J, Wu, Surf. Coat. Tech., xxx (2012) xxx–xxx (In Press)

[14] V. Swamy, L. S. Dubrovinsky, N. A. Dubrovinskaia, F. Langenhorst, A. S. Simionovici, M. Drakopoulos, and V. Dmitriev, Hans-Peter Weber, Solid State Comm., **134** (2005) 541.

[15] H. Akasaka, M. Ohto, Y. Hasebe, A. Nakamura, S. Ohshio, and H. Saitoh, Surf. Coat. Tech., **205** (2011) 3877.

[16] H. Saitoh, R. Satoh, A. Nakamura, N. Nambu, and S. Ohshio, J. Mater. Sci., **37** (2002) 4315.

[17] H. Saitoh, K. Kawahara, S. Ohshio, A. Nakamura, and N. Nambu, Sci. Tech. Adv. Mater., **6** (2005) 205.

[18] K. Komatsu, T. Shirai, A. Nakamura, A. Kato, S. Ohshio, N. Nambu, I. Toda, H. Muramatsu, and H. Saitoh, Ceram. Inter., **39** (2013) 7115.

[19] Y. Lu, Mi. Hirohashi, and K. Sato, Mater. Tran., **47** (2006) 1449.

(Received: 27 June, 2013, Accepted: 24 October, 2013)

Effect of Overlapped Clearance on Out-of-plane Cutting Characteristics of White-Coated Paperboard Subjected to Straight Punch/Die Shearing

Pusit Mitsomwang[1], Shigeru Nagasawa[1,*]
[1)] *Department of Mechanical Engineering, Nagaoka University of Technology, 1603-1 Kamitomioka, Nagaoka 940-2188, Japan*
**E-mail: snaga@mech.nagaokaut.ac.jp*

This paper describes out-of-plane cutting characteristics of a 0.43 mm thickness white-coated paperboard subjected to a straight punch/die shearing apparatus under overlaping/negative clearance condition. A Load cell and a CCD camera were installed in the cutting system to observe the cutting load resistance and the side-view deformation of the white-coated paperboard. Through the experiment, it was revealed that (i) the use of negative clearance resulted in the higher maximum cutting resistance, compared to a conventional positive clearance; (ii) separation/breaking of the paperboard in the case of negative clearance occured at a shallower indentation depth than that of the positive clearance; (iii) the probability of whisker-like dust occurence at the sheared edge of the worksheet as well as the length of the generated dust were reduced by using the negative clearance. (iv) At the sheared zone, the use of the negative clearance resulted in suppression of an in-plane tensile state of stress. This suppression seems to prevent the generation of long whisker-like dust.

1. Introduction

Coated paperboard is considered to be a fundamental material for the packaging industry due to its advantages such as high strength-to-weight ratio, surface smoothness, cost-effectiveness, recyclability and so on. The manufacture of coated paperboard is generally started from converting timber to fibers by a crushing process. These fibers are mixed with water, and some additives are sometimes added to improve the strength and/or decrease the absorbance of the paperboard. Then, the mixture is pumped onto wires to form a paperboard web. At this stage, bonding between the fibers occurs. After this, the water content of the paperboard web is gradually reduced by drying processes. The dried paperboard is then subjected to a calendering process to improve surface flatness. Finally, the surface of the paperboard is coated with some chemicals such as clay. Through the coating, features such as smoothness of the surface, final printing quality of the paperboard, etc. are improved [1].

To convert coated paperboard to packaging, either a flat bed die cutting system or a rotary cutter is employed. Since the coated paperboard is a fibrous-laminated material, to produce a clean/smart finish on the cut edge of the coated paperboard is more difficult than in the case of several kinds of metallic and polymer materials. Some examples of the difficulties include delamination of paperboard, dust generation, imperfect edge cut, etc. In the present, there are some researches concerned with the converting processes of paperboard. Nagasawa, S. et al. studied about cutting problems of a paperboard subjected to a wedge indentation. Through a blade tip thickness variation ranging from 30~160 μm, it was found that the probability of thread-dross occurrence and also the width of the thread dross were dramatically increased when increasing the tip thickness of the blade [2]. Apart from the wedge indentation, cutting characteristics of a coated paperboard subjected to punch/die shearing were investigated. It was reported that the cut edge of the paperboard was deteriorated under a too large punch/die clearance [3]. Moreover, there was a technical report concerning the effect of moisture content of paperboard on dust generation in the cutting process. Too low a moisture content caused the coated paperboard to be too fragile. As a result, the dust

tended to be generated easily [1]. Regarding the problem of dust generation, the development of a smart cutting technique/method seems to be a big challenge that packaging engineers are facing.

Punch/die shearing under overlapping/negative clearance condition has been applied and investigated as a cutting process for some metallic and resin materials. Through this clearance condition, a high compressive pressure is supposed to be applied to the material located between the punch and die [4]. By using this clearance, the quality of the cut edge in terms of smoothness, flatness and size of roll-over zone were found to be improved [5-6].

For cutting off paperboard, the shearing under negative clearance seems to also be an attractive cutting method. Even though this clearance condition is sometimes applied in rotary cutting systems for converting paperboard into a blank form, effects of the negative clearance on cutting characteristics including generation of dust seem to have never been investigated and clarified.

Therefore, in this study, a white-coated paperboard was subjected to a straight punch/die shearing set. Two cases of negative punch/die clearance were chosen for cutting off the worksheet. Cutting characteristics of the worksheet were investigated, and compared with experimental results carried out using a conventional positive clearance.

2. Material and Apparatus

A white-coated paperboard which had a thickness of 0.43 mm was chosen for the experimental investigation. The basic weight of the white-coated paperboard was 350 g·m^{-2}. The specimen was prepared to have a length l_P and a width w_P of 70 and 20 mm, respectively. The relationships between stress-strain in the machining (M.D.) and cross (C.D.) directions of the white-coated paperboard are illustrated in **Fig. 1**. These relationships were tested by an uni-axial tensile test based on the JIS-P8113 standard.

To cut off the worksheet, the straight punch/die shearing apparatus shown in **Fig. 2** was used. This punch/die set consisted of a main punch, dies, strippers and counter punch. The main punch and dies were made from cold-work tool steel (JIS-SKD11) which had a hardness of 58~60 HRC. **Table 1** lists the surface roughness of each tool component. These values of surface roughness were measured using a three dimensional laser scanning microscope. During shearing, the main punch was moved downward into the die cavity using the pushing force from the movable cylinder of a press machine. The movement of the counter punch and strippers was controlled by their attached backing springs. For the strippers, the stiffness of the backing springs was 4.5 N·mm^{-1}, while it was 5.0 N·mm^{-1} for the counter punch's backing spring. In the cutting system, a load cell (Capacity: 20 kN) and a high speed camera were installed in order to investigate the load resistance F and side-view deformation of the worksheet during shearing.

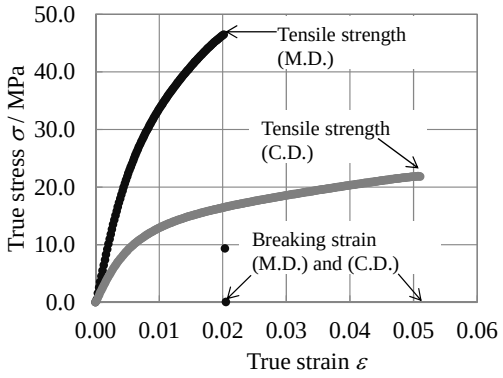

Fig. 1 Stress-strain relationships of white-coated paperboard

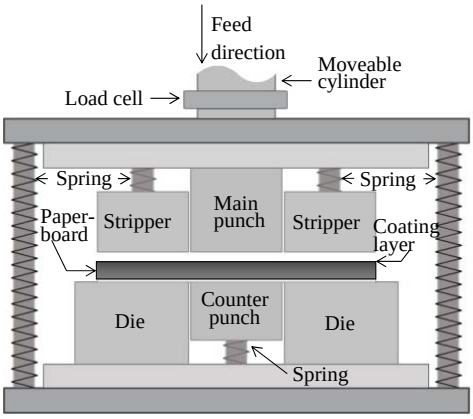

Fig. 2 Schematic of punch/die set

In the experimental investigation, the feed velocity of the upper punch V was fixed to be 0.05 mm·s^{-1}. The cutting line/direction was chosen to be perpendicular to the machining direction of the paperboard. Negative punch/die clearance c/t_S was varied as -0.105 and -0.35. In addition, to investigate the difference of cutting characteristics between the negative and conventional/positive

clearance, the positive clearance c/t_S = 0.035 was also investigated. The definition of the negative and positive clearances is shown in **Fig. 3**. The number of testing specimens was 10 pieces for each clearance case. The cutting experiment was carried out in a temperature and relative humidity controlled room. The temperature and relative humidity were controlled as 23±1 °C and 50±1 %, respectively. The paperboard specimens were also kept in the room for approximately 24 hours before the experiment.

Table 1 Surface roughness of tool component

Tool component	Surface roughness R_a of average (min. - max.) / μm
Main punch	0.46 (0.43 - 0.49)
Die	0.61 (0.60 - 0.63)
Stripper	0.50 (0.48 - 0.52)
Counter punch	0.53 (0.48 - 0.61)
Standard : Based on the JIS-B0601:2001	

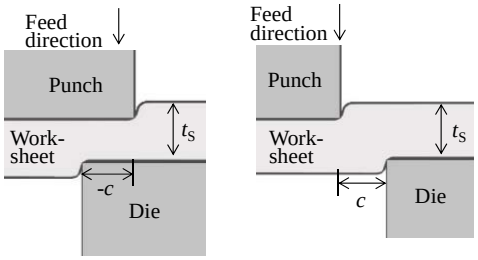

(a) Negative clearance (b) Positive clearance

Fig. 3 Definition of clearances

3. Results and Discussions

3.1 Cutting Load Resistance and Deformation Characteristic of Worksheet

Fig. 4 shows the relationship between cutting line force f ($f = F/(2w_S)$) and normalized indentation depth d/t_S. Since there was a slight fluctuation (dispersion) in the cutting line force, upper and lower bounds of the cutting line force for each clearance case were plotted. In this relationship, d/t_S was defined to be zero at the position where the lower surface of the main punch touched the coated surface of the paperboard.

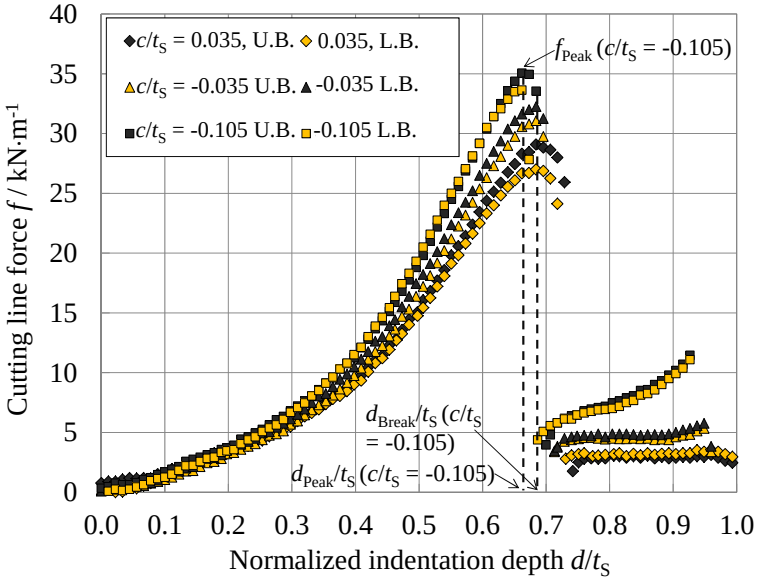

Fig. 4 Relationship between cutting line force and indentation depth for c/t_S

From this figure, the following features of the cutting line force were revealed: (i) for the shallow indentation depth, $0 < d/t_S \leq 0.2$, the tendency of the cutting line force for all of the clearance cases was rather the same, and it seemed to be not affected by the punch/die clearance. (ii) For $0.2 < d/t_S < d_{Peak}/t_S$, the increase of the cutting line force from $d/t_S \approx 0.2$ to the peak point of cutting line force f_{Peak} in the case of largest negative clearance c/t_S = -0.105 was the most rapid. When the positive clearance c/t_S = 0.035 was used, the increase of the cutting line force was slower than that of the cases of negative clearance c/t_S = -0.105 and -0.035. (iii) Considering the peak point of the cutting line force f_{Peak}, it was significantly increased when increasing the negative clearance from c/t_S =

-0.035 to -0.105. For the case of positive clearance c/t_S = 0.035, f_{Peak} was lower than that of the negative clearance c/t_S = -0.035. Regarding the peak position of the cutting line force d_{Peak}/t_S, it was also affected by the punch/die clearance. Namely, d_{Peak}/t_S occurred at the shallowest indentation depth ($d_{Peak}/t_S \approx 0.66$) in the case of c/t_S = -0.105, and it occurred at $d_{Peak}/t_S \approx 0.68$ and 0.70 in the cases of c/t_S = -0.035 and 0.035, respectively. (iv) The breaking position of the worksheet d_{Break}/t_S was significantly affected by the punch/die clearance. It occurred at $d/t_S \approx 0.68$ and 0.69 in the cases of c/t_S = -0.105 and -0.035, respectively, while this breaking position was postponed to $d/t_S \approx 0.72$ when the positive clearance c/t_S = 0.035 was used.

Fig. 5 illustrates the representative side-view photographs of the worksheet at the indentation depth $d/t_S \approx 0.25$, 0.5, 0.75 and 0.9 ~ 1.0. From this figure, for $d/t_S \approx 0.25$ and 0.5, the deformation of the worksheet was rather similar in all of the clearance cases. Namely, the roll-over (wearing) state was observed on the upper and lower surfaces of the worksheet, as drawn as dashed-yellow cures.

When the indentation depth was reached the breaking position of the worksheet, $d/t_S \approx 0.68$ ~ 0.72, the videos recorded by the high speed camera revealed that the deformation of the worksheet at this final breaking state was different when the punch/die configuration was changed. This deformation will be described later.

After the separation state of the worksheet, at the indentation depth $d/t_S \approx 0.75$ in the case of positive clearance c/t_S = 0.035, the edges of the outer and inner portions of the worksheet came into contact with the side edges of the punch and die, respectively. But, in the cases of negative clearance c/t_S = -0.105 and -0.035, both of the outer and inner portions appeared to be detached from the side edges of the tools. At the deep indentation range $d/t_S \approx 0.9$ ~ 1, the deformation characteristics of the worksheet with respect to the clearance were quite similar to those observed at $d/t_S \approx 0.75$.

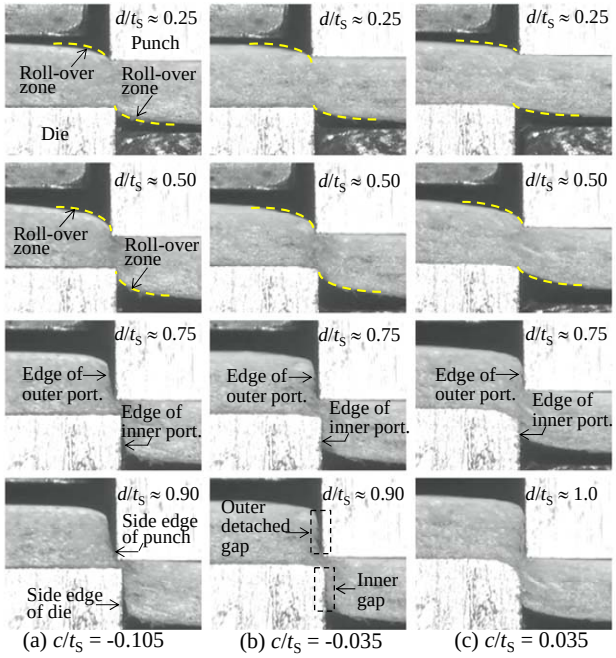

Fig. 5 Representative side-view deformation of white-coated paperboard for c/t_S

In order to describe the deformation of the paperboard at the final breaking state in each of the clearance cases, the material/fiber flow at the shearing zone was analyzed using an image-based binary process. At each interesting indentation depth, a reference photograph was taken. Also, another photograph taken at a deeper indentation depth of +18 μm were prepared and processed using the LABVIEW version 2011. **Fig. 6** shows the binary-stated deformation of the worksheet at $d/t_S \approx 0.25$, breaking position and 0.75 for all of the clearance cases. As shown in this figure, the black-gray zone represents the area where the material/fiber is flowed under a high velocity state. On

the other hand, a lower-velocity flow of the material or a dead zone is represented by the plain-gray zone.

At the shallow indentation depth, $d/t_S \approx 0.25$, the dead state indicated by the plain-gray zone was observed at the center shearing zone in the case of the largest negative clearance $c/t_s = -0.105$. At this same state, a slight flow state of the material was observed at the center shearing zone in the case of $c/t_s = -0.035$ and 0.035.

Through the investigation of the recorded video and the binary-stated analysis result at the breaking state of the paperboard, the final breaking behavior of the worksheet appeared to be characterized by the punch/die configuration. In the case of positive clearance, at this final breaking state, the outer and inner portions of the worksheet were separated. However, many uncut fibers of the paperboard that were pulled from these portions by the downward movement of the main punch were detected. This pulling is represented by the high-velocity-flow zone shown in Fig. 6 (c) at breaking position. On the other hand, in the cases of negative clearance (Fig. 6 (a) and (b) at breaking position), the paperboard tended to be completely cut without any threads due to the pulling phenomenon.

After the final breaking position, as shown in Fig. 6 (a) ~ (c) at $d/t_S \approx 0.75$, the movement of the outer portion from the center of the shearing zone was observed in the case of the negative clearance, while the outer portion seemed to be stationary when the positive clearance was used.

In order to further explain and discuss about the cutting mechanisms of the paperboard under such clearances, the conceptual schematics were introduced as shown in **Fig. 7**.

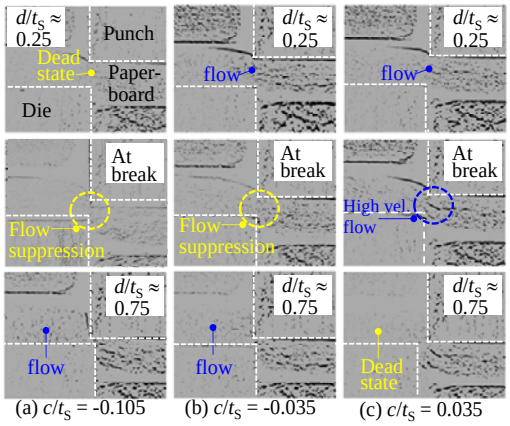

(a) $c/t_S = -0.105$ (b) $c/t_S = -0.035$ (c) $c/t_S = 0.035$

Fig. 6 Binary-stated value of material flow for of worksheet for c/t_S

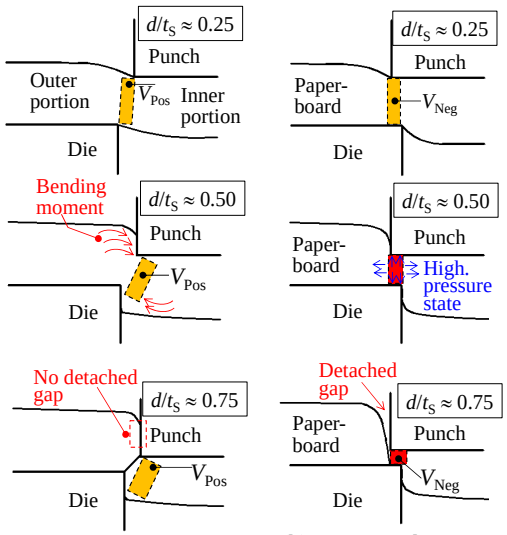

(a) Positive clearance (b) Negative clearance

Fig. 7 Conceptual schematic of material flow behavior for positive and negative clearances

First, considering the positive clearance case illustrated in Fig. 7 (a), the material volume V_{Pos} is laid in the punch/die clearance. When the main punch reaches a certain depth such as $d/t_S \approx 0.5$, the volume $V_{(pos)}$ tends to flow towards the left-lower direction. At this indentation state, an in-plane tensile state caused by the bending moment at the shearing zone is introduced in the outer and inner portions. And, since these portions are not strongly clamped by the stripper and the counter punch, the in-plane tensile state seems to contribute to the fiber debonding and fiber pulling phenomena. After that, although the main punch is pushed downward to a deep indentation depth, such pulled fibers could not be cut off. Consequently, they become the threads adhered at sheared edges. The investigation results of the generated thread are shown and explained in section 3.2.

Next, in the case of the negative clearance configuration shown in Fig.7 (b), since the bending moment at the shearing zone is not occurred or it is remarkably suppressed due to the existence of the compressed volume V_{Neg} (as shown in Fig. 7 (b) at $d/t_S \approx 0.5$), the in-plane tensile state of stress

is not introduced in the outer and inner portions. As a result, the debonding and the pulling phenomena of fibers tend to be suppressed. In other words, the paperboard is cut off by out-of-plane shearing stress.

In the negative clearance case, after the worksheet is separated, the high pressure state of the compressed V_{Neg} seems to result in the rejection of the outer and inner portions out of the center shearing zone. This is confirmed by the occurrence of the detached gaps. However, as shown in Fig. 7 (a) and (b) for $d/t_S \geq 0.75$, since the inner portion of the worksheet was restricted by the die cavity, the outer detached gap appeared to be larger than that of the inner gap.

3.2 Investigation of Dust Generation

After shearing, the generation of dust on the cut worksheet was investigated. The investigation was performed from the top-view at the three positions (investigation area A, B and C) along the sheared edge as shown in **Fig. 8**. Here, the left portion of the worksheet was chosen. **Fig. 9** shows the representative photographs taken at the area A, B and C for c/t_S = -0.105, -0.035 and 0.035. As shown in this figure, a lot of threads were observed at the sheared edge in the case of positive clearance c/t_S = 0.035. Based on the physical feature of the threads, in this investigation, they are referred to as "whisker-like dust". By using the negative clearances c/t_S = -0.105 and -0.035, the whisker-like dust was almost not observed.

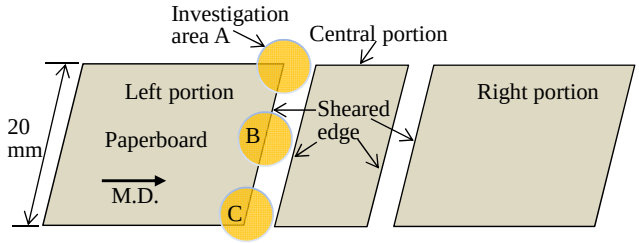

Fig. 8 Investigation areas along sheared edge of worksheet

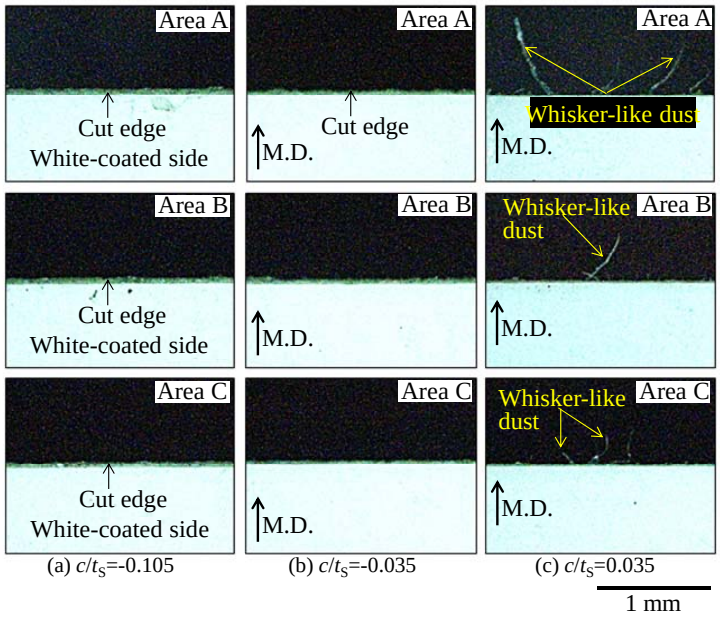

Fig. 9 Representative top-view photograph of cut worksheet

Moreover, from the dust observed at the sheared edge of the cut worksheet, the probability of the dust occurrence was investigated. **Fig. 10** shows the relationship between probability of the whisker-like dust occurrence and the punch/die clearance at each investigated area. In the case of positive clearance, the dust was observed in all of the specimens and investigation areas (p_O = 100%),

while p_O was remarkably reduced to p_O = 10 ~ 30% in the cases of negative clearance c/t_S = -0.105 and -0.035.

Fig. 11 shows the relationship between averaged length of the whisker-like dust and c/t_S. Here, the measurement was performed on the dust which was attached at the cut edge of the left portion of the sheared worksheet using an image analyzer installed in a digital microscope. As shown in this figure, the whisker-like dust generated in the case of the positive clearance was significantly longer than that of the cases of negative clearance.

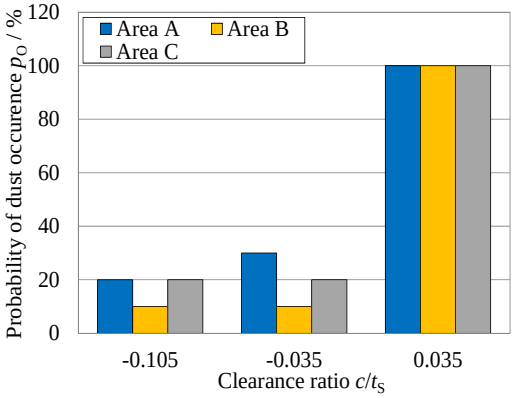

Fig. 10 Probability of dust occurrence for c/t_S (No. of specimens: 30 pieces)

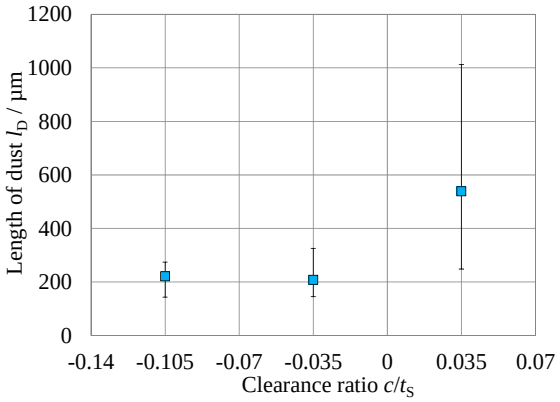

Fig. 11 Averaged length of dust for c/t_S (No. of specimens: 20 pieces)

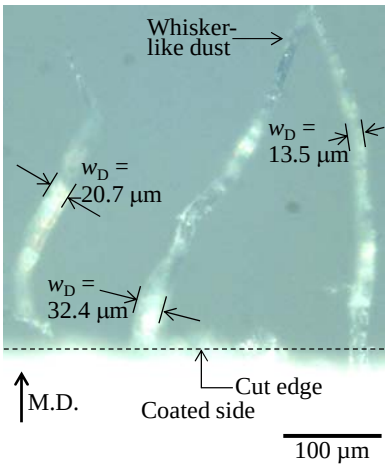

Fig. 12 Representative zoomed-up photograph of sheared edge in case of positive clearance (at left portion of worksheet)

For the further investigation of the generated dust, the zoomed-up photographs taken at the sheared edge of the cut worksheet were prepared and used for measuring dust width. Here, the investigation was done on the generated whisker-like dust in the case of positive clearance. **Fig. 12** shows the representative zoomed-up photographs of the dust. From the width-measurement result, the width of the whisker-like dust w_D was 17.39 µm in average.

Comparing the whisker-like dust in the current experiment with the dust observed in the previous study of the paperboard wedge indentation (the width of the thread-like dust ≈ 50~150 µm) [2], it was revealed that their dimensions and geometry were totally different. Also, their generation mechanisms seem to be completely different.

From the results of the probability of the dust occurrence and the length of the dust, it was confirmed that the application of the negative clearance was superior for shearing the white-coated paperboard. By using such clearances, not only the probability of the whisker-like dust occurrence

was reduced, but also the generation of the long whisker-like dust was suppressed.

4. Conclusions

In this study, the cutting characteristics of white-coated paperboard subjected to a straight punch/die shearing under a negative/overlapping clearance condition was carried out and investigated. Through the experimental investigation, the following conclusions were obtained:

(i) Comparing the case of negative clearance with the positive case, the use of the negative clearance resulted in the higher peak point of the cutting line force, and this peak point appeared to occur at the shallower indentation depth. Moreover, the breaking/separation of the paperboard in the case of negative clearance was found to happen at a shallower indentation depth than that of the positive clearance.

(ii) The material flow behavior at the sheared zone in the negative and positive clearance was found to be different. In the case of negative clearance, the material flow in the lateral direction at the sheared zone was suppressed, while it apparently occurred in the case of positive clearance.

(iii) The material flow behavior appeared to be strongly related to the generation of the whisker-like dust at the sheared edge of the worksheet. The suppression of the material flow in the case of negative clearance seemed to prevent the generation of the whisker-like dust.

(iv) The shearing under the negative clearance was confirmed to be superior for shearing the white-coated paperboard. It reduced the probability of the whisker-like dust occurrence and prevented the generation of long dust at the sheared edge of the worksheet.

References

[1] Ahokas, P. Paperboard Guide (issued by the Stora Enso corp.).
[2] S. Nagasawa, et al., SOSEI-TO-KAKOU., **43-498** (2002).
[3] S. Nagasawa, et al., International Journal of Mechanical Sciences., **52** (2010).
[4] K. Kasuyoshi, United States Patent 3724305., (1970)
[5] W.F. Fan, and J.H. Lie, Material Science and Engineering A ., **A499** (2009).
[6] P. Mitsomwang, et al., Proceeding of the JSTP spring conf., (2012).

(Received: 2 July, 2013, Accepted: 20 December, 2013)

Evaluation of relationship between radius of curvature at vertex of 3D bonded structure and intensity of stress singularity based on stress analysis using element free Galerkin method

Takahiko Kurahashi[1*], Yasuyuki Tsukada[2], Hideo Koguchi[2]
[1)]Department of Materials Science and Technology, Nagaoka University of Technology,
[2)]Department of Mechanical Engineering, Nagaoka University of Technology,
1603-1 Kamitomioka-cho, Nagaoka 940-2188, Japan
**E-mail: kurahashi@nagaoka-ct.ac.jp*

In this report, we investigate variation of stress distribution and intensity of stress singularity near the cross point of inclusion and free surface based on 3D element free Galerkin method (EFGM). We especially focus on influence of radius of curvature at vertex for stress singularity field. As for computational model, silicon and resin bonded structure is employed.

1. Introduction

Intensity of stress singularity near interface edge for bonded structures is investigated by a lot of researchers [1], [2]. Variation of intensity of stress singularity with respect to thickness of adhesive layer, interface width, slanted side surface have already investigated. As for the computational methods, the boundary element method (BEM) and the finite element method (FEM) are frequently used to compute stress distribution. In addition, the element free Galerkin method (EFGM) is also recently employed for stress analysis[3]. In this study, the EFGM is employed in stress analysis for bonded structures. In addition, eigen analysis based on the FEM is carried out to obtain order of stress singularity[4]. As the computational model, a structure made by resin with silicon plate inclusion is employed. We especially focus on influence of radius of curvature at vertex for stress singularity field in this study(See Fig.1).

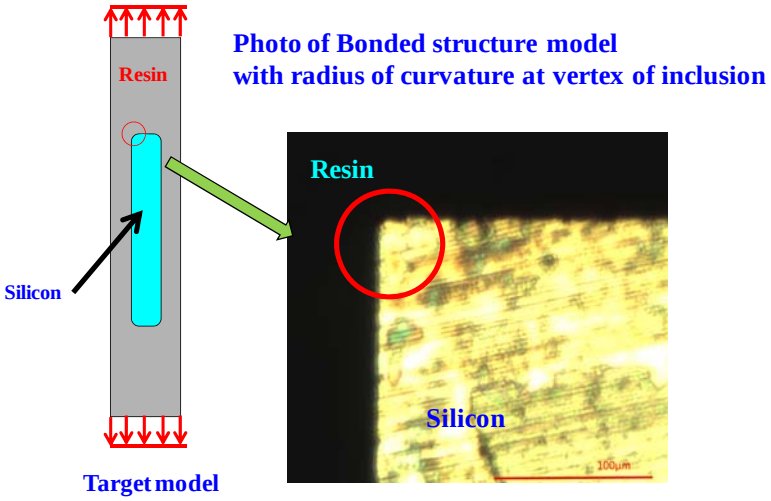

Fig. 1 Image diagram of target model

2. Stress analysis by the EFGM and analysis of order of singularity by the FEM

The characteristics of the EFGM is that the interpolation function at evaluation point is given by the information in the domain influence (See Fig 2.). Example of the interpolation function is written as Eq. (1).

$$u(\mathbf{x}) = q_1(\mathbf{x})u_1 + q_2(\mathbf{x})u_2 + q_3(\mathbf{x})u_3 + \cdots + q_n(\mathbf{x})u_n = \{q(\mathbf{x})\}^T \{u\}, \tag{1}$$

where indicates shape function, and indicates number of referred nodes in the domain influence. In addition, forth order spline function is employed as the weighting function in the EFGM. Procedure of discretization is same as the traditional FEM. Detail of discretization is shown in reference [3].

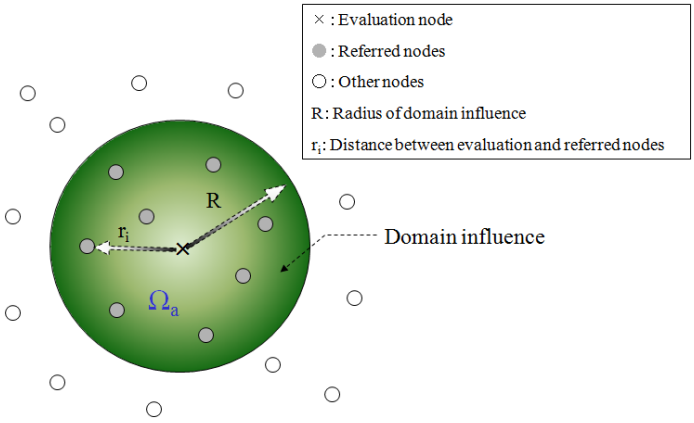

Fig. 2 Domain influence

In addition, if the order of singularity is expressed by λ, the stress distribution is written as $\sigma_{ij} \propto 1/r^{\lambda} = 1/r^{1-p} = r^{p-1}$. Here, p indicates characteristic root. Because the stress is expressed as gradient of the displacements u_i, the relationship the displacements and distance r is given $u_i \propto r^p$ by the integration of $\sigma_{ij} \propto r^{p-1}$. If displacements for each element are expressed by interpolation function shown in Eq. (2) and the interpolation function is substituted to equation of the principle of virtual work, a characteristic equation is finally derived as shown in Eq. (3).

$$\bar{u}_r(r,\theta,\phi) = \left(\frac{r}{r^0}\right)^p \sum_{i=1}^{8} h_i \bar{u}_{ri}, \tag{2}$$

$$\left(p^2[\mathbf{A}] + p[\mathbf{B}] + [\mathbf{C}]\right)\{\mathbf{x}\} = \{\mathbf{0}\}, \tag{3}$$

where $\bar{u}_i$ is expressed by $u_i - u_o$, and u_i and u_o represent spherical displacements at an arbitrary point in the spherical surface. In addition, h_i indicates the shape function. In the Eq. (3), p indicates characteristic root and vector $\{\mathbf{x}\}$ denotes superposed displacement vector in entire domain, and matrices $[\mathbf{A}]$, $[\mathbf{B}]$ and $[\mathbf{C}]$ represent the coefficient matrices derived by finite element procedure. Detail of this formulation is shown in reference [4].

3. Numerical experiments

3.1 Variation of intensity of stress singularity $K_{I\varphi\varphi}$ with respect to radius of curvature R

In this study, a structure made by resin with silicon plate inclusion shown in Fig.3 is employed as a numerical model. Nodal distribution around target area and material properties are shown in Fig.4

and Tab.1. In case of computational model of R=0, order of stress singularity λ at vertex on silicon surface is obtained as 0.436. In this study, the radius of curvature R at vertex of silicon plate is changed as shown in Tab.2.

In case that tensile stress, 10MPa, is applied to top surface, stress distribution $\sigma_{\varphi\varphi}$ on surface in silicon plate with respect to angle φ is shown in Fig.5. It is seen that gradient of stress distribution $\sigma_{\varphi\varphi}$ is almost same for each angle φ. Next, comparison of stress distribution $\sigma_{\varphi\varphi}$ on silicon surface at angle direction φ=315° is carried out. The result is shown in Fig.6. It is found that stress value decreases with increasing the radius of curvature R, and constant stress region of $\sigma_{\varphi\varphi}$ near point O, i.e., stress singularity disappearance region, increases with increasing the radius of curvature R. Furthermore, it is seen that gradient of stress distribution changes at the point distance r from singularity point O is approximately equal to the radius of curvature R at vertex. In addition, relationship between intensity of stress singularity $K_{1\varphi\varphi}$ and radius of curvature R is shown in Fig.7. The intensity of stress singularity $K_{1\varphi\varphi}$ can be obtained by least square approximation for results shown in Fig.6 by fitting equation $\sigma_{\varphi\varphi}= K_{1\varphi\varphi}r^{-0.436}$. From this result, it is found that intensity of stress singularity $K_{1\varphi\varphi}$ almost linearly decreases with increasing the radius of curvature R.

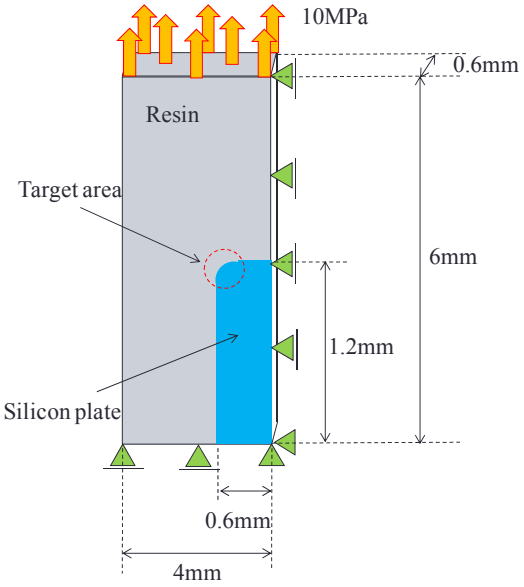

Fig. 3 Computational model

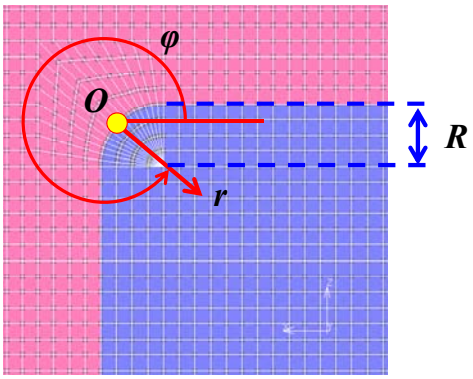

Fig. 4 Nodal distribution in target area

Table 1 Material properties

	Silicon	Resin
Young's modulus (GPa)	166	5.49
Poisson's ratio	0.26	0.32

Table 2 Computational conditions

Radius of curvature R (μm)	0.000	3.125	6.250	12.500
Number of nodes	27,607	15,467	16,423	21,727

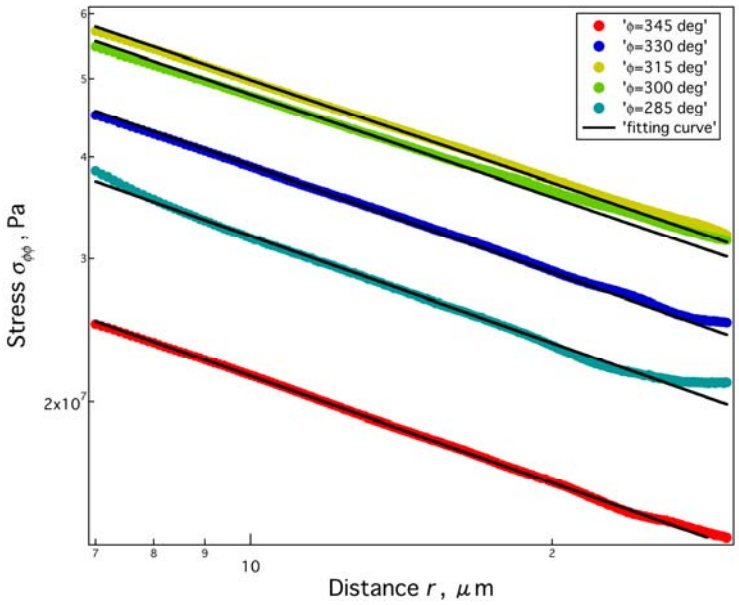

Fig. 5 Variation of stress distribution $\sigma_{\varphi\varphi}$ on silicon surface with respect to angle φ (R=0mm)

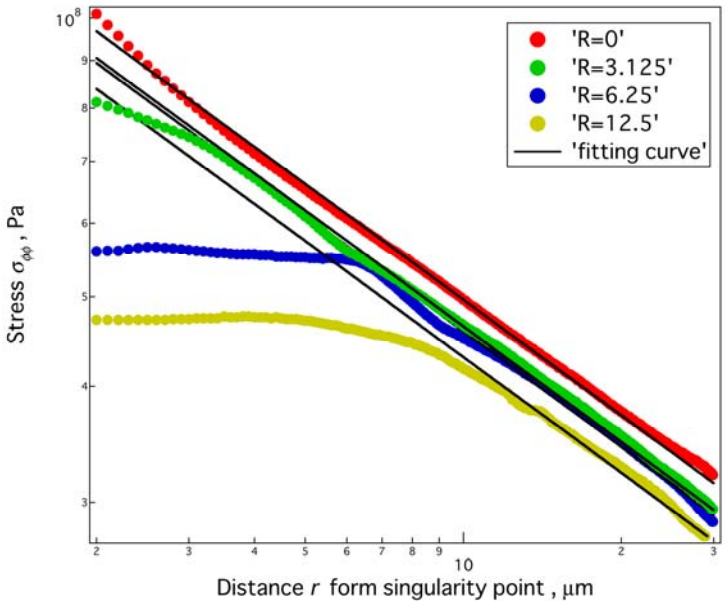

Fig. 6 Variation of stress distribution $\sigma_{\varphi\varphi}$ on silicon surface at angle direction φ =315° with respect to radius of curvature R

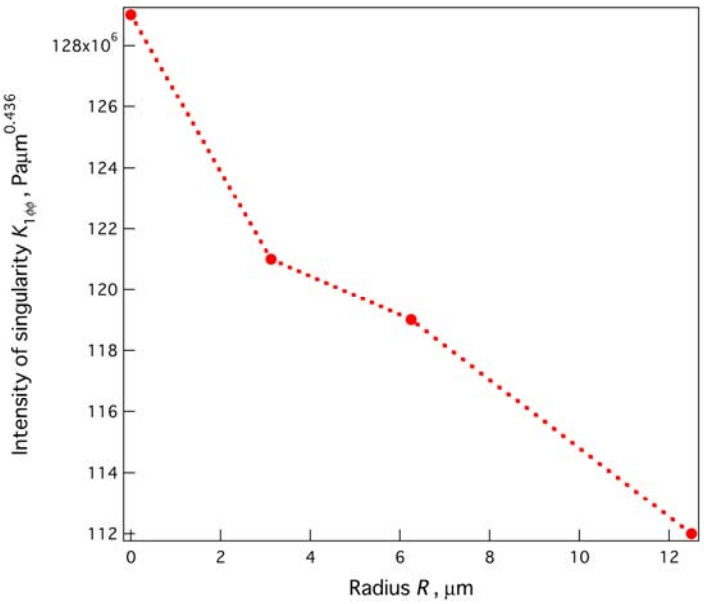

Fig. 7 Relationship between intensity of stress singularity $K_{1\varphi\varphi}$ and radius of curvature R

3.2Variation of intensity of stress singularity $K_{1\varphi\varphi}$ with respect to Young's modulus of resin

It is known that the variation of Young's modulus of resin E_2 with respect to temperature is larger than that of Young's modulus of silicon E_1. It appears that intensity of stress singularity $K_{1\varphi\varphi}$ changes by Young's modulus of resin E_2 in state of temperature variation. Therefore, in case of computational model, R=3.125μm, relationship between intensity of stress singularity $K_{1\varphi\varphi}$ and Young's modulus of resin E_2 is investigated. First of all, order of singularity λ is listed in Tab.3. It is seen that order of singularity λ gradually decreases with increasing Young's modulus of resin E_2. Fig.8 shows variation of stress distribution $\sigma_{\varphi\varphi}$ on silicon surface at angle direction, φ =315°, with respect to each Young's

modulus of resin E_2. It is found that value of stress $\sigma_{\varphi\varphi}$ decreases with increasing Young's modulus of resin E_2. In addition, variation of intensity of stress singularity $K_{1\varphi\varphi}$ with respect to Young's modulus of resin E_2 is shown in Tab.4. It is seen that intensity of stress singularity $K_{1\varphi\varphi}$ decreases with increasing Young's modulus of resin E_2.

Table 3 Order of singularity λ (In case of R=0 model)

Young's modulus of resin E_2 (GPa)	0.10	0.50	1.00	5.49	10.00
Order of singularity λ	0.545	0.437	0.429	0.436	0.384

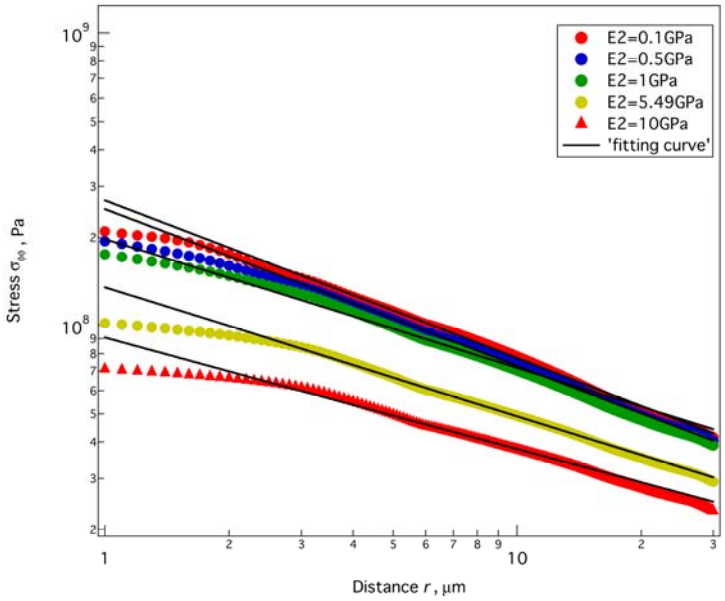

Fig. 8 Variation of stress distribution $\sigma_{\varphi\varphi}$ on silicon surface at angle direction φ=315° with respect to Young's modulus of resin

Table 4 Variation of intensity of stress singularity $K_{1\phi\phi}$ with respect to Young's modulus of resin E_2 (In case of R=3.125μm model)

Young's modulus of resin E_2 (GPa)	0.10	0.50	1.00	5.49	10.00
Intensity of stress singularity $K_{1\phi\phi}$	42.5×10^7 Pa・mm$^{0.545}$	27.0×10^7 Pa・mm$^{0.437}$	23.3×10^7 Pa・mm$^{0.429}$	13.3×10^7 Pa・mm$^{0.436}$	9.8×10^7 Pa・mm$^{0.384}$

4. Conclusions

In this study, we investigated about the relationship between intensity of singularity $K_{1\theta\theta}$ and radius of curvature R for computational model of a structure made by resin with silicon plate inclusion. As numerical methods, the EFGM is applied to stress analysis, and the finite element eigen analysis is applied to obtain order of singularity at vertex on silicon surface. Conclusions in this study are shown below.

Examinations for change of radius of curvature around singularity point

- Stress value $\sigma_{\varphi\varphi}$ decreases with increasing the radius of curvature R.
- Constant stress region of $\sigma_{\varphi\varphi}$ near point O, i.e., stress singularity disappearance region, increases with increasing the radius of curvature R.
- Intensity of stress singularity $K_{1\varphi\varphi}$ almost linearly decreases with increasing the radius of curvature R.

Examinations for change of Young's modulus of resin in case of R=3.125μm model

- Value of stress $\sigma_{\varphi\varphi}$ decreases with increasing Young's modulus of resin E_2.
- Intensity of stress singularity $K_{1\varphi\varphi}$ decreases with increasing Young's modulus of resin E_2.

Conventionally, the stress value at vertex on interface of bonded structure had been treated as infinity. But, in this study, it was found that the stress value at vertex converges to unique value in case that there is curvature at vertex on interface of bonded structure. In addition, it was found that gradient of stress distribution changes at the point distance r from singularity point O is approximately equal to the radius of curvature R at vertex. Therefore, if the relationship between the radius of curvature R at vertex and convergence value of stress value $\sigma_{\varphi\varphi}$ at r=0 can be obtained by numerical experiments for a lot of computational models with micro scale curvature at vertex, it appears that stress value $\sigma_{\varphi\varphi}$ at r=0 can be estimated for the bonded structure model with micro scale curvature at vertex.

In addition, evaluation of stress component in silicon region was carried out. To evaluate strength on interface of silicon and resin joint model, it is also necessary to obtain stress distribution in resin region. However, there is a case that stress distribution in resin can't be appropriately obtained, if nodes in resin region are not enough. In this study, width of nodal distribution was set almost same around singular point in silicon and resin regions, and stress singularity analysis was carried out, because the main objective in this study was to evaluate stress singularity in 3D bonded structure model considering radius of curvature at vertex of silicon. Therefore, in future, it is necessary to investigate stress distribution in resin, and to evaluate strength on interface around vertex in the target model considering radius of curvature at vertex of silicon.

References

[1] T. Kurahashi, A. Ishikawa and H. Koguchi, Evaluation of Intensity of Stress Singularity for 3D Dissimilar Material Joints Based on Mesh Free Method, 11th International Conference on the Mechanical Behavior of Materials, *Procedia Engineering*, 10, (2011) 3095-3100 .

[2] Hideo Koguchi, Kazuhisa Hoshi, Evaluation of joining strength of silicon-resin interface at a vertex in 3D joint structures, *InterPACK2011*, (2011).

[3] T.Belytschko, Y.Y.Lu and L.Gu, Element-free Garerkin methods, *Int. J. Numer. Meth. Engrg.*, 37(5), (1994) 229-256.

[4] S.S.Pageau and S.B.Bigger,JR, Finite element evaluation of free - edge singular stress fields in anisotropic materials, *Int.J.Numer.in Engng.*, 38, (1995) 2225-2239.

(Received: 24 June, 2013, Accepted: 03 December, 2013)

Fluid Control MEMS Constructed with Functional Polymer Materials

Akira Kawai*

Department of Electrical Engineering, Nagaoka University of Technology,
1603-1 Kamitomioka, Nagaoka, Niigata 940-2188, Japan
**E-mail:kawai@nagaokaut.ac.jp*

This paper reviews shortly that a polymer material indicates higher durability and resistance properties against to reactive gases, acid and alkaline solutions. Fluid control MEMS (micro electro mechanical systems) with micro diaphragm pumping system used for reactive gas control is constructed. A resist film made of novolac resin as a diaphragm material is employed. An Au/Si/resist multilayer structure as a diaphragm of 1mm diameter is formed by optical lithography and anisotropic wet etching techniques. A micro channel structure of 50μm width is also fabricated by employing a polymer thick film. The mechanical strength of a diaphragm is tested by applying static load using a probe system. By applying 20V bias between diaphragm and base electrodes, Coulomb attractive force acts to operate the diaphragm motion. As the fluid flow control, a silane-coupling vapor gas of HMDS (hexamethyldisilazane) is employed. A contact angle of water indicates hydrophobic of a glass substrate by HMDS vapor control using the MEMS.

1. Introduction

Recently, micro electro mechanical systems (MEMS) has been studied widely in motion sensor, power harvesting and biomedical control.[1-3] Particularly, liquid-gas interface control is one important technology in order to realize and advance these functional devices. Moreover, it is required to prevent corrosion and deteriorate of device elements by exposing to reactive gases and liquid solutions. In this regard, the author has focused on durability and resistance of polymer materials under reaction with fluid solutions. In this paper, a fluid control MEMS composed with micro pumps and channels made of polymer materials are developed. The mechanical strength and durability of polymer film are evaluated by using a probe system.[4] By using the fluid control MEMS, the silane-coupling gas flow of HMDS (hexamethyldisilazane) is controlled. By measuring a contact angle of water droplet on a glass substrate, precise control of fluid flow using the fluid MEMS is confirmed.

2. Design and Operation of Diaphragm Pump

2.1 Diaphragm pump structure

A multilayer structure of Au/Si/resist multilayer is formed for an element of diaphragm pumping device. The Si micro diaphragm is formed by anisotropic wet etching.[5] The Au film is used for an electrode for applying an electrical field between a diaphragm and a base electrode. A resist film of i-line novolac resin type is coated on a Si micro diaphragm. The fluid pump system is composed with a diaphragm, a channel and an external control unit. The diameter of diaphragm is designed to be 1mm. Figure 1 shows a schematic diaphragm of Au/Si/resist multilayer. The thickness of this multilayer diaphragm is 0.05/50/5μm. The width of micro channel is 50μm. As shown in Fig.2, micro diaphragms are arranged along with micro channel. By compressing a fluid in micro channel by the diaphragm in order, a certain fluid flow occurs. In this study, the twelve diaphragms are arranged and operated to control a reactive gas flow. Figure 3 shows a photograph of micro diaphragm. The circular shape of Si diaphragm can be formed by the anisotropic wet etching .[5] By setting a shift value on etching mask, various curved shape can be formed on a Si(100) single crystal.

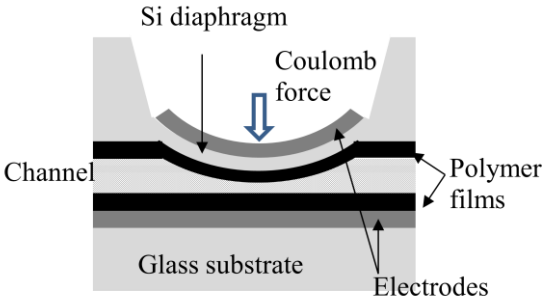

Fig.1 Diaphragm structure of Au/Si /resist multilayer film.

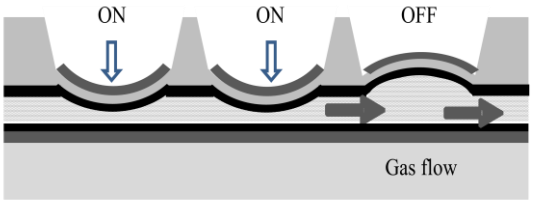

Fig.2 Fluid flow operation by compression of diaphragms in order under Coulomb force.

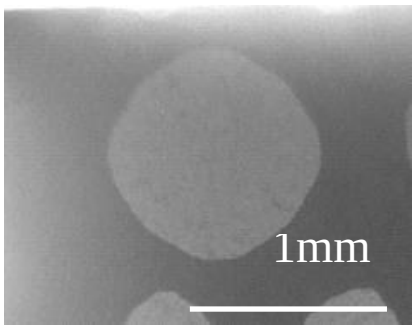

Fig.3 A photograph of micro diaphragm formed by anisotropic wet etching.

2.2 Operation test of micro diaphragm

Figure 4 shows a deflection test of micro diaphragm by using a probe system. An atomic force microscope system SPA-300 (Seiko Instrument Inc.) was used. By applying a certain load, the deflection rate of diaphragm can be determined. In the experiment, by applying the constant load from 2 to 7mN, a slight deflection of diaphragm can be monitored along with diameter direction. Figure 5 shows a slight deflection of diaphragm under applying normal load. As increasing applying load, the deflection of diaphragm increases. The deflection rate can be estimated to be 1000N/m, which is mostly same as a spring constant of the probe system.

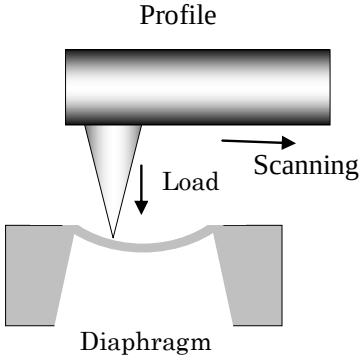

Fig.4 Displacement test of micro diaphragm by using probe system. A certain load can be applied to a diaphragm along with a diameter direction.

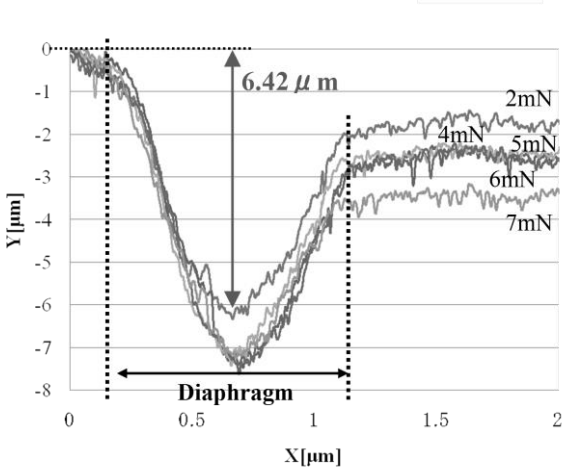

Fig.5 Deflection of diaphragm along with diameter direction under various applying load. By an inclination of probe apex, displacement curve becomes asymmetry.

3. Fabrication of Fluid Control MEMS

The fluid control MEMS is composed by micro diaphragm and micro channel. The multilayer diaphragm structure is fabricated as shown in Fig.6.

(1) A SiO_2 layer is formed by thermal oxidation of Si(100) substrate at 960 degree C for 2h in air. The thickness of SiO_2 layer was 45nm.
(2) By optical lithography, a circular resist mask was formed on the SiO_2 film surface as shown in Fig.7. A certain value of size shift was applied in order to obtain circular shape.[5]
(3) The SiO_2 mask layer was etched in 0.5wt% HF aqueous solution.
(4) The resist layer was removed by immersing into acetone.
(5) The Si(100) substrate was etched in EPW etchant for anisotropic etching. The diaphragm structure of 30μm thickness was fabricated.
(6) The resist film of 4.2μm thickness was coated by spin coating on the back side of Si diaphragm. The baking temperature of resist film was 90 degree C for 2min. The Au film of 50nm thickness was coated on the etched Si surface by DC sputtering method.

Figure 8 shows a flow-chart for micro channel fabrication. Micro channel was formed on a glass substrate. As an electrode, an Au film was formed on the glass substrate. The sputtering gas purity was Ar(99.999%). The ionic current and accelerating voltage was 1 kV. As the base and side layers of micro channel, SU-8 resist was employed by standard process condition. The width and height of micro channel were 50 and 5μm. The Au electrodes were connected to external electric lines.

As shown in Fig.9, the fabrication of the fluid control MEMS was completed by adhering the diaphragm system and micro channel system under heat treatment at 240 degree C. The alignment of these two systems was carried out under controlling microscope. Figure 10 shows photographs of micro channels after adhering process. It is clearly observed that the alignment of channel and diaphragm is well-controlled. The curved channel was formed smoothly by anisotropic wet etching technology. Figure 11 shows a photograph of fluid control MEMS after assembling on a package. By connecting to external electric lines, control signal can be applied onto the pumping system.

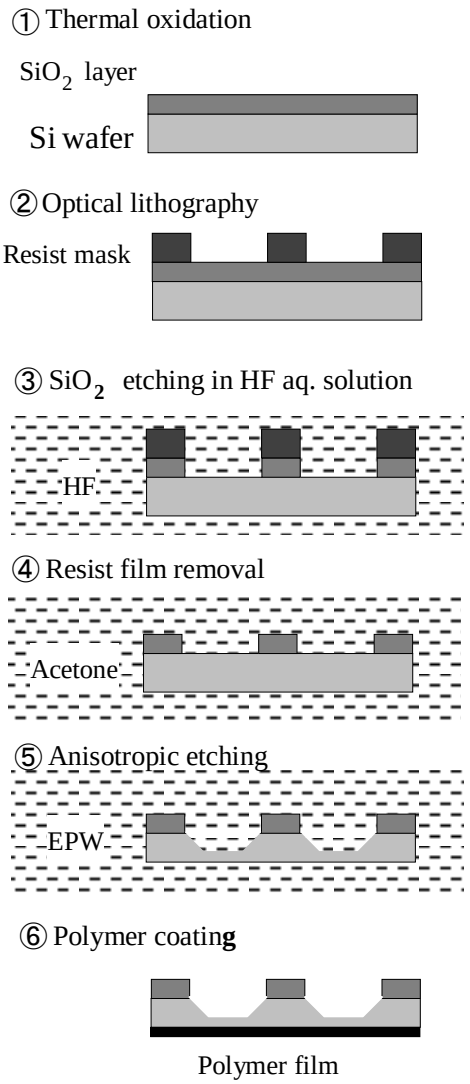

Fig.6 Process flow-chart of micro diaphragm structure.

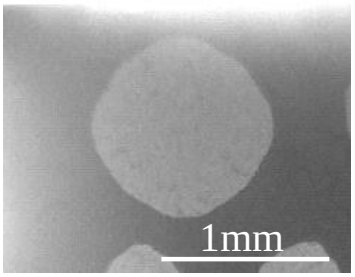

Fig.7 Optical microscope image of resist mask for circular diaphragm.

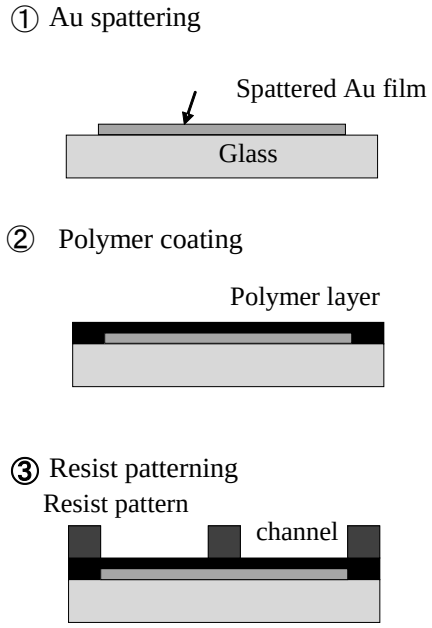

Fig.8 Process flow-chart of micro channel. An Au film was set at opposite position of micro diaphragm.

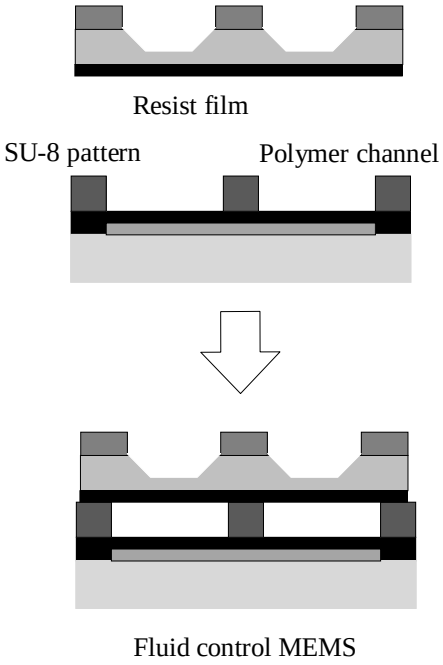

Fig.9 Fabrication of Fluid control MEMS. The registration of two layers is controlled precisely.

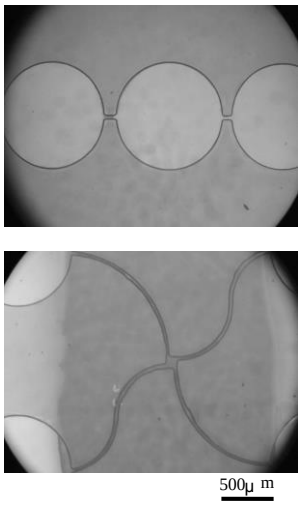

Fig.10 Photographs of micro channel aligned with diaphragm center. The straight micro channel is formed in order to connect the micro diaphragms. The cross shape channel acts to mix and separate two fluids.

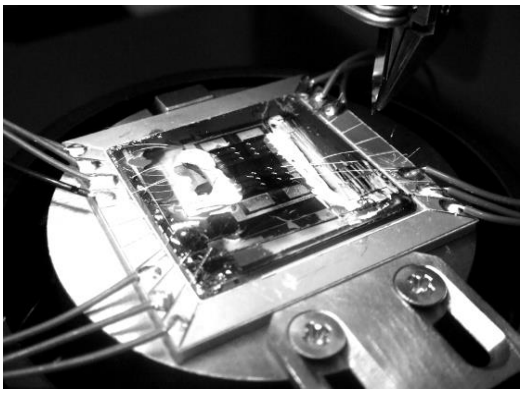

Fig.11 Photograph of fluid control MEMS after assembling. A number of electric lines are used for applying electric field to pumping system. Each electric line is connected to one diaphragm electrode. The base electrode of micro channel is set to ground level.

4. Operation of Fluid Control MEMS

Figure 12 shows a precise design of fluid control MEMS as shown in Fig.11. The inlet and outlet for fluid are designed at the both sides of MEMS. The connecting electrodes for external electric source are formed at a side of each diaphragm.

Figure 13 shows an operation diagram for fluid flow. By operating a series of diaphragms in order, fluid can flow smoothly in one direction. By controlling an electric pulse signal, the diaphragms can be operated as previously programmed. Figure 14 shows a diaphragm motion estimation under applying electrostatic force. By applying cyclic signals of 20V between two electrodes, a fluid can flow in micro channels smoothly. The pumping frequency can be changed. By programming the signal period for diaphragms, mixing and separation of two fluids can be controlled.

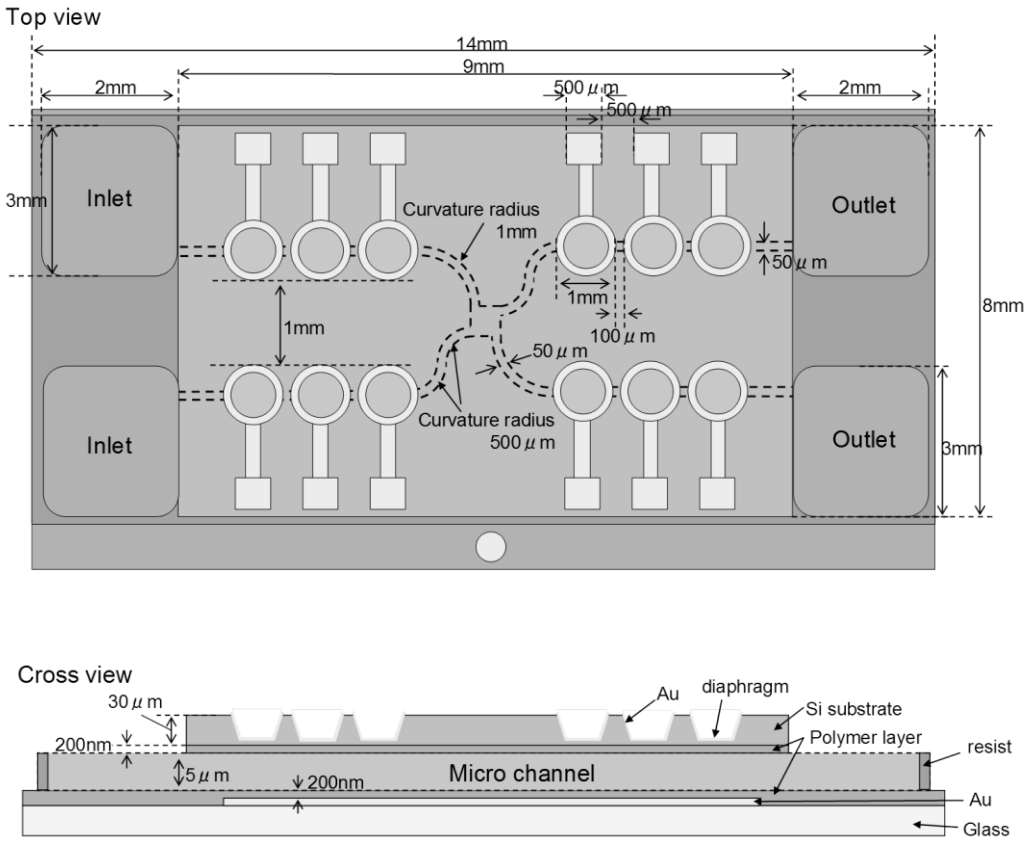

Fig. 12 Total design of Fluid control MEMS

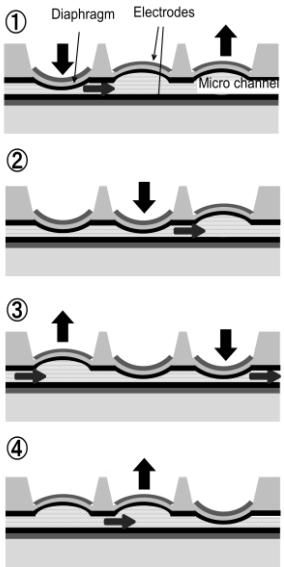

Fig. 13 Fluid flow control of MEMS by operating a series of diaphragm in order.

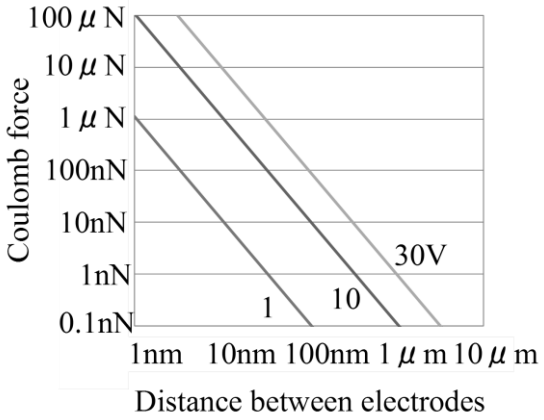

Fig. 14 Diaphragm deflection under applying electrostatic force. The electric voltage up to 30V is applied between two electrodes.

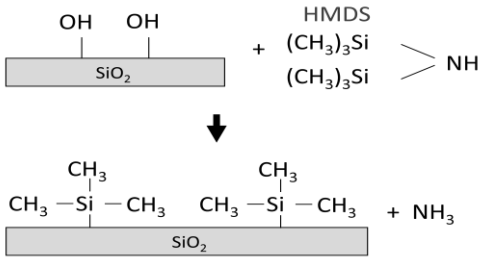

Fig. 15 Slane-coupling reaction with HMDS on SiO_2 surface.

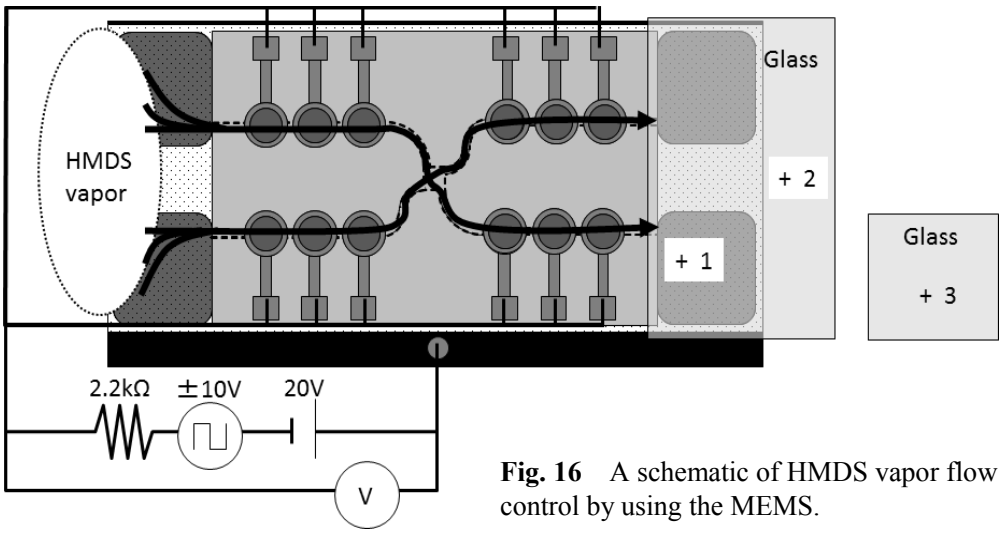

Fig. 16 A schematic of HMDS vapor flow control by using the MEMS.

In this paper, it is attempted to control HMDS vapor flow by using the fluid control MEMS. As well-known, HMDS vapor is employed to control a surface wetting properties. Figure 15 shows a fundamental reaction of silane- coupling treatment on a SiO_2 surface. Figure 16 shows a schematic of fluid control MEMS structure. The HMDS vapor is introduced from the inlet position. By applying a programmed electric signal to each diaphragm, the HMDS vapor can be introduced to outlet position of the MEMS.

The contact angle method using pure water is sensitive to surface property changes such as hydrophilic and hydrophobic. As shown in Fig.16, the three positions of substrates at a vicinity of the outlet are used for evaluating the HMDS treatment. The position 1 is an Au electrode. The positions 2 and 3 are glass substrates. After flowing HMDS vapor by using the fluid control MEMS, the contact angles of pure water were measured for 30 min. Figure 17 shows the measurement results of contact angle at the test points. At the position 1, it is clearly observed that the contact angle increases as the operating time increases. The degree of HMDS treatment at position1 is higher than those of positions 2 and 3.

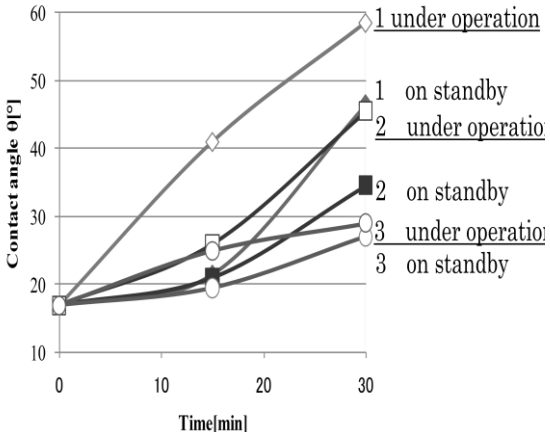

Fig.17 Contact angle evaluation of sample surfaces after operating fluid control MEMS.

Moreover, on standby mode, the contact angles are lower than those under operation in all positions. The sensitivity of contact angle method for surface wetting change is extremely high comparing with another analysis method. The monolayer change of sample surface can be detected by using the contact angle method. Therefore, it is clearly confirmed that the reactive HMDS vapor flow can be controlled by using the fluid control MEMS.

5. Conclusions

The fluid control MEMS composed with diaphragm system and micro channel are fabricated. The resist materials are employed as the walls at which the reactive fluid is contacting. The contact angle method is employed to evaluation of the HMDS treatment. It is confirmed that the HMDS vapor flow can be controlled by using the MEMS.

Acknowledgements

The author appreciates to Mr. Takashi Yamaji for the helpful through the experiment. This work was supported from the Grant-in-Aid for Scientific Research from the Ministry of Education, Science, Sports, Culture and Technology, Japan, and by Program for High Reliable Materials Design and Manufacturing in Nagaoka University of Technology.

References

[1] S. Hayamizu, K. Higashino, *Sensors and Actuators*, **A 103** (2003) 83.
[2] O. C. Jeong, S. Konishi, *Sensors and Actuators*, **A 135** (2007) 849.
[3] J. L. Charest, M. T. Eliason, Biomatrrials, **27** (2006) 2487.
[4] A. Kawai, *Microelectronic engineering* **83** (2006) 659.
[5] J. Miyazaki, A. Kawai, *J. Photopolymer Science and Technology*, **22**(6) (2009) 731.

(Received: 5 July, 2013, Accepted: 18 October, 2013)

A SU-8 Photoresist Film as Electrical Stable Layer in Liquid Environment

Yuta Noguchi, Akira Kawai
Department of Electrical Engineering, Nagaoka University of Technology,
1603-1 Kamitomioka, Nagaoka 940-2188, Japan
E-mail: kawai@nagaokaut.ac.jp

This paper reviews shortly that evaluation of a SU-8 photoresist film characteristic in terms of electrical stability as material of bio device. Surface potential V_{SU-8} of a SU-8 film is measured and compared to biopotential V_{bio} of plant leaf cells. Each potential is measured by making a metallic electrode contact. In both measurements, maximum value is indicated at a moment of contact, and then potential value is decreased with increasing measuring time. From quantitative analysis, factors of each potential, such as equilibrium, potential variation width and time constant are estimated. Factors of surface potential of a SU-8 film are similar at every point. However, there are widely varied in biopotential. As conclusion, reproducibility of electrical characteristic of a SU-8 film surface is indicated. We believe that stability of a SU-8 film exhibits promising characteristics for a bio device substance.

1. Introduction

Biocompatible materials have been investigated extensively in various bioscience and engineering fields. In particular, polymer materials, such as polydimethylsiloxane (PDMS) and polytetrafluoroethylene (PTFE), have been yielded in practical applications, e.g., an artificial blood vessel, a cell culture substratum [1,2]. With regard to biomaterial, it is critical to have no interaction with a living tissue by contacting a biocompatible material. Interface characterization of a biomaterial has often discussed in terms of surface bonding state and protein adsorption capacity [3,4]. In this study, we focus on SU-8 photoresist which is epoxy-based negative photoresist as an interface material. In general, a monomer of SU-8 photoresist has eight epoxy functionalities; high degree of cross-linking after UV exposure can be obtained [5]. Therefore, a SU-8 film is stable in terms of mechanical and chemical interaction. Moreover, SU-8 photoresist has recognized as a candidate of biocompatible material by the Food and Drug Agency (FDA) of the United States [6]. In fact, a drug delivery MEMS (MicroElectroMechanical System) device, a microfluidic device and a probe for neuronal recording applications by SU-8 photoresist were reported [7-9].

The aim of this study is to evaluate electrical stability of a SU-8 photoresist film for bio device surface. V_{SU-8} as a surface electrical potential of a SU-8 film and V_{bio} as biopotential of plant cells are measured by using a pair of tungsten needles. Then, the potentials are fitted by an exponential function model, and factors of potential (equilibrium value, time constant and potential variation width) are determined quantitatively. As conclusion, reproducibility of electrical characteristic of a SU-8 photoresist film surface is indicated. The SU-8 photoresist with surface electrical stability and micromachining is applicable to the surface layer of bio devices.

2. Experiment

2.1 Sample preparation

A double SU-8 layer structure for experimental sample was prepared in order to form a flat and low detect surfaces. Table 1 shows a sample fabrication process. First, a glass plate (Matsunami Glass, S1111, 0.9mm thickness) was sawn by 26mm×26mm square. Then the glass was ultrasonic cleaned by dipping into acetone, ethanol and deionized water for 5min respectively. Then, SU-8 3005 photoresist liquid was dropped on the glass surface. The spin rate was ramped in two steps up

to 3000 rpm. Prebaking was carried out for 10min at 95°C on a hotplate. The glass was cooled down to room temperature after baking. Then, whole area of aSU-8 film was exposed to 365nm UV light at 6.0mW/cm^2 for 8s utilizing a UV spot light system (Yamashita denso, Hypercure-200). After the exposure, a SU-8 film was cross-linked by performing a two-step post exposure bake (PEB) process on a 65°C hot plate for 1min and for 4min at 95°C. A SU-8 film was soaked in SU-8 developer for 5min in similar to the standard SU-8 lithography process. After soaking, hardbaking was carried out at 200°C for 10min. Then an upper SU-8 film was formed on the bottom SU-8 film with the same procedure parameters. Figure 1 shows a fabricated SU-8 film on a glass plate.

As shown in Fig.2a, pothos (*Epipremnum aureum*), a kind of foliage plants, was employed as a living tissue because pothos is easy to daily cultivation. The pothos cells were prepared as follows: a leaf of pothos was cut then stored under ambient conditions for 1h before the measurement. Then, a piece (10mm×10mm) was clipped from the leaf, and peeled epidermis to expose mesophyll cells as shown in Fig.2b. Figure 2c shows an optical micrograph of pothos cells. It was observed that the size of one cell was 40 to 50μm. The distance of tungsten electrodes was adjusted to be the size of 3cells as shown in Fig.2d.

Table 1 SU-8 film fabrication process.

No.	Process	Condition
1.	Organic treatment with ultrasonic	Acetone: 5min Methanol: 5min Deionized water: 5min
2.	SU-8 Spin coat (2-step) as bottom layer	1st: 500rpm/5sec 2nd: 3000rpm/30sec
3.	Softbake (hotplate)	95°C/10min
4.	UV Exposure (i-line 365nm)	Power: 6.0mW/cm^2 Time: 8sec
5.	Post exposure bake (hotplate, 2-step)	1st: 65°C/1min 2nd: 95°C/4min
6.	Development	SU-8 developer: 5min Rinse: 1min (2 cycles)
7.	Hardbake (hotplate)	200°C/10min
8.	Hydrophilic treatment (O_2 plasma)	5min
9.	Repeat process No.2～7 as upper layer	

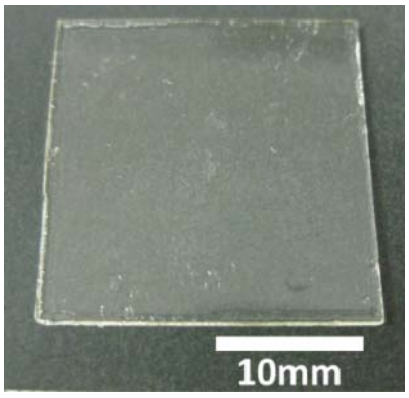

Fig.1 SU-8 film fabricated by lithography process.

(a) A pothos leaf

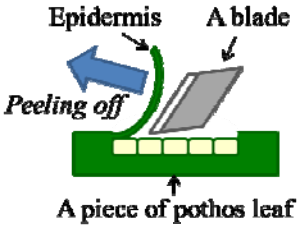

(b) Cell exposing method

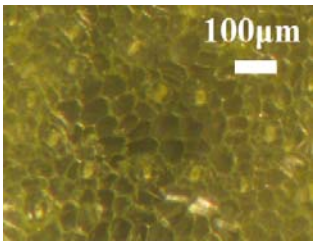

(c) Cell of a pothos leaf

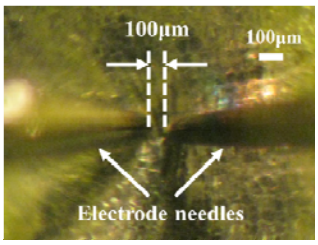

(d) Electrode needles

Fig.2 Plant sample preparation for this experiment and optical microscope images of pothos cells.

2.2 Potential measurement system

A potential measurement system is illustrated in Fig.3. In order to measure surface potential V_{SU-8} of a SU-8 film and biopotential V_{bio} of pothos cells, we employed a pair of tungsten needle as electric electrodes. Curvature radius of the needle is 20µm which is smaller than a pothos cell size (50µm). V_{SU-8} or V_{bio} were defined as potential difference between the needles. Terminals of a digital multimeter (KENWOOD DL-712, the input impedance is larger than 11MΩ) were connected to the needles.

A liquid drop of deionized water (below 0.06×10^{-4} S/cm) was put on the sample surface. The electrodes were immersed in dropped deionized water for 60s and the potential difference between the needles was set to zero by adjusting the contact area of the needle and water. Then the electrodes were moved slowly to make a contact with a SU-8 film surface or pothos cells. The distances between two tungsten electrodes were set at 409µm for a SU-8 film or 100µm for pothos cells. In order to monitor the large variation of in initial stage, the measurement interval was adjusted to be 1s until 60s of contacting time. After 60s, the data were recorded in interval 10s. Three different positions, *A*, *B* and *C* for a SU-8 film, *a*, *b* and *c* for pothos cells were selected.

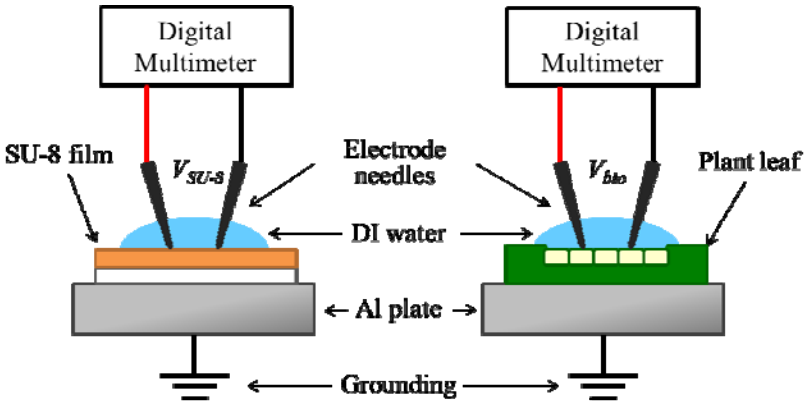

Fig.3 Potential measurement system (cross-sectional view).

3. Results and Discussion

3.1 Results of potential measurement

Figure 4 shows characteristic of surface potential V_{SU-8} on the measuring time of a SU-8 film. Initial change of the potential from t=0s to 60s is expanded and shown in Fig.4b. At every measured position (A, B, and C), V_{SU-8} indicates a maximum value just after making an electrode contact. Then V_{SU-8} exponentially decreases with the measuring time. At last, the potential V_{SU-8} reaches to the equilibrium value about +21mV at 300s.

Figure 5 shows characteristics of biopotential V_{bio} on the measuring time of pothos cells. Figure 5b shows initial change of V_{bio} from t=0s to 60s. We focus on that dynamic change of V_{bio} generates during the measuring time of electrodes at position *a* for 6s and position *c* for 32s. V_{bio} reaches to the equilibrium value in exponential function as same as V_{SU-8}. The equilibrium value is about -21mV at 300s.

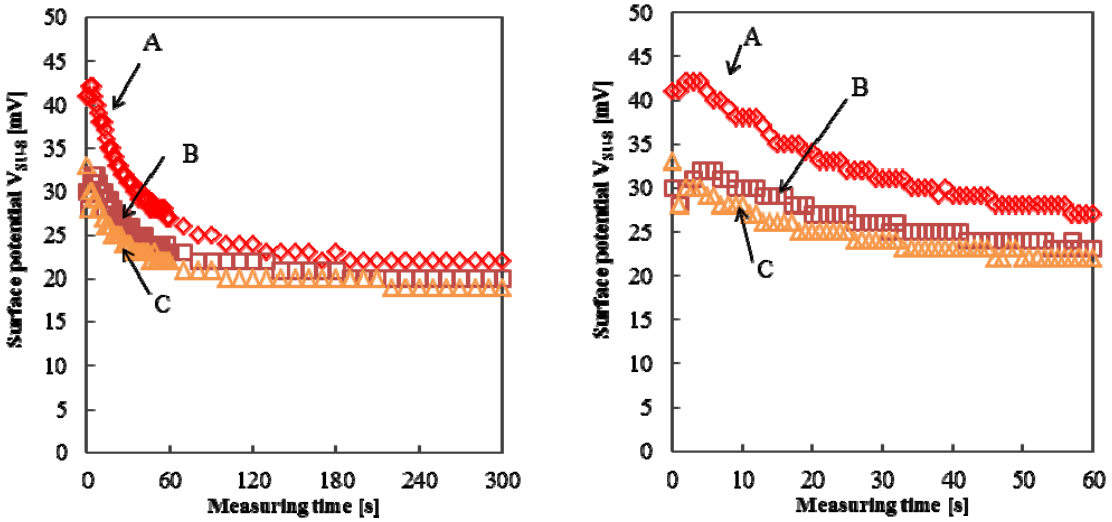

(a) Time region: 0s to 300s (b) Time region: 0s to 60s (expansion)

Fig.4 Characteristics of surface potential V_{SU-8} on measuring time of a SU-8 film.

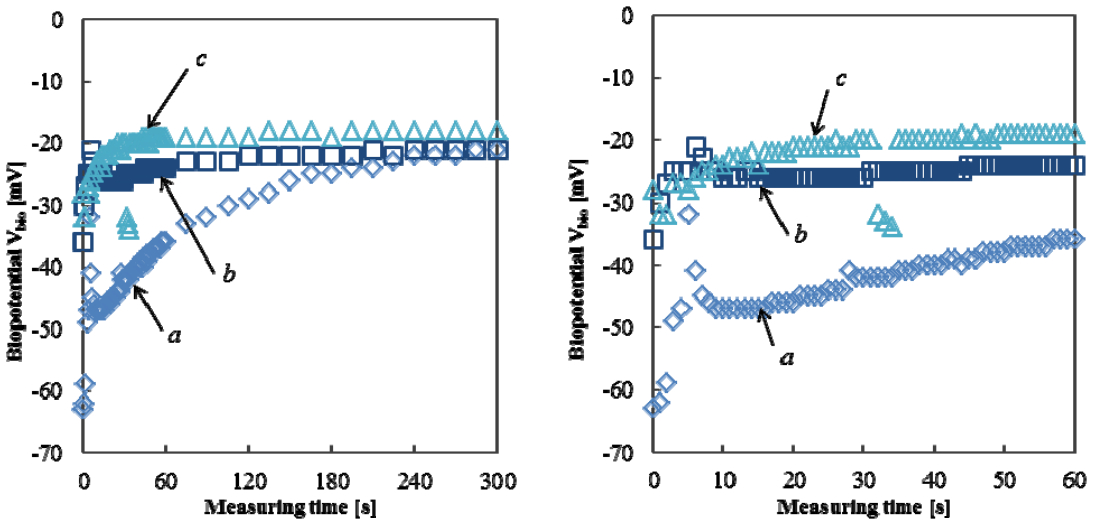

(a) Time region: 0s to 300s (b) Time region: 0s to 60s (expansion)

Fig.5 Characteristics of biopotential V_{bio} on contact time of 3-plant-cell.

Table 2 Potential change factors of V_{SU-8} and V_{bio}.

Potential	**V_{SU-8}**			**V_{bio}**		
Measurement position	**A**	**B**	**C**	**a**	**b**	**c**
Equilibrium value, V_{eq}[mV]	+22	+20	+19	-21	-21	-18
Difference between V_0 and V_{eq}, ΔV[mV]	+20	+21	+14	-42	-15	-10
Time constant τ[sec]	41.8	44.4	42.7	83.3	76.9	23.6

3.2 Quantification

In order to analyze quantitatively of V_{SU-8} and V_{bio}, we made a proposal by follow-approximated model (1),

$$V(t) = V_{eq} + \Delta V \exp\left(-\frac{t}{\tau}\right) = V_{eq} + \left(V_0 - V_{eq}\right)\exp\left(-\frac{t}{\tau}\right) \quad (1)$$

where V_{eq} is equilibrium values at t=300s and ΔV is difference between V_0 at t=0s and V_{eq}. The symbol of τ denotes the time constant. ΔV and τ can indicate stability of potential. Table 2 summarized these fitting parameters of V_{SU-8} and V_{bio}. In the following discussion, sign of factors are neglected and just focused on absolute value.

In regard to equilibrium value V_{eq}, V_{eq} of each potential is determined around 20mV. This value seems that related to zeta potential between probe needle and deionized water. ΔV of surface potential of a SU-8 film is mostly same among *A*, *B* and *C*. However, the potential range ΔV of V_{bio} indicates quite different among the measurement position *a*, *b* and *c*. The time constant τ of V_{SU-8} is 42s on average from electrodes contact, on the other hand, τ of V_{bio} is not same value at each position. With regard to non-reproducibility and dynamic potential change of biopotential, it seems that signal transfer between plant cells is related. Ion concentration difference inside and outside of a cell is one major factor of signal transfer [10,11].

As a result, reproducibility of electrical characteristic of a SU-8 photoresist film surface is indicated. The reproducibility can be thought of as one of surface stability.

4. Conclusion

In order to evaluate of electrical stability of a SU-8 photoresist film for bio device surface, we measure surface potential V_{SU-8} of a SU-8 film and compared to biopotential V_{bio} of plant leaf cells. V_{SU-8} indicates exponential decreasing and gets at +21mV as equilibrium state. Contrariwise, in regard with V_{bio}, dynamic change is observed in initial region of the measurement. Then V_{bio} gets at equilibrium -21mV. Quantitative analysis of potential measurement data is performed and factors of each potential, such as equilibrium, amount of change and time constant are estimated. Factors of surface potential of a SU-8 film are similar at every point. However, there are widely varied in biopotential.

As a result, reproducibility of electrical characteristic of a SU-8 photoresist film surface is revealed by comparing measurement result of plant cells. The reproducibility can be thought of as one of surface stability. We believe that stability of a SU-8 film exhibits promising characteristics for a bio device substance.

Acknowledgments

The present work was partially supported by Grant-in-Aid for Scientific Research, Grant-in-Aid for Scientific Research (JSPS KAKENHI B: 23360150) and Grant-in-Aid for challenging Exploratory Research (MEXT KAKENHI 23656235).

References

[1] C. M. Hwang, W. Y. Sim, S. H. Lee, A. M. Foudeh, H. Bae, S. H. Lee, A. Khademhosseini, *Biofabrication*, **2** (2010) 045001.
[2] M. Chen, P. O. Zamora, P. Som, L. A. Pena, S. Osaki, *J. Biomater. Sci. Polymer Edn*, **14** (2003) 917-935.
[3] F. Walther, T. Drobek, A. M. Gigler, M. Hennemeyer, M. Kaiser, H. Herberg, T. Shimitsu, G. E. Morfill, R. W. Stark, *Surf. Interface Anal.*, 42 (2010) 1735–1744.
[4] G. Blagoi, S. Keller, A. Johansson, A. Boisen, M. Dufva, *Appl. Surf. Sci*., **255** (2008) 2896-2902.
[5] A. del Campo, C. Greiner, *J. Micromech. Microeng*., **17** (2007) R81–R95.
[6] B. P. Chaudhri, F. Ceyssens, P. D. Moor, C. V. Hoof, R. Puers, *J. Micromech. Microeng*., **20** (2010) 064006.
[7] G. Voskerician, M. S. Shive, R. S. Shawgo, H. Recum, J. M. Anderson, M. J. Cima, R. Langer, *Biomaterials*, **24** (2003) 1959–1967.
[8] B. Bohl, R. Steger, R. Zengerle, P. Koltay, *J. Micromech. Microeng*., **15** (2005) 1125–1130.
[9] A. Altuna, L. Menendez de la Prida, E. Bellistri, G. Gabriel, A. Guimerá, J. Berganzo, R. Villa, L. J. Fernández, *Biosens. Bioelectron.*, **37** (2012) 1–5.
[10] T. Ohyabu *et al*., *Bioelectrical potential of plant and communication*, Kaibundo, (2009) 8-9 (in Japanese).
[11] J. Fromm, S. Lautner, *Plant, Cell & Environment*, **30** (2007) 249–257.

(Received: 26 July, 2013, Accepted: 24 February 2014)

Effect of Mechanical Stress on Electrolyte Film for Flexible Sheet Type Direct Methanol Fuel Cell

Yosuke Sakurai, Akira Kawai
Department of Electrical Engineering, Nagaoka University of Technology
1603-1 Kamitomioka, Nagaoka, Niigata, 940-2188, Japan
E-mail: kawai@nagaokaut.ac.jp

This paper discuss shortly that effect of mechanical stress on flexible Sheet Type Direct Methanol Fuel Cell (FS-DMFC). FS-DMFC is attractive as a portable power source for flexible devices. In this regard, it is inevitable that the FS-DMFC will operate under external mechanical loads. In addition, the mechanical stress should act to deteriorate the FS-DMFC. FS-DMFC is fabricated on the flexible substrate. Then compressive load and tensile load are applied to the electrolyte film. Contrary to our expectation, the effect of compressive load in an electrolyte film is observed as enhancement of electro motive force. By applying compressive load to an electrolyte film, proton ionic conductivity would be enhanced. On the other hand, a tensile load acts to decrease electro motive force. Therefore the electrolyte film should be designed as a laminated structure in order to enhance proton ionic conductivity of electrolyte film by compressive load from the both top and bottom films.

1. Introduction

Recently, Direct Methanol Fuel Cell (DMFC) is recognized as a candidate of portable power source [1]. Many challenging aspects of the minimization of DMFC focused on Sandwich structure with electrolyte and microfabricated silicon current collectors [2], micro fuel cell with hydrogen generator [3], flexible sheet type DMFC array with micro hole array [4]. Especially, we focused on the flexible sheet type DMFC (FS-DMFC) due to the facility of minimization and application for flexible devices. In this case it is expected that certain amount of tapping or bending stresses are applied to the FS-DMFC.

This paper focuses on deterioration of proton ionic conductivity of an electrolyte film induced by mechanical load. The compressive load and tensile loads can be applied to an electrolyte film. Our results raise the possibility that external compressive film stress enhances proton ionic conductivity of an electrolyte film. However external tensile load decreases proton ionic conductivity. The cell structure should be designed as a laminate structure in order to improve the proton ionic conductivity by the film stress.

2. Experiment

2.1 Fabrication of flexible Sheet type DMFC (FS-DMFC)

A schematic of a FS-DMFC structure is shown in Fig.1. This device is composed with two Pt electrodes and Nafion electrolyte (DE2020, DuPont). This device has an ability of electricity generation by applying a fuel.

The structure of FS-DMFC was fabricated in the flowchart as shown in Fig.2.

(a): A PET film (Apica Co., Ltd) was cut by a cutter in a size of 15mm x 30mm.

(b): Slight amount of contamination on a PET film was removed by immersing in deionized water (DIW). Then a PET film was cleaned for 6min by an ultrasonic cleaning system (EC-4515, Twinbird Co., Ltd).

(c): A piece of glass of 0.9±0.1μm thick was prepared in size of 15mm ×3mm, which was used as a mask of Pt film sputtering.

(d): A Pt film as a catalyst layer of approximately 100nm thick was sputtered at 250W for 150min by using a RF sputtering system (PDM-303, Samco Inc.). The purity of Pt sputtering target (JEOL Ltd.) was 99.99%. The purity of sputtering Ar gas was 99.9999% and flow rate was 4sccm.

(e): A glass plate on the PET film was removed, and then the Pt films for anode and cathode were formed.

(f): Electrolyte (Nafion®) solution of 0.03±0.01cc was dropped on a center of the PET film by using a dropper.

(g): Electrolyte solution is dried at 25±2˚C for 1h. The films of 37±10μm thick for compressive test and 93±20μm thick for tensile test were formed.

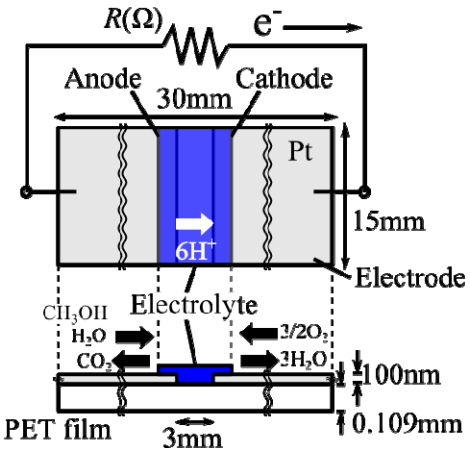

Fig.1 Schematic diagram of the FS-DMFC structure.

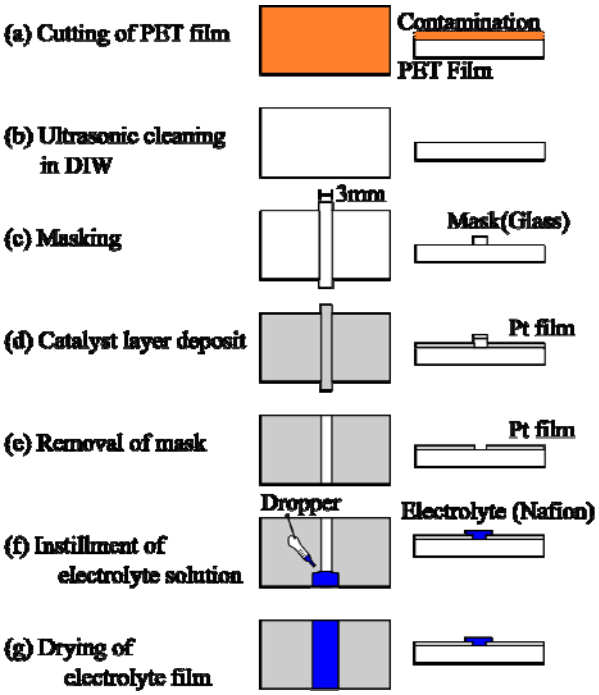

Fig.2 Fabrication process flowchart of FS-DMFC.

2.2 Electric generation Measurement

The FS-DMFC was operated in 25±2˚C by applying 3wt% methanol aqueous solution of 0.2cc. The fuel was dropped on the anode Pt film. A certain amount of oxygen molecule was allowed to diffuse the cathode electrode from ambient air. The electro motive force E between two electrodes was measured by using an electric circuit as shown in Fig.3. The circuit was composed by a variable resister (TYPE 2786, Yokogawa Electric Works, Ltd.) and the FS-DMFC. The load voltage V_R was measured by using a digital multi-meter (DL-712, Kenwood).

The electric generation power P of the FS-DMFC is estimated by the following equations.

$$P = \frac{R}{(R + R_0)^2} E^2 \qquad (1)$$

$$P_{max} = \frac{E^2_{max}}{4R_0} \qquad (2)$$

where R is resistance of variable resister, R_0 is internal resistance of the FS-DMFC and E is electro

motive force of the FS-DMFC. The values of P_{max} and E_{max} indicate maximum when $R = R_0$. In order to obtain the maximum electric generation power, the variable resister was adjusted from 100Ω to 100kΩ. The electric generation area of the FS-DMFC was designed as the interface area between Pt electrode and the electrolyte film to be 0.225cm^2.

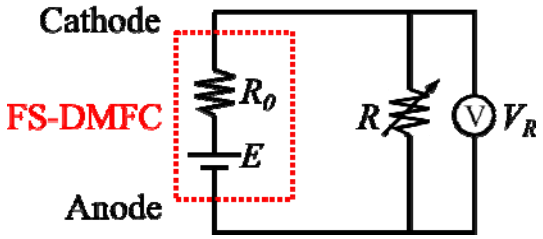

Fig.3 Measurement circuit of the electro motive force of FS-DMFC.

2.3 Compressive load

External compressive load was applied to a part of electrolyte film surface directly as shown in Fig.4. The loading experiments were carried out under (i) partially immersion and (ii) fully immersion conditions of the fuel on the electrolyte film as shown in Fig.4.

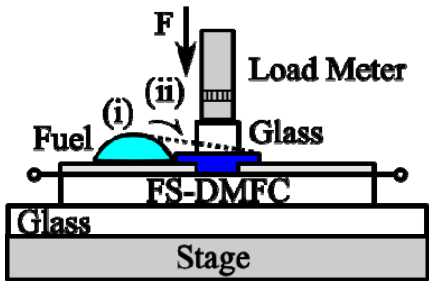

Fig.4 Schematic diagram of compressive load test. Compressive load was applied by adding a certain strain (20μm) to a center of the electrolyte film with a load meter.

2.4 Tensile load

As shown in Fig.5, the FS-DMFC was easy to bend by human fingers. External tensile load was applied by wrapping the FS-DMFC around a cylinder of 14mm diameter repeatedly in dry condition as shown in Fig.6. Therefore, tensile load was applied to the electrolyte film directly in 0, 50, 100, 200, 300, 500, 700 and 1000 times. The electro motive force E was measured after removing tensile load of each loading times.

Fig.5 Photograph of bending of the FS-DMFC by human fingers.

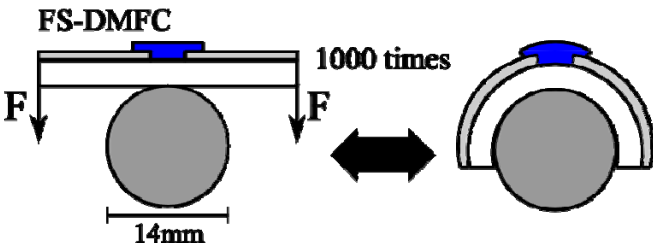

Fig.6 Schematic diagram of tensile load.

3. Results

3.1 Compressive load effect

Figure.7 shows the typical electric generation properties of DMFC. The result shows that the FS-DMFC indicates higher electric power density by immersing the electrolyte film in the fuel fully, comparing with the partial one. Moreover time dependency of the electric power density under compressive load is shown in Fig.8. By immersing electrolyte film with the fuel fully, it is clearly observed the retention property of the electric power density is enhanced by applying the compressive load.

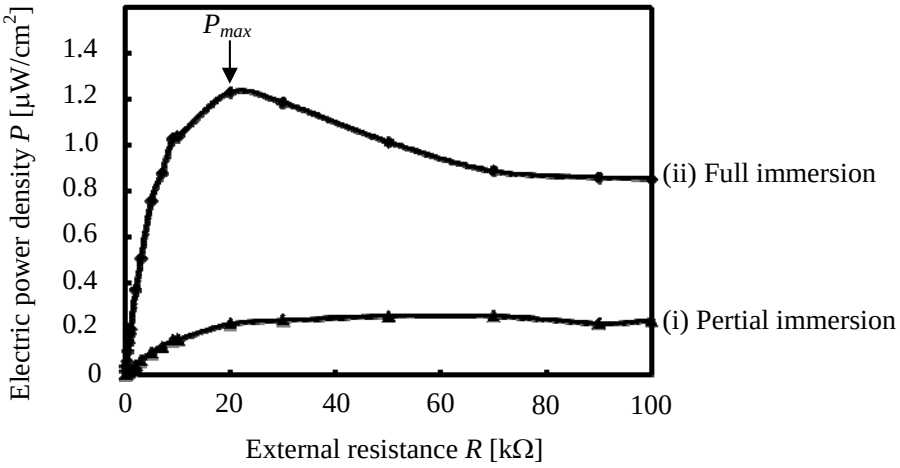

Fig.7 Typical electric generation of the FS-DMFC.

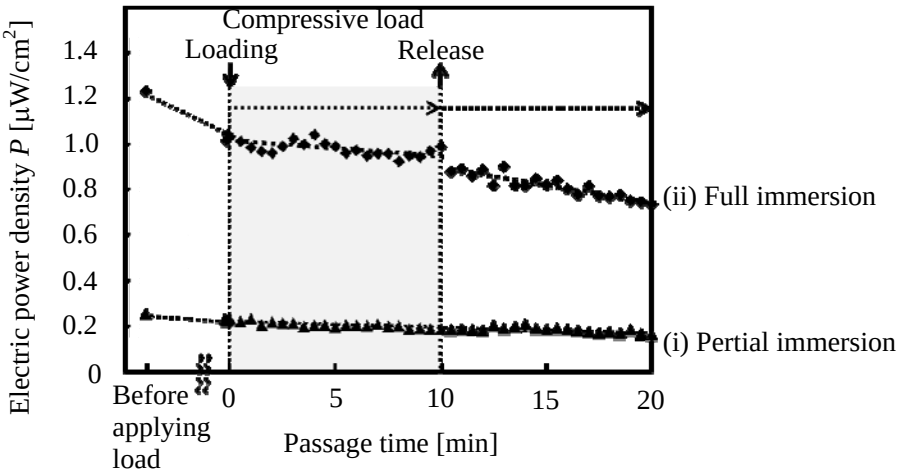

Fig.8 Electric generation of FS-DMFC by applying external compressive load.

3.2 Tensile load effect

Figure.9a shows an electric power density curve of applying times of tensile load. Fig.9b shows the maximum electric power density and internal resistance as a function of loading times increase. The maximum electric power density linearly decreases with increasing the applying load times. The internal resistance of the FS-DMFC increases slightly with the tensile loads. The result shows that repetitive tensile load causes decrease of electric generation property.

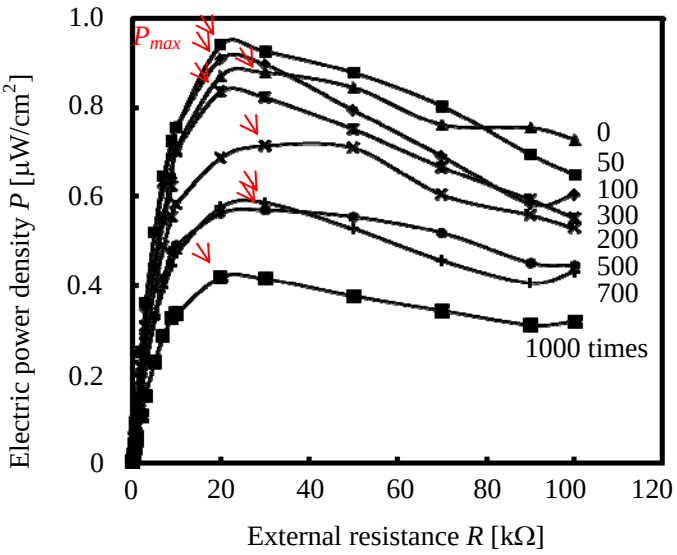

(a) Maximum power density of tensile load

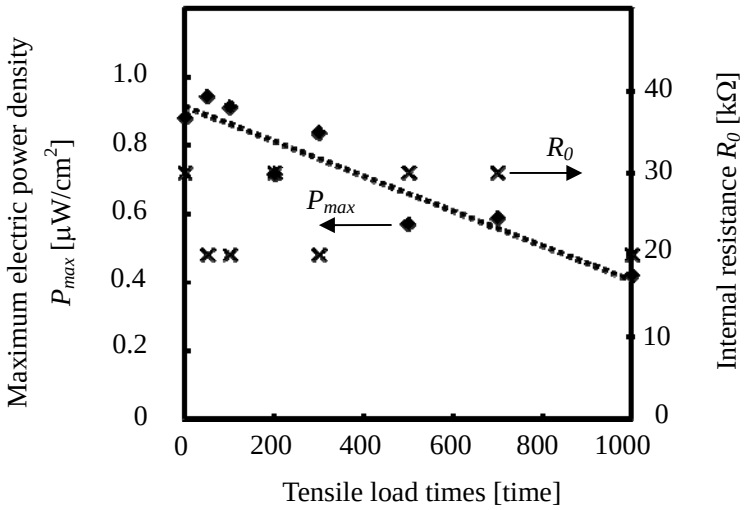

(b) Dependency on tensile loading times.

Fig.9 Electric generation of FS-DMFC by applying tensile load.

4. Discussion

4.1 Improvement of electric power density under compressive load

The electric power density difference in Fig.7 reflects clearly the fuel supply volume difference. By immersing the electrolyte film of fuel fully, it is supposed that the fuel can be supplied sufficient volume which causes the higher electric power density comparing with the partial one. The compressive load should act to compress the electrolyte film. This phenomenon probably causes higher sorption of water molecule due to condensation of sulfonic acid groups [5]. Therefore the external compressive load would act to improve the retention property of the electrolyte film.

4.2 Decrease of electric power density under tensile load

In this experiment, nano scale void would be formed and proton ionic conductivity would become low. In the literature, the peak stress of tensile load is localized at a water/electrolyte film

interface [6]. It can be supposed that bonding of sulfonic acid groups is expanded due to the stress concentration. Therefore the internal resistance R_0 of the electrolyte film can be increased and the electro motive force E can be decreased under tensile load.

4.3 Effective structure of the electrolyte film

Figure.10 shows a schematic diagram of effective structure of an electrolyte film. Our results raise the possibility that compressive stress acts to enhance a proton ionic conductivity in an electrolyte film. Then it is well-known that a film on the substrate generates significant film stress. It can be considered that compressive stress generated by pressing from both the top and bottom films enhances a proton ionic conductivity in the electrolyte film due to condensation of sulfonic acid groups. Then the electrolyte film laminated by the porous films is effective for a DMFC operation.

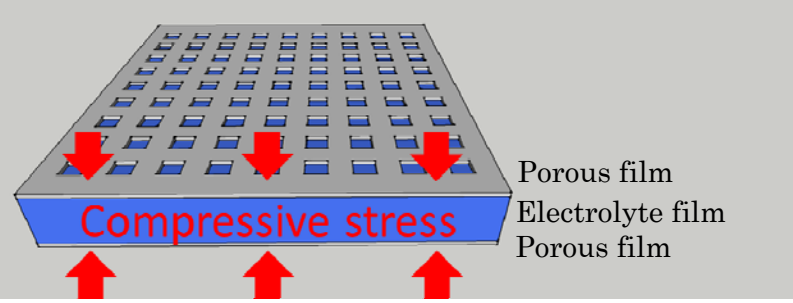

Fig.10 Schematic diagram of laminated electrolyte film.

5. Conclusion

A relationship between mechanical stress and electric generation property of an electrolyte film is discussed. Electric generation property should be enhanced by external compressive stress and should be decreased by tensile stress. Therefore it is needed to design the electrolyte film as a laminated structure.

Acknowledgments

The present work was partially supported KAKENHI B:23360150) and Grant–in–Aid for challenging Exploratory Research (MEXT KAKENHI 23656235).

References

[1] C. K. Dyer, J. Power Sources, **31** (2002) 106.
[2] N. Sabate, J. P. Esquivel, J. Santander, J. G. Hauer, R. W. Verjulio, I. Gracia, M. Salleras, C. Calaza, E. Figueras, C. Cane, L. Fonseca, Microsystem Technologies. DOI: 10.1007/s00542-013-1781-4
[3] L. Zhu, K. Y. Lin, R. D. Morgan, Vikhram V. Swaminathan, H. S. Kim, B. Gurau, D. Kim, B. Bae, R. I. Masel, M. A. Shannon, J. Power Sources, **185** (2008) 1305.
[4] T. Ito, K. Kimura, M. Kunimatsu, Electrochem. Comm., **8** (2006) 973.
[5] H. Zhang, P. K, Shen, J. Hydrogen Energy., **37** (2012) 4657.
[6] Y. Qi, Y-Hung lai, Polymer, **52** (2011) 201.

(Received: 26 July, 2013, Accepted:4 April 2014)

Amorphous Hydrogenated Carbon Films Deposited with Benzene by Plasma Enhanced Chemical Vapor Deposition

Xiaolong Zhou*, Ikumi Toda, Keiji Komatsu, Hiroyuki Muramatsu, Shigeo Ohshio, Hidetoshi Saitoh

Department of Materials Science and Technology, Nagaoka University of Technology, 1603-1 Kamitomioka-cho, Nagaoka 940-2188, Japan

**E-mail: hts@nagaokaut.ac.jp*

Amorphous hydrogenated carbon (*a*-C:H) films have been synthesized by a plasma enhanced chemical vapor deposition (PECVD) method with benzene as a source gas. A phosphorus pentoxide (P_2O_5) dehydration units and the chamber baking treatment were introduced into the CVD system to synthesize high purified *a*-C:H films, and the effects of H_2O on the structure and the chemical composition for *a*-C:H films were investigate1001d. The true density values for the *a*-C:H films were in the range of 1.18-1.23 g/cm^3 measured by X-ray reflection. These processes reduced the –OH termination structure of the films. The depth profile for the *a*-C:H films revealed that elemental composition of oxygen and hydrogen atoms were decreased significantly in the bulk regions of films. These results suggest that elimination of H_2O is an important factor for synthesizing highly purified *a*-C:H films by the PECVD method.

1. Introduction

Amorphous hydrogenated carbon (*a*-C:H) films have widely received interests by many researchers for their unique properties in mechanical and electrical applications [1-3]. In this field, hydrocarbons as the source gas such as methane (CH_4), ethylene (C_2H_4), acetylene (C_2H_2), hexane (C_6H_{14}) and benzene (C_6H_6) as reported in [4-9] are used for synthesizing *a*-C:H films. The kind of source gas has a significant effect on the *a*-C:H film properties in a plasma enhanced chemical vapor deposition (PECVD) method. It is verified that C_6H_6 is useful for the raw material in obtaining a high deposition rate on low particle energy in these source gases. For instance, the deposition rate of the film synthesized with benzene is an approximately 85 nm/min because of the low ionization potential of 9.2 eV. In contrast, CH_4 forms the film with a deposition rate of a 8 nm/min due to a high ionization potential of 12.4 eV. Robertson reported that decomposition of C_6H_6 by the PECVD method fabricated thick *a*-C:H films in a short time because of their high deposition rate [1].

Contamination of water (H_2O) is one of the main problems for synthesizing high purified the *a*-C:H films. Firstly, H_2O is easily contaminated into benzene because of high solubility of water in benzene, 1.8 g/L at 26^{o}C [10]. Secondly, H_2O in carrier gas also becomes impurity, which affect various characters of the resultant *a*-C:H films such as density, stability, and mechanical property. Models for the effect of H_2O on the *a*-C:H films by the PECVD method are shown in Fig. 1. If H_2O is contaminated into the CVD chamber, hydroxyl (-OH) groups are formed on the *a*-C:H films surface, which may also cause adsorption of additional water on the surface of the *a*-C:H films, as shown in Fig. 1(a). This phenomenon has a significant effect on the *a*-C:H film properties. In order to obtain *a*-C:H films with high purity and quality, we have to eliminate -OH groups from the *a*-C:H films, as shown in Fig. 1(b). Since phosphorus pentoxide (P_2O_5) has strong water absorption ability, water is effectively eliminated from source and carrier gases by using P_2O_5 dehydration units. In addition, absorption of H_2O into the chamber wall is also a problem. When the leak valve is opened after an experiment, substantial air enters into the chamber. Therefore, the possibility internal surface of the chamber may be adsorbed water. Chamber-baking treatment is a standard experimental technique to eliminate water adsorbed on the internal surface of the CVD chamber. Thus, a combination of the P_2O_5 dehydration unit and the chamber-baking treatment may be an effective

experimental technique to obtain highly purified *a*-C:H films.

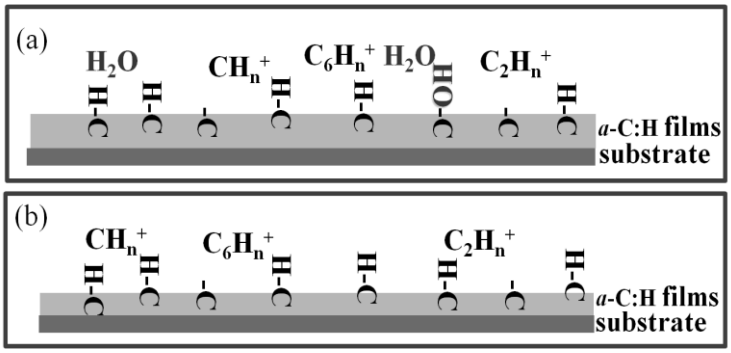

Fig. 1 Models for the effect of H_2O on *a*-C:H films by PECVD method(a) with H_2O and (b) without H_2O.

In this study, *a*-C:H films were synthesized by the PECVD method using C_6H_6 as a raw material. To investigate the effects of H_2O on the deposition of the *a*-C:H films, the P_2O_5 dehydration units and the chamber-baking treatment were added in the process of *a*-C:H film deposition. We demonstrated the effects of H_2O on the properties of the *a*-C:H films based on the true density values, surface structure, and cross-sectional elemental distributions

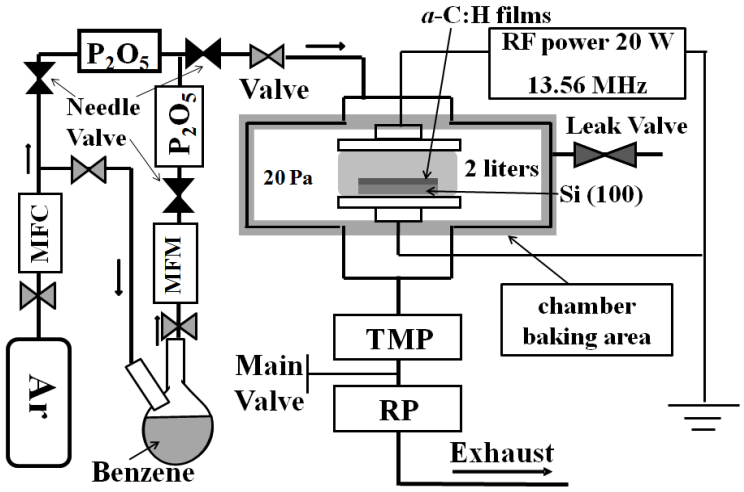

Fig. 2 Schematic diagram of PECVD apparatus

2. Experiment

The Si (100) surface-deposited with *a*-C:H films by the PECVD technique with radio-frequency at 13.56 MHz as shown in Fig. 2. The Si substrates were cut size of 1 × 1 × 0.6 mm^3. Then, the samples were rinsed by distilled water, acetone and ethanol solution before coating. The pure argon gas (Taiyo Nippon Sanso, purity of 99.9999%) and benzene liquid (Wako Pure Chemical Industries, purity >99%; liquid at room temperature) were used as carrier and source gasses, respectively. In the experiment, a two-necked flask whose volume as 100 ml was used for containing liquid benzene. A combination of a rotary Pump (RP) and a turbo Molecular Pump (TMP) was used to exhaust air in the chamber whose volume was 2 L. Prior to the film synthesis, the following steps was made. First, the chamber was evacuated to 1.5×10^{-4} Pa by using above pumping system. Second, we have made the Ar carrier gas fill into the two-necked flask with a flow rate of 20 cm^3/min for 3 min with the exit valve of benzene closed, and then, have closed the valve of carrier-gas inlet with the exit valve of

benzene opened for 5 min. The second process was repeated three times to eliminate fully the residual air at the top of the two-necked flask. When the pressure was less than 13.3 kPa (the vapor pressure of benzene is 13.3 kPa, at 26.1 ^{o}C), benzene was vaporized, and then argon gas with a flow rate of 20 cm^3/min carries benzene with a flow rate of 5 cm^3/min. The flow of Ar and benzene were regulated by a mass flow controller (MFC) and a mass flow meter (MFM), respectively.

All these gases were passed through the P_2O_5 dehydration units, and were introduced into the CVD chamber with pressure about 20 Pa using the above pumping system. In the experiment with the chamber-baking treatment, the ribbon heater was wrapped around the chamber and the temperature was raised to about 100 ^{o}C for 30 min before the film deposition, and this temperature was kept during the film deposition. The radio-frequency electromagnetic wave with a power of 45 W was introduced during the film deposition. The deposition time was 10 min for each film. The benzene and argon valve was closed immediately after the end of films deposition, when the power was turned off the plasma disappeared. The above pumping system continued work for 1 hr to exhaust these gases, at the same time the chamber wall was cooled to room temperature. But the residual benzene would be still adsorbed into the pipeline and chamber wall a little. In order to observe the influence of water on the films, also the films were synthesized under the conditions of presence or absence of the P_2O_5 dehydration units and the chamber-baking treatment as shown in Table 1.

The true density of the *a*-C:H films estimated by the X-Ray reflectivity (XRR) method (M03XHFMXP3, Mac science) as reported in [13] and shown in Fig. 3. The XRR data were obtained using a Cu$K\alpha$ X-ray source (wavelength of 1.54 Å) under the conditions of a scan range (2θ) of 0.184°-2.500° and a step size of 0.004°. The XRR is one of the most widely used analytical methods [11-13] which has many attractive characteristics such as non-destructiveness and ability of quantitative measurements of the crystal structure under the ambient conditions.

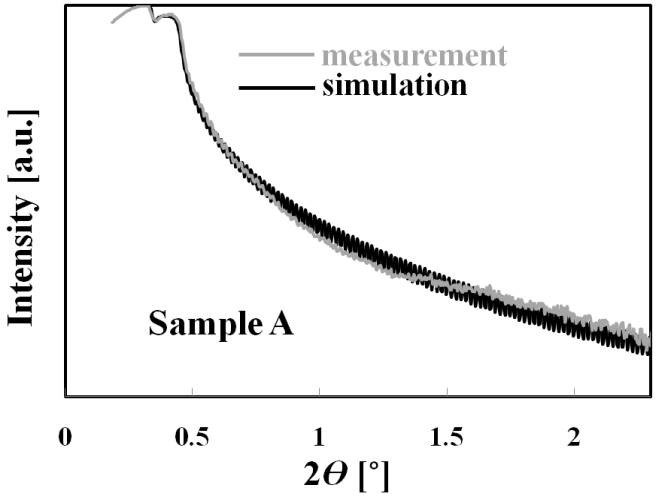

Fig. 3 XRR data and simulation for sample A

An analysis of the structural changes of the films was made by using Fourier transform infrared (FT-IR) spectroscopy (NICOLET 6700, Thermo Fisher Scientific). All the spectra were obtained from 500 to 4000 cm^{-1} with 100 scans for each spectrum. Glow-discharged optical-emission spectroscopy (GDOES) is one of the effective tools to analyze the elemental distribution in the depth direction of the film, where the time profiles of the atomic transitions are measured with short time periods by Ar-ion sputtering induced by the glow-discharge plasma [14-16]. The depth profiles of carbon (λ=165.7 nm), hydrogen (λ=121.6 nm), oxygen (λ=130.2 nm) and silicon (λ=288.2 nm) of the films were measured using GDOES (HORIBA, GD-Profiler 2).

3. Results and Discussion

Table 1 shows the true density of samples A-D. The true densities of samples were 1.18, 1.20,

1.22 and 1.23 g/cm^3, respectively. As results, it is obvious that the sample A has true density less than the sample B, C and D, while the true densities of sample C and D are the similar. However, the chamber baking process effect to the increasing of the true density. In addition, the observed differences in the film densities suggested that the structure and chemical composition of a-C:H films depend on the desiccation procedures.

Table 1 The H_2O elimination conditions and true density for samples A-D

Sample	A	B	C	D
Dehydration unit	×	○	○	×
Chamber baking	×	×	○	○
True density (g/cm^3)	1.18	1.20	1.22	1.23

The FT-IR spectra of the *a*-C:H films were shown in Fig. 4. Sample A indicated the stretching vibration peaks assigned to be the hydroxyl (-OH) group around 3300 cm^{-1}[18]. The -CH group was also observed in a region of about 3000 cm^{-1}[17,19]. In addition, adsorption of H_2O in the sample A-D was confirmed in a region of about 1500 cm^{-1}.

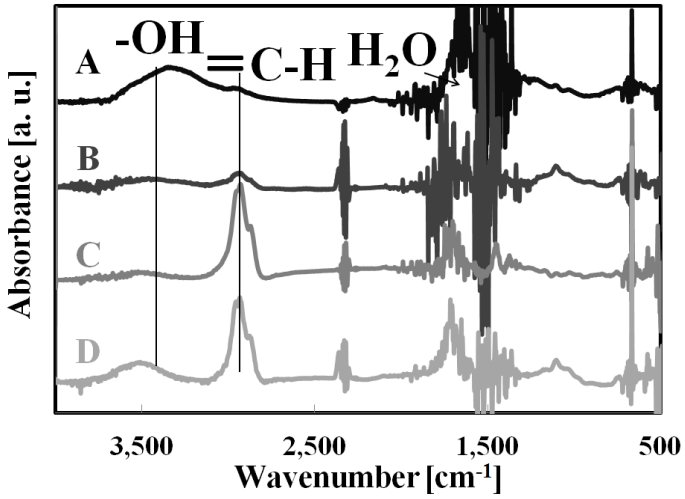

Fig. 4 FT-IR spectra of the *a*-C:H films, samples A-D

These results indicated two facts. The first is that the intensity of the –OH absorption band is significant when films were deposited under the condition without the P_2O_5 dehydration units and chamber-baking treatment. The second is that films with the P_2O_5 dehydration units or with the chamber-baking treatment (sample B, C and D) show clear absorptions due to the -CH group and significant decrease of those of the -OH group. In addition, samples B and C exhibits low intensity of the OH group, whereas sample D had a significantly high intensity of this group (though less than that in A whose origin can be attributed to the H_2O adsorbed onto wall of chamber).

The results can be explained by physical and chemical processes that take place during deposition of the *a*-C:H films. H_2O molecules contaminated into the CVD chamber will be dissociated to form OH and H radicals during the discharge process. Therefore, the –OH groups were formed on the *a*-C:H films surface in the cases of samples A and D. The immediate cause of the significant increases of the CH absorption peaks of samples C and D was the benzene residue on the surface of *a*-C:H films according to the IR spectrum of benzene which has the significant CH group absorption peaks in a region of about 3000 cm^{-1} [20].

The essential point of the phenomenon of the inclusion of benzene molecules into the samples C and D seems to be a thermal gradient between the substrate and the chamber wall. For sample C and D, the temperature of the chamber inner wall is higher than the substrate; thermal gradient is

generated between the wall and the substrate causing the thermal flow of benzene molecules into the substrate from the chamber inner wall. On the other hand, if the wall is not heated, the thermal gradient does not generate, and the flow of benzene molecules into the substrate will be negligible or not. This is the case of sample A and B.

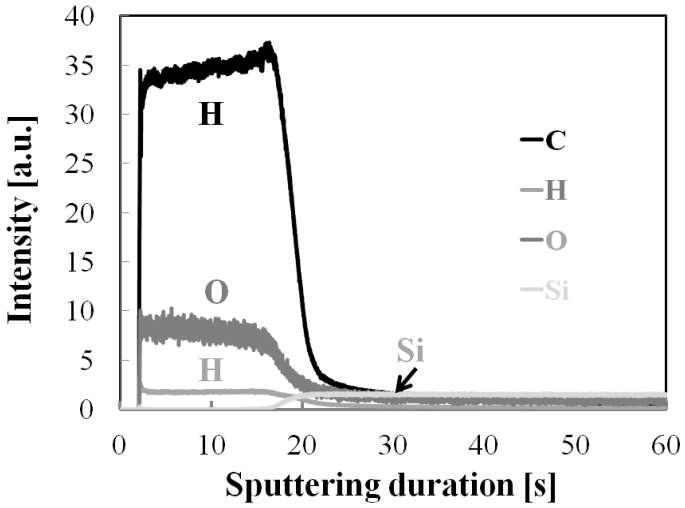

Fig. 5 GDOES profile of the *a*-C:H film of sample A

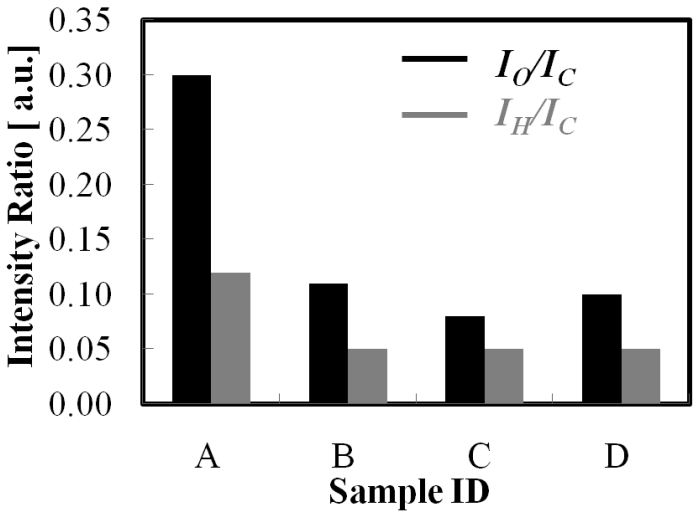

Fig. 6 I_O/I_C and I_H/I_C values estimated from the GDOES profiles of samples A-D

Fig. 5 shows a GDOES profile for the *a*-C:H film of sample A. Four elemental depth distributions, carbon (C), hydrogen (H), oxygen (O), and silicon (Si), were obtained. The emission of these elements were detected in the observed time range of 2-60 s. Maximum emission intensities for C, H and O atoms were obtained in the ranges of 3-20 s. In contrast, the detection for Si atom began at 15 s, and its intensity increased gradually. Then, the maximum intensity of emission from Si atom was obtained after 20 s. These observations indicate that the etching times in the rages of 2-60, 15-20, and 20-60 s correspond to the bulk region of film, the boundary region, and the silicon substrate, respectively. Therefore, the analysis is significant in the range of 2 - 15 s.

We estimated the intensity ratio of hydrogen to carbon (I_H/I_C) as well as that of oxygen to carbon (I_O/I_C) for samples A-D. Fig. 6 shows the I_O/I_C and I_H/I_C values estimated from the GDOES profiles

of the *a*-C:H films. For instance, the value for sample D was smaller than that of sample A. The I_O/I_C values were reduced from 0.3 to less than 0.1. Moreover, the I_H/I_C values were also decreased from 0.12 to 0.05. These decreases in the I_O/I_C and I_H/I_C values suggest that elemental composition of oxygen and hydrogen atoms were decreased significantly using P_2O_5 dehydration units and chamber-baking treatment

4. Conclusions

The *a*-C:H films were successfully deposited on the Si (100) by the PECVD technique using benzene diluted with Ar gas. The effect of elimination of H_2O from the reaction system on the physical and chemical structures of *a*-C:H films were demonstrated using the P_2O_5 dehydration units and the chamber-baking treatment. The true densities of the samples were in the range of 1.18-1.23 g/cm^3. The compositional analysis method (GDOES) revealed that the hydrogen and oxygen atoms contained in the *a*-C:H films were decreased significantly.

References

[1] J. Robertson, Mater. Sci. Eng. R **37** (2002) 129−281.
[2] S. M. Chiu, S. C. Lee, C. H. Wang, F. C. Tai, C. W. Chu, D. Gan, J. Alloy. Compd., **449** (2008) 379−383.
[3] N. Dwivedi, S. Kumar, H. K. Malik, Govind, C. M. S. Rauthan, O.S. Panwar, Appl. Surf. Sci., **257** (2011) 6804−6810.
[4] H. Akasaka, N. Gawazawa, S. Kishimoto, S. Ohshio, H. Saitoh, Appl. Surf. Sci., **256** (2009) 1236−1239.
[5] Y. Yamauchi, M. Kuzuya, Y. Sasai, S. Kondo, Thin Solid Films, **519** (2011) 6693−6697.
[6] H. Ito, K. Koshimura, S. Onitsuka, K. Okada, T. Suzuki, H. Akasaka, H. Saitoh, Plasma Chem. Plasma P., **32** (2012) 231−248..
[7] G. A. Abbas, S. S. Roy, R. Papakonstantion, J. A. McLaaughlin, Carbon, **43** (2005) 303−309.
[8] G. A. Abbas, J.A. McLaaughlin, E. Harkin-Jones, Diam. Relat. Mater., **13** (2004) 1342−1345.
[9] A. Erdemir, I. B. Nilufer, O.L.Eryimaz, M. Beschliessr, G.R. Fenske, Surf. Coat. Tech., **120-121**(1999) 589−593.
[10] Material Safety Data Sheet, Benzene MSDS, http:// www3.kanto.co.jp/ catalog/ msds/ J_04084PDF.
[11] S. B. Singh, A. K. Poswal, M. Pandey, R. B. Tokas, N. Chand, S. Dhara, B. Sumdaravel, Surf. Coat. Tech., **203** (2009) 986−991.
[12] N. Paik, Diam. Relat. Mater., **14** (2005) 196−200.
[13] A. Libassi, A. C. Ferrari, V. Stolojan, B. K. Tanner, J. Robertson, L. M. Brown, Diam. Relat. Mater., **9** (2000) 771−776.
[14] R. E. Galindo, R. Gago, D. Duday, Anal. Bioanal. Chem., **396** (2010) 2725−2740.
[15] J. L. Endrino, M. Allen, R. E. Galindo, H. Zhang, A. Anders, J. M. Albella, Lawrence Berkeley National Laboratory, 2007.
[16] K. Petrikowski, M. Fenker, J. Gabler, A. Hageman, S. Pleger, L. Schafer, Diam. Relat. Mater., **33** (2013) 38−44.
[17] M. H. Ahmed, J. A. Byrne, Appl. Surf. Sci., **258** (2012) 5166−5174.
[18] R. Pena Alonso, F. Rubio, J. Rubio, J. L. Oteo, J. Anal. Appl. Pyrol., **71** (2004) 827−845.
[19] S. M. Smith, S. A. Voignt, H. Tompkins, A. Hooper, A. A. Talin, Thin Solid Films, **398-399** (2001) 163−169.
[20] Y. Shen, Q. Zhao, X. Y. Li, D. L. Yuan, Y, Hou, S. M. Liu, J. Hazard. Mater., **241-242** (2012) 472−477.

(Received: 8 October, 2013, Accepted: 29 November, 2013)

Luminescence of Activator-Doped Alunite Synthesized under Hydrothermal Condition

Shingo Kimura[1], Yuichiro Kuroki[1], Tomoichiro Okamoto[1,*], and Masasuke Takata[1, 2]
[1] *Nagaoka University of Technology, Nagaoka, Niigata 940-2188, Japan*
[2] *Japan Fine Ceramics Center, Atsuta-ku, Nagoya 456-8587, Japan*
**E-mail: okamoto@vos.nagaokaut.ac.jp*

A novel luminesecent material, "copper-doped hydronium alunite ($(H_3O)Al_3(SO_4)_2(OH)_6$:Cu)" exhibited a blue luminescence. One of the originality of this phosphor is that the host crystal structure consists of crystal water (hydronium ions and hydroxyl radicals). Various activator-doped hydronium alunite and potassium alunite were synthesized under hydrothermal conditions. Mn-doped hydronium and potassium alunite were non-luminescent because concentrations of Mn contained in the samples were low. Cu-doped hydronium alunite exhibited a blue luminescence peak at wavelength of 428 nm, while Cu-doped potassium alunite did not. It might be suggested that the blue luminescence requires the existence of not only Cu^+ ion but also H_3O^+ ion. Ce-doped hydronium and potassium alunite showed an ultraviolet luminescence peak at wavelength of 314 nm. XPS measurements revealed that the ionic state of the cerium ion exhibiting ultraviolet luminescence was trivalent.

1. Introduction

Potassium alunite, $KAl_3(SO_4)_2(OH)_6$, is one of the most abundant sulfate minerals. It contains potassium and aluminum with hexagonal crystal system (space group of R-3m). Fig.1 shows the crystal structure of hydronium alunite. The general formula for alunite is $AB_3(SO_4)_2(OH)_6$, where A can be K^+, Na^+, Rb^+, Tl^+, Ag^+, NH^{4+}, H_3O^+, Ca^{2+}, Pb^{2+}, Sr^{2+}, Ba^{2+}, Hg^{2+}, Ce^{3+}, and B can be Al^{3+}, Fe^{3+} or minor Cu^{2+}, Zn^{2+} [1,2]. Natural Potassium alunite is generally potassium deficient; this is commonly compensated by the hydronium ion (H_3O^+) [2,3]. Potassium alunite in which K has been completely substituted by H_3O^+ is often called hydronium alunite ($(H_3O)Al_3(SO_4)_2(OH)_6$) and it does not occur naturally.

Our research group demonstrated that copper-doped hydronium alunite ($(H_3O)Al_3(SO_4)_2(OH)_6$:Cu) as a novel phosphor was successfully synthesized under hydrothermal conditions [4,5]. The blue cathodoluminescence (CL) and photoluminescence (PL) peaks at about 420 nm was observed from the phosphor [5]. In our previous study, it was reported that the luminescence is related to the presence of Cu^+ ion and structural water (OH^+ and/or H_3O^+ ions) [5]. In this study, we focused on the effects of the crystal water in A-site (H_3O^+) on the luminescence properties. The relationship among crystal structure, chemical composition and luminescence property is discussed from the results of X-ray diffraction, X-ray fluorescence analysis, cathodoluminescence and X-ray photoelectron spectroscopy.

In this paper, H- and K-alunite denote hydronium and potassium alunite, respectively.

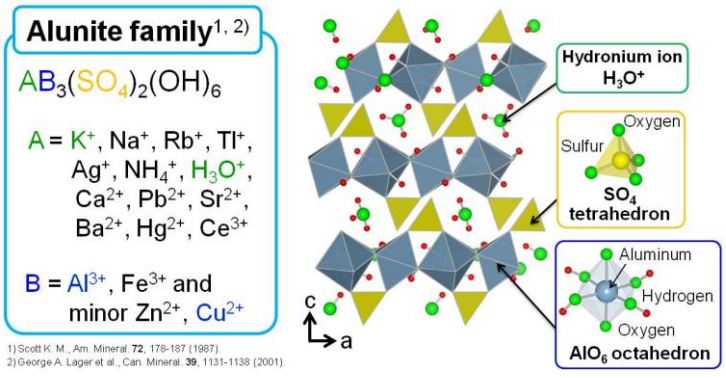

Fig. 1 Crystal structure of hydronium alunite.

2. Experiment

The powders of K_2SO_4 and $Al_2(SO_4)_3 \cdot 15H_2O$ were used as starting materials. Also, $MnSO_4 \cdot 4H_2O$, $CuSO_4 \cdot 5H_2O$ and $Ce_2(SO_4)_3 \cdot 5H_2O$ were used as activators (M). The sulfates were dissolved in distilled water. The molar ratio of K : Al : M was set to 1 : 3 : 0.5. The concentrations of potassium, aluminum and activators were 0.083, 0.250 and 0.042 mol / l, respectively. The mixture of solutions of 10 ml was sealed into a pressure vessel with a quartz inner tube which has the volume of 26 ml. The solutions were heated using an electric furnace with a rate of 1.5°C / min, maintained at 240°C (red point in Fig.2) for 60 min and then cooled to room temperature in the furnace. The obtained products were filtered and dried at 80°C for 4 h.

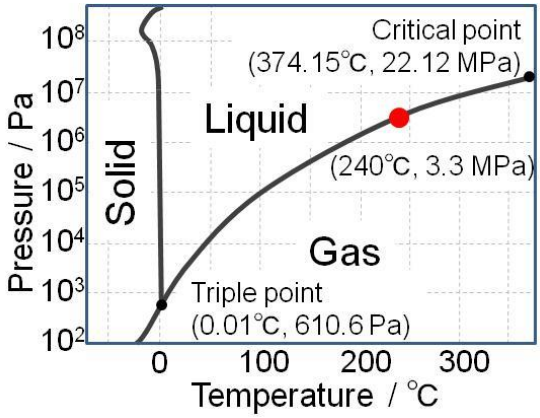

Fig. 2 The phase diagram of the water.

The powder X-ray diffraction (XRD) patterns were obtained using a Rigaku MultiFlex diffractometer (Cu Kα radiation) with a graphite monochromator. The elemental compositions in the obtained products were analyzed using a wavelength dispersive X-ray fluorescence spectrometer (XRF, Rigaku, ZSX Primus II). The cathodoluminescence (CL) was measured at room temperature using a system consisted of a grating monochromator, optical fiber and a liquid-nitrogen-cooled CCD detector (HORIBA, MP-32M-0MT). The accelerating voltage and electron beam current were 20 kV and 1.5 nA, respectively. In order to determine the valency of the activator ions, X-ray photoelectron spectroscopy (XPS) profiles were measured using JEOL JPS-9010TR with the Mg Kα line running at 10 kV and 10 mA as an excitation source. The XPS binding energy was calibrated using C (1s) at 284.6 eV.

3. Results and Discussion

Figure 3 shows XRD patterns of the products. All obtained products had the alunite type crystal structure. In addition, peaks due to other phase such as boehmite (γ-AlO(OH), ICDD; 083-1505) were not detected. It was difficult to identify each sample because the XRD pattern of K-alunite ($KAl_3(SO_4)_2(OH)_6$, ICDD 072-1630) is quite similar to that of H-alunite ($(H_3O)Al_3(SO_4)_2(OH)_6$, ICDD 016-0409). Therefore, the elemental composition analysis of the samples was carried out using XRF.

Table 1 shows elemental compositions for the products obtained by XRF. The theoretical values were calculated as follows: for H-alunite, $(H_3O)Al_3(SO_4)_2(OH)_6$, three Al atoms, two S atoms and O atoms of 15 were taken as 100 mol % (Hydrogen cannot be detected). The products obtained from the solutions containing Al and activator ions showed almost the same as theoretical compositions. Also, the products prepared from the solutions including K ion also showed almost the same as theoretical compositions of the K-alunite. The concentration of the activators in the samples were lower than initially added amount of activator ions (2.4 mol %). From the combination of the results of XRD and XRF, it was found that the single-phase activator-doped H- and K- alunite were successfully prepared under hydrothermal conditions.

In XRD patterns of Mn- and Cu-doped alunite, distinct peak shift was not observed because the concentrations of these activator ions contained in the samples were very low. Therefore, it was difficult to decide the site of activator ion. On the other hand, the peak positions for Ce-doped

alunite were higher angle than that for non-doped alunite. Keith *et al.* reported that the A site is substituted by Ce ion[1]. In this study, shift to the higher angle side of the diffraction peaks is considered to be the substitution of Ce ion (Ce^{3+} : 1.03 Å) for the A site ions (H_3O^+ : 1.24 Å, K^+ : 1.33 Å), supporting the claim of Keith *et al.*

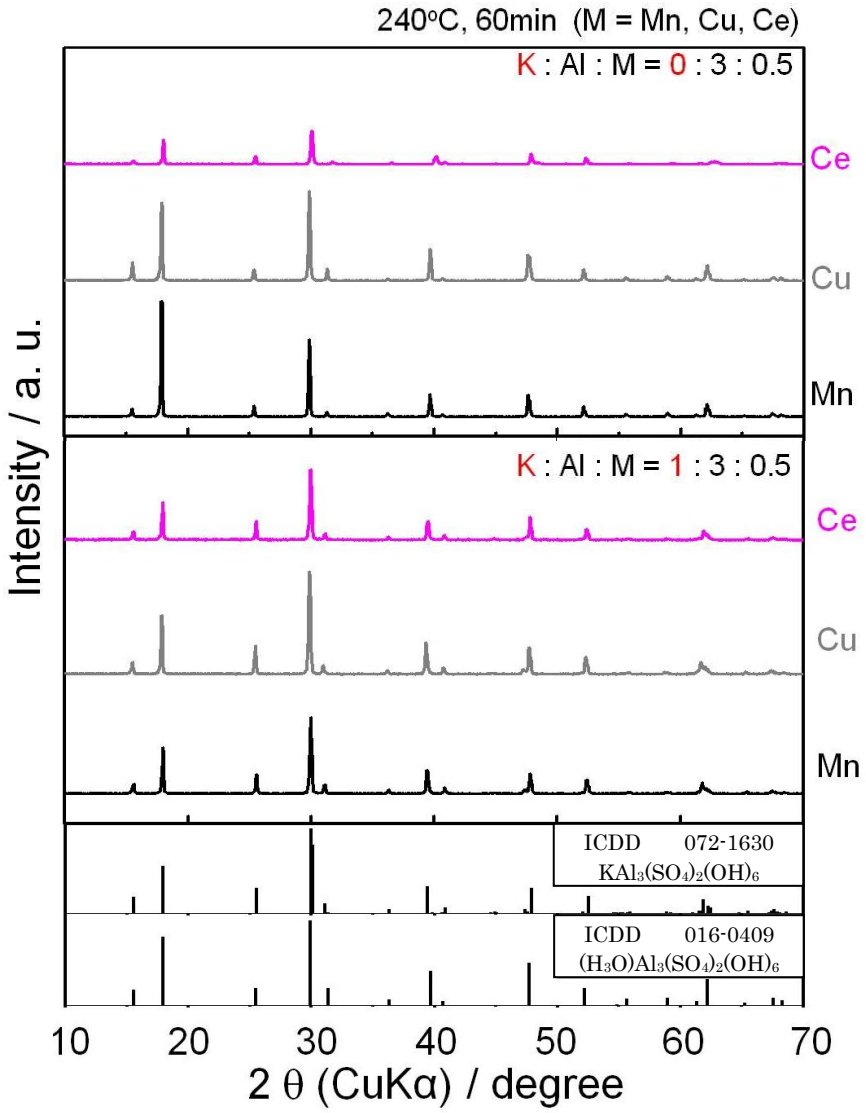

Fig. 3 XRD patterns of the obtained products.

Table 1 Molar ratio of elemental compositions for the obtained products.

	H-alunite				K-alunite				
	Al	S	O	M	K	Al	S	O	M
	mol %				mol %				
Theory	15	10	75	0	5	15	10	70	0
Mn - doped	14.98	10.62	74.40	0.01	4.25	13.61	9.48	72.66	0.01
Cu - doped	14.92	10.19	74.85	0.04	4.54	13.84	9.70	71.79	0.13
Ce - doped	14.79	10.74	73.24	1.23	3.83	13.54	10.30	71.94	0.39

Figure 4 shows CL spectra of the products. Mn-doped H- and K-alunite were non-luminescent because the concentrations of Mn contained in the samples were low (Table 1, same as detection limit ~ 0.01 mol %).

In our previous reports, Cu-doped H-alunite showed the blue luminescence peak at wavelength of 428 nm. However Cu-doped K-alunite in which copper concentration was higher than Cu-doped H-alunite was non-luminescent. This result is a very important to understand a role of H_3O^+ ion in the A-site for the luminescence property of the Cu-doped H-alunite. It was suggested that a blue luminescence requires the existence of not only copper ion but also hydronium ion. On the other hand, both of H- and K-alunite doped with cerium showed an ultra violet luminescence peak at wavelength of 314 nm. CL intensity of Ce-doped H-alunite was about 3 times higher than that of K-alunite, reflecting that concentration of cerium in H-alunite (1.23 mol %) was higher than that of K-alunite (0.39 mol %). The contribution of the presence of H_3O^+ ion is considered to be low for the luminescence due to Ce^{3+}.

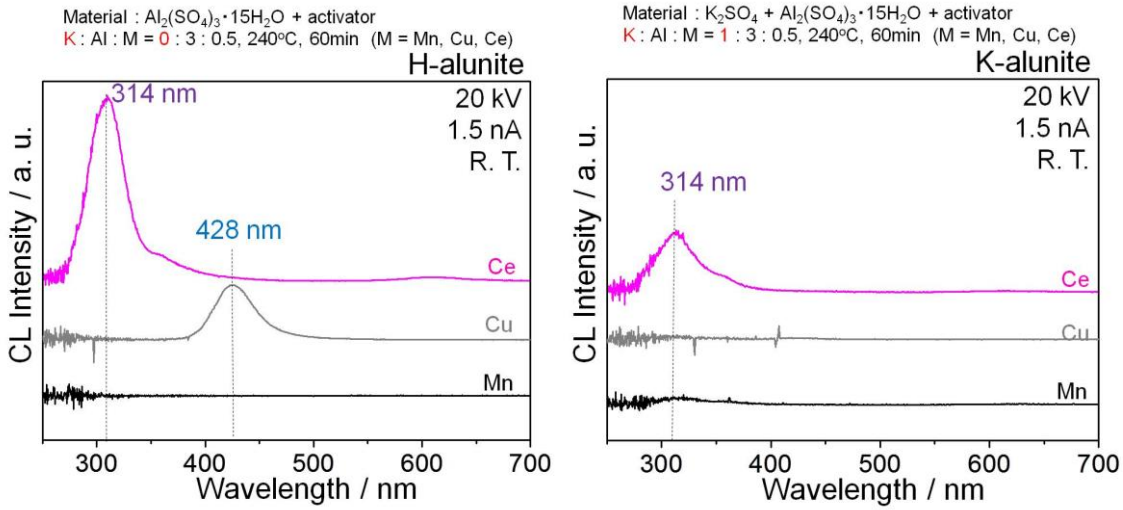

Fig. 4 Cathodoluminescence spectra of the obtained products of H-alunite and K-alunite.

In our previous report, XPS measurement revealed that the blue luminescence was caused by the Cu^+ ion [4]. For the ultra violet luminescence, it is necessary to reveal the valency of the Ce ion. Figure 5 shows XPS spectra of the Ce $3d_{5/2}$ electrons after removal of background. Peaks were fitted using Gaussian function. As a result, it was found that XPS Ce $3d_{5/2}$ profiles had the two peaks due to Ce^{3+} and Ce^{4+}. Therefore Ce-doped H- and K-alunite are thought to contain the Ce^{3+} and Ce^{4+} ions. It is well known that fluorescence of Ce^{3+} ions is originated from 5d-4f transition because the trivalent cerium ion with one 4f electron is optically active [6]. Therefore, it was revealed that the ultra violet luminescence peaked at 314 nm is caused by the 5d-4f transition of Ce^{3+} ions.

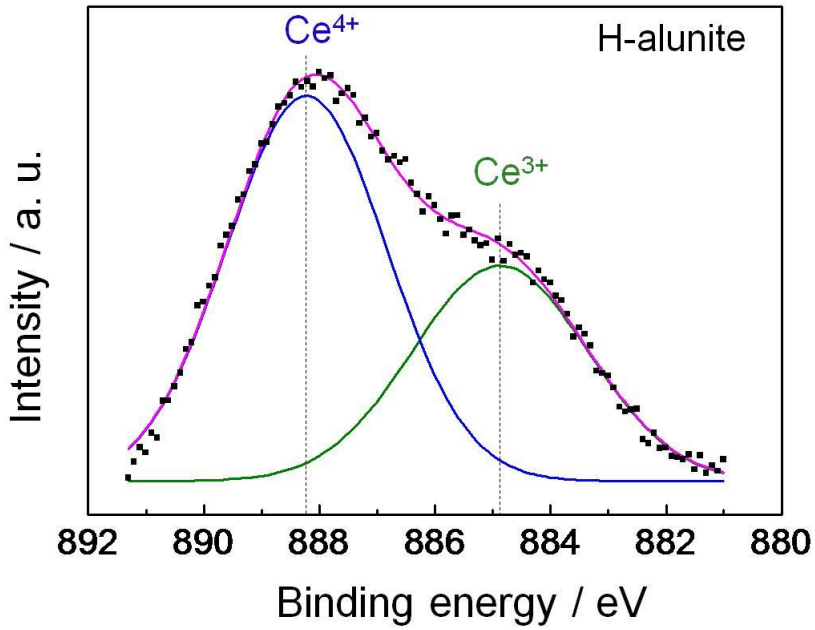

(a) $(H_3O)Al_3(SO_4)_2(OH)_6$:Ce

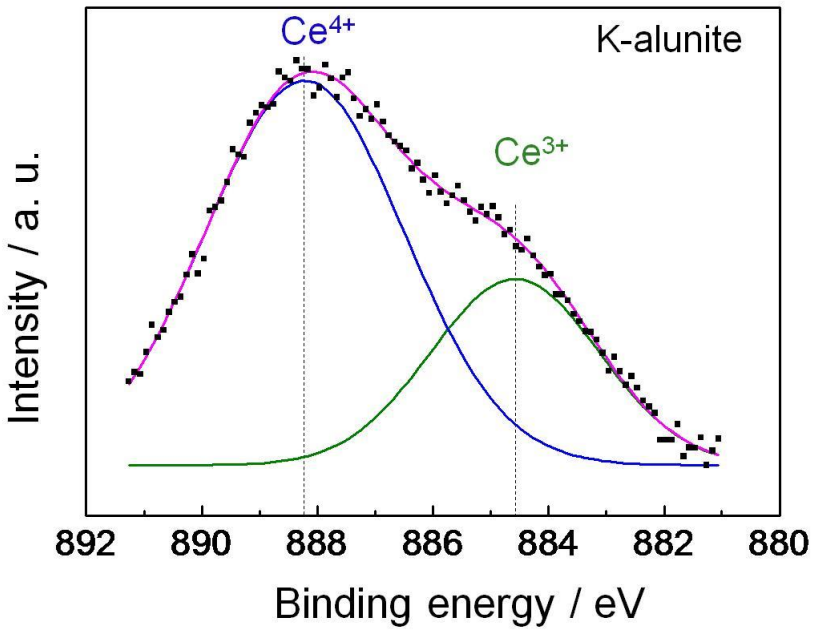

(b) $KAl_3(SO_4)_2(OH)_6$:Ce

Fig. 5 The X-ray photoelectron spectra of the Ce $3d_{5/2}$ electrons of (a) H-alunite ($(H_3O)Al_3(SO_4)_2(OH)_6$:Ce) and (b) K-alunite ($KAl_3(SO_4)_2(OH)_6$:Ce).

4. Conclusion

Synthesis of various activator-doped alunite was attempted under hydrothermal conditions. XRD and XRF measurements revealed that the single-phase activator-doped H- and K-alunite were successfully prepared under hydrothermal conditions.

(1) Mn-doped H- and K-alunite were non-luminescent because concentrations of Mn contained in the samples were low.

(2) Cu-doped H-alunite exhibited the blue luminescence peak at 428 nm, while Cu-doped K-alunite did not. The blue luminescence requires the existence of not only Cu^{+} ion but also H_3O^{+} ion.

(3) Ce-doped H- and K-alunite showed an ultra violet luminescence peak at wavelength of 314 nm. Luminescence intensity of Ce-doped H-alunite was about 3 times higher than that of K-alunite. XPS measurements revealed that the ionic state of the cerium ion exhibiting ultraviolet luminescence was trivalent.

References

[1] K. M. Scott, Am. Mineral. **72** (1987) 178

[2] G.A. Lager, G.A. Swayze, C.-K. Loong, F.J. Rotella, James W. RichardsonJr., R.E. Stoffregen,, Can. Mineral. **39** (2001)1131

[3] Parker L R, Am. Mineral. **47** (1962) 127

[4] Y. Kuroki, N. Iwata, T. Okamoto and M. Takata, Ceram. Inter., **38S** (2012) S567

[5] Y. Kuroki, N. Iwata , T. Okamoto and M. Takata, IOP Conf. Series, **21** (2011) 012004

[6] G. Q. Xu, Z. X. Zheng, W. M. Tang, Y. C. Wu, J. Lumin., **126** (2007) 475

(Received: 12 August, 2013, Accepted: 24 October, 2013)

Study on Generation and Measurement Methods for Analysis on Solid-Plasma Transition Process

Takashi Kikuchi[1,*], Toru Sasaki[1], Yasutoshi Miki[1], Fumitaka Tachinami[1], Hirotaka Saito[1], Ryota Hayashi[1], Nobuyuki Anzai[1], Takuya Takahashi[1], Tsukasa Aso[1], Kazumasa Takahashi[1], Nob. Harada[1], Weihua Jiang[1], Kenji Kashine[2], Akira Tokuchi[1,3]

[1)] *Nagaoka University of Technology, 1603-1 Kamitomioka, Nagaoka, Niigata 940-2188, Japan*

[2)] *Yuge National College of Maritime Technology, Kamijima 794-2593, Japan*

[3)] *Pulsed Power Japan Laboratory Ltd., Kusatsu 525-0027, Japan*

**E-mail: tkikuchi@vos.nagaokaut.ac.jp*

To evaluate property data of warm dense matter (WDM) and solid-plasma transition regime, we investigate the generation and measurement methods by a pulsed power discharge with isochoric heating. In this paper, both numerical and experimental approaches were proposed, and were applied to the evaluation for WDM. To evaluate the optical properties, a fast spectroscope, which consists of a 16-channel photodiode array, a 4-channel voltage adder, and a flat diffraction grating, was developed for spectroscopic ellipsometry. The numerical model based on a time-dependent one-dimensional thermal diffusion equation including a radiation transfer equation was considered, and the calculation result was compared to the experimental one. Also, the calculation results by a multi-group analysis of the radiation predict the radiation energy density profile for the experimental approaches.

1 Introduction

Warm dense matter (WDM) is in a transition regime from a solid to plasma, and the property data are important to control implosion dynamics in a fuel pellet of inertial confinement fusion (ICF) [1], to clear interior of giant planets (e.g. Jupiter) [2], and so on. To irradiate an energy driver such as intense lasers, high power X-ray, and high-current heavy ion beams, the material phase of the fuel pellet changes from solid to plasma conditions.

Since the WDM regime is in an extreme high pressure situation, it is difficult to create stationary condition with a measurable setup. Consequently, the properties in the WDM regime are unclear such as the equation of state, the transport properties of both electrons and ions, and the optical properties. To understand the physical properties, the quantum molecular dynamics or ab-initio simulations have predicted the optical properties and the equation of state in WDM regime [3–5]. Desjarlais [4] has predicted the low density WDM in disagreement with the Drude model. Yoneda [6] and Widmann [7] have experimentally demonstrated the ultrashort-pulse ellipsometric pump-probe experiments and the pump-probe transmission experiments, respectively. However, these experimental results have obtained by the single wavelength of a probe light. Thus, the experimental data were insufficient to evaluate the numerical results.

Pulsed power discharge devices were used to generate the extreme state of matter from a solid to plasma [8–10]. For the generation of WDM with a well-defined condition, the apparatus with isochoric heating using a sapphire hollow capillary as a rigid body wall was proposed by using a table-top pulsed-power device [11]. In the experimental apparatus, the emission from the heated sample was observable due to the transparent sapphire capillary. Because of usable transparent tamper as a sapphire, the method easily observed optical properties for WDM with well-defined density-temperature condition. The lifetime of generated WDM in this method is longer than that for laser experiments. For the prolonged timescale, a spectroscopic ellipsometry is possible to apply the method.

The spectroscopic ellipsometry is generally used as the condense matter physics [12]. To observe the optical property, the ellipsometer requires four sensitive spectrometers, in which observe the reflectivity and the phase for each polarization. In case of WDM generated by the pulsed-power discharges, the typical

timescale of emission from WDM is several tens of microseconds [11]. The spectrometer with fast response is required to analyze the optical properties observed by the spectroscopic ellipsometry. In this study, to evaluate the optical properties in WDM, we propose a semi-empirical multi-group analysis approach. The WDM spectrum is assumed by black or gray body radiations. Thus, the optical properties in WDM are broadly observed by the spectroscopic ellipsometry from experimental observation.

In our previous studies [13–16], we numerically investigate to generate the WDM by using pulsed power discharge devices to obtain the properties of the WDM. In comparisons with the experimental observation and the numerical estimation, the reliability of the optical properties for WDM is possible to evaluate. To demonstrate the spectroscopic ellipsometry for the experimental observation, the fast multi-group spectroscope as several MHz is required to use the conventional system. Therefore, we develop the fast-conventional spectroscope by using planner focused grating and fast photodiode array. In this study, the numerical model based on the thermodynamics and the radiation transport is developed to obtain the thermal and optical properties of the WDM.

To understand the radiation transport in WDM and the dense plasma, it is important to know the optical properties of the medium, such as opacity, absorption coefficient, dielectric constant, and refractive index. The imaginary part of the refractive index $k(\lambda)$, which depends on the wavelength λ, is obtained by $k = \lambda_0/4\pi\tau$, where λ_0 is the wavelength in vacuum and τ is the optical depth, respectively. The optical depth is defined by $\tau = 1/\kappa_\nu$, where κ_ν is the frequency ν dependent absorption coefficient. Consequently, the absorption coefficient κ_ν can be given by the refractive index measured in a medium. In this study, we propose and investigate the semi-empirical approach for the optical properties of WDM in comparison with the experimental and numerical results.

2 Semi-empirical Approach for Radiation Transport in WDM using Spectroscopic Ellipsometry

We propose the semi-empirical multi-group analysis approach for the radiation transport in WDM. To evaluate the optical properties in WDM, we develop the spectroscopic ellipsometry system with the isochoric heating of foamed material using pulsed-power discharges as shown in Fig. **1**. In this setup, the typical parameters of generated WDM were reported by Ref. [11]. Because the generated WDM is optically thick from self-emission spectrum, the observing optical properties for WDM are suitable for the reflection method. Thus, we select the reflection method as the spectroscopic ellipsometry in this study.

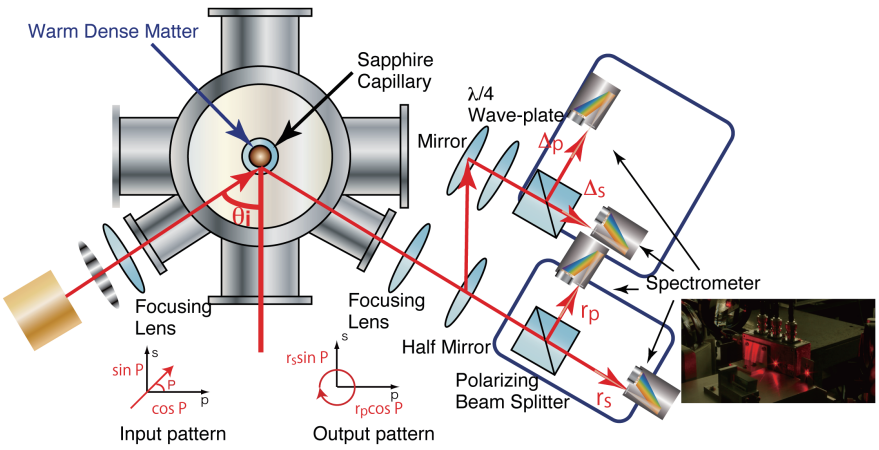

Fig. 1 Spectroscopic ellipsometry system with isochoric heating of foamed material using pulsed-power discharge.

The principle of spectroscopic ellipsometry [12] is required to measure the polarization state such as

the polarization angle $\Psi = \tan^{-1}(r_p/r_s)$ and the phase difference $\Delta = \Delta_p - \Delta_s$. The relations of complex refractive index are

$$n^2 - k^2 = \sin^2\theta_i \left[1 + \frac{\tan^2\theta_i \left(\cos^2 2\Psi - \sin^2 2\Psi \sin^2\Delta\right)}{(1 + \sin 2\Psi \cos\Delta)}\right], \tag{1}$$

$$2nk = \frac{\sin^2\theta_i \tan^2\theta_i \sin 4\Psi \sin\Delta}{(1 + \sin 2\Psi \cos\Delta)}, \tag{2}$$

where, n and k are the real and imaginary parts of the complex refractive index, and θ_i is the incident angle. To obtain Stokes parameters of the polarization angle Ψ and the phase difference Δ, four spectroscopes are required to measure the spectroscopic ellipsometry.

Figure **1** shows the constructing spectroscopic ellipsometry for observing WDM generated by the pulsed-power discharge device. The structure of generated WDM is cylindrical symmetry. The spectroscopic ellipsometry consists of a probe light with linearly polarized light, amplitude and phase detectors from reflected polarization light. The incident angle θ_i is set to be 30 deg. The probe light is a polarized high intensity discharge lamp. The reflected probe light is focused to the conventional lens of ϕ80 mm. The generated WDM has black or gray body emission. To neglect the self-emission from the WDM, we also observe the spectrum of WDM at the different angle.

3 Fast Multi-group Analyzing Spectroscope of Ellipsometry to Observe Optical Properties for WDM

In the previous section, the spectroscopes for spectroscopic ellipsometry observing the optical properties of WDM were required to be a few MHz of frequency response. To measure the detailed spectrum, the conventional spectroscopes are too slow due to the slower reading of charge-coupled-device (CCD) signals. On the other hand, the fast spectroscopes such as one mounted on the steak camera or the fast flaming intensified CCD are expensive.

In the WDM observation, the emission spectrum of WDM is almost broad such as black or gray body, and becomes the strong emission intensity. To observe the WDM emission, the spectroscopes are required to be simple, controllable observation region, and constructible design. Consequently, we develop a spectrometer based on a data logger and a plane focusing grating.

Figure **2** shows the schematic diagram of spectroscope for ellipsometry [24]. The spectroscope consists of 50 μm of slit, the plane-focusing grating (SHIMADZU: E0600-01TR), 16-channel photodiode array (HAMAMATSU: S4111-16R) with a merging circuit as a 4-channel voltage adder, and a data logger (YOKOGAWA: SL1000). Because the data logger can observe 16 channels and the all spectroscopes are paralleled operation, the detection signals should be merged by the voltage adder. The frequency response and detection yield of the photodiode detector are determined by the possibility of the spectroscopic ellipsometry.

We evaluate the frequency response of the 4-channel voltage adder. The 4-channel voltage adder consists of three Op-Amps (ANALOG DEVICES: AD8130), which are operable up to $\pm$12 Vp-p. It also reveals that the output voltage evolution after merged signals includes high frequency noise. However, the high frequency noise can be neglected from the viewpoint of the emission duration of the generated WDM. The gain of 4-channel voltage adder is in the plateau up to 1 MHz. In the high frequency regime, the gain of 4-channel voltage adder increases. From these results, the 4-channel voltage adder is required to be set as the low pass filter up to 10 MHz.

4 Numerical Modeling for WDM generated by Isochoric Heating with Pulsed Power Discharge

In this study, we solve simultaneously the time-dependent one-dimensional thermal diffusion equation

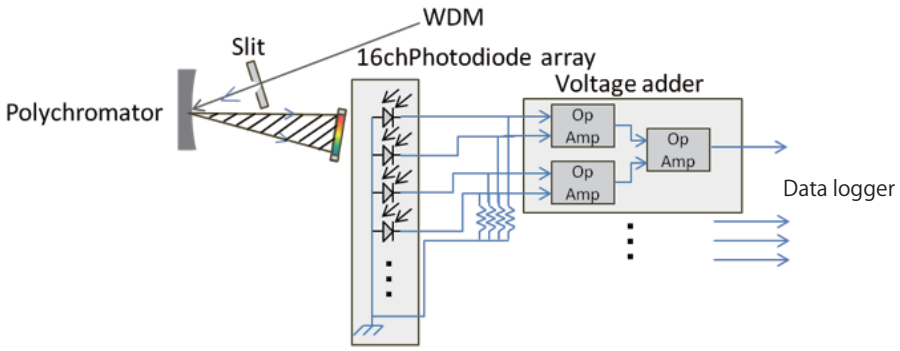

Fig. 2 Schematic diagram of spectroscope for ellipsometry.

with cylindrical symmetry configuration for the WDM generation in the compact pulsed power discharge experiment [11].

In the experimental setup [11], we can assume to calculate the phenomena in the foam/plasma ignoring the hydrodynamics, because the fluid dynamics of the sample plasma is limited by the capillary. For this reason, we only calculate the thermodynamics in the foam/plasma without the fluid dynamics of plasma. In the apparatus, a foamed copper is used as a sample, and is surrounded with a hollow sapphire capillary. The computational box is adjusted in the experimental setup [11], and is shown in Fig. **3**. The inner region

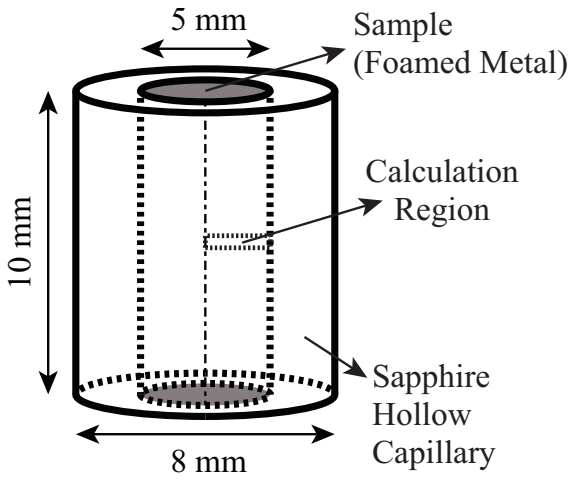

Fig. 3 Computational box for time-dependent one-dimensional thermal diffusion and radiative transfer equations with cylindrical symmetry configuration [13–16].

($0 < r < 2.5$ mm) is the foamed copper as a sample, and the outer region (2.5 mm $< r <$ 4 mm) is the sapphire as a rigid capillary. The capillary length L_{cap} is 10 mm.

The density of the foamed copper surrounded in the hollow capillary is 0.1 times the solid density (8920 kg/m^3). The mass density of the sapphire is 3970 kg/m^3 as the solid. Since the sample is a foamed material, we assumed that the skin effect can be ignored. As a result, the discharge current distribution is assumed as uniform in the copper region.

The initial temperature is set as 300 K by a room temperature in the whole computational region. The conventional thermal property data of copper in solid, liquid, and gas phases are given by Refs. [17–20]. In the sapphire region, the material parameters for numerical simulation are 42 W/m·K for the thermal conductivity and 750 J/kg·K for the specific heat, as room temperature values.

4.1 Thermal Diffusion

The temperature T of the sample is the function of spacial position and time t, and the thermodynamics is given by

$$\rho\, C_{\rm v} \frac{\partial T}{\partial t} = \nabla \cdot (\kappa \nabla T) + S_{\rm J} - S_{\rm r}, \tag{3}$$

where ρ is the mass density of the sample, $C_{\rm v}$ is the specific heat, κ is the thermal conductivity, $S_{\rm J}$ is the source term due to Joule heating, and $S_{\rm r}$ is the source term due to the absorption and emission of radiation, respectively. The source term due to Joule heating is obtained by

$$S_{\rm J} = \frac{P_{\rm in}}{V_{\rm foam}}, \tag{4}$$

where $P_{\rm in}$ is the input power from the pulse power supply and $V_{\rm foam}$ is the volume of the sample.

The above equation is rewritten by

$$\rho\, C_{\rm v} \frac{\partial T}{\partial t} = \frac{1}{r} \frac{\partial}{\partial r} \left(r \kappa \frac{\partial T}{\partial r} \right) + S_{\rm J} - S_{\rm r}, \tag{5}$$

along the radius r in the cylindrical coordinate.

4.2 Thermodynamic Property

The initial temperature is set as 300 K by a room temperature in the whole computational region. The conventional thermal property data of copper in solid, liquid, and gas phases are given by Refs. [17–20].

4.3 Radiative Transfer

The radiative transfer equation is solved by the diffusion approximation [21]. Although, the WDM regime is expected to be quite thick optically, the radiation generated in the interior of the WDM region is not able to pass through the WDM region. For this reason, the diffusion equation for the radiation energy density E^g is modified by

$$\frac{\partial E^g}{\partial t} = (4\pi\, B^g - c\, E^g)\, \kappa_{\rm P}^g, \tag{6}$$

along the radius r in the cylindrical coordinate with a multi-group approximation in the frequency domain group g [22]. Here, E^g is the radiation energy density at g th group,

$$E^g = \frac{\int_{\nu_g}^{\nu_{g+1}} E_\nu \, d\nu}{\int_{\nu_g}^{\nu_{g+1}} d\nu}, \tag{7}$$

and

$$\kappa_{\rm P}{}^g = \frac{\int_{\nu_g}^{\nu_{g+1}} \kappa_\nu \, B_\nu \, d\nu}{\int_{\nu_g}^{\nu_{g+1}} B_\nu \, d\nu}, \tag{8}$$

is the Planck absorption coefficient at g th group [23], and the blackbody intensity is

$$B^g = \frac{\int_{\nu_g}^{\nu_{g+1}} B_\nu \, d\nu}{\int_{\nu_g}^{\nu_{g+1}} d\nu}. \tag{9}$$

4.4 Opacity

According to the measuring instrument in the experimental setup [24], the frequency domain is divided and grouped as Table 1.

The κ_ν (1/cm) is the frequency ν dependent absorption coefficient [25],

$$\kappa_\nu = 7.13 \times 10^{-16} \frac{n_{\rm i} (Z^* + 1)^2 \exp\{-(\xi - \chi)\}}{T^2 \chi^3}, \tag{10}$$

Table 1 Relation between group number and frequency domain for multi-group approximation of radiation energy density. Here, the wavelength λ of radiation is defined as the speed of light c divided by the frequency ν.

Group g	Wavelength λ
1	$>$ 800 nm
2	800 $\sim$ 680 nm
3	680 $\sim$ 520 nm
4	520 $\sim$ 370 nm
5	370 $\sim$ 340 nm
6	$<$ 340 nm

where $n_{\rm i}$ is the ionic density (1/cm^3), Z^* is the mean ionization degree (0.5 is assumed from the previous experimental result [11]), $\chi = h\nu/T$, and $\xi = I_0/T$. h is the Planck constant, I_0 is the mean ionization potential (7.73 eV for Cu), and T is the temperature with unit eV in this equation.

The radiative transfer with the flux limited diffusion approximation [26] is calculated by

$$\frac{\partial E^g}{\partial t} = -\frac{c}{r}\frac{\partial E^g}{\partial r}, \tag{11}$$

in the sapphire region.

4.5 Input Power

Figure **4** shows the input power history, which is given by the corresponding experimental data [11, 24].

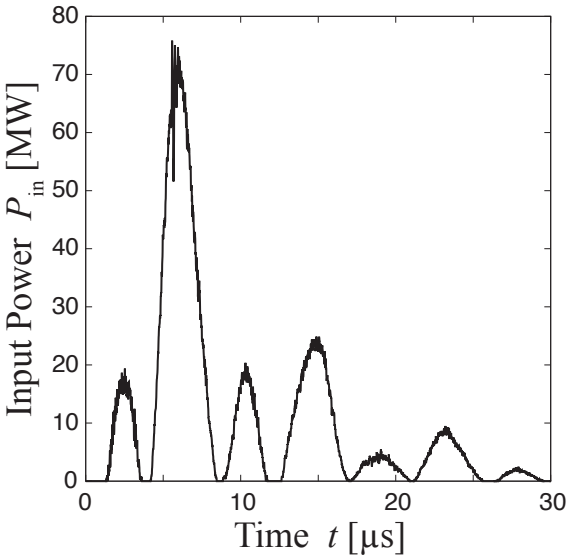

Fig. 4 Input power history by pulsed power discharge experiment.

5 Experimental and Numerical Results

The numerical simulation confirmed that the sample was achieved to be the temperature generating WDM [13, 14], and the result could be compared with the experimental result [11].

Figure **5** shows the typical time evolution of WDM emission intensity I_ν acquired by the streak camera for ablating foam experiment from 8.5 to 13.5 μs [11] and the histories of radiation energy density obtained

by the numerical simulations [15, 24]. The radiation energy densities as shown in Fig. **5** were evaluated

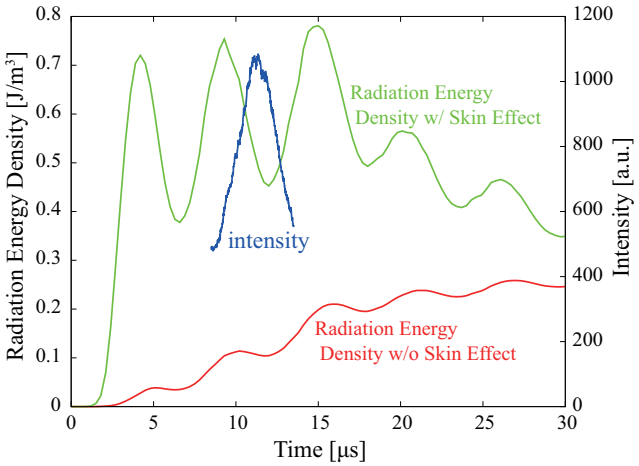

Fig. 5 Histories of radiation energy density by numerical simulation and emission intensity by experiment [15].

at the outer boundary of the sapphire capillary. The emission intensity given by the experiment implies the oscillated distribution in time. Consequently, the radiation energy density obtained by the numerical simulation qualitatively corresponded to the experimental result.

The results indicated that the emission duration from WDM generated by in this system is estimated to be about 4 μs. Thus, the required frequency response of detector as the spectroscopes is estimated to be order of a few MHz.

Figure **6** shows the radiation energy density distributions as a function of time at each frequency group given by the numerical simulation of time-dependent phenomena in the copper foam and the sapphire capillary regions. The radiation energy density distribution at each frequency group corresponds to the temperature distribution [14].

Figure **7** shows the numerically obtained radiation energy density observed at edge of capillary (r = 4 mm) as a function of time at each frequency group. The previous experiment indicated that the sample temperature achieved to be around 5000 K [11]. From Wien displacement law [27], the wavelength of the maximum black-body emission, which is given by $\lambda_W = 2.5 \times 10^{-7}/T$ (where the unit of T is eV), is estimated at 580 nm for 5000 K. In this calculation, the wavelength of 580 nm is included in the domain at $g = 3$, and the calculation result in Fig. **7** is confirmed with the experimental result.

The radiation energy density is described by

$$E_\nu = \frac{1}{c}\int_{4\pi} I_\nu \, d\Omega, \tag{12}$$

to integrate the emission intensity I_ν by the solid angle Ω. In the case of uniform distribution of WDM, $E_\nu = 4\pi I_\nu/c$ is assumed by the isotropic emission from the WDM. As a result, the radiation energy density can be compared to the emission intensity measured by using the fast multi-group analyzing spectroscope proposed in the previous section. When the emission intensity measurement with the multi-channel spectroscopy system is completed, the radiative transfer calculation can be confirmed with the experimental results, and the calculation result will support the experimental results through the radiation distribution.

6 Conclusion

In this study, it was considered that both the numerical and experimental approaches were applied to

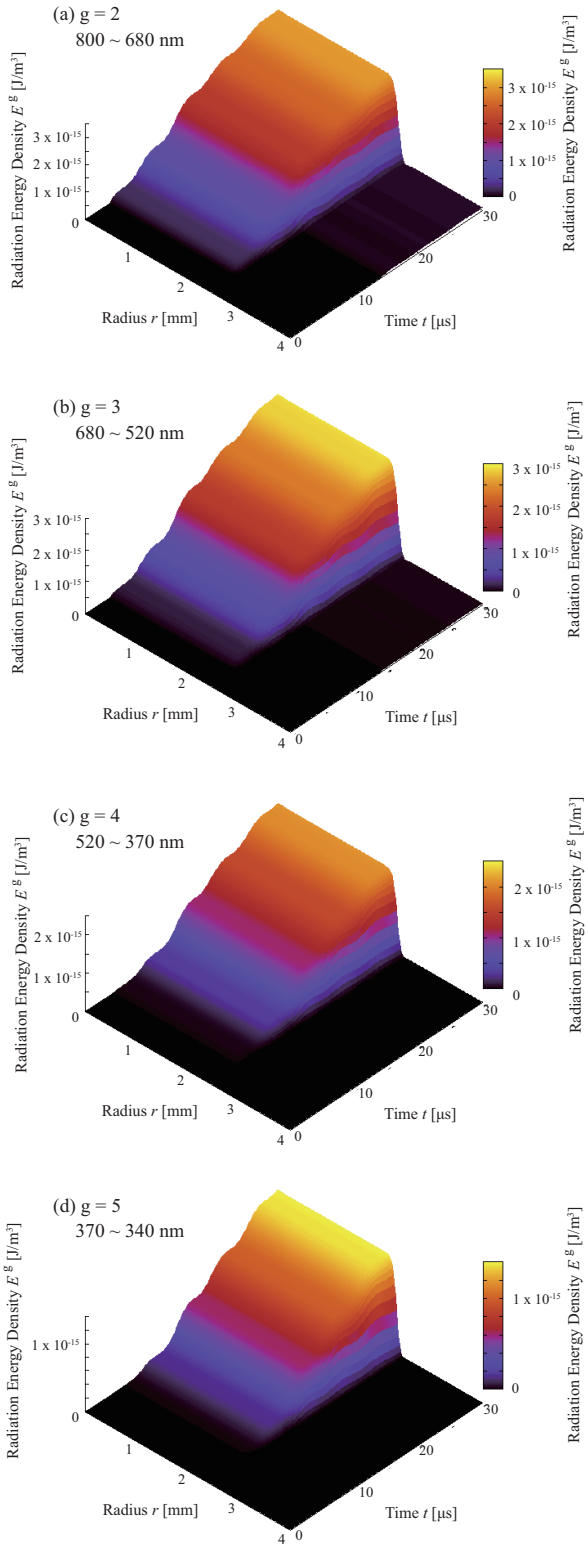

Fig. 6 Radiation energy density distributions as a function of time at each frequency domain grouped, (a) for $g = 2$, (b) for $g = 3$, (c) for $g = 4$, and (d) for $g = 5$, respectively.

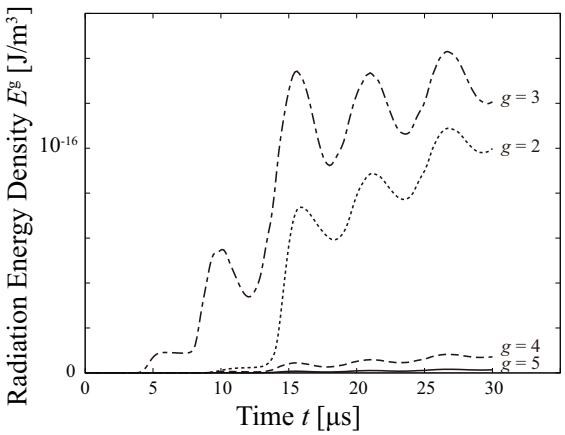

Fig. 7 Radiation energy density numerically observed at edge of capillary ($r = 4$ mm) as a function of time at each frequency grouped. The dotted line indicates the radiation energy density for $g = 2$, the dashed-dotted curve indicates the radiation energy density for $g = 3$, the dashed line shows the radiation energy density for $g = 4$, and the solid curve shows the radiation energy density for $g = 5$, respectively.

the generation and evaluation for WDM. To evaluate the properties in WDM and solid-plasma transition process, we proposed the multi-group analysis approach from both the experimental observation and the numerical simulation. The optical properties of WDM are observed by the fast spectroscopic ellipsometry. To evaluate the multi-group optical properties, we developed the simple and fast spectroscope, in which consists of the 16-channel photodiode array, the 4-channel voltage adder, and the flat diffraction grating. The results indicated that the frequency response of the 4-channel voltage adder is to confirm detection efficiency of spectroscope from radiation energy density, and it was considered that the constructed detector is enough for spectroscopic ellipsometry.

To clear the thermal and optical properties of WDM, the numerical simulation of time-dependent one-dimensional thermal diffusion with radiative transfer was carried out in the compact pulsed-power discharge device. The numerical model was described to include the multi-group approximation for the radiation energy density. The radiation energy density can be compared to the emission intensity measured by using the fast multi-group analyzing spectroscope. Using the numerical model, the radiation energy density depended on the frequency was shown with the experimental condition.

For the evaluation of the optical and thermal properties in the WDM regime, the numerical model developed will be applied in the various experimental conditions, and the calculation results will be confirmed with the experimental results in our near future work.

Also, to investigate the properties of WDM in the timescale of ICF implosion process, we plan the experiment by using the intense pulsed power generator "ETIGO-II", which has large amount of output power in short time. And in the plan, the numerical simulation developed in this study will be effective tool to support the solution of the phenomena obtained by the experiment.

Acknowledgment

This work was supported from MEXT Grant-in-Aid for Scientific Research, and by Program for High Reliable Materials Design and Manufacturing in Nagaoka University of Technology, and by JSPS Grant-in-Aid for Challenging Exploratory Research No.25630418. This work was partly supported by a Grant-in-Aid for Young Scientists (B) from the Japan Society for the Promotion of Science (23740406).

References

[1] S. Atzeni and J. Meyer-Ter-Vehn, *The Physics of Inertial Fusion: Beam Plasma Interaction, Hydrodynamics, Hot Dense Matter* (Oxford Univ., N.Y., 2004).

[2] J.J. Fortney, N. Nettelmann, Space Sci. Rev., **152** (2010) 423.

[3] M.W.C. Dhama-Wardana, Phys. Rev. **E 73** (2006) 036401.

[4] M.P. Desjarlais, J.D. Kress, and L.A. Colins, Phys. Rev. **E 66** (2002) 025401.

[5] S. Mazevet, M.P. Desjarlais, L.A. Collins, J.D. Kress, N.H. Magee, Phys. Rev. **E 71** (2005) 016409.

[6] H. Yoneda, H. Morikami, K. Ueda, and R. More, Phys. Rev. Lett., **91** (2003) 075004.

[7] K. Widmann, T. Ao, M.E. Foord, D.F. Price, A.D. Ellis, P.T. Springer, and A. Ng, Phys. Rev. Lett., **92** (2004) 125002.

[8] A.W. Desilva and J.D. Katsouros, Phys. Rev. **E 57** (1998) 5945.

[9] T. Sasaki, M. Nakajima, T. Kawamura, and K. Horioka, Phys. Plasmas, **17** (2010) 084501.

[10] T. Sasaki, T. Suzuki, Y. Amano, Y. Miki, T. Kikuchi, Nob. Harada, and K. Horioka, IOP Conf. Series: Material Science and Engineering, **21** (2011) 012016.

[11] Y. Amano, Y. Miki, T. Sasaki, T. Kikuchi, and Nob. Harada, Rev. Sci. Instrum., **83** (2012) 085107.

[12] E. Collett, Surf. Sci., **96** (1980) 156.

[13] T. Kikuchi, T. Sasaki, Nob. Harada, W. Jiang, and A. Tokuchi, "Numerical Analysis for Low-Temperature and Dense Plasma Generation using Pulsed Power Discharge Devices", Plasma 2011, Kanazawa, Nov. 22-25, (2011) 23P162-R.

[14] T. Kikuchi, H. Saito, R. Hayashi, T. Sasaki, and Nob. Harada, "Numerical Analysis and Experimental Evaluation for Low-Temperature and Dense Plasma Generation using Pulsed Power Discharge Device", NIFS -PROC, **94** (2013) 80.

[15] T. Kikuchi, Y. Miki, H. Saito, R. Hayashi, T. Takahashi, T. Sasaki, T. Aso, and Nob. Harada, Proceedings of 4th Euro-Asian Pulsed Power Conference and 19th International Conference on High-Power Particle Beams (EAPPC2012 / BEAMS2012), September 30 - October 4, 2012, Karlsruhe, Germany, P2C-3, Paper_320.

[16] T. Kikuchi, H. Saito, Y. Miki, R. Hayashi, T. Takahashi, T. Sasaki, T. Aso, and Nob. Harada, "Numerical Analysis for Evaluation of Thermal and Optical Properties in Warm Dense Matter Generated by Pulsed Power Discharge", NIFS -PROC, **93** (2013) 1.

[17] C.Y. Ho, R.W. Powell, and P.E. Liley, "Thermal Conductivity of the Elements", JPCRD, **1(2)** (1972) 279.

[18] C.Y. Ho, R.W. Powell, and P.E. Liley, "Thermal Conductivity of the Elements: A Comprehensive Review", JPCRD, **3(Suppl. 1)** (1974) 1.

[19] NIST Standard Reference Database Number 69, http://webbook.nist.gov/chemistry/

[20] M.W. Chase, NIST-JANAF Thermochemical Tables, Fourth Edition, J. Phys. Chem. Ref. Data, Monograph 9 (1998).

[21] J.I. Castor, *Radiation Hydrodynamics* (Cambridge University Press, 2007).

[22] S. Atzeni and J. Meyer-Ter-Vehn, *The Physics of Inertial Fusion: Beam Plasma Interaction, Hydrodynamics, Hot Dense Matter* (Oxford Univ., N.Y., 2004) Chap. 7.3.

[23] L. Drska and M. Sinor, Computer Phys. Communications, **997** (1996) 1.

[24] H. Saito, Y. Miki, T. Takahashi, T. Sasaki, T. Kikuchi, T. Aso, and Nob. Harada, "Study on Optical Properties for Warm Dense Matter Generated by Pulsed-Power Discharge Device", 11th APCPST (Asia Pacific Conference on Plasma Science and Technology) and 25th SPSM (Symposium on Plasma Science for Materials), Kyoto, October 2-5, 1-P67, 2012.

[25] A. Mancic, J. Robiche, P. Antici, P. Audebert, C. Blancard, P. Combis, F. Dorchies, G. Faussurier, S. Fourmaux, M. Harmand, R. Kodama, L. Lancia, S. Mazevet, M. Nakatsutsumi, O. Peyrusse, V. Recoules, P. Renaudin, R. Shepherd, and J. Fuchs, High Energy Density Phys., **6** (2010) 21.

[26] C.D. Levermore and G.C. Pomraning, Astrophysical Journal, **248** (1981) 321.

[27] J.D. Huba, *NRL Plasma Formulary* (Naval Research Laboratory, 2011).

(Received: 2 September, 2013, Accepted:20 December 2013)

Vibration Isolation Stand for Transporting the Injured using Pleasure Boat

Yoshiaki MITSUMA[1], Shigehiro TOYAMA[1*], Fujio IKEDA[1], Hiroaki SETA[2]
[1)]Nagaoka National College of Technology, Nagaoka, Niigata, Japan 940-8532
[2)]Toba National College of Maritime Technology, Toba, Mie, Japan 517-8501
**E-mail: toyama@nagaoka-ct.ac.jp*

In various places of Japan, huge earthquakes are expected to occur. Transportation of the injured from the isolated islands of Japan is an exigent requirement. Using pleasure boats is considered as one of the transportation method. Because shallow draft of pleasure boats enables to easily reach and leave damaged coasts of the islands. Few pleasure boats have automatic control system with fins and hydrofoils to stabilize the vibration of their hulls in the same way as large ships. The vibration of pleasure boats, which could aggravate wounds of the injured, should be suppressed by vibration isolation stands. This paper investigates two methods to reduce the natural frequency of vibration isolation stands, so that the proposed stand is ready for low-frequency vibration by waves. One of the methods is using the tri-linear spring mechanism to realize a low stiffness in equilibrium. The other method is using rotational inertia mechanism with a clutch to increase the apparent sprung mass.

1. Introduction

In the various places of Japan, huge earthquakes, such as the 2011 off the pacific coast of Tohoku earthquake, are expected to occur. The government of Japan is planning emergency responses and instituting policies to meet such anticipated disasters [1]. As an emergency response, the transportation of the injured from the isolated islands of Japan is an exigent requirement. The use of pleasure boats such as the training boat “Asama”, which belongs to Toba National College of Maritime Technology and is shown in Fig. 1, is considered as a valid transportation method, since the shallow draft of pleasure boats enables to easily reach and leave the damaged coasts of the islands. Although large ships have automatic control systems with fins and hydrofoils to stabilize the vibration of their hulls, few pleasure boats have such a stabilization system. If the injured were carried on pleasure boats without taking any stabilization measures, the vibration of the boats could aggravate their wounds. Therefore, vibration isolation stands should be investigated for pleasure boats. The vibration isolation stands of high standard ambulances have been studied [2], [3] and have been put to practical use. These stands, however, are inappropriate for use in pleasure boats, due to the low-frequency and high-amplitude vibration by waves. Apparently, no research has been carried out on vibration isolation stands for pleasure boats.

This paper proposes two mechanisms to reduce the natural frequency of vibration isolation stands, so that the proposed stand is ready for the low-frequency vibration. One of these mechanisms is a tri-linear spring mechanism, which exhibits low stiffness in equilibrium. The other is a rotational inertia mechanism to increase the apparent sprung mass. A clutch mechanism of the rotational mechanism and its control law are proposed by a consideration of excitation condition for the rotational inertia mechanism.

Fig. 1 Training boat "Asama"

2. Vibration isolation characteristics of typical passive type stand

2.1 Standard of vibration isolation

While pleasure boats are moving straight, their main hull vibration is pitching motion. The pitching motion is assumed to be a vertical vibration whose largest amplitude is 0.105[m], and the maximum frequency of the spectrum is 5.2[rad/s], according to a number of our experiments and multiple references [4-6]. Based upon the level of ride quality and the reported experience of seasickness [7], [8], it can be seen that the condition of the subjects took a turn for the worse when their vertical acceleration exceeded 0.3[m/s^2].

Based on these results, a standard of vibration isolation is defined so that the vertical acceleration of the injured, who are transported on the proposed stand, must not exceed 0.3[m/s^2] for the vertical vibration. Therefore, the gain characteristics of the transfer function $G(s)$, from the acceleration of the installation floor of the proposed stand to the acceleration of the injured, need to satisfy the following inequality.

$$\left|G(j\omega)\right| \le \frac{0.3}{0.105\omega^2} \quad (\omega \le 5.2\,[\text{rad/s}]) \tag{1}$$

Figure 2 graphs Eq. (1). In this figure, slant line area shows an undesirable zone to be unsatisfied with Eq. (1). If the gain characteristics of the transfer function for the propose stand reaches the slant line area, the hull vibration can negatively effects the injured.

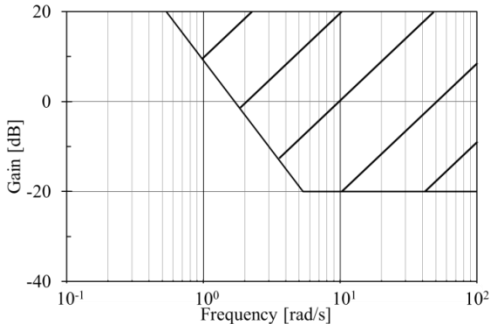

Fig. 2 Standard of vibration isolation from acceleration of installation floor to acceleration of the injured

2.2 Typical model of passive type vibration isolation stand

Several kinds of the vibration isolation stand have been examined for the standard. One of those is a typical passive model for vibration isolation stands, as shown in Fig. 3. In this model, *m* is the sprung mass including the injured, *k* is the spring constant, and *c* is the viscous damping coefficient. Then, transfer function $G(s)$, from the acceleration a_f of the installation floor of the proposed stand to the acceleration a_s of the injured, is described as follows.

$$G(s) = \frac{cs + k}{ms^2 + cs + k} \tag{2}$$

The natural frequency ω_n of the passive type stand is given as follows.

$$\omega_n = \sqrt{\frac{k}{m}} \tag{3}$$

Figure 4 shows the tendency of change for the gain diagram of the transfer function Eq. (2) when the viscous damping coefficient c varies. From this figure, it can be seen that the gain around the natural frequency is decreased by the increase in the viscous damping coefficient c, though the gain in the high frequency range is increased. It is difficult for the passive type stand to satisfy the standard with adjustment of the viscous damping coefficient c. Therefore, some mechanisms of reducing the natural frequency itself are required.

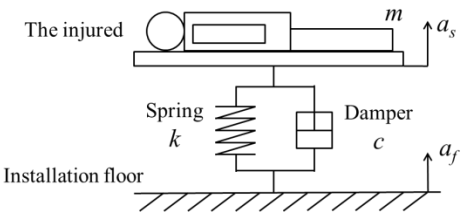

Fig. 3 Passive type vibration isolation stand

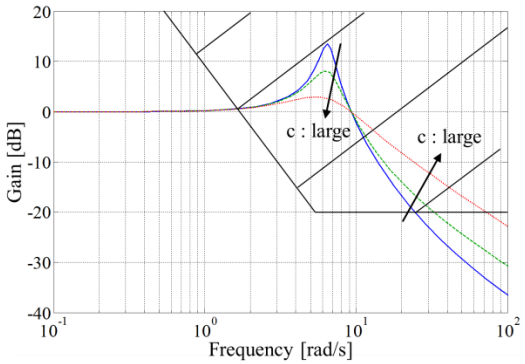

Fig. 4 Gain diagram of Eq. (2) when viscous damping coefficient c varies

3. Tri-linear spring mechanism

3.1 Tri-linear spring characteristics

As a method to reduce the natural frequency of the propose stand, the bi-linear spring characteristics, which decrease stiffness in equilibrium as shown in Fig. 5, have been studied [9]. The characteristics can secure both support stiffness of the injured and low stiffness in equilibrium. Excessive acceleration, however, can be caused by bumping against the stopper at the time of over stroke, because the low stiffness can produce more compression deflection than necessary. To solve this problem, this paper proposes the use of the tri-linear spring characteristics, as shown in Fig. 6. The high degree of stiffness, which is given to the both sides of the low stiffness area near the equilibrium position, can absorb the kinetic energy of the injured on the proposed stand before hitting the stopper. Figure 7 shows a spring mechanism with such spring characteristics [10]. The outer case places restrictions on the motion of the slide board in the range h_b. The pre-compression force P_{01} is given by the helical compression spring I, whose spring constant is k_1. Until the load P exceeds P_{01}, only the helical compression spring II, whose spring constant is k_2, is compressed. When the load P exceeds P_{01}, both spring I and spring II are connected in series, and the equivalent spring constant becomes $k_1 k_2 / (k_1 + k_2)$. In the case that the spring constant k_1 is equal to the spring constant k_2, the equivalent spring constant becomes the minimum $k_1/2$. After the load P exceeds P_{02} and the slide board travels h_b, only spring II is compressed by the load P. These tri-linear spring characteristics can be described as follows.

$$P = \begin{cases} k_2 x & (0 \le x < x_{01}) \\ \dfrac{k_1 + k_2}{k_1 k_2}(x - x_{01}) + P_{01} & (x_{01} \le x < x_{02}) \\ k_2 (x - x_{02}) + P_{02} & (x_{02} \le x < x_{\lim}) \end{cases} \tag{4}$$

where $x_{\lim}$ is the maximum deflection of the spring mechanism, l_1 is the free length of spring I, the other parameters are described as follows.

$$x_{01} = \frac{P_{01}}{k_2} \tag{5}$$

$$x_{02} = \frac{k_1 + k_2}{k_1 k_2}\left(P_{02} - P_{01}\right) + x_{01} \tag{6}$$

$$P_{01} = k_1\left(l_1 - h_r\right) \tag{7}$$

$$P_{02} = k_1\left(l_1 - h_r + h_b\right) \tag{8}$$

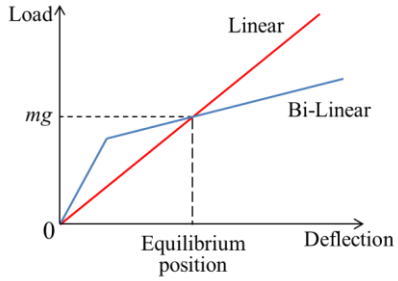

Fig. 5 Bi-linear spring characteristics

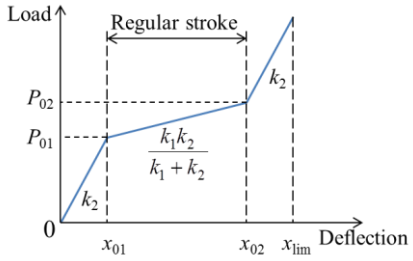

Fig. 6 Tri-linear spring characteristics

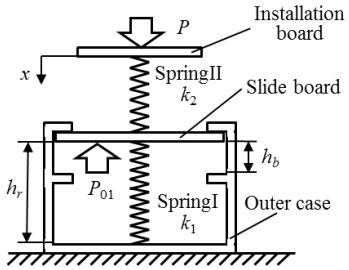

Fig. 7 Fundamental mechanism of tri-linear spring

3.2 Tri-linear spring mechanism

In order to secure the stroke of the proposed stand, the helical compression springs of the fundamental spring mechanism shown in Fig. 7 need to have a long free length. These long springs need to be guided, though, either in a tube or over a rod, to minimize buckling. However, friction against the tube or rod could prevent smooth motion of the proposed stand, and these guides could limit the carrying space. Therefore, a different mechanism that employs only helical extension springs is proposed here. Figure 8 shows the proposed tri-linear spring mechanism. The principle of its action is the same as that of the fundamental spring mechanism shown in Fig. 7. In Fig. 8, it can be seen that the iron wires and pulleys can position the extension springs horizontally. It can thus be expected that the laid springs would reduce the overall height of the proposed stand.

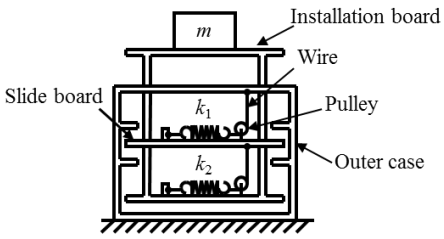

Fig. 8 Proposed tri-linear spring mechanism

Figure 9(a) shows prototype of the proposed spring mechanism. Figure 9(b) shows the composition of the prototype, and Fig. 9(c) shows the arrangement of the extension springs in the

slide board. The other extension springs arranged under the installation board are arranged like those of the slide board. By the parallel connection of four extension springs, which have a free length of 0.269 [m] and a spring constant of 1500 [N/m], the spring constants k_1 and k_2 are each set as 6000 [N/m] for the weight of the injured. That is, the equivalent spring constant near the point of equilibrium is 3000 [N/m]. The normal stroke $x_{02} - x_{01}$ near the equilibrium is designed as 0.377 [m], and the length x_{01} and $x_{\lim} - x_{02}$ for absorbing the kinetic energy at the time of over stroke are designed as 0.08 [m]. Figure 10 shows the experimental results for the spring characteristics of the prototype with the proposed tri-linear spring mechanism. From this figure, it can be seen that the low stiffness for the normal stroke and the high stiffness against over stroke can be realized in the design, and that each stroke length of the tri-linear spring characteristics can be achieved as desired.

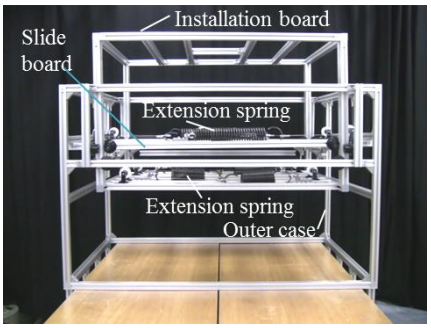

(a) Outside of experimental setup

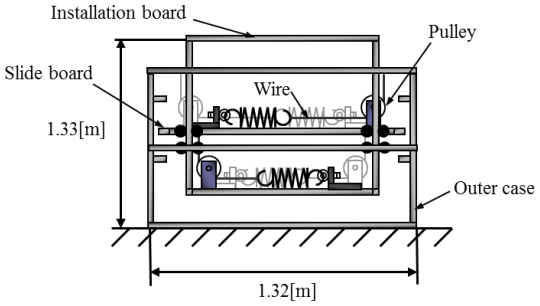

(b) Composition of experimental setup

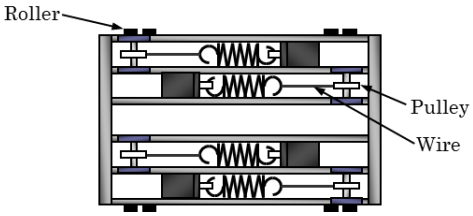

(c) Arrangement of extension springs in slide board

Fig. 9 Prototype of proposed tri-linear spring mechanism

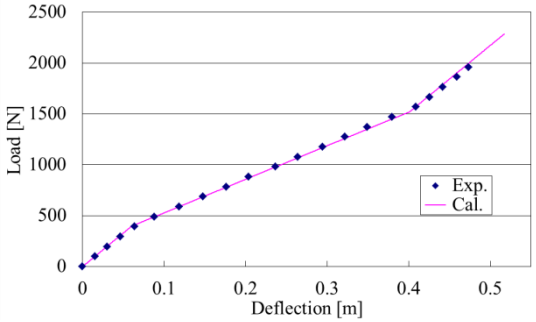

Fig. 10 Characteristics of prototype with proposed tri-linear spring mechanism

4. Rotational inertia mechanism

4.1 Fundamental rotational inertia mechanism

As a method to reduce the natural frequency, applying of the rotational inertia mechanism into the proposed stand is considered. A simple mechanism of the ball screw type dampers [11], which use function of rotational inertia as shown in Fig. 11, is investigated. The displacement z of the ball screw shaft is transformed into the rotation angle θ of the flywheel with the moment of inertia J. The resistance force F satisfies the following equation.

$$F = \frac{J\ddot{\theta}}{(L/2\pi)} = i^2 J\ddot{z} \tag{9}$$

where $i = 2\pi/L$ and L is the lead of the ball screw shaft. From Eq. (9), it can be seen that the resistance force F of the rotational inertia mechanism is proportional to the acceleration $\ddot{z}$ of the load column. That is $i^2 J$ refers to the inertial mass.

To verify the effectiveness of the rotational inertia mechanism, let us assume a model of a passive vibration isolation stand with a rotational inertia mechanism as shown in Fig. 12. In Fig. 12, m is the sprung mass including the injured, k is the spring constant of the support spring in equilibrium, y is the displacement of the injured, and d is the displacement of the floor. Then, the equation of motion for the stand model is described as follow.

$$m\ddot{y} = -i^2 J\left(\ddot{y} - \ddot{d}\right) - k\left(y - d\right) \tag{10}$$

Further, the transfer function $G(s)$, from the acceleration of the installation floor of the proposed stand to the acceleration of the injured, is described as follows.

$$G(s) = \frac{i^2 Js^2 + k}{\left(m + i^2 J\right)s^2 + k} \tag{11}$$

The natural frequency ω_n of the propose stand with rotation inertia mechanism is described as follows.

$$\omega_n = \sqrt{\frac{k}{m + i^2 J}} \tag{12}$$

From this equation, it can be seen that the propose stand with rotational inertia reduces the natural frequency ω_n. Because apparent sprung mass of the propose stand increases by the inertia mass $i^2 J$ in comparison to the typical passive type stand, which consists of the linear spring and a viscous damper as described in Eq. (3).

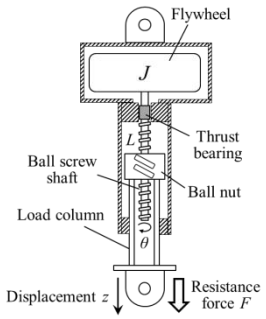

Fig. 11 Typical structure of rotational inertia mechanism

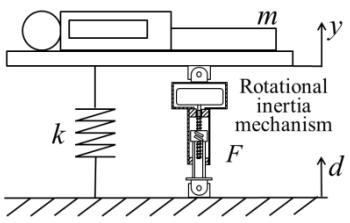

Fig. 12 Passive model with fundamental rotational inertia mechanism

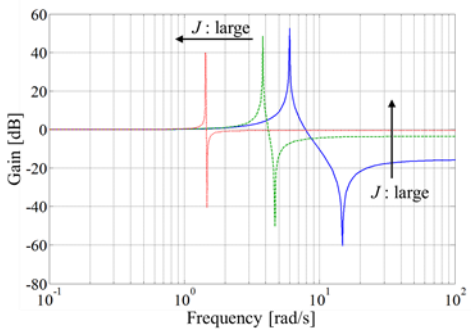

Fig. 13 Gain diagram of passive model with fundamental rotational inertia mechanism

Figure 13 shows an example of the gain diagram of the transfer function Eq. (11) varies with the moment of inertia *J*. From this figure, it can be seen that the gain characteristics in the high frequency range is increased, though the natural frequency ω_n is reduced by the increase in the moment of inertia *J*. Therefore, the propose stand requires new mechanism to reduce the gain in the high frequency range.

4.2 Proposed rotational inertia mechanism and its control law

From Chapter 4.1, the gain characteristics of the passive model with the fundamental rotational inertia mechanism are investigated. As a result, it can be seen that the gain characteristics increases in the high frequency range, although the natural frequency is reduced. The result causes the relative degree of the transfer function in Eq. (11) is zero. If the resistance force F of the ball screw shaft is proportional to the acceleration $\ddot{y}$, the numerator polynomial of Eq. (11) is *k*, the relative degree of the transfer function is one. As a result, the mechanism can reduce both the gain around the natural frequency and that in the high frequency range at the same time.

The resistance force *F* could work as an excitation force corresponding to the phase condition between the acceleration $\ddot{y}$ and the relative acceleration $\ddot{y}-\ddot{d}$. Therefore, taken note of the phase condition, a new mechanism installing a clutch in the rotational inertia mechanism in order to cut off flywheel and its control law are considered. Figure 14(a) shows state of cutting off the clutch, so that the rotational inertia mechanism cannot occur the excitation force. Figure 14(b) shows state of connecting the clutch. Then, the resistance force occurs in proportion to the acceleration. The control law to cut off the flywheel with the clutch is described as follows.

$$F=\begin{cases} i^2 J\left(\ddot{y}-\ddot{d}\right) & \ddot{y}\left(\ddot{y}-\ddot{d}\right)>0 \\ 0 & \ddot{y}\left(\ddot{y}-\ddot{d}\right)\le 0 \end{cases} \tag{13}$$

To verify the effectiveness of the rotational inertia mechanism with clutch, the gain diagram was calculated by numerical simulation, as shown in Fig. 15. Table 1 shows the parameter values in the numerical simulation. From this figure, it can be seen that the gain decreased by 7dB degree in the high frequency range. However, it can be seen that the gain is not improved dramatically in all frequency range, although new mechanism can solve the gain characteristics of high frequency range.

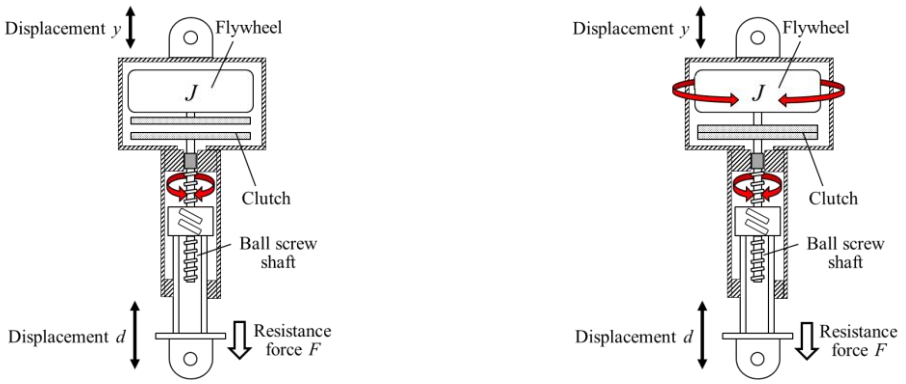

(a) cut off clutch **(b)** connect clutch

Fig. 14 Rotational inertia mechanism with clutch

Table 1 Simulation parameters

Sprung mass including the injured *m*	70 [kg]
Spring constant with proposed tri-linear spring mechanism *k*	3000 [N/m]
Lead of ball screw shaft *L*	0.02 [m]
Moment of inertia *J*	1.4×10^{-2} [kg· m^2]

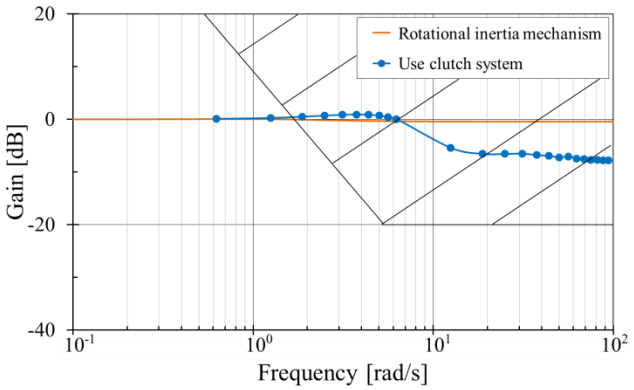

Fig. 15 Gain diagram of passive stand with proposed rotational inertia mechanism

5. Conclusion

Two methods to reduce the natural frequency of the vibration isolation stands were proposed. The one method is the tri-linear spring mechanism with extension springs. The prototype of the tri-linear spring mechanism shows the desired spring characteristics. Also, installing the rotational inertia in the vibration isolation stands was investigated as the other method in order to decrease the natural frequency. From simulation results, it can be seen that the proposed rotational inertia mechanism with clutch can improve the gain around the natural frequency and the gain in high frequency range at the same time. However the gain is not improved dramatically in all frequency range.

Acknowledgments

This study was supported by a Grant-in-Aid for Young Scientists (B) No. 23710210 from the Japan Society for the Promotion of Science (JSPS), for which the authors express their deepest gratitude.

References

[1] Cabinet Office, Government of Japan, White Paper on Disaster Management, (2010)
[2] T. Ono and H. Inooka, 2 Degree-of-freedom Actively-controlled Bed for Ambulances, Transactions of the Japan Society of Mechanical Engineers, Series C, Vol. 71, No. 711, pp.3152-3158, (2005)
[3] G. Kawashima, Study for Active Controlled Pendulum Type Bed for Vehicle (Prevention of the Patient Sliding on the Bed), Transactions of the Japan Society of Mechanical Engineers, Series C, Vol. 68, No. 670, pp.1626-1632, (2002)
[4] S. Toyama, H. Seta and F. Ikeda, Development of Semi-active Suspension System for Boat Seat, Proceedings of the 8th International Conference on Motion and Vibration Control, pp.712-717, (2006)
[5] M. Hineno and Y. Yamauchi, Spectrum of Ocean Waves, The Society of Naval Architects of Japan, Vol. 609, pp.160-180, (1980)
[6] T. Fossen, Marine Control Systems, Marine Cybernetics, (2002)
[7] T. Gotou, Oscillating Limit from Human Body Response, The Society of Naval Architects of Japan, Vol. 583, pp.10-20, (1978)
[8] Y. Ikeda and R. Shigehiro, Evaluation Method of Ride Comfort for Vessels, The Kansai Society of Naval Architects RAN, Vol. 20, pp.17-22, (1993)
[9] M. Ueda, K. Ohmata, R. Yamagishi, J. Yokoo, Vertical and Three-Dimensional Seismic Isolation Tables with Bilinear Spring Force Characteristics : For Which a Λ-Shaped Link Mechanism Is Used (Mechanical Systems), Transactions of the Japan Society of Mechanical Engineers, Series C, Vol. 73, No. 735, pp.60-67, (2007)
[10] M. Kunieda, Practical Mechanics, Rikougaku-sha, (1999)
[11] K. Ohmata and H. Shimoda, Studies on Ball Screw Type Damper with Flyball Governor : 1st Report, Case in Which Ball Nut Is Attached to Primary Mass, Transactions of the Japan Society of Mechanical Engineers, Series C, Vol. 51, No. 467, pp.1472-1481, (1985)

~~*(Received: 23 June, 2013, Accepted: 31 July, 2013)*~~

Small-Size MHD Experiments and Simulation at WNCT and NUT

Shinji Takeshita[1,*], Naoya Ikoma[1],
Yusuke Sasaki[2], Toru Sasaki[2], Takashi Kikuchi[2], Nobuhiro Harada[2]
[1)]Department of Electrical and Computer Engineering, Wakayama National College of Technology,
77 Noshima, Nada, Gobo, Wakayama 640-0023, Japan
[2)]Department of Electrical Engineering, Nagaoka University of Technology,
1603-1 Kamitomioka-cho, Nagaoka 940-2188, Japan
**E-mail: takeshita@wakayama-nct.ac.jp*

The purpose of this paper is to introduce and study small-size MHD power generation experiment and simulation of pulse MHD acceleration in Nagaoka University of Technology (NUT) and Wakayama National College of Technology (WNCT). As results, in the simulations for pulse MHD acceleration in NUT, the acceleration effect of electrodes length of 5 mm was stronger than for the case of electrodes length of 5 mm, and the gain of thrust efficiency of 8 % was obtained at the MHD channel exit. Because high negative current density distribution on the electrodes induced increase of the gas pressure, the plasma was shifted to the downstream of the MHD channel with time variation, and Lorenz force was not generated effectively for electrodes length of 50 mm. On the other hand, high negative current density was only generated on the electrodes at the center of the MHD channel. It means Lorenz force was generated effectively for the case of electrodes length of 5 mm. In preliminary study of MHD power generation experiment in WNCT, it is found output voltage of 0.1 V with plasma injection.

1. Introduction

Recently, space missions, for example, the cargo shipments to International Space Station (ISS), planetary exploration vehicles and artificial satellites, are actively pursued. The researchers have to select the best propulsion system corresponding to the destination, the mission term and the running cost. For example, chemical rocket is suitable for the launching because it has high thrust and it is possible to reach the space for a short time. However in space exploration outside the solar system, the high thrust is not needed and we must choose the propulsion system which has high specific impulse. As one of representative case, ion thruster, which was the propulsion system of "Hayabusa" explorer, achieved to move about 60 hundred million km [1].

A magnetohydrodynamics (MHD) accelerator is one of the candidates for next generation propulsion system, for example, R. J. Rosa proposed new concept propulsion system, which is MHD generator with nuclear technology extracts output power to apply combustion gas [2]. In addition, Holt et al studied MHD generator which applied liquid fuel and O_2 gas mixture as working gas [3]. Propulsion principle of MHD acceleration is performed by interaction of magnetic field and current. Figure 1 is indicated principle of the MHD acceleration. Firstly, plasma flows in the channel with a uniform magnetic field, and then if we supply electrical field to beat internal electromotive force (i.e. $\boldsymbol{u}\times\boldsymbol{B}$) by the plasma itself, Lorenz force F is generated by the current density J and the magnetic field B (i.e. $\boldsymbol{J}\times\boldsymbol{B}$). Therefore plasma is accelerated by Lorenz force eventually.

Conventional MHD experiments need huge budget and human resource because it is necessary to set up combustion gas plasma sources superconducting coils, power supplies and MHD channels of large size etc. In fact, a small number of research institutes only could carry out by MHD generation/acceleration experiments all over the world.

In Nagaoka University of Technology (NUT), they have been studying small-size MHD

experiments and simulation since 2008 [4]-[11], and clarifying plasma behavior and its characteristics in both by MHD experiments and simulations. The advantages of small-size MHD experiment are low cost, simple instruments, and it is possible to observe plasma behavior even if in the small-size MHD channel because governing equations are quite same and fundamental properties are not varied. Although Moeller et al have also studied small-size pulse MHD acceleration experiment, this work focused on application to nuclear electric propulsion system [12]. Moreover one of our concepts is to utilize solid rocket fuel. It means MHD accelerator combined with solid rocket engine to operate flow control.

The purpose of this paper is to study the approach of MHD experiments and simulations at NUT in particular relationship of applied magnetic flux density and acceleration effects for pulse MHD acceleration, and preliminary study of MHD experiment in Wakayama National College of Technology (WNCT), and its results.

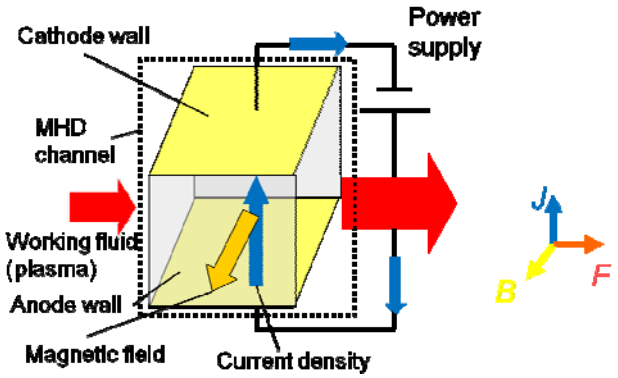

Fig. 1 Principle of MHD acceleration

2. MHD Experiment and Simulation at NUT

Here, we introduce in both pulse MHD acceleration experiment and the numerical simulation at NUT. The aim of this section is to verify the relationship of applied magnetic flux density and acceleration effect for the experiments and behaviour of the plasma for the experiment as pulse current is supplied on simulation. The configuration of small-size MHD channel at NUT is indicated in Fig. 2, and the channel length is 75 mm, and its cross sectional area is constantly 20×20 mm^2 in the channel. In addition, the electrodes are set in the middle of the channel. Applied magnetic flux density is supplied by neodymium magnets. Pulse forming network (PFN) is shown in Fig.3. This circuit consists of a three-stage ladder LC circuit, a matching load, a power supply and the load (MHD channel). It has a possibility that the output current is varied by the plasma resistance. Therefore matching load of 2 Ω is inserted to the circuit. Figure 4 shows waveform of input pulse current, whose peak is −1.2 kA and width is 200 μs, is applied to the MHD channel. In Fig. 5, the profiles of applied magnetic flux density of experimental data and simulation curve are indicated. The peak value is about 0.2 T at the MHD channel of 40 mm however the profile in simulation is fitting by Gaussian distribution and the peak value is shifted to the channel length of 35 mm. Moreover plasma source is obtained by the fuel of an Estes Corp. model rocket engine C6-0.

As a numerical simulation model for 1D simulation, these governing equations are applied as follow [9]. Analytical scheme is upwind scheme, in addition, analysis condition is indicated Table 1. Inlet gas velocity of 300 m/s, inlet gas temperature of 1900 K and mass flow rate of 1.293 kg/m^3 are kept at the channel inlet as initial condition. As boundary condition, free outflow condition by advection equation at channel exit is applied, in addition wall temperature, collision to the wall of channel and viscosity are not considered in this simulation.

In this simulation, electrodes lengths of 5 and 50 mm are applied. This current density is also varied to −12.0 MA/m^2 for the case of 5 mm, and −1.2 MA/m^2 for the case of 50 mm at that same time, and then the effect of self-magnetic field by high current is not considered. Moreover applied magnetic flux density is also varied because acceleration effect by Lorenz force is directly linked applied magnetic flux density and current density.

continuity equation;

$$\frac{\partial \rho}{\partial t} + u_z \frac{\partial \rho}{\partial z} = -\rho \frac{\partial u_z}{\partial z} ,$$

where ρ is density and u_z is gas velocity of z-direction.
momentum equation;

$$\frac{\partial u_z}{\partial t} + u_z \frac{\partial u_z}{\partial z} = -\frac{1}{\rho}\frac{\partial P}{\partial z} - \frac{J_y B_x}{\rho} ,$$

where P is gas pressure and B_x is magnetic flux density of x-direction.
energy equation;

$$\frac{\partial H}{\partial t} + u_z \frac{\partial (H+P)}{\partial z} = \frac{J_y^2}{\sigma} - (H+P)\frac{\partial u_z}{\partial z} ,$$

where H is enthalpy, J_y is current density of y-direction (Faraday current density), and σ is gas conductivity,
equation of state;

$$P = \rho R T_g ,$$

where R is gas constant, and T_g is gas temperature,
and equation of enthalpy;

$$H = \rho\left(c_v T_g + \frac{1}{2}|u|^2 \right)$$

Here, we note fluid of x-direction and y-direction are assumed uniformity distribution, and gas velocity of z-direction, gas pressure, density and enthalpy are varied temporally and spatially by above governing equations.

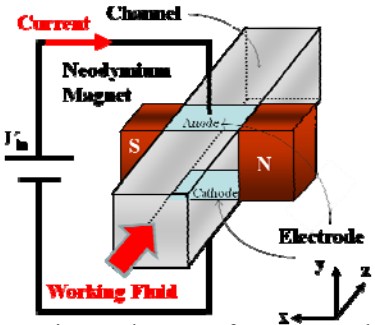

Fig. 2 Experimental setup of MHD acceleration

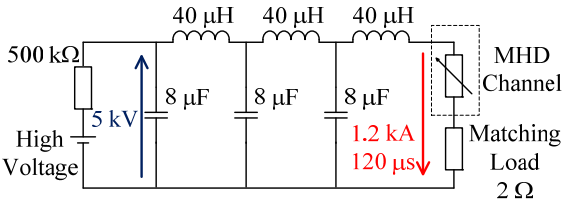

Fig. 3 Pulse current generating circuit using by pulse forming network (PFN)

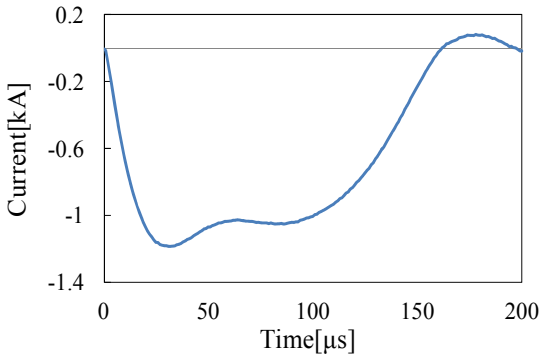

Fig. 4 Waveform of input pulse current

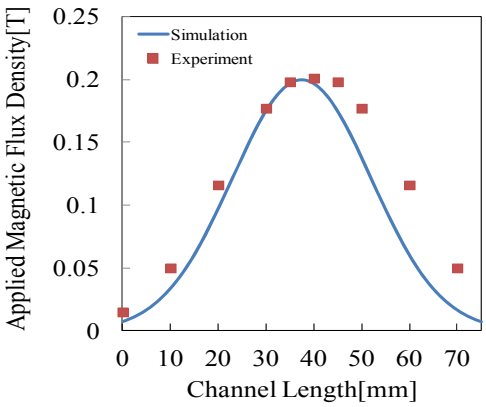

Fig. 5 Distribution of applied magnetic flux density

Table 1 Analysis condition

Channel length (m)	0.075
Cross sectional area of channel (mm^2)	20×20
Electrode length (mm)	5,50
Inlet gas velocity (m/s)	300
Inlet gas temperature (K)	1900
Inlet mass flow rate (kg/m^3)	1.293
Applied magnetic flux density (T)	0-2.0 (peak)

3. Results and Discussion

The profiles of outlet gas velocity for simulation are shown in Fig. 6. Both profiles of outlet gas velocity was accelerated by increased applied magnetic flux density, in particular, for the case of current density of −12.0 MA/m^2 (electrodes length of 5 mm), the inclination of acceleration was more significant. And then it is accelerated to 510 m/s for the case of magnetic flux density of 2 T. Here, both gas velocities for the case of applied magnetic flux density of 0 T was also increased to about 400 and 480 m/s. Because joule heating induced increasing of gas pressure by the equation of state, and then fluid density is also decreased. Therefore gas velocity is finally increased by continuity and momentum equations.

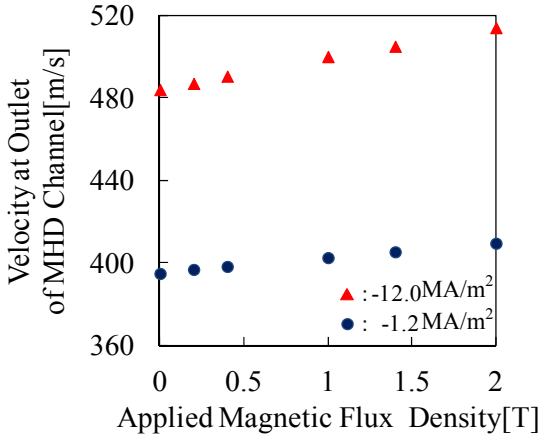

Fig. 6 Relationship of outlet gas velocity and applied magnetic flux density

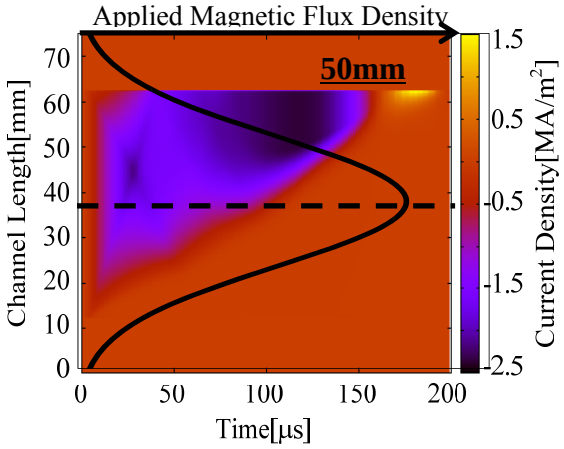

Fig. 7 Current density distribution for electrodes length of 50 mm

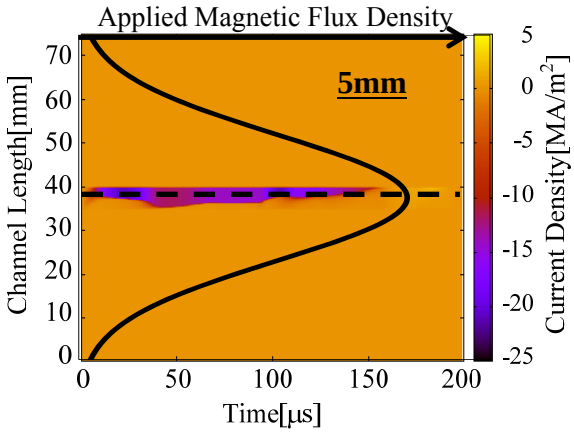

Fig. 8 Current density distribution for electrodes length of 5 mm

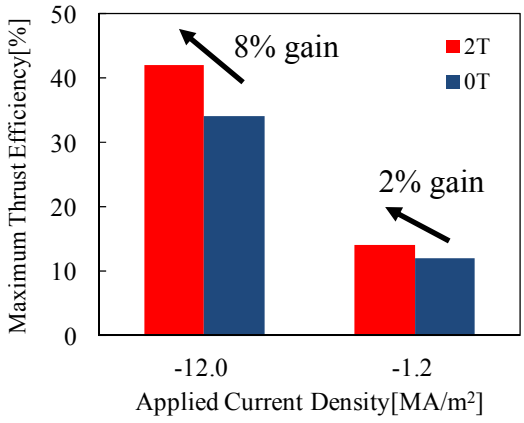

Fig. 9 Relationship of applied magnetic flux density, current density and thrust efficiency

Current density distribution with time variation is indicated Figs.7 and 8 respectively. Here, we note that negative high current density is operated to Lorenz force to accelerate the plasma effectively (see in Fig.4), and applied magnetic flux density in both cases is 2 T at the center of MHD channel. For the case of electrodes length of 50 mm (current density is −1.2 MA/m^2), negative current density about −1.5 to −2.5 MA/m^2 was generated from channel length of 12 to 62 mm at 0 μs. As time goes by, negative current density was shifted to downstream of the MHD channel, and after about 70 μs, high negative current density was concentrated from channel length of 45 to 62 mm. This is because pressure gradient by joule heating generated and propagated to the upstream and downstream of MHD channel, in addition, and then flow-in of the plasma prevented to the midstream of MHD channel. Moreover, the peak of applied magnetic flux density was the center of MHD channel. Accordingly, Lorenz force was not generated effectively. On the other hand, the case of length of electrodes is 50 mm (current density is −12.0 MA/m^2), negative current density about −10 to −20 MA/m^2 was generated about from the center of the MHD channel. This current density distribution was just agreed with the peak of applied magnetic flux density, thus we could estimate easily Lorenz force was also generated effectively. In Fig.9, this figure shows thrust efficiency for the cases of −1.2 and −12.0 MA/m^2, and then gain of thrust efficiency of 8 % was obtained for the case of −1.2 MA/m^2.

4. Preliminary Study of MHD Experiment at WNCT

We carried out preliminary MHD power generation experiment which starts just from this year. As plasma source, we employed electron gas torch by Style Index Corp. PRINCE GT100. Because this gas combustion temperature is between 2100 and 2400 K, the price is affordable price, long time driven is available and it has the possibility to driven without seed material due to suitable high temperature for conservation of plasma condition. The purpose of this experiment at WNCT is to extract the output power from plasma by gas torch directly as electrical energy using more simplified and portable facilities. If it is achieved, we are able to perform also MHD acceleration experiment with the plasma by gas torch using by repetitively pulse power technology. It means it has possibility to perform continuity operation for MHD experiment. Moreover, this experiment will apply in open lecture of WNCT for local junior high and elementary school students to induce interest to the science.

In Fig.10, experimental setup at WNCT is shown. As experimental condition, specification of MHD channel is almost same with the experiment at NUT (see in Table 1), applied magnetic flux density is 0.307 T (peak) and external load of 15 kΩ is connected with the electrodes of the MHD channel. Gas combustion in the MHD channel is shown in Fig.11, and we can understand the plasma is generating from gas torch slightly.

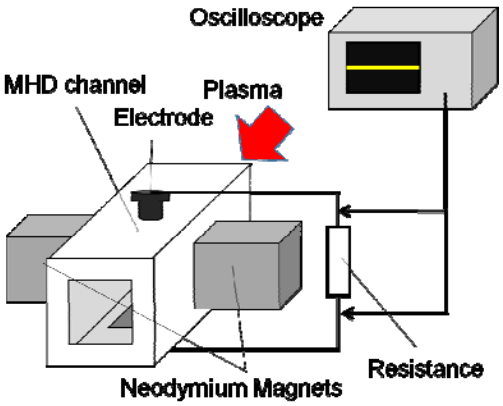

Fig. 10 Experimental setup in WNCT

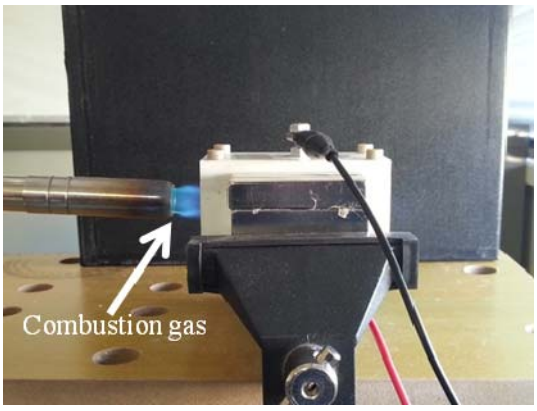

Fig. 11 MHD power generation experiment using by gas torch

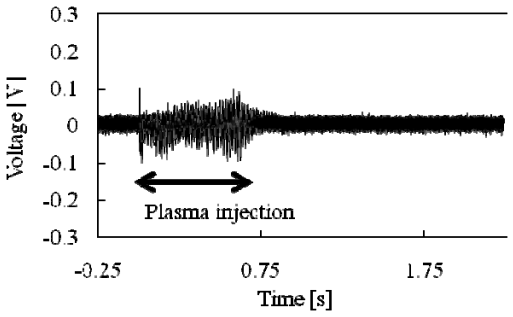

Fig. 12 Output voltage by plasma without seed material for external load of 15 kΩ

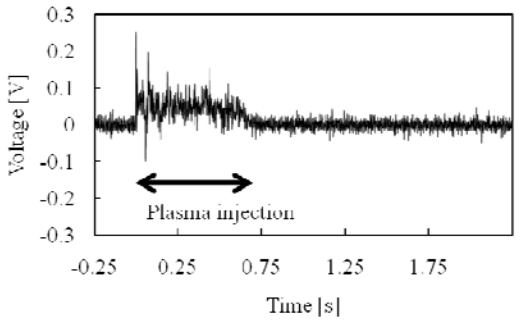

Fig. 13 Output voltage by plasma without seed material for external load of 63 MΩ

As a result, output voltage obtained is shown in Fig.12. The duration of plasma generation was about 1 sec and magnitude of the voltage is gained from −100 to 100 mV at that duration. This is a sign of power extraction because the amplitude of the output voltage vibrated sharply. However, normal MHD output power should be direct current. The cause is induced by various factors for example, difference in temperature, lack of plasma volume, thermal noise etc., here we derived plasma resistance by waveform of plasma discharge for CR discharge circuit, and external load of 63 MΩ is set again. As a result, in Fig.13, output voltage of about 0.1V is obtained finally.

5. Conclusion

In this paper, small-size MHD experiments and simulation at NUT and WNCT are introduced and studied. Particularly, MHD simulation for the relationship of applied magnetic flux density and acceleration effects for pulse MHD acceleration at NUT, and preliminary study of MHD experiment at WNCT, and we obtained as follow.

In the simulations for pulse MHD acceleration at NUT, the acceleration effect of shorter electrodes length (electrodes length of 5 mm) was stronger than for the case of longer electrodes length (electrodes length of 5 mm), the gain of 8 % was obtained at the MHD channel exit. Because high negative current density distribution between the electrodes induced increase of the gas pressure, the plasma was shifted to the downstream of the MHD channel with time variation, and Lorenz force was not generated effectively for the case of electrodes length of 50 mm. On the other hand, high negative current density was only generated between the electrodes at the center of the MHD channel, it means Lorenz force was generated effectively for the case of electrodes length of 5 mm.

In preliminary study of MHD power generation experiment at WNCT, it was found the sign of output power with plasma injection. Although this output signal contained hard noise signal and it was vibrated to positive and negative, however to derive external resistance, and output voltage of 0.1 V is obtained.

Acknowledgments

This research is partly supported by College of Technology - NUT joint research aid. We would like to express us gratitude to Nagaoka University of Technology. In addition, we would like to anonymous reviewers for their valuable moments on the paper.

Nomenclature

u_z:	gas velocity of z-direction (m/s)
ρ:	density (kg/m^3)
J_y:	current density of y-direction (A/m^2)
P	static gas pressure (Pa)

T_g:	static gas temperature (K)
H:	enthalpy (J/m^3)
B_x:	applied magnetic flux density of z-direction (T)
R:	gas constant (J/mol/K)
c_v	specific heat at constant volume (J/kg/K)

References

[1] S. Hosoda, and H. Kuninaka, *J. Plasma Fusion Res*., **86** (2010) 5.

[2] R. Rosa, *AIAA/SAE/ASME 18th Joint Propulsion Conference*, (1982) AIAA-1982-1212.

[3] J. Holt, and D. Swallom, *Annual Intersociety Energy Conversion and Engineering Conference*, (1975)A75-45920.

[4] A. Kubo, K. Suwa, T. Sasaki, T. Sasaki, T. Kikuchi, and N. Harada, *17th International Conference on MHD Energy Conversion*, (2009)4-6.

[5] N. Harada, A. Kubo, T. Suzuki, W.Watahiki, T.Kikuchi and T. Sasaki, *41st Plasmadynamics and Lasers Conferences*, (2010) AIAA-2010-4305.

[6] Y. Takai, Y. Naganuma, S. Takayanagi, T. Sasaki, T. Kikuchi, and N. Harada, *50th AIAA Aerospace Sciences Meeting including the New Horizons Forum and Aerospace Exposition*, (2012)AIAA-2012-0357.

[7] S. Takeshita, Y. Sasaki, T. Sasaki, T. Kikuchi, and N. Harada, *Kosen Education Forum 2012*, (2012)PO_A27(Japanese).

[8] Y. Takai, S. Takayanagi, T. Tanaka, T. Sasaki, T. Kikuchi, T. Aso, and N. Harada, *IEEJ Trans. FM*, **132**(2012)12 .

[9] Y. Takai, S. Takayanagi, T. Tanaka, T. Sasaki, T. Kikuchi, T. Aso, and N. Harada, *51th AIAA Aerospace Sciences Meeting including the New Horizons Forum and Aerospace Exposition*, (2013)AIAA-2013-0176.

[10] Y. Sasaki, T, Sasaki, T. Aso, T. Kikuchi, and N. Harada, IEEJ National Convention 2013, (2013)1-086 (Japanese).

[11] N. Harada, J. Ikewada, and Y. Terasaki, *33rd AIAA Plasmadynamics and Lasers Conference*, (2002) AIAA-2002-2175.

[12] T. Moeller, D. Keefer, and R. Rhodes, *IEEE International Conference on Plasma Science*, (2004)4P52.

(Received: 23 June, 2013, Accepted: 6th April, 2014)

Usability Evaluation of Steering System for Pleasure Boat with Eye Tracking Device

Kohei IIHAMA[1], Shigehiro TOYAMA[1,] Fujio IKEDA[1,] Hiroaki SETA[2], Nobuo EZAKI[2]
[1)]Nagaoka National College of Technology, Nagaoka, Niigata, Japan 940-0532
[2)]Toba National College of Maritime Technology, Toba, Mie, Japan 517-8501
**E-mail: toyama@nagaoka-ct.ac.jp*

The reason for the increase in the number of maritime accidents are the rise of beginner captains and complicated maneuverability of pleasure boats. Although good usability should be secured against the complicated maneuverability of manual hydraulic steering systems, which are widely used for pleasure boats, is not satisfactory. Ahead of the developing steer-by-wire (SBW) system that could improve the usability dramatically, an evaluation method to quantitate the usability has already been proposed. The evaluation method decides to value effectiveness, effciency and satisfaction, which are selected as the evaluated standards based on ISO 9241-11, in a task programmed into a simplified ship simulator. This paper proposes new evaluation criteria adding gaze of the subjects into the those selected standards of the previous method. The availability of the new evaluation method is verified through some experiments with the simplified ship simulator. As a result, it can be seen that the new evaluation method can judge the usability more clearly than the previous method.

1. Introduction

The number of maritime accidents of pleasure boats has a trend to increase in recent years [1]. The factors of the trend are rise of beginner captains and complicated maneuverability of pleasure boats. If especially beginner captains steer pleasure boats, it is necessary to secure good usability of steering system. It is, however, hard to say that the usability of manual hydraulic steering mechanism, which is widely used in pleasure boats, is superior. One of the reasons is that reaction torque of the helm through steering systems is not so rich that captains can feel nonlinear characteristics at normal pressure of rudder. Another reason is not so quick steering, since the helm lock to lock is generally 4–7 turns. As a method of improving the usability, steer-by-wire (SBW) system as developed for airplanes and automobiles [2]-[12] can also be considered for pleasure boats [13], [14].

Ahead of developing SBW system, an evaluation method to quantitate the usability has already been proposed by us [15]. The evaluation method sets subjects a task programmed into a simplified ship simulator. In trials of the task, effectiveness, efficiency and satisfaction, which are selected as the evaluated standards based on ISO 9241-11, are valued. This paper proposes new evaluation criteria adding gaze of the subjects into those evaluated standards, so that the usability can be judged more clearly than the previous method. The availability of the new evaluation method is verified through some experiments with the simplified ship simulator.

2. Simplified ship simulator

Figure 1(a) shows the components of the simplified ship simulator programmed a task to evaluate the usability of steering systems. The simplified ship simulator can execute high safety and reproducible experiments. The ship simulator composes HILS (Hardware In the Loop Simulation), which is a technique used the development and test of complex real-time embed system. As the hardware of the HILS, manual hydraulic steering system such as a helm pump (NE1073-00, Nippatsu Telefrex Inc.), a hydraulic cylinder (NE1009-00, Nippatsu Telefrex Inc.) and a rudder mechanism are employed as shown in Figure 1(b) and 1(c). The helm lock to lock is 5.4 turns. The simulation software "NAUTIS" from VSTEP, which is widely used in voyage training, is installed as the software of the HILS. The simulator can output some simulation data such as ship motions,

rudder angle and propeller revolution in real-time. The measurement signal of the rudder angle with the potentiometer is sent to the rudder angle indicator and the simulation PC. Also, the propeller revolution signal with the throttle lever is sent to the simulation PC. Then, the simulation software "NAUTIS" calculates the ship motion corresponding to those inputs. Based on the computation, the ship motion is described on the three monitors from a view point of captain.

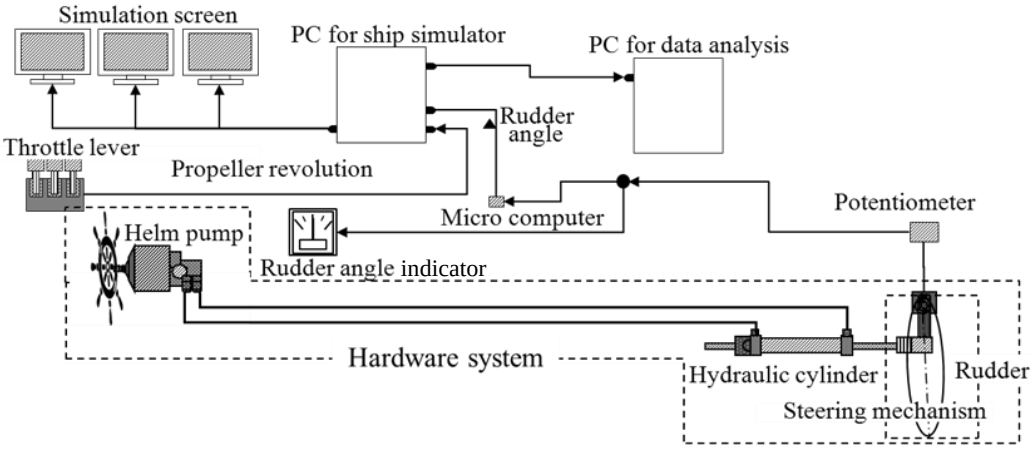

(a) Components

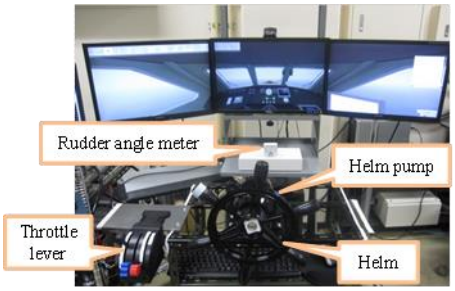

(b) Steering mechanism

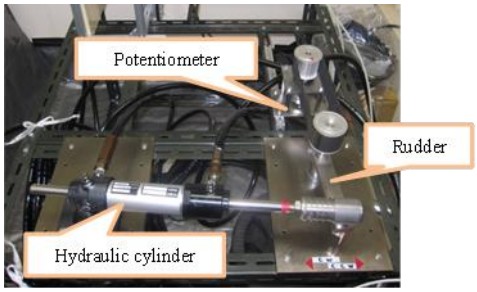

(c) Hydraulic cylinder and rudder mechanism

Fig. 1 Simplified ship simulator

3. Eye tracking system "View Tracker"

Figure 2 shows "View Tracker" from Ditect inc., which is employed as a head mount type eye tracking system in this research. Measuring pupil motion with reflection light from a cornea, the eye tracking system can digitize and visualize the point of gaze. The view camera acquires a scenery image, and the pupil camera acquires the pupil image with the reflecting mirror. Figure 3(a) and 3(b) show an example of digitizing the eye tracking data. Figure 3(a) graphs the pupil position and the point of gaze. Figure 3(b) shows steady gaze time by area in the scenery image.

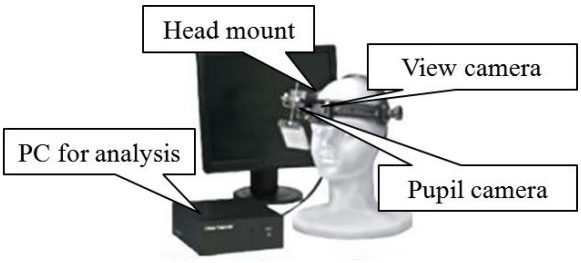

Fig. 2 Eye tracking system "View tracker" [16]

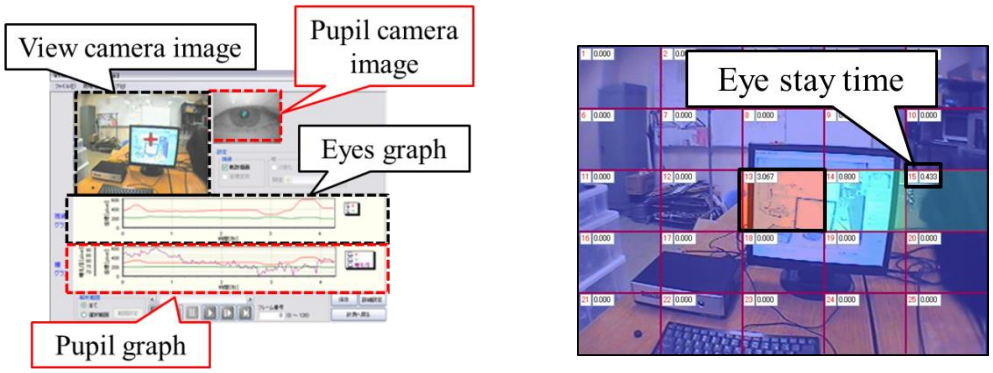

(a) Pupil and point of gaze **(b)** Steady gaze time by are

Fig. 3 Example of digitizing eye tracking data with "View tracker"

4. Evaluation method of usability

4.1 Experimental environment and task

In order to compare with the previous evaluation method of usability, the experiment environment and the task of the new evaluation method are set in the same way. The experimental environment is formed from simulation with the simplified ship simulator. The experimental task is avoiding an obstacle and resuming the original course safety and urgently in poor visibility of a dense fog as shown in Fig. 4. Before the simulation, the guidance of subjects are carried out to explain the simulation object, the outline of the manual hydraulic steering system, the turning principle of pleasure boats, the simplified ship simulator, and the simulation task.

Avoiding the obstacle is judged by the following condition

$$\psi(t) = \psi_a(t),$$

where $\psi(t)$ is the course of the pleasure boat, and $\psi_a(t)$ is the angle with the segment $O_g - O_e$ for the *y* axis as shown in Fig. 4.

Resuming the original course is judged by the following conditions.

$$|\theta(t)| \le 0.5[\text{rev}], \quad |\psi(t)| \le 8[\text{deg}],$$

where $\theta(t)$ is the revolutions of the helm, and those inequalities are empirically defined.

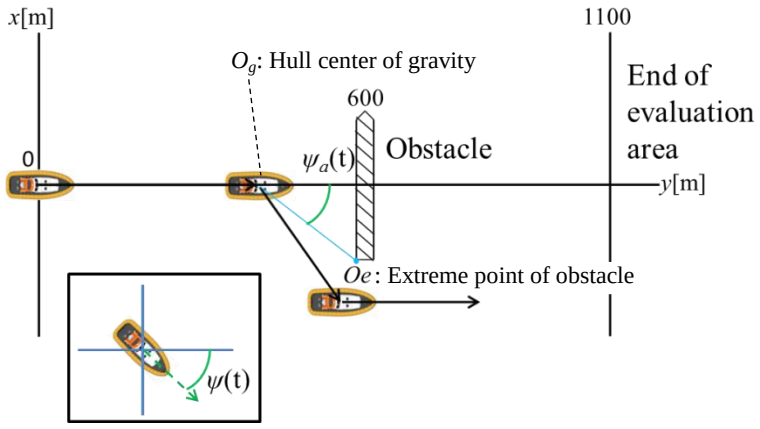

Fig. 4 Experimental task for evaluation of usability

4.2 Basic evaluation criteria by previous method

Referencing to the standard of usability in ISO 9241-11, the previous evaluation method decides some basic criteria on effectiveness (responsiveness and safety) and efficiency [15]. Those criteria are evaluated quantitatively for Phase 1 (avoiding the obstacle) and Phase 2 (Resuming the original course).

The responsiveness of the effectiveness is quantitated by *DRAR* (Delay Rate of Avoiding and Resuming) as follows.

$$DRAR = CL + RD\,, \tag{1}$$

where *CL* and *RD* are given as follows.

$$CL = \frac{(\text{Avoidance time})}{(\text{Predict time to collision at the finding time of the obstacle})} \times 100 \tag{2}$$

$$RD = \frac{(\text{Resuming time})}{(\text{Predict time to arrive at the end of evaluation area})} \times 100 \tag{3}$$

The safety of the effectiveness is quantitated by *RRC* (Risk Rate of Capsizing) as follows.

$$RRC = CP_1 + CP_2 \tag{4}$$

where CP_1 and CP_2 are given as follows.

$$CP_1 = \frac{(\text{Maximum roll angle in Phase 1})}{(\text{Limit roll angle})} \times 100\,, \tag{5}$$

$$CP_2 = \frac{(\text{Maximum roll angle in Phase 2})}{(\text{Limit roll angle})} \times 100\,, \tag{6}$$

and the limit roll angle is empirically fixed on 21 [deg].

The efficiency is quantitated by *RSRO* (Revolution Speed of Operating) as follows.

$$RSRO = \frac{HR_1 + HR_2}{(\text{Maximum helm revolution speed of helm}) \times (t_r - t_a)} \times 100\,, \tag{7}$$

where the maximum revolution speed of the helm is empirically fixed on 0.5 [rev/s], and HR_1 and HR_2 are the integrated revolution angle of turning the helm for each Phase as follows.

$$HR_1 = \int_0^{t_f} \left|\dot{\theta}(t)\right| dt\,, \tag{8}$$

$$HR_2 = \int_{t_a}^{t_r} \left|\dot{\theta}(t)\right| dt\,. \tag{9}$$

t_f is the complete time of avoiding the obstacle, t_a is the start time of resuming the original course, and t_r is the complete time of that.

4.3 New evaluation criteria with eye tracking system

This paper proposes new evaluation criteria with eye tracking system so as to add to the basic criteria shown in the previous section, so that the usability can be judged more reliably and clearly

than the previous method. Figure 5 shows some important points including two nautical instruments of the simplified ship simulator in the scenery image with the eye tracking system. The point X_1 is the center, the point X_2 is a radar screen, which shows the position and the course of pleasure boats, and the point X_3 is a rudder angle indicator. These points exist in the right side of the scenery image, and subjects do not need to pay attention to the left side under the task. Because the guidance before the simulation explains to subjects the situation that there is not any ships, and subjects can recognize the distance to the obstacle even if they keep their gaze on the point X_1 in the avoidance of the obstacle. Frequently, beginner pilots read those nautical instruments X_2 and X_3 to recognize the motion of the pleasure boat for their operation, because they do not master the complicated maneuverability caused by nonlinear hydrodynamic forces. In especially emergency case such as avoiding obstacle, such eye movement could degrade the safety.

The safety of the effectiveness for eye tracking data is quantitated by *SGR* (Steady Gaze Rate) as follows.

$$SGR = \frac{\sum_{i=2}^{3}(\text{Steady gaze time}) \times (\text{Distance from the point } X_1 \text{ to the point } X_i)}{(\text{Simulation time}) \times (\text{Distance from the point } X_1 \text{ to the point } X_2)} \times 100 \tag{10}$$

SGR means the rate of total steady time, which is weighted according to the distance for each point, to the worst case of staying the gaze on the radar screen X_2. That is, *SGR* could be set on 100 if subjects gaze on the X_2 for the all simulation time.

On the other hand, the efficiency for eye tracking data is quantitated by *MRG* (Moving Rate of Gaze) as follows.

$$MRG = \frac{(\text{Total distance})}{\dfrac{(\text{Distance from the point } X_1 \text{ to the point } X_3)}{(\text{Reference time of eye movement})} \times (\text{Simulation time})} \times 100 \tag{11}$$

MRG means the rate of total distance to a reference time, which is set on 700 [msec] [17] in this paper. If the gaze is frequently moved to the radar screen X_2 or the rudder angle indicator X_3, *MRG* could be evaluated as getting worse.

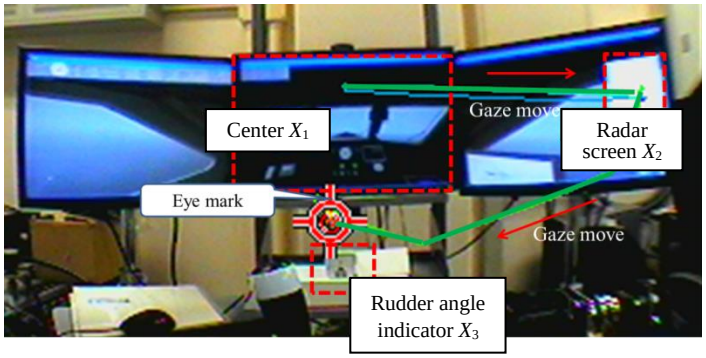

Fig. 5 Nautical instruments of simplified ship simulator in scenery image of captains

5. Verification experiment of new evaluation method

The verification experiments of the new evaluation method were performed to typical three subjects in order to investigate how usability of steering system is evaluated. Subject No. 1 was a trained captain, who could achieve the task independent of the nautical instruments. The others, Subjects No. 2 and No. 3, were untrained captains, who rely on the instruments and do not often succeed the task. As the experimental condition, the visibility was prepared two patterns, 200 [m] and 300 [m], and the propeller revolution was prepared three patterns, 1200 [rpm], 1500 [rpm], and

1800 [rpm].

In the case of the visibility 300 [m], there was no large difference between the wakes for each subject and the propeller revolution condition. Because they could notice the obstacle so early that even though Subject No. 2 and No. 3, who were untrained captains, could afford to carry out the task relying on the nautical instruments. However, in the emergency case of the visibility 200 [m], there was a difference of the wakes with the skill level and the propeller revolution condition. Figure 6 shows the wakes for each subject in the case of the visibility 200 [m]. Figure 6(a) shows that Subject No. 1 of trained captain could achieve the task, which is avoiding the obstacle and resuming the original course safety and quickly. Figure 6(b) shows that Subject No. 2 of untrained captain could avoid the obstacle, however he could not quickly resume the original course and needed a lot of operating the helm. Figure 6(c) shows that Subject No. 3 of untrained captain could avoid the obstacle and could resume the original course so quickly that *DRAR* could be evaluated better than Subject No. 1. However, the subject brought too large roll angle to lead poor *RRC* evaluation, and could not achieve the task safety. That is, the experimental data of Subject No. 1 should be judged the steering system to have good usability, and those data of Subject No. 2 and No. 3 should be judged it to have poor usability.

Table 1 shows the averaged results to be evaluated with the proposed method under the experimental condition, and Figure 7 presents the results of Table 1 as a radar chart. In this radar chart, small area means good usability. From these results, it can be seen that adding the new evaluation criteria to the basic evaluation criteria proposed in the previous method [15] could further improve the reliability of the evaluation, since the clear difference appears in the area of the radar chart for each subject. Also, it can be seen that *DRAR* and *RSRO* of the basic evaluation criteria not to be added eye tracking data seldom show a difference for those three subjects, while *RRC* shows clear difference. On the other hand, it can be seen that the new evaluation criteria with eye tracking system can indicate obvious difference for those simulation data. Because Subject No. 2 first tried to operate without relying on the nautical instruments as well as trained captains, *MRG* of Subject No. 2 shows the almost same value as that of Subject No. 1. However, a large estimation error occurs from the end of avoiding the obstacle to the beginning of resuming the original course, since Subject No. 2 could not master the complicated maneuverability. Then, Subject No. 2 struggled to achieve the task with relying on those instruments. As a result, *SGR* of Simulation data No. 2 grew worse and some wakes are winding as shown in Fig. 6 (b). On the other hand, *MRG* of Subject No. 3 grew worse, since the untrained captain continued to move their gaze point during the simulation. Therefore, the new evaluation criteria with eye tracking system could be available for analysis of poor usability.

6. Conclusion

This paper proposed an evaluation method of usability for steering system of pleasure boats with eye tracking system. Two of new evaluation criteria for eye tracking data were defined and added to the basic criteria of the effectiveness and the efficiency, which have been already proposed. The verification experiments of the new evaluation method were performed. From the results, it can be seen that adding the new evaluation criteria to the basic ones proposed in the previous method could further improve the reliability of the evaluation. And, it can be seen that the new criteria can indicate the evaluation of the usability more clearly than the basic ones, and can analyse cause of poor usability from a view point of the steady gaze time or the eye movement. As a future work applied this proposed evaluation method, we will investigate an electronic steering system to have some functions such as transferring arbitrary reaction torque to captains through the helm. For example, if captains get information of the rudder angle from the reaction torque, they could keep their gaze in front of them. As a result, decreasing both the moving rate and the steady rate of their gaze to realize safety operation is highly expected.

Acknowledgements

This study was supported by a Grant-in-Aid for Scientific Research (C) No. 25350487 from Japan Society for the Promotion of Science (JSPS), for which the authors express their deepest gratitude.

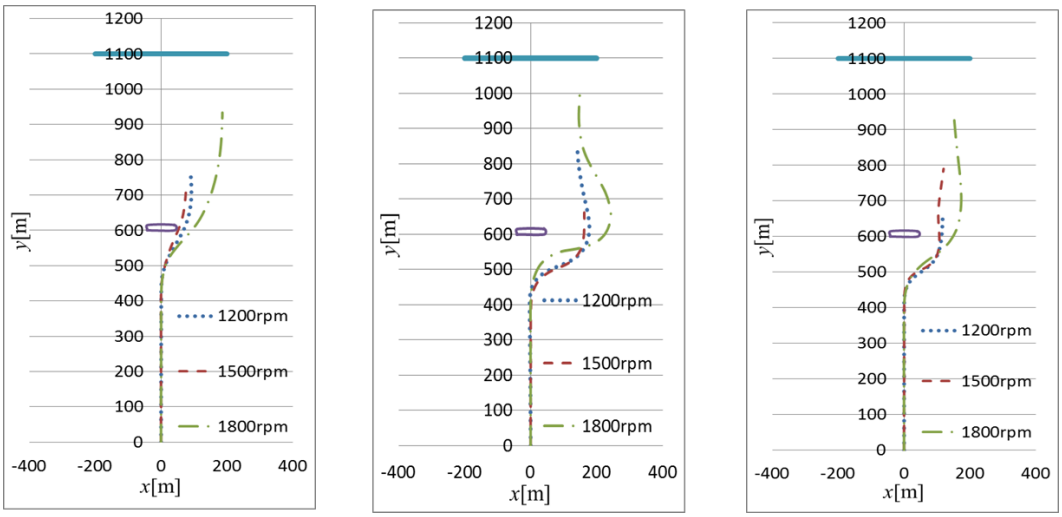

(a)Subject No.1 (b)Subject No.2 (c)Subject No.3

Fig. 6 Wakes for each subject in case of visibility 200m

Table 1 Averaged result of usability for typical three subjects

Subject	*DRAR* (Responsiveness of effectiveness	*RRC* (Safety of effectiveness)	*RSRO* (Efficiency)	*SGR* with eye tracking system (Safety of effectiveness)	*MRG* with eye tracking system (Efficiency)
No. 1 (Trained captain)	54.9	14.9	23.0	8.5	12.8
No. 2 (Untrained captain)	49.1	29.5	22.3	28.3	13.8
No. 3 (Untrained captain)	45.4	31.2	25.9	17.7	25.9

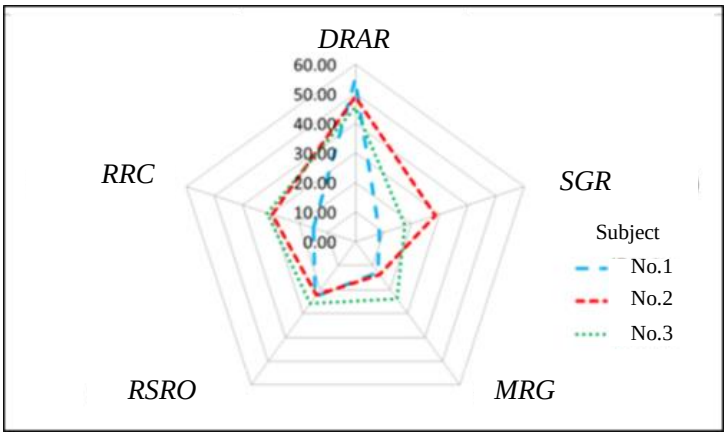

Fig. 7 Rader chart for usability evaluation shown in Table 1

References

[1] Cabinet Office of Japan, Maritime Accident Trends, White Paper on Traffic Safety in Japan 2012, (2013), pp.105-110.
[2] J. B. Leonard, The All-Electric Fighter Airplane Flight Control Issues, Capabilities, and Projections, IEEE Transactions on Aerospace and Electronic Systems, Vol. 20, Issue 3, (1984), pp.234-242.
[3] J. Rea, Boeing 777 high lift control system, IEEE Aerospace and Electronic Systems Magazine, Vol. 8, Issue 8, (1993), pp.15-21.
[4] H. Buus, R. McLees, M. Orgun, E. Pasztor, L. Schultz, 777 flight controls validation process, IEEE Transactions on Aerospace and Electronic Systems, Vol. 33, Issue 2 , (1997), pp. 656-666.
[5] R. Hammett, Design by extrapolation: an evaluation of fault tolerant avionics, IEEE Aerospace and Electronic Systems Magazine, Vol. 17, Issue 4, (2002), pp.17-25.
[6] R. Schroer, Cockpit Instruments [A century of powered flight:1903-2003], IEEE Aerospace and Electronic Systems Magazine, Vol. 18, Issue 7, (2003), pp.13-18.
[7] N. Matsunaga, J. Im, S. Kawaji, Control of Steering-by-Wire System of Electric Vehicle using Bilateral Control Designed by Passivity Approach, Journal of System Design and Dynamics, Vol. 4, No. 1, (2010), pp. 50-60.
[8] R. Rajamani, D. Piyabongkarn, New paradigms for the integration of yaw stability and rollover prevention functions in vehicle stability control, IEEE Transactions on Intelligent Transportation Systems, Vol. 14, Issue 1, (2013), pp.249-261
[9] C. E. Beal, J. C. Gerdes, Model Predictive Control for Vehicle Stabilization at the Limits of Handling, IEEE Transactions on Control Systems Technology, Vol. 21, Issue 4, (2013), pp.1258-1269.
[10] N. Kanghyun, H. Fujimoto, Y. Hori, Lateral Stability Control of In-Wheel-Motor-Driven Electric Vehicles Based on Sideslip Angle Estimation Using Lateral Tire Force Sensors, IEEE Transactions on Vehicular Technology, Vol. 61 , Issue 5, (2012), pp.1972-1985.
[11] M. J. Jensen, A. M. Tolbert, J. R. Wagner, F. S. Switzer, J. W. Finn, A Customizable Automotive Steering System With a Haptic Feedback Control Strategy for Obstacle Avoidance Notification, IEEE Transactions on Vehicular Technology, Vol. 60, Issue 9, (2011), pp.4208-4216.
[12] Y. Yamaguchi, T. Murakami, Adaptive Control for Virtual Steering Characteristics on Electric Vehicle Using Steer-by-Wire System, IEEE Transactions on Industrial Electronics, Vol. 56 , Issue 5, (2009), pp.1585-1594.
[13] S. Toyama, F. Ikeda, H. Seta, A Sliding Mode Controller of Rudder Angle Servomechanism in Steer-by-Wire System of Pleasure Boat, Journal of System Design and Dynamics, Vol. 5, No.5, (2011), pp. 1127-1140.
[14] F. Ikeda, S. Toyama, H. Seta, N. Ezaki, Improvement of Steering Feeling on Maneuverability for Pleasure Boat, Journal of System Design and Dynamics, Vol. 5, No.5, (2011), pp. 1119-1126.
[15] K. Iihama, S. Toyama, F. Ikeda, H. Seta, N. Ezaki, Operability Evaluation of Pleasure Boats Based on Usability as Addressed by ISO 9241-11, Transactions of the Japan Society of Mechanical Engineers, Series (C), Vol. 79, No. 801, (2013), pp.1415-1426.
[16] Eye Tracking System “View Tracker”, www.kk-co.jp/detail/view_.php
[17] S. K. Card, T. P. Moran, A. Newell, The model human processor: An engineering model of human performance, Handbook of Human Perception, 1986.

(Received: 23 June, 2013, Accepted: 31 July, 2013)

Experimental Study on Turn Operation of 3D Quasi-Passive Dynamic Walking Robot

Fujio Ikeda[1*], Shigehiro Toyama[2], Yuki Hirasawa[3]
[1)]Department of Mechanical Engineering, Nagaoka National College of Technology,
888 Nishikatakai, Nagaoka, Niigata 940-8532, Japan
[2)]Department of Electronic Control Engineering, Nagaoka National College of Technology,
[3)]Department of Mechanical Engineering, Nagaoka University of Technology,
**E-mail: ikeda@nagaoka-ct.ac.jp*

Passive dynamic walking robots can walk down a shallow slope without actuators and controllers. Most researches of passive bipedal robots have only be focused on walking on a straight line, although one of the important issues of walking robots is to be headed for a target direction as ones desired. The purpose of this paper is to develop an upper body driven quasi-passive 3D walking robot which can turn right and left on a flat surface with direction control mechanism. A walking gait of our 3D robot has a roll motion from side to side of both legs on a frontal plane which synchronizes a pitch motion of a swing foot on a sagittal plane. The direction control mechanism has a micro switch to turnover which is attached on a hip joint above each leg. This mechanism makes use of yaw motion of the stance leg.

1. Introduction

Recent studies have been focusing on passive dynamic walking that makes active use of robot dynamics to focus on a smoother walk that closely resembles human walking [1]. Passive walking robots step forward on a shallow slope and perform without using actuators by repeating an operation in which the legs fall forward like pendulums [2, 3]. Using the potential energy obtained from falling forward, the legs make up for the energy lost during collision with the ground surface, thereby achieving a smooth, natural, continuous walk with high energy efficiency [4, 5]. Many experimental robots have been developed using the passive dynamic walking method, and complete experimental results have been released [6–8]. Further, a number of walking methods based on passive dynamic walking which can walk on a flat surface with the minimum drive power called quasi-passive walking have been studied [9]. The many studies that are in progress in this area range from two-dimensional walking that only considers motion in the sagittal plane to three-dimensional walking that also considers yaw and roll motions in the frontal plane [10–13].

One of the major challenges of walking robots is to move freely toward a target direction. Achieving this goal requires walking accompanied by control in the forward direction or right and left turn operations. However, to the best of our knowledge, all research on passive walking thus far has only focused on straight-line walking and there is no research on walking styles that enable turning operations. To remedy this situation, we designed and built an experimental robot having the minimum number of actuators needed for flat surface walking; on this robot, we mounted a simple turn control mechanism. Our aim is to achieve stable, continuous flat surface walking and turn operations. Our walking robot has an upper-body oscillator that generates roll motion in the frontal plane through motions of pendulum [14]. By synchronizing this roll motion with the swing leg motion in the sagittal plane, the robot achieves continuous three-dimensional walking. Toggling a simple switch installed in the waist area of the legs enables the active use of the yaw motion generated by the stance leg to produce turn operations and move the robot in the desired direction.

Firstly, straight-line walking tests of our robot have enabled us to determine the appropriate parameters for synchronizing the roll motion in the frontal plane and the swing leg motion in the

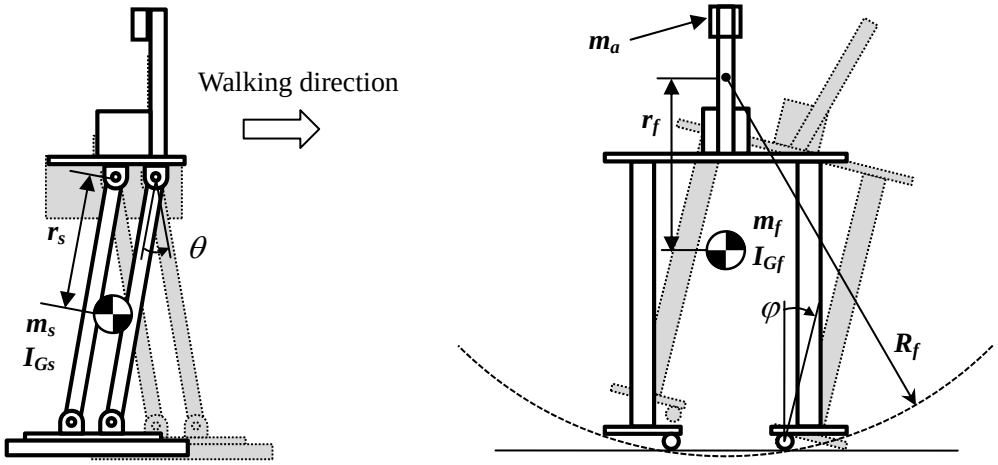

(a) Pitch motion on sagittal view (b) Roll motion on frontal view

Fig. 1 Schematics of our 3D walking robot and notations for physical parameters.

Table 1 Value of the parameters for the physical model of our 3D walking robot.

Parameter	Unit	Value	Parameter	Unit	Value
I_{Gs}	kg·m^2	6.6×10^{-3}	I_{Gf}	kg·m^2	5.2×10^{-2}
m_s	kg	0.45	m_f	kg	1.4
r_s	m	0.21	r_f	m	0.29
m_a	kg	0.0~0.25	R_f	m	0.50

sagittal plane, as well as achieve stable continuous walking on a flat surface. Then, we have tested the right and left turn operations by toggling the abovementioned switch and have verified the effectiveness of the turn performance.

2. Preliminary Analysis of Straight-line Walking

It is necessary to match the step period of roll motion of frontal plane with the period of the swing leg's pendulum motion of a sagittal plane as much as possible for achieving stable continuous walking [15]. So we use numerical simulations to coordinate these periods of roll and pitch motion for purely passive version of a robot without actuation in following way. First the step period of the robot is estimated through numerical simulations whose motion is constrained to the sagittal plane. The step period is measured from one swing foot collision through the other foot collision. Then a center position of rotation for roll motion is coordinated by adjusting positions of each bar attached on a foot sole so as to let the step period of pitch motion and roll motion be the same.

2.1. Pitch motion of swing leg on sagittal plane

The swing leg can swing like a pendulum supported by the stance leg which are shown in Figure 1 (a). The equation of motion, in terms of pitch angle θ, for this planar model on a sagittal plane is given by

$$\left(I_{Gs} + m_s r_s^{\,2}\right)\ddot{\theta} + m_s g r_s \sin\theta = 0 \tag{1}$$

where I_{Gs} and m_s are moment of inertia and mass of a swing leg, r_s is distance between the center of rotation and the center of mass of a swing leg. We assume the pitch angle θ is small and

(1) is linearized, then we have the step period T_s as

$$T_s = \frac{\pi}{\omega_s} \cong 0.53\,[s] \quad , \tag{2}$$

where the natural frequency of the pitch motion is

$$\omega_s = \sqrt{\frac{m_s g r_s}{I_{Gs} + m_s {r_s}^2}} \, , \tag{3}$$

which is calculated by the parameters for the physical model of our 3D walking robot in Table 1.

2.2. Roll motion of whole body on frontal plane

To model the dynamics in the frontal plane, we assume that the robot is always in contact with the ground at exactly one point and that the foot rolls without slipping. The equation of motion without actuation of an upper-body oscillator, in terms of a roll angle φ, for this planar model on the frontal plane shown in Figure 1 (b) is given by

$$\left(I_{Gf} + m_f ({R_f}^2 - 2R_f r_f \cos\varphi + {r_f}^2)\right)\ddot{\varphi} + m_f R_f r_f \sin\varphi \cdot \dot{\varphi}^2 + m_s g r_s \sin\varphi = 0 \tag{4}$$

where I_{Gf} and m_f are moment of inertia and mass of a whole body of the robot, r_f is distance between the center of rotation and the center of the mass, R_f is a length of pseudo-radius of rotation. We also assume the roll angle φ is small and (4) is linearized, then we have the step period T_f of the form which is given by

$$T_f = \frac{\pi}{\omega_f} \quad , \tag{5}$$

where the natural frequency of the roll motion is

$$\omega_f = \sqrt{\frac{m_f g r_f}{I_{Gf} + m_f (R_f - r_f)^2}} \quad . \tag{6}$$

In this simulation study, we can change the step period and let it be the same as ones of the pitch motion as $T_f = T_s (\cong 0.53[s])$. For a given mass and moment of inertia, T_f can easily change by the parameter of the length of pseudo-radius of rotation R_f which is adjusted by the position of the each bar attached on the foot sole.

3. Design and Production of Robot for Turn Operation

We attempted to take advantage of the following two characteristics of the gait produced by purely passive dynamic walking:

1. There is no use of control (not intelligent).
2. Walking is maintained by means of interaction between the robot's own dynamics and the environment.

While making use of above characteristics, we set the design guidelines in order to achieve 3D quasi-passive dynamic walking on a flat surface as follows:

1. Maintain walking by combining frontal-plane roll motion with the natural swing leg motion in the sagittal plane.
2. Generate a roll motion by using the robot's upper-body oscillator as a drive unit to maintain walking.
3. Achieve turn operations by using the swing force of the swing leg to generate yaw motion in the stance leg.
4. Toggle between straight-line motion and a right and left turn operation with a single switch.

Figure 2 (a), (b) shows the appearance of the robot that we designed using the abovementioned

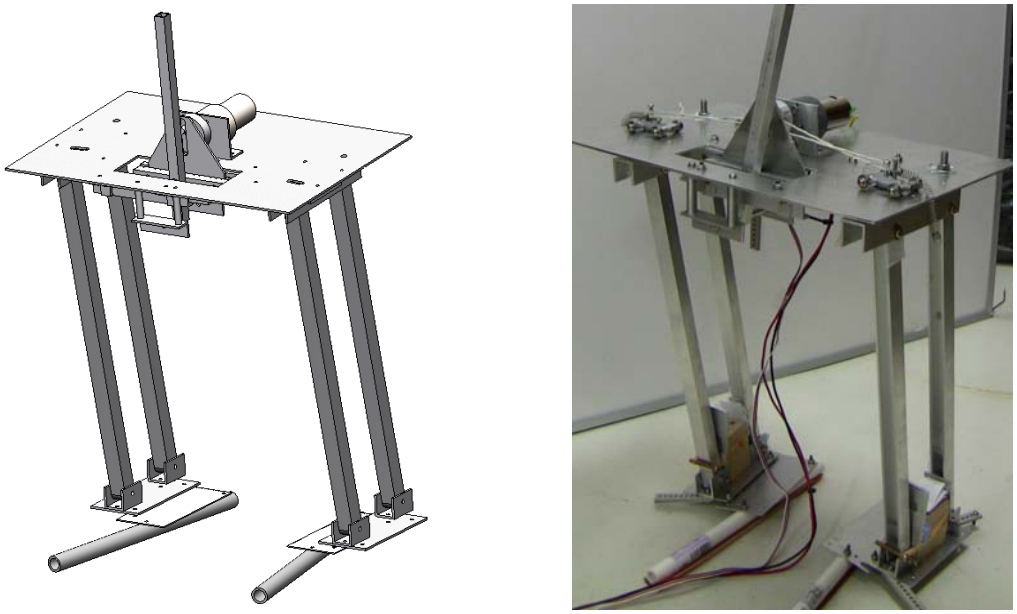

(a) Overview of the robot designed by 3D-CAD

(b) Photo of the robot manufactured by aluminum flames

Fig. 2 A straight-legged quasi-passive walking robot actuated by an upper-body oscillator.

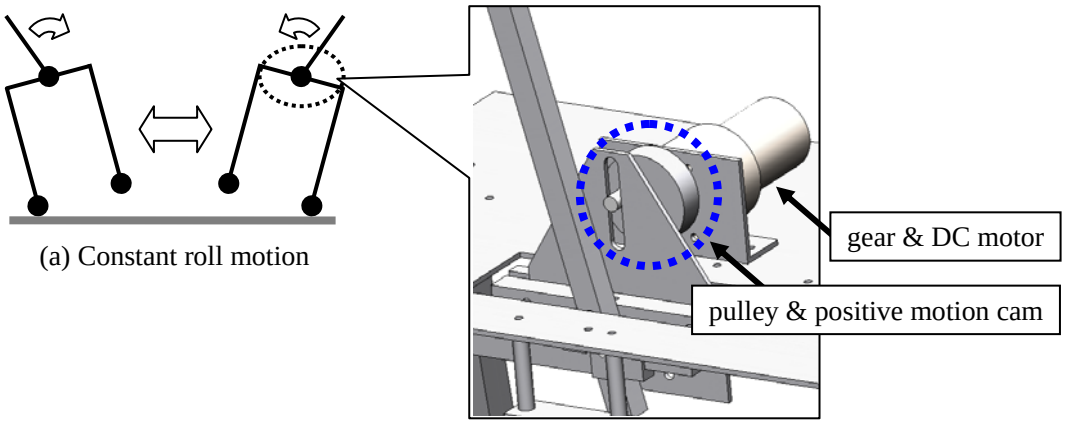

(a) Constant roll motion

(b) Enlarged drawing of a waist joint

Fig. 3 An actuation mechanism made up of an oscillator and a DC-motor.

design guidelines. To verify the basic characteristics of the robot's right and left turn motion, the robot was configured with right and left hips having two degrees of freedom in pitch and yaw motion and waist having one degree of freedom in roll motion actuated by an oscillator, giving it five degrees of freedom so as to maintain a small number of degrees of freedom.

3.1. Roll motion mechanism actuated by upper-body oscillator

We attached an oscillator to the robot's upper body to enable its pendulum motion for generating the roll motion in constant periods which is schematically shown in Figure 3 (a). As shown in Figure 3 (b), we attached a gear head with a gear ratio of 300 to a DC motor (Mabuchi model RS-380PH) to serve as the actuator generating the drive power for the oscillator, and attached the pulley and positive motion cam in order to convert from rotation motion of the motor to repetitive motion of the oscillator. The oscillation period is determined to 1.0 [s] which is approximately twice the step

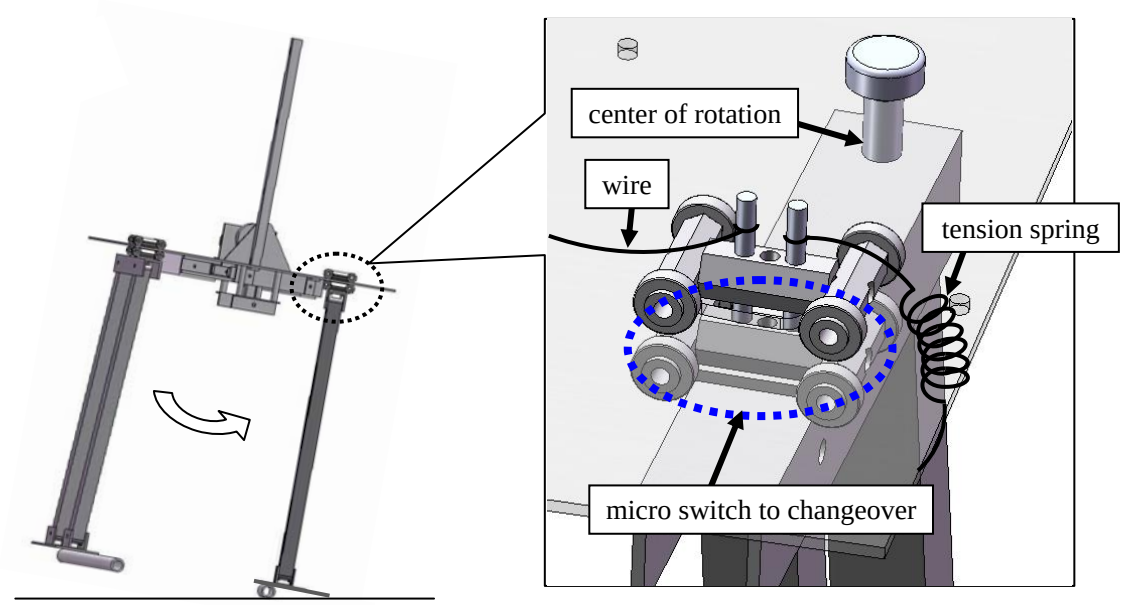

(a) Left turn of yaw motion in frontal view (b) Enlarged drawing of a left hip joint

Fig. 4 Mechanism of the yaw motion control.

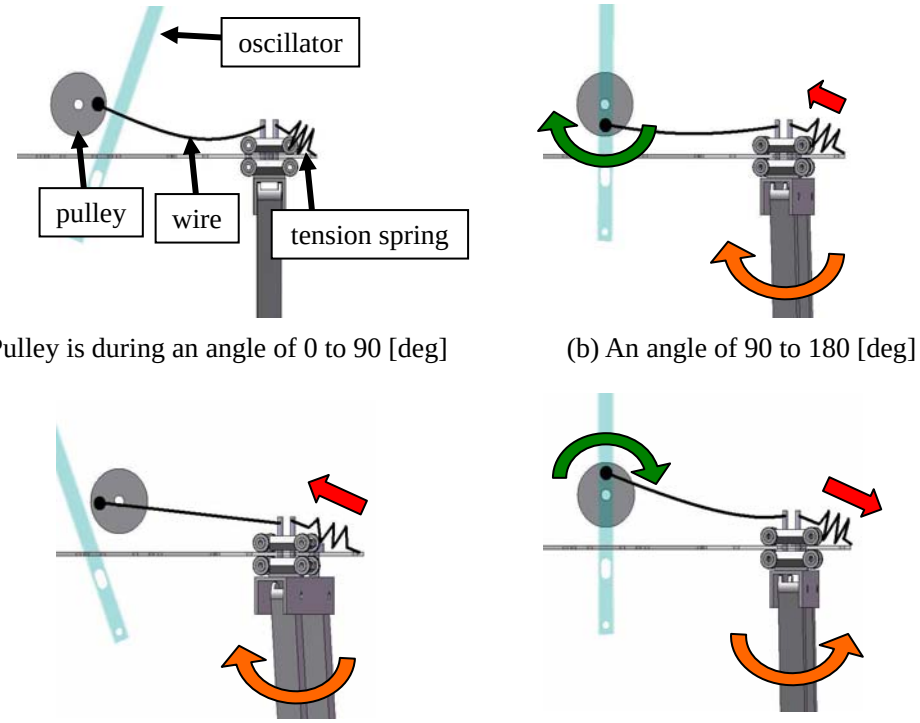

(a) Pulley is during an angle of 0 to 90 [deg] (b) An angle of 90 to 180 [deg]

(c) An angle of 180 to 270 [deg] (d) An angle of 270 to 360 [deg]

Fig. 5 Schematic procedure of one cycle of turning to left with a left leg.

period of un-actuated version of the roll motion $T_f\ (\cong 0.53[s])$.

3.2. Yaw motion mechanism of stance leg for turn operation

Figure 4 shows the yaw motion generation mechanism that we attached to a left leg to achieve

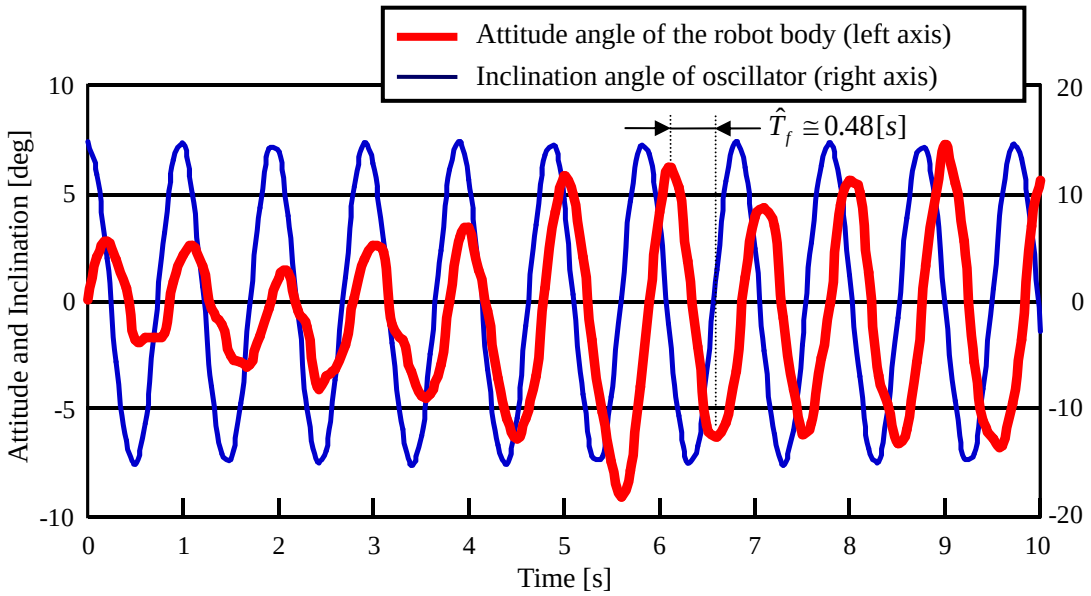

Fig. 6 Experimental result of a stable gait and it's verification of step period of roll motion.

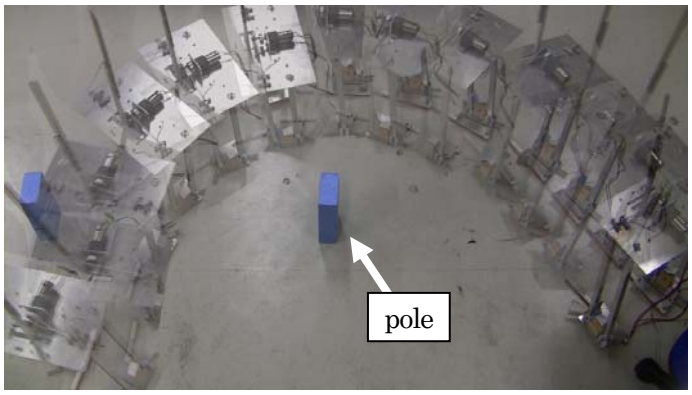

Fig. 7 Sequential photographs of a walking gait on the route (a).

the case of a left turn operation. The left leg is rotated around the center of rotation shown in the figure 4(a), and it generates the yaw motion of whole body of the robot. In order to synchronize this yaw motion to the constant roll motion driven by the upper body oscillator, the pulley attached on the gear head shown in Figure 3 (b) link to a wire with a pin on the changeover micro switch shown in Figure 4 (b). To turn back the yaw motion, the other side of the pin on the changeover switch is attached to a tension spring linked to the edge of the body.

Figure 5 shows the front view of the left leg, which is the case of the left turn to describe one cycle of a turn operation. In order to rotate the leg, the inside pin attached on top of the leg is connected to the pulley by a wire. In order to reverse the leg, the outside pin is connected to the tension spring linked to the edge of the body. The cycle starts with the left leg making contact with the ground, when the pulley's angle is during from 0 to 90 degrees as shown in Figure 5 (a). During the stance-leg phase of the left leg shown in Figures 5 (a)–(c), the turn mechanism is pulled by a string as the pulley rotates to 270 degrees. This pulling process makes the stance-leg rotated right direction which is equivalent to the body's yaw motion rotated left direction. In Figure 5 (c), the left leg starts to leave the ground around 270 degrees of pulley's angle. Next the string is loosened as the pulley rotates until the operation returns to the state of 360 degrees of pulley's angle shown in Figure 5 (d). The tension spring installed on the edge pulls the left leg back to reverse direction and returning to its original state shown in Figure 5 (a). The left turn of a constant angular velocity is

achieved by repeating this operation. To generate a right turn operation, the same movement is performed on the right leg.

4. Experiment

4.1. Straight-line walking test

The behavior of the actuated version of the robot is slightly different from the purely passive version of the robot presented in section 2. Due to forced vibration of the oscillator on the upper body, the oscillation period of roll motion is deviated and the center of gravity point of whole body is fluctuated. These deviations are likely to disturb the stable gait of passive walking. To keep the stable waking of the actuated robot, we adjust the step period of roll motion T_f by adding an auxiliary mass m_a to the top of the oscillator for the sake of convenient design and construction. We carefully observe stable walking situations starting from a state without an auxiliary mass and gradually adding more auxiliary mass in increment of 50[g] to determine an appropriate value of m_a by trial-and-error method. Our testing showed that an auxiliary mass of 150[g] resulted in the motion having the roll motion period T_f and the swing leg motion period T_s approximately synchronized, achieving stable continuous walking. The time histories of the attitude angle of the robot body and the inclination angle of oscillator are measured, the results obtained from this testing are shown in Figure 6. The step period of the actuated version of the roll motion is $\hat{T}_f \cong 0.48[s]$ is about 9% smaller than the un-actuated version. This error between the experimental and theoretical value are mainly assumed to be caused by following two factors. First is because that the rotation angle is beyond over a small range of linearity and linearity assumption in equation (4) is not guaranteed. Second is affected by deformation of the plastic rod and small plates which are attached under the each sole of the foot (see Figure 2(b)) in order to achieve a stable gait. These factors are not taken into consideration in equations of motion and further study is required.

4.2. Direction control example of turn operation

Walking ability of right and left turn are tested for two types of walking route which the instructions are described as follows, and evaluated these turn performance.

(a) Firstly walk along straight-line, secondly turn left, and lastly walk along straight-line again.

(b) Turn right and left (S-shaped route) are repeated several times.

Figure 7 shows sequential photographs of a walking test on a type (a) route. The walking robot could achieve a turn radius of 650 mm as the mean value of several trials of stable walking. This length is similar to the height of the experimental robot 600 mm tall.

5. Conclusion

We presented an experimental robot that can walk on a flat surface through 3D quasi-passive dynamic walking and can perform turn operations by having a simple turn control mechanism mounted on it. The robot achieved stable, continuous walking on flat surface in experimental walking tests. We also tested the robot's right and left turn operations by toggling the abovementioned switch and verified the effectiveness of the robot's turn performance. We found out that our robot with turn mechanism has these characteristics,

(a) Simple mechanism; turning operation can change by one micro switch,

(b) Only one actuation; one actuation source by synchronizing yaw and roll motions.

We also found out that our future works remain as follows,

(a) Improve performance of stability and velocity of straight walking,

(b) Propose the mechanism to change the turn radius of curvature.

References

[1] T. McGeer, "Passive dynamic walking", International Journal of Robotics Research, Vol. 9, No. 2 (1990) pp. 62-82.

[2] S. Collins, A. Ruina, R. Tedrake and M. Wisse, "Efficient bipedal robots based on passive-dynamic walkers", Science, Vol. 307, No. 5712 (2005) pp. 1082-1085.

[3] A. Goswami, B. Thuilot, and B. Espiau, “Compass-like biped robot-part I: stability and bifurcation of passive gaits”, Technical Report 2996, INRIA (1996).
[4] M. Garcia, A. Chatterjee, A. Ruina, and M. Coleman, “The simplest walking model:stability, complexity, and scaling”, Journal of Biomechanical Engineering, Vol. 120, No.2 (1998), pp. 281-288.
[5] K. Osuka, “Passive Dynamic Walking as base of Walking Mechanics” (in Japanese), Systems, Control and Information, Vol. 49, No. 10 (2005) pp. 393-398.
[6] M. J. Coleman and A. Ruina, “An uncontrolled walking toy that cannot stand still”, Physical Review Letters, Vol. 80, No. 16 (1998), pp. 3658-3661.
[7] Y. Ikemata, A. Sano and H. Fujimoto, “Robust Passive Walking Based on a Global Stabilization Principle of Fixed Point”, Vol. 26, No. 2 (2008), pp. 178-183.
[8] S. Collins, M. Wisse and A. Ruina, “A three-dimensional passive-dynamic walking robot with two legs and knees”, International Journal of Robotics Research, Vol. 20, No. 7 (2001) pp. 607-615.
[9] M. Wisse and R. Q. vander Linde, “Delft Pneumatic Bipeds”, Springer-Verlag (2007).
[10] A. D. Kuo, “Stabilization of lateral motion in passive dynamic walking”, International Journal of Robotics Research, Vol. 18, No. 9 (1999) pp. 917-930.
[11] M. Wisse, A. L. Schwab and R. Q. vander Linde, “A 3D passive dynamic biped with yaw and roll compensation”, Robotica, Vol. 19, (2001) pp. 275-284.
[12] R. Tedrake, T. W. Zhang, M.-F. Fong and H. S. Seung, “Actuating a simple 3D passive dynamic walker”, Proceedings of the IEEE International Conference on Robotics and Automation, Vol. 5 (2004) pp. 4656-4661.
[13] T. Narukawa, K. Yokoyama, M. Takahashi and K. Yoshida, “Design and construction of a simple 3D straight-legged passive walker with flat feet and ankle springs”, JSME Journal of System Design and Dynamics, Vol. 3, No. 1 (2009) pp. 1-12.
[14] M. Haruna, M. Ogino, K. Hosoda and M. Asada, “Yet another humanoid walking - passive dynamic walking with torso under simple control” (in Japanese), Proceedings of the 2001 IEEE/RSJ International Conference on Intelligent Robots and Systems (2001) pp. 259-264.
[15] T. Kinugasa, T. Haji, M. Iribe, T. Kobayashi, S. Fujimoto and K. Yoshida, “3-D Passive Dynamic Walker Made of Cardboard for Robot Education” (in Japanese), Journal of the Robotics Society of Japan, Vol. 31, No. 2 (2013) pp. 154-160.

Recent Progress In The Intense Pulsed Power Generator "Etigo-Ii"

Kenji Kashine[1]*, Takashi Kikuchi[2], Toru Sasaki[2], Ryota Hayashi[2], Fumihiro Tamura[2], Arata Watabe[2], Takahiro Kudo[2], Tsukasa Aso[2], Kazumasa Takahashi[2], Nob. Harada[2], Weihua Jiang[2], Akira Tokuchi[3]

[1)] Yuge National College of Maritime Technology, 1000 Yuge, Kamijima 794-2593, Japan
[2)] Nagaoka University of Technology,1603-1 Kamitomioka-cho, Nagaoka 940-2188, Japan
[3)] Pulsed Power Japan Laboratory Ltd., Kusatsu 525-0027, Japan
and Nagaoka University of Technology, Nagaoka 940-2188, Japan
**E-mail: kashine@mech.yuge.ac.jp*

This paper reviews the application study using the intense pulse generator ETIGO-II in Nagaoka University of Technology.
The nominal voltage specifications of ETIGO-II are 1 MV, 50 ns (FWHM), and capable load current is up to 1 MA.
Using this particular and unique pulse generator, we study the several applications such as the intense pulsed ion beam and electron beam technologies.
Moreover, we have been working on the preliminary studies of Inertial Confinement Fusion (ICF).
In this paper, we introduce the flyer acceleration and high pressure generation by using the ablation plasma which is generated by the intense pulsed ion beam.
In addition, we introduce the study on the volumetric warm dense matter (WDM) of foamed metal using the ETIGO-II.

1. Introduction

In a nuclear fusion power plant, inner protective walls of the reactor chamber are exposed to the several radiations such as the alpha particles, X-ray and the high energy plasmas. Therefore, the materials of the inner protective wall are under extremely high temperature condition. To secure the fusion reactor safety, researching the material characteristics under the high energy plasma condition are important.

When an intense pulsed ion beam or electron beam irradiates a solid target, the beam energy deposits a target material within a depth of the range. Therefore, the surface of the solid targets is evaporated to high temperature and density ablation plasma in less than 100 ns [1]. Using this high temperature ablation plasma, we can research on the characteristics of the materials used for the inner protective wall of the reactor chamber.

In addition, the ablation plasma has very high pressure that pushes the target toward the opposite direction of the plasma expansion. Due to the high energy density of the plasma, its pressure may exceed GPa [2-3]. This pressure and impact on solid target have many interesting physical issues especially in material applications [4-6].

The intense pulsed generator ETIGO-II was constructed at the Nagaoka University of Technology. The nominal voltage specifications of ETIGO-II are 1 MV, 50 ns (FWHM), and capable load current is up to 1 MA. This facility can generate the positive or negative single pulse, so we can treat the ion beam or electron beam by changing the diode which is located at the load section of ETIGO-II.

This paper consists of 5 sections. The constructions and specifications of ETIGO-II are pointed out in section 2. The ion beam applications, especially the foil acceleration are described in section 3. The pulse-heating applications which have been researched in our laboratory are discussed in section 4. Section 5 is the summary of this paper.

2. Pulse generator ETIGO-II

The pulse generator ETIGO-II has been operated at the Extreme Energy-Density Research Institute (EDI) in Nagaoka University of Technology.

Figure 1 shows the photograph and cross sectional view of ETIGO-II. The energy storage capacitor (ESC) to impedance conversion line (ICL) is coaxial structure with the water dielectric. The Marx generator, with a stored energy of 160 kJ, produces a high voltage pulse of 3 MV for about 1 μs. A 12-channel water gap switch is used to decrease the inductance. Using an impedance conversion line, for conversion from 1.7 Ω to 6.5 Ω, a high voltage pulsed power output was achieved with a voltage of ~3 MV, current of ~460 kA, pulse width of ~50 ns (FWHM), and energy of ~70 kJ.

Unfortunately, this facility was damaged by the earthquake in 2004 (Chuetsu earthquake). After this disaster, we fixed the whole devises and system of ETIGO-II, and the impedance conversion line was changed from 6.5 Ω to 1.7 Ω. The present nominal specification is 1 MV, 590 kA, 50 ns (FWHM). The polarity of pulse can be changed easily, so we are able to treat the ion beam diode and electron beam diode, respectively.

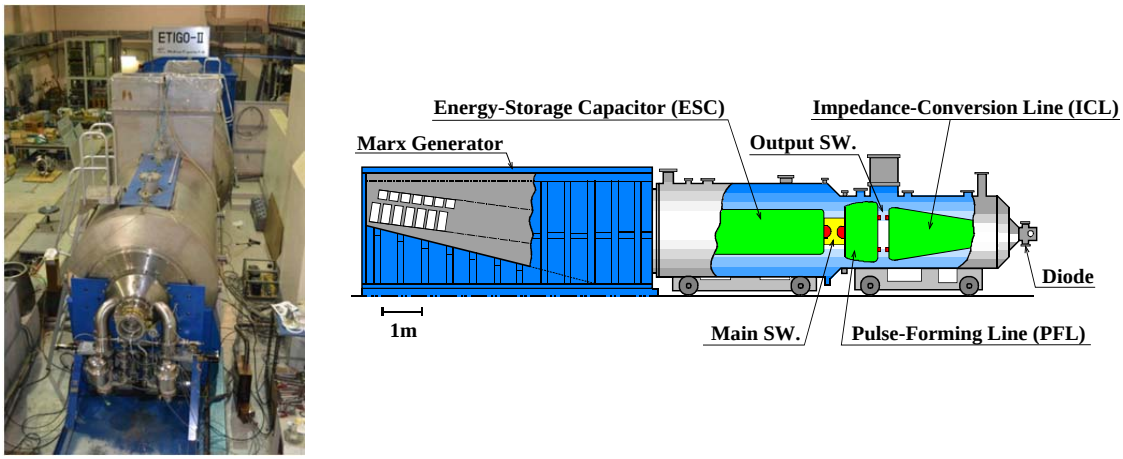

Fig. 1 The photograph and cross sectional view of ETIGO-II.

3. Ion beam application

Intense pulsed ion beams have been found to be very efficient in producing high-density ablation plasma. Using this ablation plasma, we can carry out a variety of applications, such as the preparation of thin films and the synthesis of ultrafine nano-size powders [7-8]. In this paper, we pick up the foil acceleration experiment by using the magnetically insulated ion beam diode (MID) [9].

The configuration of a MID is shown in Figure 2. The MID consists of an anode with thin polyethylene sheet on the surface as an ion source, and a cathode that has slits over the area that faces the anode. The cathode serves as the one-turn coil to generate the insulation magnetic field as well. Before the high voltage pulse is applied between the electrodes, a current was driven through the cathode that generates a magnetic field between the anode and the cathode. This magnetic field is high enough to prevent electron from crossing the diode gap even at the peak diode voltage. As a result, the energy fed to the diode can efficiently be used to accelerate the ion beam that is extracted from the diode region through the cathode slits. The generated ion beams are practically made of proton. The ion beam energy density of MID is ~100 J/cm^2 at the beam focusing point.

In the foil acceleration experiment, an aluminum foil target was used. Experimental set up of the foil acceleration which use the MID is shown in Figure 3. The specification of the aluminum target is 10 x 10 mm and thickness of 50 μm. The target was set behind the aperture (φ7 mm) located at the beam focusing point. The target which would become the flyer was observed by the high speed camera.

Figure 4 shows the high speed photographs for target with thickness of 50 μm. The flight distance of flyer was 5 mm and the time of inter flame was 500 ns. From this observation, we obtained the velocity of flyer was ~1.7 km/s in maximum. Supposing the flyer had a constant acceleration, the ablation pressure was estimated to be 0.4 GPa at the instant of beam irradiation.

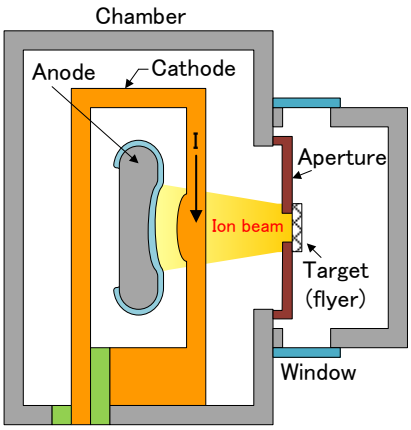

Fig. 2 Configurations of a MID.

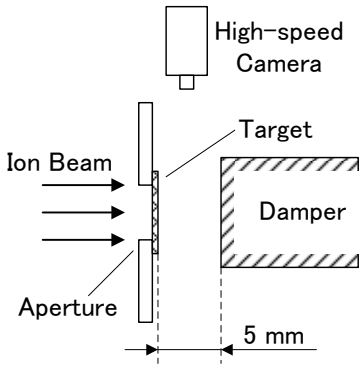

Fig. 3 Experimental set up of the foil acceleration.

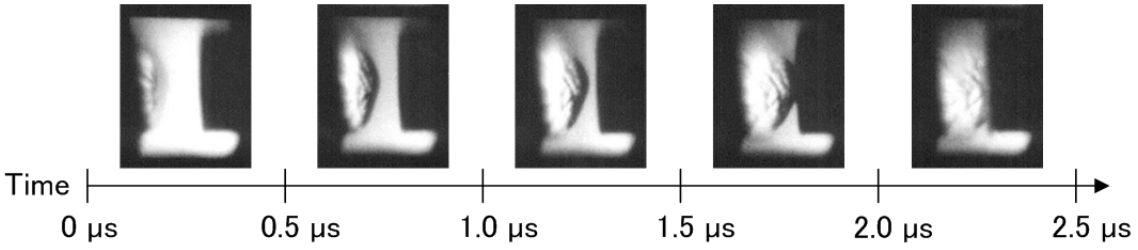

Fig. 4 High speed photographs for target with thickness of 50 μm.

To increase the velocity of the flyer, we experimented with a 2-layer target. In this experiment, the gold was coated on the aluminum target with the thickness of 50 μm by a sputtering device. The thicknesses of the gold coating were 0.5 μm, 1.0 μm, 1.5 μm and 2.0 μm. The MID diode was used and the beam energy density was 120 J/cm^2. Figure 5 shows the average velocity of the flyer as a function of gold thickness. From Fig.5, we see that the average foil velocity of 2.1 km/s is achieved at a gold thickness of 1.5 μm. This velocity is about 20% higher than that of non-coated target. The results were explained as follows.

When the pulsed ion beam was irradiated to the target, the target is separated into two parts. One is the ablation plasma which is produced by the deposition of the incident beam energy within the short range inherent to the ion beam in solids. The other part is a flyer above the range. The equations of momentum and energy conservation can be written as

$$m_1 \cdot v_1 = m_2 \cdot v_2 \qquad (1)$$

$$\frac{1}{2} m_1 \cdot {v_1}^2 + \frac{1}{2} m_2 \cdot {v_2}^2 = \mathrm{E} \qquad (2)$$

Here, m_1 is the mass of the ablation part, m_2 the mass of the flyer, v_1 the velocity of the ablated part, v_2 the velocity of the flyer, and E the energy of the irradiated beam. From these equations, we obtained the following equation.

$$v_2 = \sqrt{\frac{2E}{m_1+m_2} \cdot \frac{m_1}{m_2}} \qquad (3)$$

This equation suggests that the flyer velocity increases with increasing the mass of the ablated

part, and that the peak point appears at a certain value of m_1. In our experiments, the ablated part is practically gold which the mass is heavier than that of flyer. Thus, it has been found that the foil velocity is enhanced by the heavier element coated on the lighter target such as aluminum.

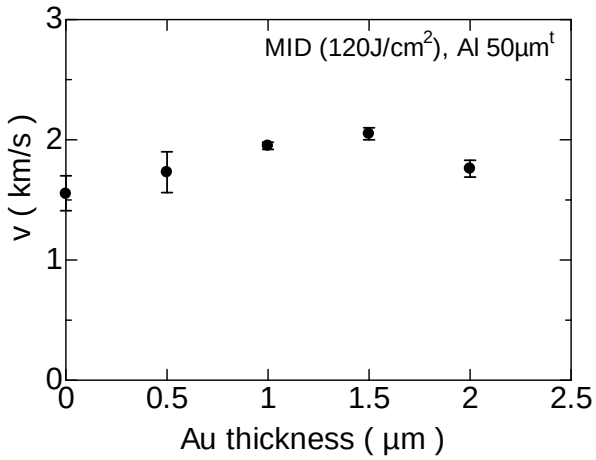

Fig. 5 Average velocity of the flyer as a function of gold thickness.

4. Recent study using the ETIGO-II

The main characteristic of the ETIGO-II is treating the amount of pulse current which exceeds several hundreds of kiro-amperes in a hundred nano-seconds. Therefore, this device can be used not only for generating the particle beams but also for heating by the pulsed current for conductor load.

In the inertial confinement fusion (ICF), a foamed material is used for an ablator layer and an X-ray converter in a fuel target [10-11]. The foamed material becomes plasma through the warm dense matter (WDM) state during the implosion process [12].

Investigating the characteristic of WDM state is necessary for the numerical simulation in the implosion process of the ICF study. In the measurement of the WDM of foamed material in implosion process, the temperature increases up to 10^5 K with a few 10 ns is required [13]. In this study, we generate the volumetric WDM of foamed metal using an ETIGO-II in short time, and the input energy is controlled by the electron beam diode.

Figure 6 shows the arrangement of the load section for the WDM generation. This experiment is underway. A sample of the foamed metal is setting between the center feeder and electron beam diode. The foamed metal is packed into a hollow sapphire capillary (φ5mm x 10mm).

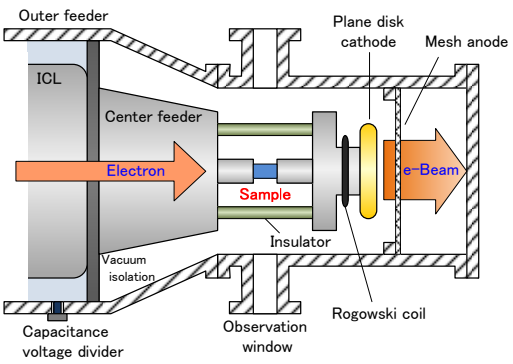

Fig.6 Arrangement of the load section for the WDM generation.

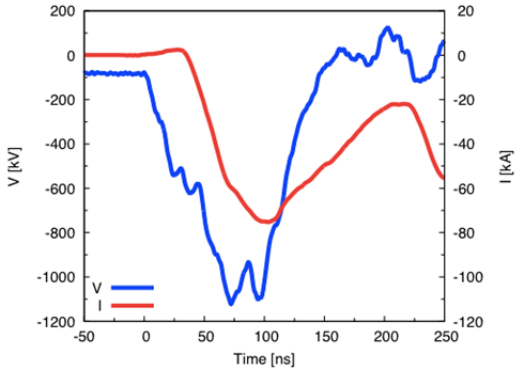

Fig. 7 Typical output waveforms of load section.

To estimate the input energy for the foamed metal, the electron beam diode was used as the

terminal without sample of foamed metal. The electron beam was generated by using the disk cathode and mesh anode. The capacitance voltage divider was used for measuring the output voltage. The Rogowski coil was used for measuring the output current. To suppress the electrical breakdown, the inner pressure of the diode chamber was around 10^{-2} Pa.

Figure 7 shows the typical output waveforms of load section using the electron beam diode which gap distance was 50 mm. The pulse width was ~100 ns, and the peak voltage and current were -1.1 MV and -70 kA, respectively. Using these waveforms, the peak power and input energy for the foamed metal up to 50 ns were estimated to be ~10 GW and ~300 J. In the numerical simulations, the temperature increase of the foamed metal of copper was estimated to be 4500 K up to 50 ns [14]. This result indicates that ETIGO-II can generate WDM of foamed metal to the extent comparable to the implosion timescale in ICF.

5. Conclusion

We presented the result of a various studies by using the pulse generator ETIGO-II.

In the ion beam application, the foil acceleration experiment was carried out. With ion beam energy density of 100 J/cm^2, the aluminum foil target was accelerated to the velocity of ~1.7 km/s by the pressure of ablation plasma. The estimated ablation pressure is 0.4 GPa at the condition of constant acceleration. At an instant of beam irradiation, we consider that the rapid velocity change had been occurred. To estimate the realistic ablation pressure, we need a detailed observation.

To increase the velocity of the flyer, the 2-layer target which the thin layer of gold was coated on an aluminum target was used. The velocity of the 2-layer target is about 20% higher than that of non-coated target. These studies have made a significant contribution to a shock-induced experiment such as a meteor's collision.

In the recent application using ETIGO-II, we presented the pulse heating experiment for WDM study. To control the heating current, the electron beam diode was used. The input energy for the foamed metal was estimated by the output waveforms of diode voltage and current. Using these waveforms, the peak power and input energy for the foamed metal sample until 50 ns were estimated to be ~10 GW and ~300 J. In the numerical simulations, the temperature increase of the foamed metal of copper was estimated to be 4500 K up to 50 ns. This result indicates that ETIGO-II can generate WDM of foamed metal comparable to the implosion timescale in ICF.

Acknowledgments

This work was supported from the Grant-in-Aid for Scientific Research from the MEXT, Japan, and by Program for High Reliable Materials Design and Manufacturing in Nagaoka University of Technology.

References

[1] K. Yatsui, Laser & Part. Beams, **7** (1989) 733.
[2] N. Harada, H. Shinkai, W. Jiang and K. Yatsui, Proc. 12th Int. Conf. High-Power Particle Beam, **2** (1998) 1048.
[3] K. Yatsui, H. Shinkai, K. Kashine, W. Jiang, M. Kagihiro and N. Harada, Jpn. J. Appl. Phys., **40** (2001) 955.
[4] Y. Shimotori, M. Yokoyama, H. Isobe, S. Harada, K. Masugata and K. Yatsui, J. Appl. Phys., **63** (1988) 968.
[5] K. Kashine, T. Suzuki, H. Suematsu, W. Jiang, K. Yatsui and Y. Tanabe, Trans. MRS-J, **28** (2003) 417.
[6] K. Kashine, H. Suematsu, W. Jiang and K. Yatsui, Trans. IEEJ, **124** (2004) 47.
[7] K. Yatsui, X. D. Kang, T. Sonegawa, T. Matsuoka, K. Masugata, Y. Shimotori, T. Satoh, S. Furuuchi, Y. Ohuchi, T. Takeshita and H.Yamamoto, Phys. Plasmas, **1** (1994) 1730.
[8] K. Yatsui, C. Grigoriu, H. Kubo, K. Masugata and Y. Shimotori, Appl. Phys. Lett., **67** (1995) 1214.

[9] K. Yatsui, A. Tokuchi, H. Tanaka, H. Ishizuka, A. Kawai, E. Sai, K. Masugata, M. Ito and M. Matsui, Laser & Part. Beams, **3** (1985) 119.
[10] S. Atzeni and J. Meyer-ter-vehn, "The Physics of Inertial Fusion: Beam Plasma Interaction, Hydrodynamics, Hot Dense Matter" (Oxford Univ. Press, N.Y.), Chap. 9. (2004)
[11] Y. Iizuka, S. Kawata, T. Kodera, A. I. Ohoyski, T. Kikuchi, NIMA, **606** (2009) 165.
[12] R. P. Drake, Phys. Plasmas, **16** (2009) 055501.
[13] T. Kikuchi, T. Someya, S. Kawata, IEEJ Trans. FM, **125** (2005) 515.
[14] R. Hayashi, K. Kashine, A. Tokuchi, T. Sasaki, T. Aso, T. Kikuchi, W. Jiang, and Nob. Harada, EAPPC 2012 / BEAMS 2012, (2012) P2D-10.

(Received: 23rd June, 2013, Accepted: 15th October, 2013)

An Assessment of Radionuclide Transport in the Atmosphere A Case Study of Hypothetical Reactor Accident in Ninh Thuan Province, Vietnam

Ho Quoc Dung[1,*], **Mikami Yoshiki**[1]
[1)]*Nagaoka University of Technology, 1603-1 Kamitomioka-cho, Nagaoka 940-2188 Japan*
**E-mail: hoquocdung@gmail.com*

Vietnamese government has a nuclear energy program with the goal of building 14 units of nuclear power plants (NPPs) by 2030. The implementation of long-term nuclear energy program in Vietnam opens up many challenges such as the legal and technical infrastructure, human training and management skill, nuclear safety and security. Recently, Fukushima nuclear accident in Japan has raised the international public concern about nuclear safety issue in many countries, especially for a newcomer like Vietnam.

, estimating the consequence of severe nuclear reactor accident is currently the most common and essential part for estimating these consequences and for proposing the policies to protect the public health and safety.

One of the first stages in PCA scheme is to analyze the early radionuclide doses that cause harm to human health. An assessment of early dose of a severe nuclear accident starts with identifying an accident scenario and estimating the transport of radioactive materials to the atmosphere combining with meteorological conditions at the release time. In this research, a simulation model, namely, Simplified Wind Transport Model (SWTM) is proposed to estimate the transport of radioactive materials based on the historical wind data collected in Ninh Thuan meteorological station. This model can simulate the centerline of the radionuclide plume during transport process in the atmosphere. Based on that, the areas that will be affected by radioactive materials in case of NPP accident can be predicted.

The results of this assessment are the quantitative distribution of radionuclide to the public at a certain area. This result is the practical information for the local government to create emergency plan to protect the public in case of accidental releases of radionuclide materials to the environment.

1. Introduction

Vietnamese government has a nuclear energy program with the goal of building 14 reactor units by 2030. The implementation of long-term nuclear energy program in Vietnam opens up many challenges such as the legal and technical infrastructure, human training and management skill, nuclear safety. For prevention and mitigation the consequences of a severe nuclear reactor accident, Probabilistic Consequence Assessment (PCA) is currently the most common and essential tool for estimating the consequences of nuclear accidents and for proposing the policies to protect the public health and safety[1].

PCA models are an integral part of Level 3 Probabilistic Safety Assessment of nuclear installations. They are used to assess the consequences of potential accidental releases to the atmosphere, taking into account the range of environmental conditions at the time of the accident and the probability associated with these conditions. These methods describe the behavior of radioactive material through the environment following a release to the atmosphere and calculate the subsequent dose distributions and health effects in the population [2].

Radionuclide released to the atmosphere as a fine aerosol or gas will create a plume which is carried downwind. During this transport process, it expands horizontally and vertically owing to diffusion and turbulent eddies in the atmosphere. Both transport and diffusion processes are called as "dispersion". The starting point of a consequence assessment is modeling the behavior of radionuclide released in the atmosphere. In this step, the radionuclide concentration profiles (crosswind and vertical) and downwind transport of the dispersing plume evaluation are needed. The atmospheric dispersion models are used to estimate or to predict the downwind concentration of radionuclide from accidental NPP. Currently, the most commonly used dispersion models are Gaussian-plume models which are based on mathematical approximation of plume behavior. The Gaussian-plume formulae are derived assuming 'steady-state' conditions. That is, the Gaussian-plume dispersion formulae do not depend on time, although they do represent an ensemble time average. The meteorological conditions are assumed to remain constant during the dispersion from source to receptor, which is effectively instantaneous. Emissions and meteorological conditions can vary from hour to hour but the model calculations in each hour are independent of those in other hours. Due to this mathematical derivation, it is common to refer to Gaussian-plume models as steady-state dispersion models. However, because they incorporate a simplistic description of the dispersion process, and some fundamental assumptions are made, the results by Gaussian-plume may not accurately reflect reality. These formulae provide a better representation of reality if conditions do not change rapidly within the hour being modeled (i.e. conditions are reasonably steady and do not deviate significantly from the average values for the hour being modeled). Therefore, these models should only be applied under certain conditions.

More recently, better ways of describing the spatially varying turbulence and diffusion characteristics within the atmosphere have been developed. The new generation dispersion models adopt a more sophisticated approach to describe diffusion and dispersion using the fundamental properties of the atmosphere rather than relying on general mathematical approximation. This enables better treatment of difficult situations such as complex terrain and long-distance transport. These advanced dispersion models maybe grouped into three categories (Particles, Puffs, and Grid Points) depending on the way the air pollutants are represented by the model [3]. Particle models represent the pollutant release as a stream of particles, which are transported by the model winds and diffuse randomly according to the model turbulence. Particle models are computationally expensive, needing at least 10^5 particles to represent a pollutant release, but may be the best type to represent pollutant concentrations close to the source. The random walk is applied for each particle in three-dimension space. The simulation of more than 10^5 particles takes the highest computational expenditure in comparison with the other model. However, this model simulates atmospheric dispersion similar with the behavior of radionuclide release to the atmosphere. Therefore, the output of particle model is very close to the real radionuclide released. In Puffs model, pollutant releases can also be represented by a series of puffs, which are also transported by the model winds. Each puff represents a discrete amount of pollution, whose volume increases due to turbulent mixing Each puff simulate the air dispersion as the Gaussian shape. In other words, each puff simulates air dispersion like Plume model. The computational expenditure for Puff models is normally higher than 5 to 10 times compared with Plume model. It depends on the times of changing weather condition in releasing period. Puff models are far less computationally expensive than particle models, but are not as realistic in their description of the pollutant distribution. Grid Points model simulates the concentration of pollutant on a (regular) three-dimensional grid of points. This is the cheapest formulation computationally, but difficulties arise when the scale of the pollutant release is smaller than the grid point spacing.

Meteorological data is one of the most important inputs into any air dispersion model. Ground-level concentrations of contaminants are primarily controlled by two meteorological elements: wind direction and speed (for transport), and turbulence and mixing height of the lower boundary layer (for dispersion). The meteorological data requirements for steady-state Gaussian-plume models and advanced dispersion models vary considerably. Steady-state Gaussian-plume models require meteorology data from a single surface station. They assume that the single station data are applicable to the whole modeling domain up to the top of the boundary layer and that conditions do not vary with height. Advanced dispersion models, including Puff, Particle and Grid Points models, allow meteorological conditions to vary across the modeling domain and up through the atmosphere. This is a much more complex situation than for steady-state modeling and thus requires much more complex meteorological data. This includes inputs from surface networks (land and sea) and upper air stations. Because the meteorological data requirements vary greatly between these model types, the choice of which dispersion model to use can depend on questions regarding the expected meteorological conditions.

In four atmospheric dispersion models Gaussian Plume, Grid Point, Puff and Partial model, the output of latter model is the more realistic in determining the air concentration at different critical time, geography and meteorology. Moreover, the later model needs more complexity in computation to calculate the result. The table 1 shows the summary comparison among these models in different aspects.

Table 1 The comparison among Gaussian Plume, Particles, Puffs and Grid Point Models

	Gaussian Plume Model	Grid Points Model	Particles Model	Puffs Model
Computational expenditure	Low	Moderate	Very High	High
Meteorological data	Simple	Complex	Complex	Complex
Meteorological condition	Steady-state	Non-steady-state	Non-steady-state	Non-steady-state
Model result (the output close to the reality)	Lightly Close	Close	Very Close	Close
Impact range	Short range (<50 km)	Long range (>50km)	Long range (>50km)	Long range (>50km)

2. Research Objectives

This research is intended to propose a model for predicting the potential areas that will be affected by radioactive materials in case of hypothetical NPP accident in Ninh Thuan province, Vietnam, based on the situation of meteorological data availability. Currently, there is one surface meteorological station located near Ninh Thuan NPP sites. In this station, the historical meteorological data is the surface meteorological data of single site. It did not collect the upper air (i.e. anything above the height of a tower) meteorological data. Therefore, the available meteorological data lacks some important parameters. In that, the most important lacking parameter is solar radiation parameter that is fundamental for calculating the atmospheric stability class. This is the critical input data for Gaussian Plume Model and others model. Therefore, because of the lacking of meteorological data on Ninh Thuan NPP sites, neither Gaussian-plume model nor any other advanced dispersion models can be used in this case. Moreover, Gaussian-plume models which requires the modest set of input data among these other models, are usually only applicable to near-field (within 50 km from the source) calculations. Meanwhile, this research aims to estimate the affected area in the range of 300 km radius far from the NPP site. Therefore, even the Gaussian plume model is not suitable to apply in this case.

In this research, a simulation model, namely, Simplified Wind Transport Model (SWTM) is proposed to estimate the transport of radioactive materials based on the historical wind data. This model can overcome the limitation on the meteorological data on the investigated NPP site and improve the range of calculation.

SWTM can simulate the centerline of the radionuclide plume during transport process in the

atmosphere. Base on that, the areas that will be affected by radioactive materials in case of NPP accident can be predicted. The results of the assessment by using SWTM are the quantitative distribution of radionuclide to the public at a certain area. This result is the practical information for the local government to create emergency plan to protect the public in case of accidental releases of radionuclide materials to the environment.

3. Data and Methodology

3.1. Research Sites

Ninh Thuan, located in the southern part of Vietnam Central Coastal region, borders Khanh Hoa Province in the north, Binh Thuan Province in the south, Lam Dong Province in the west, East Sea in the East. The province has total natural surface of 3,360 km^2, 7 administrative units including 1 City and 6 districts. The City of Phan Rang - Thap Cham, as provincial City, constitutes a political, economic and cultural center of the province, distant from Ho Chi Minh City by 350 km, from international Cam Ranh airport by 60 km, from the City of Nha Trang by 105 km and from Da Lat by 110 km with favorable conditions for circulations in service of socio-economic development.

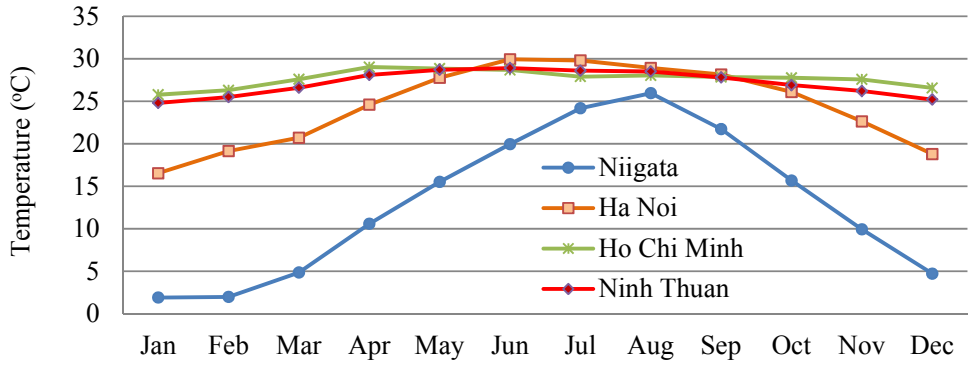

Fig. 1 Monthly mean air temperature

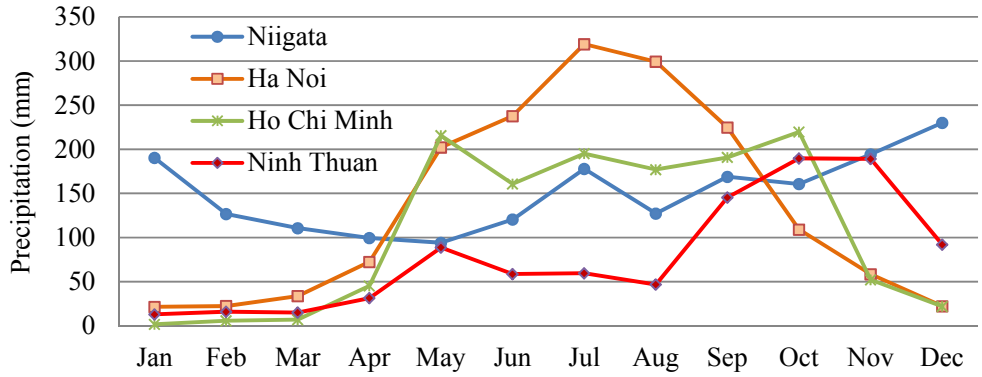

Fig. 2 Monthly total of precipitation

Ninh Thuan has a typically tropical monsoon climate, with the features of draught, heat, much wind, strong evaporation; annual average temperature around 26- 27°C; annual average rainfall of 700-800 mm in Phan Rang City and gradually increasing to more than 1,100mm in mountainous areas; humidity around 75-77%. There are two different seasons: rainy season (from September to November) and dry

season (from December to August). By making a comparison of the monthly temperature and precipitation among Ninh Thuan and other domestic cities (Hanoi in the north and Ho Chi Minh City in the south) and especially with Niigata (where Kashiwazaki, the largest NPP in Japan is located), the overview of Ninh Thuan's geographical features can be clearly represented. It shows that the temperature in Ninh Thuan stays very high while the rainfall level is very low. That explains why Ninh Thuan can be seen as one of the hottest and the driest places in Vietnam.

3.2. Simplified Wind Transport Model

During the NPP accident, radioactive materials released to the atmosphere in unsteady weather condition. The radionuclide plume can divided into a series of radionuclide puffs [4]. Puff initializes a collection of puffs representing a sample of the eruption cloud and calculates transport, turbulent dispersion and fallout for each puff. In Lagrangian form, given a time step Δt, the position vector for each particle is updated from time t to time $t + \Delta t$ by the equation [5]:

$$R_i(t + \Delta t) = R_i(t) + V(t)\,\Delta t + Z(t)\,\Delta t + G_i(t)\,\Delta t \qquad (1)$$

where R_i is the position vector of the i^{th} puff at time t, V is the local wind velocity, Z is a vector representing turbulent dispersion and G_i is the terminal gravitational fallout vector, dependent on the i^{th} puff's size. If the concentration of radionuclide or mass part is not rejected from calculating, the above equation become: $R_i(t + \Delta t) = R_i(t) + V(t)\,\Delta t$. This can calculate the next position of puff according to the shorten formulation and required data is just wind data. Based on the shorten formulation, the Simplified Wind Transport Model (SWTM) is produced to trace the position of released puffs.

The SWTM focuses on simulating the centerline of radioactive material plume under un-steady atmosphere condition. Specifically, SWTM layouts the connection line of the central point of puffs. The released point O is from NPP sites. A distance S_i of radioactive materials moving in the period of time Δt_i under the average wind velocity V_i equals to V_i times with Δt_i ($S_i = V_i \times \Delta t_i$). A wind direction is defined as angle θ_i. A wind vector $\overrightarrow{W_i}$ composes two components: the distance S_i and the moving period Δt_i. Fig. 3 defines an example centerline by Simplified Wind Transport Model, which contains the combination of all wind vectors.

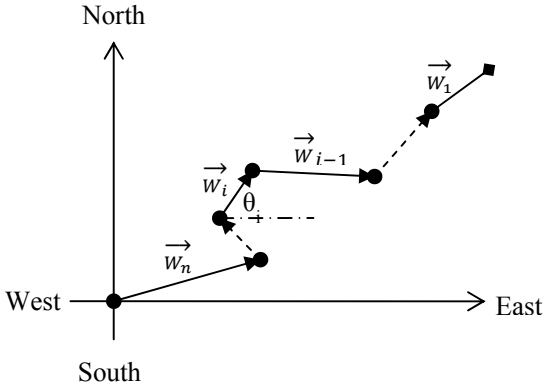

Fig. 3 Example of Simplified Wind Transport Model

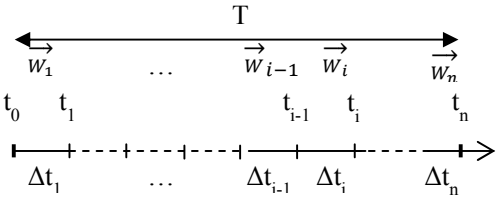

Fig. 4 Conceptual diagram of the discrete time scale and the travel time for the i^{th} wind vector

According to the wind velocity V and wind direction θ (e.g. θ=0 means wind blows from west to

east; θ=90 means wind blows from south to north), the center of the i^{th} released puff reaches:

$$\begin{cases} x_i = V_i \times \Delta t_i \times \cos\theta + x_{i-1} \\ y_i = V_i \times \Delta t_i \times \cos\theta + y_{i-1} \\ z_i = 0 \end{cases}$$

The equation of SWTM is the set of component wind vectors:

SWTM = $\overrightarrow{W_1} + \overrightarrow{W_2} + \cdots + \overrightarrow{W_n}$

The flowchart of simplify wind transport model

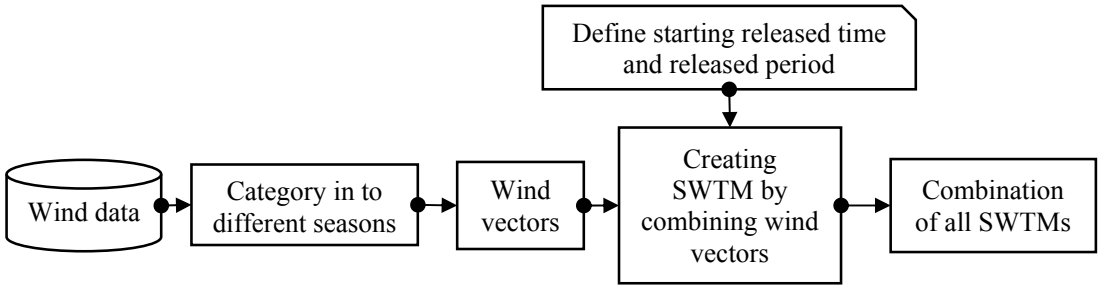

By using SWTM, the endpoint of release puff can be determined after period of time T released of radionuclide. In other words, the boundary area that will be affected by radionuclide material can be detected by the endpoint of SWTM. By combining SWTM at different condition of weather on the whole year, the overview picture about how radionuclide distributed can be determined. Based on the density of endpoint SWTM, each area around the NPP has the different frequency in appearing the endpoints SWTM.

Table 2 The comparison of required meteorological data for SWTM and others

	SWTM Model	Gaussian Plume Model	Grid Points Model	Particles Model	Puffs Model
Simulate the Transport	Yes	Yes	Yes	Yes	Yes
Simulate the Disperse	No	Yes	Yes	Yes	Yes
Surface Meteorological Data					
Wind	Yes	Yes	Yes	Yes	Yes
Rainfall	Yes	Yes	Yes	Yes	Yes
Atmospheric Stability	No	Yes	Yes	Yes	Yes
Upper-air Meteorological Data	No	No	Yes	Yes	Yes

3.3. Data

3.3.1. Seasonal Wind Patterns

Meteorological data is collected from Phan Rang meteorological station, nearby the Ninh Thuan NPP. Based on the statistic of wind, the weekly wind direction pattern in one-year average is created. Fig. 5 shows that from the first week of the year to week 14, and from week 39 to 52, the main wind direction blows from northeast. This time period is named as winter season. From week 20 to 38, the wind is mainly from the southwest direction. It is defined as summer season. One another period is the transition period between winter and summer season from week 14 to week 20. During this period, there is the calm wind and light wind in many directions. It is then classified as season transition period.

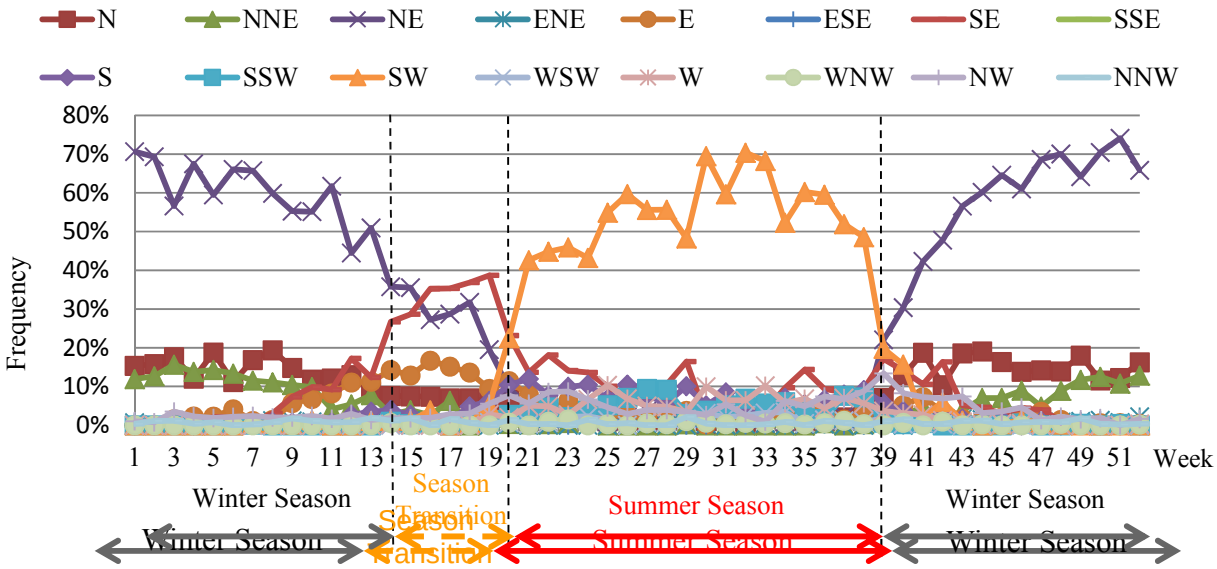

Fig. 5 Weekly Wind Direction Patterns

It is because that the distribution of radionuclide is affected by wind speed and wind direction, the purpose of categorization wind into different seasons is to see more clearly the boundary and the main distribution trend of radionuclide in different period time of a year. Based on the categorization, the first prediction can be derived from the feature of seasons is that the radionuclide transport line will mainly shape on the southwest sector of NPP sites in winter season. In summer season, radionuclide is predicted to release in the northeast of NPP sites. Because of many wind directions with low speed in season transition period, it is predicted that radionuclide will distributed near around NPP sites in case that the accident happens.

3.3.2. Hourly Wind Patterns

The hourly wind direction pattern in one-year average is also created. Basically, wind direction changes to the opposite direction between daytime and nighttime because of the different of heat transferring in land and sea. However, in case of Ninh Thuan, the graph shows that, in winter season, from 6:00 PM to 6:00 AM (nighttime), the main wind direction is northeast and north. In the daytime, the wind direction is not significant different compared with the nighttime.

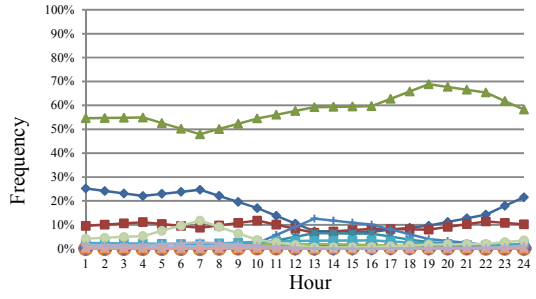

Fig. 6 Hourly Wind Direction in Winter Season

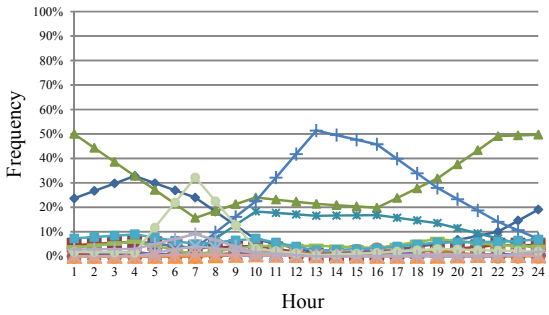

Fig. 7 Hourly Wind Direction in Season Transition Period

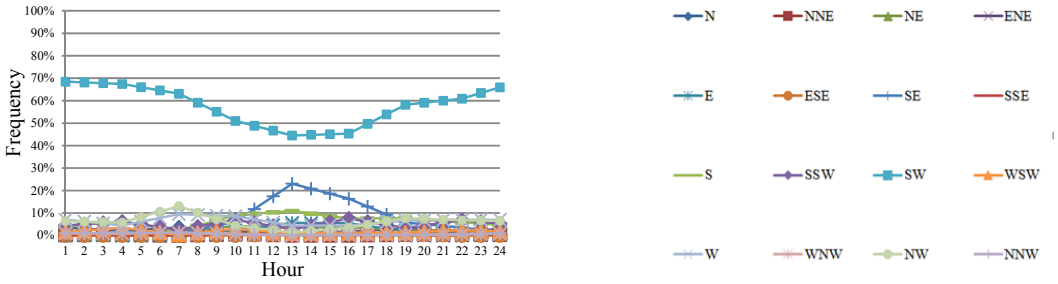

Fig. 8 Hourly Wind Direction in Summer Season

For summer season, for the whole day, the main wind direction is southwest. Besides that, there are some southeast winds at the noontime.

In season transition period, even in daytime or nighttime, there are many wind directions. The wind velocity in this period also is lower than in winter and summer season. Therefore, it is difficult to find the hourly wind pattern in a day average in this period.

4. Application and Discussion

Atmospheric dispersion model can be divided into two parts: transport and disperse part. Currently, Puff model can used to overcome the limitation of Plume model and has it owns advantage features. It is the model represent for traditional atmospheric dispersion model and the advanced dispersion model. Puff model can simulate transport and disperse part. Therefore, the result of this model is not only the transport direction of radionuclide but also the concentration (mass) of radionuclide. This is the advantage of Puff model because it cover all part of dispersion process. However, Puff model result just can be visualized at single weather condition. Other while, the overview picture of how radionuclide released and distributed in one year can be created by combination of many dispersion simulation results at different weather conditions. By using SWTM, the combination of many SWTM result is solved by the set of wind transport vectors. On the other hand, Puff model requires many meteorological indicators that did not collect in Phan Rang meteorological station. By rejecting the disperse part, Puff model becomes SWTM, that can simulate only the transport and the meteorological data requires for this model is wind data. The other meteorological indicators do not need for simulate SWTM such as temperature, rainfall, cloud cover rate, etc. In conclusion, SWTM can overcome the limitation on meteorological data and can combine the set of atmospheric dispersion result to visualize the overview picture of how radionuclide distributed in the whole year.

Based on the hourly wind pattern in daily average, wind pattern in winter and summer seasons can be detected. These patterns can represent for all wind conditions. In this research, one application of SWTM is produced by combine all SWTM endpoints. SWTM endpoint is the final point of released puff, it also the final affected area by radionuclide released. Each SWTM starts at 7AM and the released period time is one day (24 hours). This application can show the boundary distribution of radionuclide in different season of a year.

A hypothetical nuclear reactor acceded assumes that it happens in Ninh Thuan NPP. The figures from 9 to 11 present the distribution of end puff after 24 hours release of radionuclide in the atmosphere by using SWTM with the starting time at 7 AM. The distribution of end puff is represented by plotting in the two-dimensional Cartesian system. The point where the two coordinate axis meet, namely origin, i.e. ordered pair (0,0) represent the location of Ninh Thuan NPP. The color of each scatter point reflects the frequency of end puff reach to each pixel. The lighter color is the lower frequency of puff reach to each pixel. In these figures, each pixel presents for an area of 20km x 20km.

The blue color area shows the safe place that didn't appear any end puffs through the period from

1996 to 2006. During eleven-year period, there are 4020 days; it means that 4020 simulation of SWTM are created to detect the boundary distribution of radionuclide application. The yellow color has the frequency appears of SWTM endpoint from 1 to 9. The red and dark red color has the double and triple frequency compared with yellow color at scale of 10 to 19 and 20 to 29 respectively. The highest frequency of SWTM endpoint is the dark green area with that frequency is higher than 30.

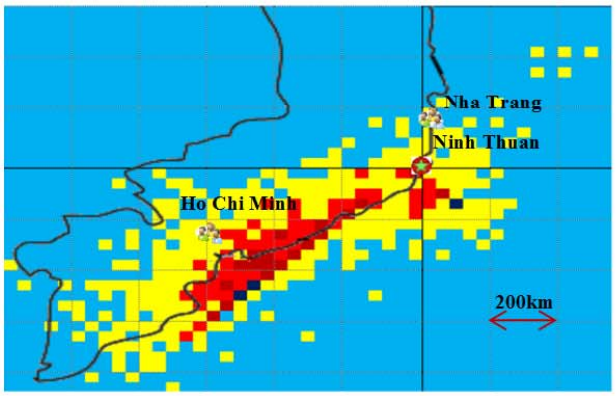

Fig. 9 The distribution of end puff released to the atmosphere after 24 hours in winter season

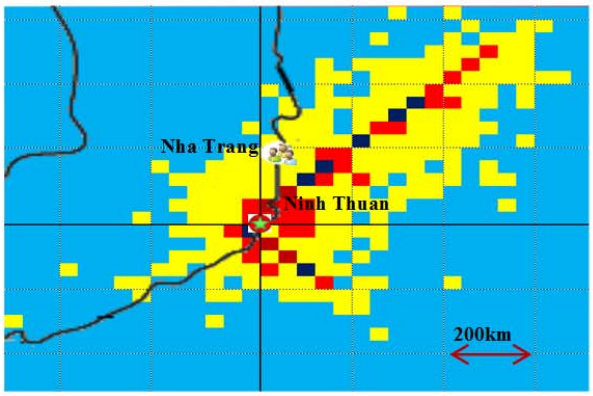

Fig. 10 The distribution of end puff released to the atmosphere after 24 hours in summer season

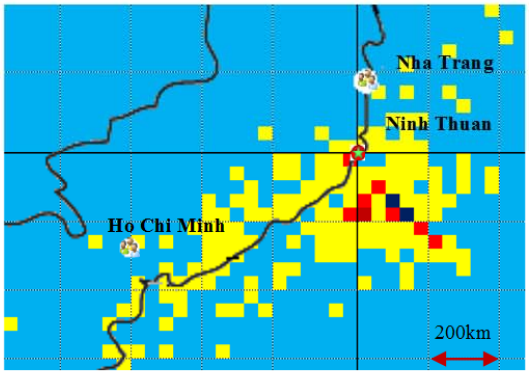

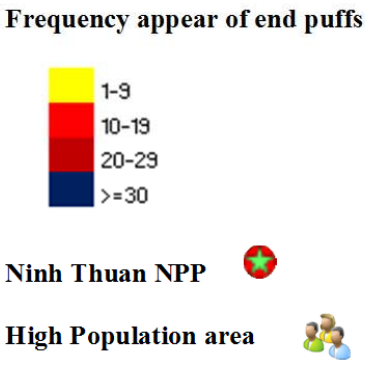

Fig. 11 The distribution of end puff released to the atmosphere after 24 hours in season transition period

Figure 11 shows that, in summer, the end point of radionuclide distributes mainly in the east sea area by the northeast direction. However, the winter season reflects different results. There is a high density of puff ending at southwest area. The southwest area covers the high population density City such as Ho Chi Minh City, Vung Tau City, Can Tho City and Binh Duong… In season transition period, even that there are many different wind directions, the distribution of end puffs are mainly in the sea. However, a small number of puffs can reach to Ho Chi Minh City. In summary, in case that the accident happens, the risk of harm to the public will be lower in summer and season transition period than in winter season.

Simplified Wind Transport Model is proposed to estimate the transport of radioactive materials based on the historical wind data collected in Ninh Thuan meteorological station. This model can simulate the centerline of the radionuclide plume during transport process in the atmosphere. One of the big advantages of SWTM model is that it can be applied even under the limitation of meteorological data. Specifically, only wind data is sufficient as the input data to model the transport of radionuclide. Moreover, the computational requirement is very low. It can quickly simulate thousands of the

radionuclide transport and output the results in a short time. It can solve some of the demerit points of other models, such as the Gaussian-plume model and other advanced dispersion models which require a complex set of meteorological data and take a significant length of time for simulation. The other advantage is the combination feature of SWTM, it is easy to combine the result of thousand SWTM result and visualize it one scatter chart.

However, along with its merit as a simplified and fast simulation model, the limitation of SWTM is that it not take account the dispersion of radionuclide. In case that the complex set of meteorological data is ready, of course, the application of other advanced models should be carried out for the more sophisticated expected results. However, in the opposite situation where the meteorological data is not sufficient, estimating the transport of radioactive materials released to the atmosphere still can be implemented by SWTM. Based on the result of SWTM, the local government will have more evidence to predict the distribution of radionuclide in case of NPP accident, and to identify the period that it is necessary to increase level of accident alarm to the public.

References

[1] Ralph R. Fullwood, "Probabilistic Safety Assessment in the Chemical and Nuclear Industries", ISBN 0-1239-0812-4, pages 1-34

[2] Toshimitsu Homma, Kenichi Tomita and Sinji Hato, "Uncertainty and sensitivity studies with the probabilistic accident consequence assessment code OSCAAR", Nuclear Engineering and Technology, Vol.37, No.3, June 2005

[3] Ministry for the Environment, New Zealand, "Good Practice Guide for Atmospheric Dispersion Modelling", ISBN 0-478-18941-9

[4] Suzanne M. Viessman and Sethu Raman, Atmospheric Environment Vol. 22, No. 5, pages 839-851, 1988

[5] Searcy, C., Dean, K., Stringer, W., 1998, PUFF: A Lagrangian Trajectory Volcanic Ash Tracking Model, Journal of Volcanology and Geothermal Research (80) 1-16

(Received: 23 June, 2013, Accepted: 31 July, 2013)

Investigation of reaction selectivity for oxygen reduction in the presence of methanol at sputtered Co-C-N electrocatalyst

Sayoko Shironita, Yosuke Matsumoto, Minoru Umeda*
Department of Materials Science and Technology, Faculty of Engineering,
Nagaoka University of Technology
1603-1, Kamitomioka, Nagaoka, Niigata 940-2188, Japan
**E-mail: mumeda@vos.nagaokaut.ac.jp*

The mixed reactant direct methanol fuel cells (MRFC) is expected to become one of the smallest fuel cells for mobile electronic applications. For its realization, a reaction selectivity is indispensable for each anode and cathode catalyst, where a methanol-oxygen mixture is fueled. In this study, we prepared a Co-C-N electrocatalyst for an MRFC cathode using a reactive sputtering equipment. The oxygen reduction selectivity of the prepared Co-C-N electrocatalyst was assessed in an acidic solution containing O_2 and CH_3OH. The substrate temperature furing the sputtering deposition was varied from room temperature to 773 K. As a result, the oxygen reduction current increased with an increase in the substrate temperature. The prepared Co-C-N electrocatalyst at 773 K had a high activity and selectivity for the oxygen reduction in the presence of methanol.

1. Introduction

Direct methanol fuel cells (DMFCs) are expected to be highly efficient convertors of chemical energy to electric energy [1-4], and have attracted much attention because of low-temperature operation, small size, and light weight. However, a methanol crossover phenomenon has prevented the practical utilization of DMFCs. This phenomenon causes both a loss of fuel and a decline in power as a result of methanol transmission through the electrolytic membrane from the cathode side to anode side.

Some techniques, such as laminar flow fuel cells (LFFC) [5], FlowCath® technology [6], and mixed reactant direct methanol fuel cells (MRFC) [7-9], have been developed to solve this problem of methanol crossover. In particular, the MRFC utilizes a methanol and oxygen mixture as fuel without a separator, thereby solving the issues of fuel loss and power decline. Additionally, the removal of the separator is an effective way to reduce the weight and size of the fuel cell. However, in order to facilitate the practical utilization of MRFCs, it is important for the electrocatalysts to have methanol oxidation selectivity at the anode and oxygen reduction selectivity at the cathode.

Thus far, Pt-based catalysts have been widely used for the anode and cathode of DMFCs because of their high catalytic activities for both oxygen reduction reaction (ORR) and methanol oxidation reaction (MOR). However, in the presence of both methanol and oxygen, the methanol oxidation current and the oxygen reduction current mix, which results in a reduction of power generation. It is therefore necessary to develop electrocatalysts that have selectivity for the MOR at the anode and for the ORR at the cathode of the MRFC.

Our previous study reported that the methanol oxidation current at a Pt-C co-sputtered electrocatalyst under an O_2 atmosphere is higher than at a Pt electrode as the anode catalyst [10]. For reaction selective cathode catalysts, there have been several reports of Pt/Ru, Pt/Sn, and Ru_xSe_y as possible electrocatalysts [11], but these do not produce a high current density for the ORR. Unexpectedly, a commercially available Pt/C electrocatalyst was shown to have reaction selectivity for ORR [12]. However, it is difficult for a Pt-based cathode to reduce the MOR current to zero.

We have focused our attention on the cathode catalyst for the MRFC, which requires a high ORR activity and negligible MOR activity. Non-platinum electrocatalysts, e.g., Ru_xSe_y [11], a carbon alloy [13, 14], M1-CNO [15], M1-CNO (M1=Ta, Zr) [16], M2-C-N [17], and M2-C-N-B (M2=Co,

Fe) [18] appear to be suitable cathode catalysts. Multi-target sputtering can be a powerful technique for the preparation of cathode materials, and allows for the easy control of cathode composition [19-21]. In particular, reactive sputtering enables one to introduce N atoms to a metal-based catalyst layer from N_2 gas. In this study, we report that a Co-C-N electrocatalyst prepared by reactive sputtering at 773 K displayed high ORR activity in the presence of methanol.

2. Experiment

Co-C-N thin-layer electrocatalysts were prepared by a reactive sputtering method using a load-lock type sputtering system (ULVAC, CS-200S). A Co disk and two C disks of 8-mm diameter were used as the sputtering target. An Au flag electrode of 8-mm diameter and 0.05-mm thickness was used as the sputter-deposition substrate for the electrochemical measurements and for the physical characterizations. The substrate was washed by ultrasonic agitation first in acetone and then in Milli-Q water for 10 minutes each before being placed in the sputtering system. The reactive sputtering procedure is as follows: a rotating holder equipped with the substrate was installed in a vacuum chamber, and the chamber was evacuated to a base pressure of 3.0×10^{-4} Pa. The substrate was etched at an output of 200 W for 120 s in order to clean its surface. Subsequently, Ar (99.9999%) and N_2 (99.999%) gases (volume ratio is 11:1) were introduced into the chamber to a pressure of 5.0 Pa, and Co and C were simultaneously sputtered onto the substrate. During the sputtering, the substrate holder was rotated at 10 rpm, and the substrate temperature was controlled from room temperature (r.t.) to 773 K.

The prepared Co-C-N surface was observed using a scanning electron microscope (SEM: JSM-6060A, JEOL Ltd.) at 20 kV, and its composition was analyzed by energy dispersive spectroscopy (EDS: JED-2300, JEOL Ltd.). The bulk structure was measured by X-ray diffraction (XRD: XD-D1, Shimadzu Corporation) using CuKα radiation at 30 mA, 30 kV, in the 2θ range from 20 to 80 degrees.

The electrochemical measurements were performed using a potentiostat (HAB-151, Hokuto Denko Corporation) and a three-electrode glass cell consisting of the prepared Co-C-N electrocatalyst as the working electrode, a Pt wire as the counter electrode, and Ag/Ag_2SO_4 as the reference electrode. A supporting electrolyte of a 0.5 mol dm^{-3} H_2SO_4 solution was prepared by diluting concentrated H_2SO_4 (special grade of Wako Pure Chemical Industries, Ltd.) with Milli-Q water. All electrode potentials in this study were referenced to the normal hydrogen electrode potential (NHE) at the same temperature. Prior to the measurements, the working electrode was electrochemically cleaned by a potential cycle of 0–1.0 V vs. NHE at the rate of 10 mV s^{-1} in a N_2-saturated 0.5 mol dm^{-3} H_2SO_4 solution (N_2: 99.999%) for 60 min so that the electrode surface was stabilized. The last cycle of the voltammograms was recorded as the background cyclic voltammograms (CVs).

Oxygen reduction at the prepared Co-C-N electrocatalyst was evaluated from the current-potential (i-E) curves obtained in the O_2-saturated 0.5 mol dm^{-3} H_2SO_4 solution. The i-E curves were measured at the sweep rates of 0.1 and 10 mV s^{-1}. To investigate reaction selectivity, the i-E curves were obtained in an O_2-saturated 0.5 mol dm^{-3} H_2SO_4 + 1 mol dm^{-3} CH_3OH (special grade of Wako Pure Chemical Industries, Ltd.) solution at the sweep rate of 10 mV s^{-1}. All current values were normalized to a current density using the geometric surface area of the electrode, and all electrochemical measurements were conducted at 298±1 K.

3. Results and Discussion

The Co-C-N electrocatalysts were prepared by the reactive sputtering at various substrate temperatures and characterized by XRD, SEM, and EDS. The prepared Co-C-N electrocatalysts are presented as $Co_xC_yN_z$, with the subscripts referring to atomic ratios that were calculated by EDS measurement. Within the figures, the substrate temperature is included in parentheses after each electrocatalyst. Figure 1 shows the XRD patterns of the prepared Co-C-N electrocatalysts, indicating that the Co-C-N catalyst has an amorphous phase with a broad peak at approximately 26 degrees originating from the natural graphite carbon (002) [22]. There is no peak of the metallic Co phase. Therefore, the prepared layer contains both Co and N in the C phase. However, our previous study had shown that the Pt-C co-sputtered electrode had a Pt and C phase-separated structure [10].

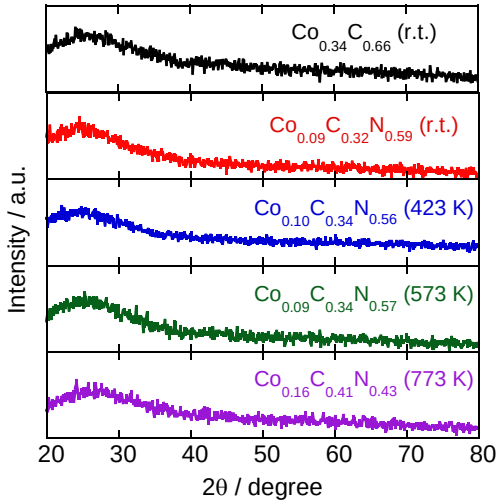

Fig. 1 XRD patterns of the sputtered Co-C and the Co-C-N electrocatalysts prepared at r.t., 423 K, 573 K and 773K.

The SEM images of the prepared Co-C-N electrocatalysts in Fig. 2 show that the surfaces of the electrocatalysts are smooth and clear of any particles. The changes in Co-C-N composition for the different electrocatalysts as seen in Figs. 1 and 2 were a result of changing only the substrate temperature, while keeping other conditions constant. The reaction between N_2 gas and the depositing materials during the sputtering process is therefore dependent on the substrate temperature.

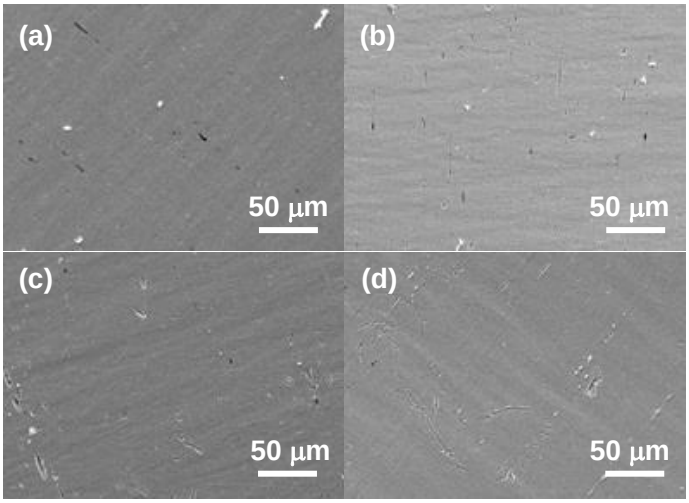

Fig. 2 SEM images of the sputtered Co-C-N electrocatalysts; (a) $Co_{0.09}C_{0.32}N_{0.59}$ (r.t.), (b) $Co_{0.10}C_{0.34}N_{0.56}$ (423 K), (c) $Co_{0.09}C_{0.34}N_{0.57}$ (573 K), and (d) $Co_{0.16}C_{0.41}N_{0.43}$ (773 K).

Figure 3 demonstrates the background CVs of the prepared Co-C-N electrocatalysts. There is no current peak based on the adsorption/desorption of the H or OH species similar to that observed at the Pt electrode. Because the electric double-layer capacity increases from the background CVs in Fig. 3, it can be inferred that the surface area of the electrocatalysts is increasing with the increase in substrate temperature. Therefore, substrate temperature was found to influence the electrochemical surface area of the electrocatalyst. In addition, no Co dissolution was observed from the background CVs. Consequently, the prepared Co-C-N was found to be an electrochemically stable electrode.

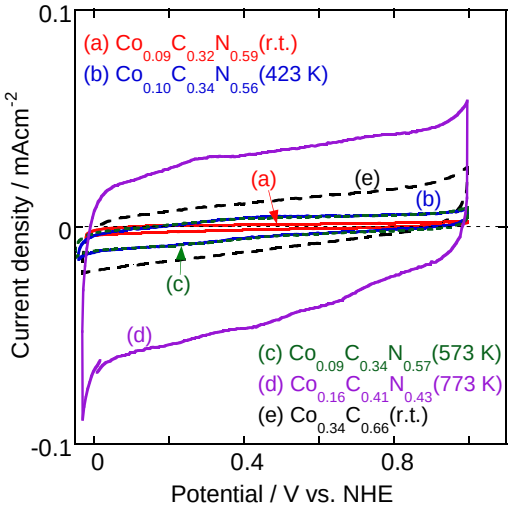

Fig. 3 Background cyclic voltammograms of the sputtered Co-C and the Co-C-N electrocatalysts prepared at r.t., 423 K, 573 K and 773K in a N_2-saturated 0.5 mol dm^{-3} H_2SO_4 solution. Sweep rate: 10 mV s^{-1}.

Figure 4 shows ORR voltammograms obtained in the O_2-saturated 0.5 mol dm^{-3} H_2SO_4 solution without any methanol. The results show that the diffusion limited current increases with increasing substrate temperature. Also, the onset potential of the prepared Co-C-N at 773 K was found to be significantly enhanced when compared to the other electrocatalysts. Consequently, the ORR activities were found to be improved with the increase of substrate temperature from r.t. to 773 K.

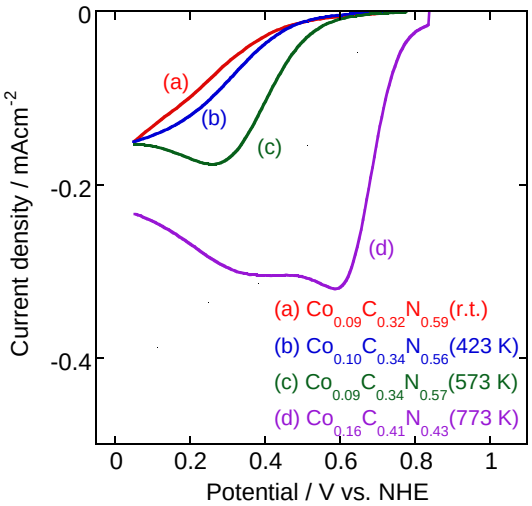

Fig. 4 Voltammograms of oxygen reduction at the sputtered Co-C-N electrocatalysts prepared at r.t., 423 K, 573 K and 773K in an O_2-saturated 0.5 mol dm^{-3} H_2SO_4 solution. Sweep rate: 10 mV s^{-1}. Voltammograms were measured at r.t.

In comparison, Fig. 5A shows that Pt electrocatalysts have a high activity for both methanol oxidation and oxygen reduction, which are represented by curves (i) and (ii), respectively. Accordingly, in the presence of both methanol and oxygen, a mixed curve (iii) is observed as both MOR and ORR simultaneously occur. However, analysis of the activity of the prepared Co-C-N electrocatalyst at 773 K shows only the ORR property in the presence of methanol, seen in curve (iii) of Fig. 5B. This result strongly suggests that only the ORR occurs, without any accompanying MOR. A comparison of curves (iii) in both Figs. 5A and 5B, the ORR currents of the Pt and Co-C-N electrocatalysts are observed to be < 0.65 V vs. NHE and at < 0.85 V vs. NHE, respectively.

Therefore, the ORR activity of the Co-C-N electrocatalyst was observed to be superior to that of the Pt electrocatalyst in the presence of methanol.

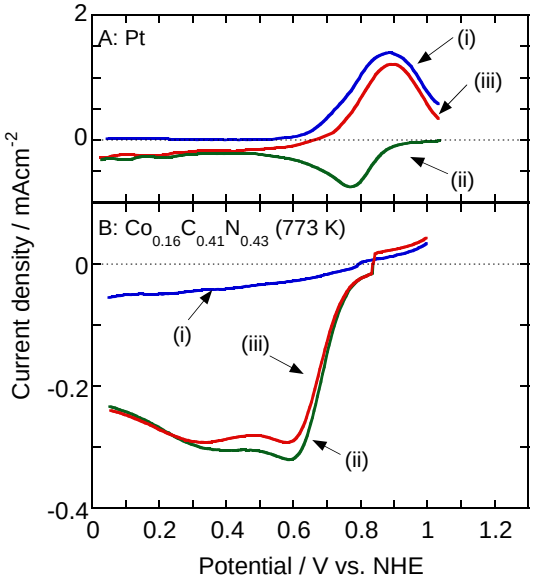

Fig. 5 Voltammograms of oxygen reduction and methanol oxidation at A) the sputtered Pt and B) the sputtered Co-C-N (773 K) electrocatalyst in (i) N_2-saturated 0.5 mol dm^{-3} H_2SO_4 + 1 mol dm^{-3} CH_3OH, (ii) O_2-saturated 0.5 mol dm^{-3} H_2SO_4, and (iii) O_2-saturated 0.5 mol dm^{-3} H_2SO_4 + 1 mol dm^{-3} CH_3OH. Sweep rate: 10 mV s^{-1}. Voltammograms were measured at r.t.

Finally, in order to compare the ORR mechanism between the prepared Co-C-N electrocatalyst and Pt electrode, Tafel plots of the two electrodes are shown in Fig. 6. Two slopes of 60 and 120 mV $decade^{-1}$ are obtained in the Tafel plots of the Co-C-N electrocatalyst as well as the Pt electrode. Therefore, we postulate that the ORRs at the Co-C-N electrocatalyst and the Pt electrode occur via the same mechanism. Based on these results, the Co-C-N sputtered electrocatalyst was found to possess characteristics that would allow it to function as an effective MRFC cathode catalyst.

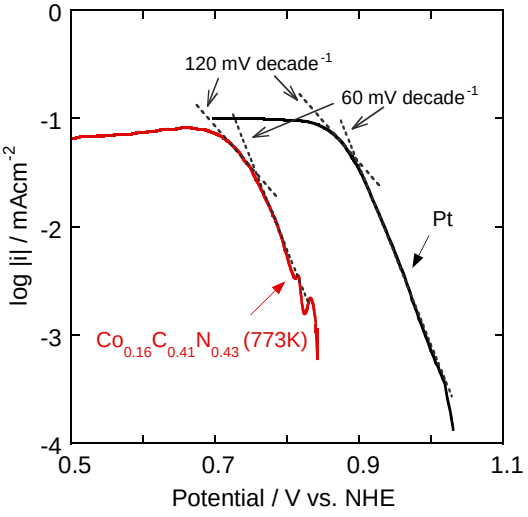

Fig. 6 Tafel plot of oxygen reduction reaction at the sputtered Pt and the sputtered Co-C-N electrocatalysts (773 K) in an O_2-saturated 0.5 mol dm^{-3} H_2SO_4 solution. Sweep rate: 0.1 mV s^{-1}.

4. Conclusions

We succeeded in preparing Co-C-N electrocatalysts using a reactive sputtering technique. The ORR catalytic activity of the prepared electrode was found to be dependent on its composition and the substrate temperature. The $Co_{0.16}C_{0.41}N_{0.43}$ electrocatalyst prepared at 773 K showed the highest ORR activity and ORR selectivity in the presence of methanol in this study. The ORR mechanism of the Co-C-N electrocatalyst was postulated to be the same as that of the Pt electrode.

Acknowledgment

This work was supported by an Adaptable and Seamless Technology Transfer Program through Target-driven R&D Grant (AS231Z02288C) from the Japan Society and Technology Agency (JST), Japan.

References

[1] R. Dillon, S. Srinivasan, A.S. Aricò, and V. Antonucci, in: Fuel Cells Compendium, N. Brandon and D. Thompsett, Eds. Elsevier, Amsterdam, Netherlands, 2005, p. 167.
[2] D.C. Dunwoody, H. Chung, L. Haverhals, and J. Leddy, in: Alcoholic Fuels, S. Minteer, ed. Taylor & Francis, FL, 2006, p. 155.
[3] S. Prakash, W.E. Mustain, and P.A. Kohl, in: Micro Fuel Cells: Principles and Applications, T.S. Zhao, ed. Elsevier, Amsterdam, Netherlands, 2009, p. 1.
[4] Y.C. Park, D.H. Peck, S.K. Kim, S. Lim, D.H. Jung, and D.Y. Lee, Int. J. Hydrogen Energ., **36** (2011) 5655.
[5] R.S. Jayashree, S.K. Yoon, F.R. Brushett, P.O. Lopez-Montesinos, D. Natarajan, L.J. Markoski, and P.J.A. Kenis, J. Power Sources, **195** (2010) 3569.
[6] A.M. Creeth, K.J. Knuckey, and A.R. Potter, Abstract of Fuel Cells Science and Technology (2008) 3B.3.
[7] S.C. Barton, T. Patterson, E. Wang, F.T. Fuller, and A.C. West, J. Power Sources, **96** (2001) 329.
[8] D.C. Papageorgopoulos, F. Liu, and O. Conrad, Electrochim. Acta, **52** (2007) 4982.
[9] R. Kothandaraman, W. Deng, M. Sorkin, A. Kaufman, H.F. Gibbard, and S.C. Barton, J. Electrochem. Soc., **155** (2008) B865.
[10] M. Umeda, K. Nagai, M. Shibamine, and M. Inoue, Phys. Chem. Chem. Phys., **12** (2010) 7041.
[11] C. Lamy, A. Lima, V. LeRhun, F. Delime, C. Coutanceau, and J-M Léger, J. Power Sources, **105** (2002) 283.
[12] T. Sakai, S. Shironita, M. Inoue, and M. Umeda, Electrochemistry, **79** (2011) 349.
[13] H. Niwa, K. Horiba, Y. Harada, M. Oshima, T. Ikeda, K. Terakura, J. Ozaki, and S. Miyata, J. Power Sources, **187** (2009) 93.
[14] T. Iwazaki, H. Yang, R. Obinata, W. Sugimoto, and Y. Takasu, **195** (2010) 5840.
[15] M. Tamura, A. Ishihara, T. Tada, K. Matsuzawa, S. Mitsushima, and K. Ota, ECS Transactions, **16** (2009) 125.
[16] Y. Ohgi, A. Ishihara, K. Matsuzawa, S. Mitsushima, K. Ota, M. Matsumoto, and H. Imai, ECS Transactions, **33** (2010) 609.
[17] E.B. Easton, R. Yang, A. Bonakdarpour, and J.R. Dahn, Electrochem. Solid-State Lett., **10** (2007) B6.
[18] A. Garsuch, R. Yang, A. Bonakdarpour, and J.R. Dahn, Electrochim. Acta, **53** (2008) 2423.
[19] M. Umeda, H. Ojima, M. Mohamedi, and I. Uchida, J. Power Sources, **136** (2004) 10.
[20] M. Umeda, H. Sugii, and I. Uchida, J. Power Sources, **179** (2008) 489.
[21] C-G Lee, H. Ojima, and M. Umeda, Electrochim. Acta, **53** (2008) 3029.
[22] P. Kim, J.B. Joo, W. Kim, J. Kim, I.K. Song, and J. Yi, Catal. Lett., **112** (2006) 213.